Sensitivity of the Atlantic Meridional Overturning Circulation to Surface Forcing

Helen Pillar

Department of Earth Sciences

University of Oxford

A thesis submitted for the degree of

Doctor of Philosophy

Michaelmas Term 2013

Abstract

The determination of the mechanisms setting the strength and structure of the large scale circulation is a fundamental and long-standing problem in physical oceanography. In this thesis, we seek to explore the mechanisms contributing to the steady state and variability of the large scale flow, with a focus on better understanding the dynamics of the Atlantic meridional overturning circulation (AMOC).

In the first part of this thesis, we explore the linear sensitivity of the monthly mean subtropical AMOC to surface fluxes of buoyancy and momentum. Our approach is to use a numerical adjoint. Key insights are provided into the memory of the AMOC to historic atmospheric forcing. We find that significant memory to wind forcing is confined to timescales of less than a year. In contrast, we identify significant memory to surface buoyancy forcing spanning multi-decadal timescales and characterised by a large scale oscillation in the sign of sensitivity between the eastern and western North Atlantic basin. An important result is that to understand the origins of seasonal variability in the modelled AMOC, we must examine the response to a multidecadal history of atmospheric forcing.

In the second part of this thesis, a new tool is presented that enables a clean diagnosis of the force balance controlling the circulation regime for a Boussinesq fluid. Specifically, the tool is based on the development of the "rotational momentum" equations and sets of scalar "velocity potentials" and analogous "force functions". The latter allow the projection of all forces onto the acceleration of the vertical shears and external modes of overturning to be visualised in isolation. The rotational momentum decomposition is applied to the modelled circulation in idealised Atlantic and global configurations of the MITgcm, with a focus on elucidating the dynamics of the simulated AMOC. We discuss the key role played by the rotational buoyancy forcing right on the western boundary.

Acknowledgements

First and foremost, I thank my supervisors, Helen Johnson and David Marshall for all their guidance and support. I am grateful to Helen for keeping a keen eye on my progress and for always making time for me when there was really none to spare. I also thank Helen for helping me get out to sea. To David I am indebted for his encouragement, great kindness and mentorship over the last seven years, and for his boundless enthusiasm which inspired me to study oceanography back in my undergraduate days.

I owe huge thanks to many other people who have generously shared their expertise during the course of my studies. In particular, I thank Patrick Heimbach for enormous support with the adjoint model, for answering even the crazy questions, for hosting my visit to MIT and for saving the day when all hope seemed lost. Thanks are also due to Lars Czeschel for generously sharing his adjoint experiences. Mirek Andrejczuk, Ralf Geiring, David Baker, and the support team at OSC also provided invaluable technical assistance. I would like to acknowledge my funding agencies, NERC and the UKMO, and thank Matt Palmer for supporting my project from Exeter and for hosting my residency there. We are lucky to have a brilliant administrative team in the department and I am very grateful to Elaine Sherrott, Emma Brown and Yasuko Nakajima for all their help.

During my time at Oxford, I have felt privileged to have been based in an exciting and enthusiastic group. I am grateful to all members, past and present, for interesting discussions. Special thanks are due to Laure Zanna for all her advice and encouragement and David Munday, my MITgcm guru, for always keeping the door open.

I thank all of my friends in Oxford for their comradeship and for all the happiness over the past few years. Maria Broadbridge, Matt Thomas, and Matt Hills have also played a big role in keeping me sane from afar. Special thanks are due to Ivana Barisin, my brilliant officemate, for all her friendship and kindness, and also to Rob and Helena, for all the porridge during the final stages of my write-up. I would also like to thank the whole Weatherley family for welcoming me in and looking after me over the years.

Finally, I thank my parents and sisters for their love and unending support and for getting me through it all (despite not knowing exactly what I've been doing all this time), and I thank Sam for sharing everything over the last 4 years and for the excitement of everything to come.

ACC	Antarctic Circumpolar Current
AD	Algorithmic differentiation
AMOC	Atlantic meridional overturning circulation
ECMWF	European Centre for Medium Range Weather Forecasting
GCM	General circulation model
GIN	Greenland-Iceland-Norwegian
GM	Gent-McWilliams (eddy parameterisation scheme)
ITCZ	Inter-tropical convergence zone
KPP	K-profile parameterisation (of oceanic vertical mixing)
MAR	Mid-Atlantic Ridge
MDD	Meridional density difference (discrete)
MDG	Meridional density gradient (continuous)
MOC	Meridional overturning circulation (in the local $y - z$ plane)
NAO	North Atlantic Oscillation
NCAR	National Center for Atmospheric Research
NCEP	National Center for Environmental Prediction
OMIP	Ocean Model Intercomparison Project
PV	Potential vorticity
RAPID	The Rapid Climate Change Programme
SSS	Sea surface salinity
SST	Sea surface temperature
TLM	Tangent linear model
ZOC	Zonal overturning circulation (in the local $x - z$ plane)

Contents

Abstract iii

Acknowledgements v

Abbreviations vii

Contents 1

1 Introduction **3**

1.1 Background and Motivation 3

1.2 A Focus on 26.5°N 8

1.3 The AMOC in the 3D System 10

1.4 Thesis Objectives 12

1.5 Thesis Outline 13

2 Numerical Modelling Experiments **15**

2.1 Introduction 15

2.2 Modelling Philosophy 16

2.3 Model Selection 16

2.4 Model Description 17

2.4.1 Domain Discretisation 17

2.4.2 Approximate Dynamics 18

2.4.3 Thermodynamics 20

2.4.4 Mixing Parameterisations 20

2.4.5 Numerical Details 22
2.5 Model Configurations 23
2.5.1 Sector Model 24
2.5.2 Global Model 29
2.6 Summary 38

3 Pathways and Timescales of AMOC Variability 39
3.1 Introduction 39
3.1.1 Past Work 40
3.1.2 Present Objectives 43
3.2 Numerical Sensitivity Studies 44
3.2.1 Traditional Sensitivity Studies 44
3.2.2 Adjoint Sensitivity Studies 46
3.2.3 Obtaining the Adjoint 49
3.2.4 Technical Challenges 51
3.3 Experiment Design 53
3.3.1 Model Configuration 53
3.3.2 Objective Function Selection 53
3.3.3 Control Variables 54
3.3.4 Adjoint Model Execution 54
3.4 Numerical Experiment Results 55
3.4.1 Key Regions and Propagation Pathways 57
3.4.2 AMOC Memory to Wind and Buoyancy Variability 72
3.4.3 Importance of Seasonality in the Background State 74
3.4.4 Importance of Nonlinear Dynamics 75
3.5 Conclusions and Discussion 85
3.5.1 Limitations 86
3.5.2 Implications 88

4 Origins of Modelled AMOC Variability 91

4.1 Introduction . . . 91

4.1.1 Present Objectives . . . 91

4.2 Origins of Modelled AMOC Variability . . . 92

4.2.1 Estimated AMOC Variability . . . 92

4.2.2 Temporal Origins of AMOC Variability . . . 97

4.3 Conclusions and Discussion . . . 104

4.3.1 Limitations . . . 105

4.3.2 Implications . . . 106

5 Rotational Momentum Balance of the MOC: Introduction and Analytics 107

5.1 Introduction . . . 107

5.1.1 Motivation . . . 107

5.1.2 Past Work . . . 108

5.1.3 Present Aims . . . 109

5.1.4 Chapter Outline . . . 110

5.2 Methodology . . . 110

5.2.1 Vorticity - Vector Potential Formulation . . . 111

5.2.2 Barotropic and Overturning Potentials . . . 113

5.2.3 Relating the MOC and Velocity Potential . . . 119

5.2.4 Boundary Condition on the Barotropic Velocity Potential . . . 120

5.2.5 Rotational Momentum Equation . . . 122

5.2.6 Boundary Condition on the Barotropic Force Function . . . 125

5.3 New Analytical Results . . . 127

5.3.1 Generation of Overturning Circulations . . . 128

5.3.2 Ageostrophic Maintenance of the MOC . . . 130

5.4 Discussion and Conclusions . . . 133

5.4.1 Rotational Momentum Framework: Summary 133
5.4.2 Limitations 134
5.4.3 Analytical Solutions Summary 135

6 Rotational Momentum Balance of the MOC: Numerical Modelling Experiments 137

6.1 Introduction 137
6.1.1 Present Aims 137
6.2 Idealised Modelling Studies 138
6.2.1 Technical Details 138
6.2.2 Momentum Closure 142
6.2.3 Analysed State 145
6.2.4 Vertical Shear Modes 145
6.2.5 External Modes 148
6.2.6 AMOC Summary 151
6.2.7 Generation of the AMOC and ZMOC 154
6.3 Extension to Complex Global Geometries 175
6.3.1 Technical Details 175
6.3.2 Momentum Closure 177
6.3.3 Analysed State 177
6.3.4 MOC Overturning and External Modes 179
6.3.5 ZOC Overturning 193
6.3.6 Generation of the AMOC 195
6.4 Conclusions and Discussion 206
6.4.1 Limitations 207
6.4.2 Implications 209

7 Key Role of Western Boundary Buoyancy Gradients 211

7.1 Introduction 211
7.1.1 Past Work 211
7.1.2 Chapter Outline 215
7.2 A Linear AMOC-MDG Scaling 215
7.2.1 Derivation 215
7.2.2 Numerical Experiment Design 217
7.2.3 Results: A Range of AMOC States 218
7.2.4 Results: Empirical Support for the Linear Scaling 219
7.3 The "buoyancy-beta" Scaling 224
7.3.1 Derivation 224
7.3.2 Results: Empirical Support for the "buoyancy-beta" Scaling . 230
7.4 Conclusions and Discussion 232
7.4.1 Limitations 233
7.4.2 Implications 233

8 Conclusions **235**

8.1 Adjoint Sensitivity Analysis 235
8.1.1 Key Insights 236
8.1.2 Broader Implications and Further Work 238
8.2 Rotational Momentum Balance 240
8.2.1 Key Insights 241
8.2.2 Broader Implications and Further Work 242

Bibliography **245**

Chapter 1

Introduction

This thesis is an effort to improve our understanding of the mechanisms contributing to the Atlantic meridional overturning circulation (AMOC). We start by describing the importance of the AMOC in the global climate system and discuss what is known about the variability of the AMOC at present.

1.1 Background and Motivation

The transport of heat from the Equator to the poles is a key aspect of the Earth's climate system. Observational estimates of the total poleward heat transport (*Trenberth and Caron*, 2001; *Wunsch*, 2005) suggest that at middle and high latitudes, the poleward heat flux is principally achieved by the atmosphere, while in the tropics, the ocean plays the dominant role (figure 1.1a). On decomposing the global ocean heat flux into contributions from individual basins, it emerges that the Pacific transports heat poleward (i.e down-gradient) in both hemispheres, but the Atlantic transports heat northwards throughout the basin (figure 1.1b) (*Trenberth and Caron*, 2001).

The meridional redistribution of mass through the Atlantic basin is summarized by defining the AMOC. Formally, the AMOC is the zonally integrated meridional flux of mass and therefore represents the projection of the 3-dimensional Atlantic

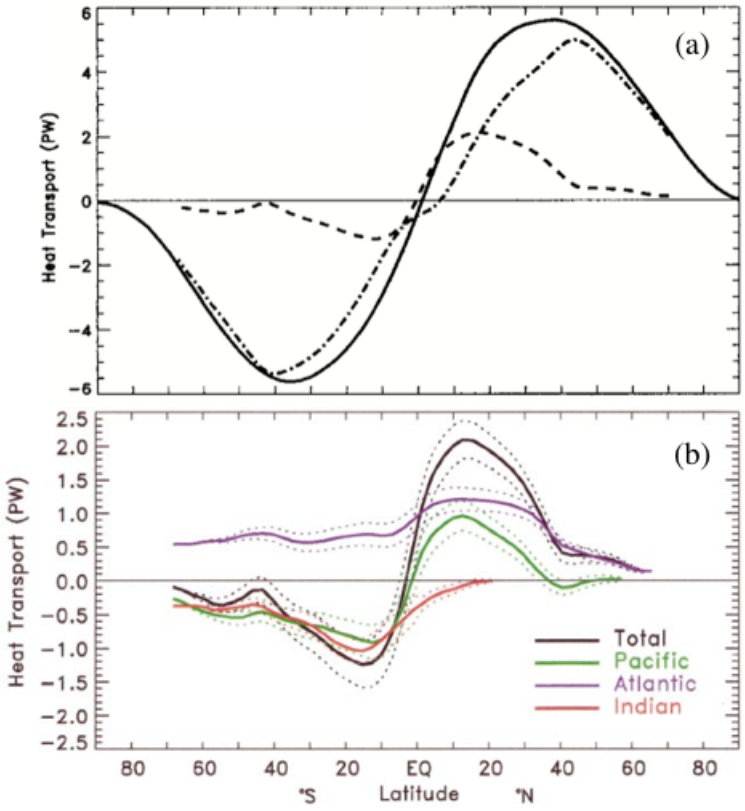

Figure 1.1: (a) The total northward heat transport required to cancel the radiative imbalance between the Equator and the poles (solid line) is achieved by contributions from the atmosphere (dash-dot line) and the ocean (dashed line), given here as estimates from *Trenberth and Caron* (2001). (b) The total oceanic heat flux (black line) across each latitude is decomposed into contributions from the major ocean basins. The Pacific transports heat polewards in both hemispheres, whereas the Atlantic transports heat upgradient in the South Atlantic. Both panels are taken from *Trenberth and Caron* (2001) (c)American Meteorological Society. Used with permission.

circulation onto the (2-dimensional) latitude-depth plane. It is characterized by upper ocean currents transporting relatively buoyant water to northern high latitudes where the waters become denser and sink. The deep return flow crosses the Equator and upwells in the region of the Antarctic Circumpolar Current (ACC) (*Sloyan and Rintoul*, 2000), closing the circulation in the latitude-depth plane. AMOC variability is expected to be a good indicator of ocean heat transport[1] variability because the

[1]In this chapter, the common expression "heat transport" is used synonymously with "enthalpy transport", although we acknowledge that heat is not a fluid property that can be advected by the circulation (*Warren*, 1999)[see][for further discussion]

mean vertical temperature gradient exceeds mean horizontal temperature gradients and state estimates (*Wunsch*, 1996), models (*Jayne and Marotzke*, 2001) and observations (*Johns et al.*, 2011) suggest ocean heat transport is dominated by advection of the mean temperature by velocity perturbations.

The maximum northward oceanic heat transport is achieved near 25°N in the Atlantic. Here, the northward oceanic heat transport is estimated as 1.3 ± 0.26 PW (1 PW = 10^{15} W) (*Ganachaud and Wunsch*, 2000), accounting for approximately one quarter of the total poleward heat transport that must be achieved by the atmosphere-ocean system at this latitude to ensure radiative equilibrium. The AMOC thus maintains a western european climate that is anomalously warm for its latitude and plays a key role in maintaining the extent of the arctic sea ice (e.g. *Winton*, 2003; *Mahajan et al.*, 2011). Furthermore, the North Atlantic is a key region for strong uptake of atmospheric CO_2 by the ocean (*Takahashi and Coauthors*, 2009, see figure 1.2a). Despite covering only 15% of the global ocean area, the North Atlantic stores 23% of the total anthropogenic CO_2 sequestered in the global ocean (*Sabine et al.*, 2004, see figure 1.2b). As a result the AMOC plays a critical role in partitioning CO_2 between the atmosphere and deep ocean reservoir.

Large ensembles of coupled model integrations indicate that over the course of the next century, a weakening of the AMOC is "very likely" (see section 10.3.4 of *Solomon et al.*, 2007), following warming (*Bindoff et al.*, 2007) and freshening (*Dickson et al.*, 2002; *Curry et al.*, 2003) of the high latitude North Atlantic and a concomitant reduction in deep water formation. However, the ensemble investigation simulates a broad range of AMOC states and as a result, the magnitude and timing of AMOC weakening is highly uncertain. Observational estimates of AMOC variability are too coarse (both temporally and spatially) to provide support for a weakening trend (*Bindoff et al.*, 2007). Although *Bryden et al.* (2005) suggested that the AMOC had decreased by 30% between 1957 and 2004, their estimate was based

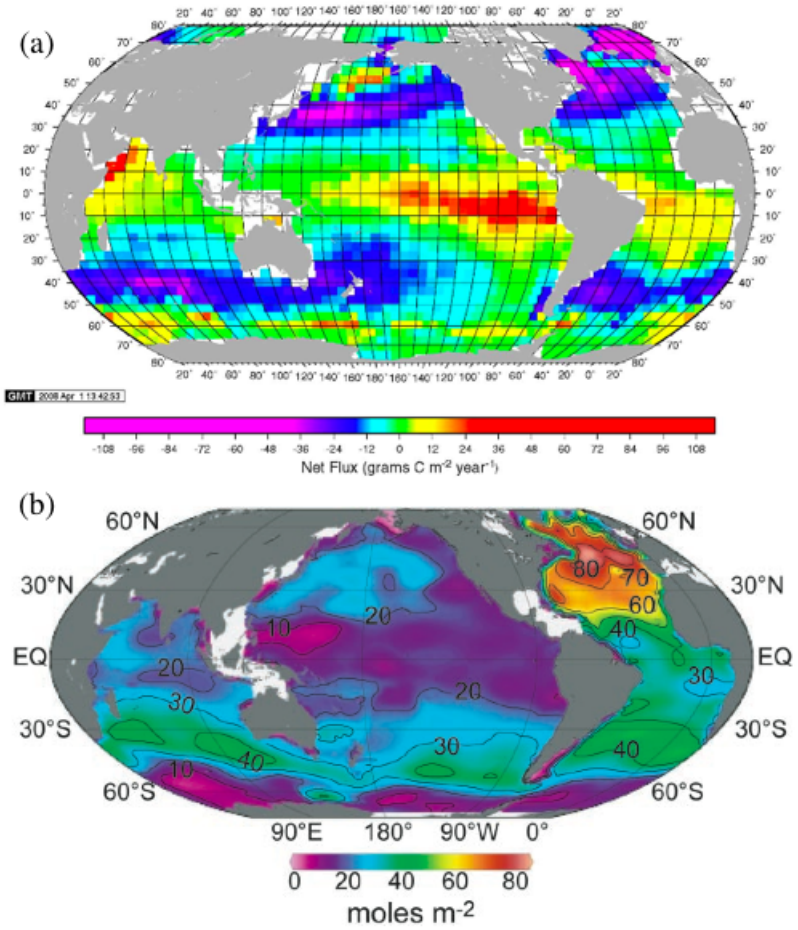

Figure 1.2: (a) Climatological mean annual sea-air CO_2 flux (g $Cm^{-2}yr^{-1}$) for non-El Niño conditions. The map is based on 3 million surface water pCO_2 measurements obtained since 1970. Figure (and adapted caption) from *Takahashi and Coauthors* (2009). (b) Column inventory of anthropogenic CO_2 in the ocean (mol m^{-2}). The highest inventories are associated with deep water formation in the North Atlantic. Total inventory of shaded regions is 106 ± 17 PgC. Figure (and adapted caption) from *Sabine et al.* (2004). The reader is referred to the original articles for full details of the calculations.

on only 5 hydrographic sections along 25°N. It has since been suggested that the inferred weakening can be explained by aliasing of seasonal variability in the AMOC (*Wunsch*, 1996; *Kanzow et al.*, 2010). Using a dynamically consistent state estimation, *Wunsch* (1996) conclude that between 1992-2004 a slight, but statistically significant, weakening of the net meridional North Atlantic volume flux above 1200 m is observed. The estimated rate of weakening is -0.19 ± 0.05 Sv yr^{-1}. However, no significant trend is detected in heat transport.

Numerical investigations have provided substantial evidence that the anticipated variability in the AMOC may have significant ramifications for global climate. Experiments in coupled general circulation models (GCMs) predict cooling over the North Atlantic (acting to offset predicted greenhouse-induced warming to some extent) and less notable warming over the South Atlantic, resulting from a weakening of the northward heat flux associated with the AMOC (e.g. *Manabe and Stouffer*, 1988; *Delworth et al.*, 1993; *Vellinga and Wood*, 2002; *Zhang and Delworth*, 2005). Basinwide cooling of the North Atlantic sea surface temperature (SST) characterizes a negative phase of the Atlantic multidecadal oscillation (AMO *Kerr*, 2000), which has been linked with AMOC variability (*Delworth and Mann*, 2000; *Knight et al.*, 2005). This general pattern of perturbed SST has been associated with anomalous intensification of the northeasterly trades and southward migration of the intertropical convergence zone (ITCZ) (e.g. *Dong and Sutton*, 2002; *Vellinga and Wood*, 2002; *Zhang and Delworth*, 2005). It has been suggested that this in turn, can affect the amplitude of the El Niño Southern Oscillation (ENSO) (*Timmermann et al.*, 2007), and alter precipitation patterns associated with the African and Indian monsoons (*Zhang and Delworth*, 2006). An anomalous increase in the meridional SST gradient may increase the baroclinicity of the lower troposphere, favouring storm growth (e.g. *Brayshaw et al.*, 2008) and linking the AMOC to variations in the storm track trajectory and intensity. This causal connection was made transparent in a recent study by *Woollings et al.* (2012). Applying regression analysis to an ensemble of coupled climate models, the authors show that at least 50% of the spread in simulated storm track response to anthropogenic greenhouse-gas forcing is due to differences in the simulated response of the AMOC. Similarly, *Pardaens et al.* (2011) identify a causal connection between the AMOC and patterns of regional sea level by demonstrating that the spread in predicted sea level change can be explained, in part, by the spread of predicted AMOC response across the ensemble. Both enhanced storm activity

and substantial rise in regional sea level are expected to have significant societal impacts over the coming century. The results of these two studies promote efforts to better understand the driving processes of the AMOC and to reduce uncertainty in the projected variability.

1.2 A Focus on 26.5°N

The potential consequences of abrupt change in the AMOC motivated the formation of the RAPID monitoring programs. Since April 2004 the RAPID array has continuously monitored the volume and heat flux associated with the AMOC at 26.5°N. The location of the array was chosen to incorporate the submarine cable that has provided estimates of the Florida Current transport for over 20 years (*Baringer and Larsen*, 2001), whilst also lying close to the meridional heat flux maximum. The placement is therefore favourable for reducing the challenge of monitoring ageostrophic transports in the western boundary jet and allowing estimation of ocean heat flux convergence in the North Atlantic (*Hirschi et al.*, 2003). A full description of the instrument calibration and array configuration during the course of the field campaign is presented by *Kanzow et al.* (2010).

At 26.5°N, it is of practical value to decompose the basin wide flow into three major contributions; Gulf Stream, Ekman, and midocean transports (*Kanzow et al.*, 2007; *Cunningham et al.*, 2007). In brief, direct estimates of the Gulf Stream transport, $T_{GS}(z,t)$, through the Florida Straits are based on measurements from voltage changes induced in a submerged telephone cable and historic hydrographic sections. The latter allow depth-dependence of the transport estimates to be recovered (*Baringer et al.*, 2008). Measurement of the Ekman component, $T_{EK}(z,t)$, is based on satellite scatterometer measurements. The depth-dependent profile is achieved by assuming the wind-driven transport is evenly distributed between 0-100 m depth. Measurement of the midocean component, $T_{MO}(z,t)$, relies on an array of perma-

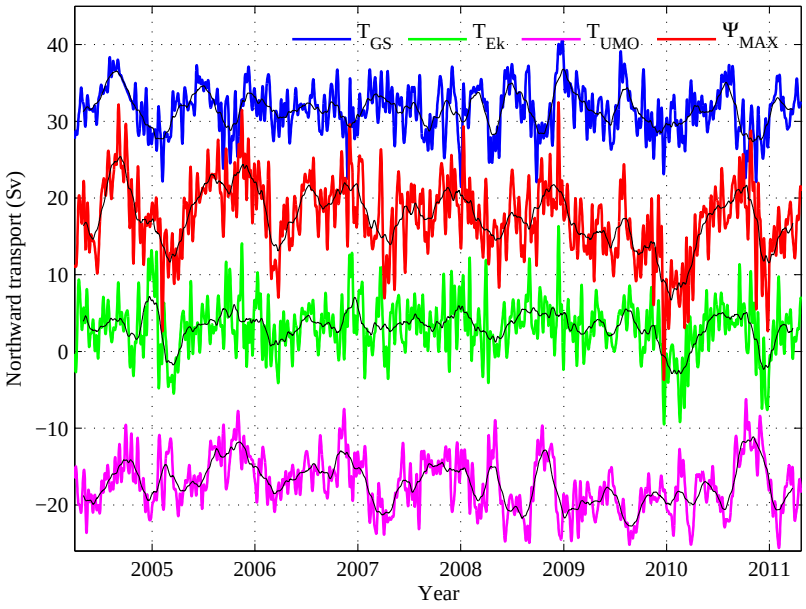

Figure 1.3: The coloured lines show timeseries of the AMOC, Ψ_{MAX} (red), and separate contributions from Gulf Stream, T_{GS} (blue), Ekman, T_{EK} (green) and upper mid-ocean, T_{UMO} (magenta) components (where the latter is found by integrating T_{MO} over the upper, northward flowing branch of the AMOC). The black lines show the timeseries low pass filtered using a 2-month running mean.

nent moorings on the east and west continental margins (and on the flanks of the Mid-Atlantic Ridge) mounted with temperature and salinity sensors. Using the thermal wind equations (e.g. *Vallis*, 2006), the meridional geostrophic velocity may be estimated from the cross-basin density gradients. $T_{MO}(z,t)$ also incorporates (i) the transport contribution from the western boundary current lying outside the Florida Straits using direct velocity measurements, and (ii) a barotropic signal that ensures mass conservation across the array.

In figure 1.3 we show the timeseries for each of the transport components for the full available data set. The net AMOC, Ψ_{MAX}, resulting from T_{GS}, T_{EK} and T_{UMO} combined is shown in red. Continuous monitoring has revealed many surprising results, including that interannual variability in the subtropical AMOC exceeds the amplitude of the low frequency variability expected over decades if change. Further-

more, low frequency trends from sparse hydrographic surveys (*Bryden et al.*, 2005) are mostly explained by aliasing of seasonal variability (*Kanzow et al.*, 2010). Although the AMOC appears to exhibit a robust seasonal cycle during the first five years of observations - which has been attributed to the wind stress curl on the eastern boundary (*Chidichimo et al.*, 2010) and predicted to be representative of much longer time periods (*Kanzow et al.*, 2010) - the seasonal cycle is not present in the sixth year of measurement. Furthermore, in the winter of 2009/2010 the AMOC appears to reverse for a few months. The mechanisms behind such dramatic excursions have yet to be fully explained (*Srokosz et al.*, 2012).

1.3 The AMOC in the 3D System

Above, we have discussed the net meridional overturning in the latitude-depth plane. However, there is significant longitudinal variability in the Atlantic circulation which is masked on zonal integration. In figure 1.4 we present a schematic of the major currents in the Atlantic basin (*Srokosz et al.*, 2012). The Agulhas leakage (around South Africa) is the principal source of warm salty waters that enter the Atlantic to form the upper limb of the AMOC (*Biastoch et al.*, 2008). This leakage takes place as large mesoscale eddies are shed from a complex retroflection regime. The upper limb of the AMOC crosses the Equator, forming an intense boundary jet on the western side of the basin. Upon separation, Gulf stream waters either recirculate in the subtropical gyre or migrate north-eastwards in the North Atlantic Current, eventually entering the marginal seas. Here, heat loss to the atmosphere and salinification due to brine rejection by sea ice formation leads to densification. Deep water formed in the marginal seas re-enters the major Atlantic basin and flows southward to eventually upwell in the vicinity of the ACC.

As discussed by *Lozier et al.* (2010) the conveyor model (*Broecker*, 1991) is known to be a gross oversimplification of the Atlantic overturning, and some attempt has

been made to adopt an idealised view that more faithfully represents he ocean's complexity (*Richardson*, 2008). Despite this, many ideas associated with the conveyor model have been translated into over-simplistic notions for the dynamics of the AMOC. These include that the overturning is principally achieved in boundary currents, coherent in space and time, and highly sensitive to changes in deepwater production as a result. However, recent contributions from modelling and observational studies have challenged this paradigm, revealing the greater spatial and temporal complexity of the Atlantic overturning.

The existence of deep western boundary currents (DWBCs) was proposed by *Stommel* (1958), assuming steady-state dynamics of he large-scale circulation. Early modelling studies (*Holland and Lin*, 1975) revealed that instabilities in the western boundary current system could spawn strong recirculations in the vicinity of the jet. Theoretical developments led to the recognition of potential vorticity (PV) homogenisation as a key signature of the eddy-driven recirculation (*Rhines and Young*, 1982). This facilitated the identification of extensive recirculations in observational data sets and prompted the hypothesis that deep waters may take an alternative path to Stommel's DWBC, by spreading through the ocean interior (*Lozier*, 1997). Float release experiments (*Bower et al.*, 2009) and modelling studies (e.g. *Bower et al.*, 2011) have subsequently provided substantial support for the thesis that the DWBC is not the primary pathway taken by water parcels, following export from the Labrador Sea. Furthermore, *Dengler et al.* (2004) have shown that at present, the Atlantic DWBC at 8°S is observed to operate as a series of coherent eddies, as opposed to a laminar boundary flow.

The assumption that the overturning is continuous through time and space has recently been challenged by observational and modelling evidence of a break in coherence at the subtropical-subpolar gyre boundary. *Lozier et al.* (2010) examine historical hydrostatic data for the period 1950-2000 and determine that the sub-

Figure 1.4: A simplified schematic of the AMOC showing both the overturning and gyre recirculation components. Warm water flows north in the upper ocean (red), gives up heat to the atmosphere (atmospheric flow gaining heat represented by the changing colour of the broad arrows), sinks and returns as a deep cold flow (blue). Figure and (partial) caption from *Srokosz et al.* (2012) (c)American Meteorological Society. Used with permission.

tropical gyre has weakened over the 50 year period, whilst the subpolar gyre has strengthened. *Bingham et al.* (2007) examine the simulated AMOC variability in a range of ocean models and find that variability to the north of 40°N has a notable decadal component, whilst variability further south is dominated by higher frequencies. They stress that caution must be taken in extrapolating variability from a single monitored latitude to elsewhere in the basin. Finally, we note that patterns of potential predictability (see *Pohlmann et al.*, 2004, for details) assessed the AMOC and its associated heat transport in a state estimation product, varies with latitude, and changes notably between the subtropical and subpolar gyres (*Tiedje et al.*, 2012).

1.4 Thesis Objectives

In this thesis, we seek to explore the dynamics governing the Atlantic meridional overturning circulation (AMOC), via the application of two distinct and innovative

tools. By employing (1) the numerical adjoint of a GCM, we seek to determine the memory of the subtropical AMOC to perturbations in the surface forcing fields, elucidating teleconnection mechanisms and quantifying expected anomalies in the AMOC on seasonal to decadal timescales. By deriving (2) the "rotational momentum" budget, we seek to elucidate the force balance setting the strength and structure of the circulation in complex GCMs.

1.5 Thesis Outline

In chapter 2, we provide an introduction to the numerical framework that will be used in the following chapters of this thesis. In chapter 3, we introduce the adjoint approach to sensitivity studies, highlighting the advantage of this method over traditional approaches. We then proceed to explore the linear sensitivity of the monthly mean subtropical AMOC to global surface fluxes of buoyancy and momentum in a GCM. We present a thorough assessment of the teleconnections that may influence the monthly mean subtropical AMOC on timescales of 1 month to 15 years. In chapter 4, we estimate the origins of AMOC variability on sub-seasonal to decadal timescales by projecting global surface fluxes of buoyancy and momentum from reanalysis onto the corresponding sensitivity patterns derived in chapter 3.

In chapter 5 we present a new tool that enables a clean diagnosis of the force balance controlling the circulation regime for a Boussinesq fluid in hydrostatic balance. Specifically, the tool is based on the development of the "rotational momentum" equations and the introduction of a set of scalar "velocity potentials" and corresponding "force functions". By design, we are able to examine the force balances controlling the overturning and depth-integrated circulations separately. Furthermore, the overturning is decomposed into "external mode" and "vertical shears" components for independent examination. We present analytical solutions for the vertical shears component of the overturning. In chapter 6 we apply the rotational

momentum decomposition to the modelled circulation in idealised Atlantic and globally realistic configurations of a hydrostatic GCM, with a focus on elucidating the dynamics of the simulated AMOC. We present numerical solutions for the vertical shears velocity potential and corresponding force function in both cases. For the idealised basin, this fully describes the modelled AMOC and we are able to demonstrate that diagnosis of the rotational momentum budget can be both straightforward and highly accurate. In chapter 7 we employ the rotational momentum equations to derive simple scalings relating the AMOC to specific measures of the meridional density gradient (MDG). Finally, in chapter 8 we present our conclusions for the work as a whole and suggest important avenues for future research.

Chapter 2

Numerical Modelling Experiments

2.1 Introduction

The ocean exhibits variability across a broad range of spatial and temporal scales. Large scale circulations spanning entire basins recirculate on decadal to millennial timescales. These large scale flows are subject to instabilities that spawn eddies on the scale of kilometers at high latitudes with typical life cycles of weeks to months. These eddies are themselves subject to instabilities, continuing the turbulent cascade of properties across all scales; from planetary scale, through the mesoscale, to the micro-scale. General circulation models (GCMs) have become an invaluable experimental tool for probing the dynamics of this complex, nonlinear system. They serve as controlled laboratories in which key aspects of the system may be studied in isolation, allowing the processes governing the variability of past, present and future ocean states to be explored (see *Griffies*, 2004). Scientific bases may thus be rigorously and repeatedly tested, and further refined.

2.2 Modelling Philosophy

In pursuit of a deeper mechanistic understanding of the ocean circulation, it is of considerable value to construct highly simplified models of the real system. Removal of complex geometry and reduction of the atmosphere to a prescribed boundary condition are examples of the gross simplifications that will be made in the experiments performed in this thesis. Given these - and many other - idealisations, care will be taken in interpreting the model results. However, it is emphasised here that the current aim is to provide some insight into causal mechanisms controlling AMOC variability, as opposed to producing quantitative predictions.

2.3 Model Selection

In the following chapters of this thesis, results are presented from the solution of the hydrostatic primitive equations in one highly idealised and one realistic global configuration of the MITgcm (*Marshall et al.*, 1997a,b). This choice of dynamical core is primarily motivated by the existence of fully-developed, well-maintained and efficient tangent linear and adjoint complements to the standard forward model, permitting the sensitivity analysis presented in chapters 3 and 4 of this thesis. A pre-existing adjoint of a complex GCM is both rare and extremely valuable. Moreover, great expertise has been invested in developing the MITgcm and its adjoint in synchrony and exact consistency, via the application of an algorithmic differentiation (AD) tool. This discussion will be continued in more detail in chapter 3. The model is well documented in the scientific literature and only details relevant to the present study will be repeated below. The model has a long history of use in the investigation of atmosphere, ocean and coupled climate system dynamics. A list of previous applications is available on the model webpage (http://mitgcm.org/).

2.4 Model Description

In this section, some important features shared between the two model configurations employed in this thesis are discussed. Notable differences in geometry, boundary conditions and sub-grid scale parameterisations are identified in the following section.

2.4.1 Domain Discretisation

The model is formulated in depth, z, coordinates on a spherical polar grid. Partial cells are used to better represent bottom topography whilst focusing resolution in the upper ocean. The horizontal resolution in all configurations of the model is $1^\circ \times 1^\circ$. Fundamentally important processes - most notably mixing associated with the highly energetic mesoscale eddy field - remain unresolved in the experiments below. This important omission will be recalled when conclusions are drawn from the coarse resolution modelling studies. However non-eddying dynamics are considered most suitable here for four principal reasons:

1. Most critically, the utility of the linear sensitivity study performed in chapter 3 is severely limited in eddying regimes.

2. A clear presentation of the rotational momentum budget is sought, and most easily delivered in chapter 6 for non-eddy resolving regimes.

3. Coarse resolutions ensure ensemble integrations of the MITgcm in chapters 4 and 7 are computationally tractable.

4. We seek to understand the nonlinear system in a laminar state before tackling the eddying regime.

The primitive variables are computed on an Arakawa C grid (*Arakawa and Lamb*, 1977). C grid staggering is a natural choice when using centred differencing schemes,

facilitating the evolution of velocity components from pressure gradients. Furthermore, the governing equations may be written in flux form, allowing volume conservation to be easily enforced. The C grid does, however, suffer from one computational mode that arises from velocity interpolation required for computation of the Coriolis force. This mode is manifested as spurious minima in the dispersion relation for inertia-gravity waves. A solution proposed by *Adcroft et al.* (1999) avoids interpolation issues by solving for the velocity components on both the C and D grids, periodically recoupling the two. Although an imbalance between the associated number of discrete momentum and continuity equations renders this an imperfect solution (see the discussion in *Ham*, 2006), priority here is given to the generation of useful model experiments and the avoidance of intolerable levels of grid-scale noise. The 'C-D' scheme of *Adcroft et al.* (1999) is therefore adopted in the computation of the Coriolis force below.

2.4.2 Approximate Dynamics

The modelled ocean is assumed to be Boussinesq; density anomalies are only considered where they appear in terms multiplied by g, the gravitational acceleration. As discussed by *Cushman-Roisin and Beckers* (2011), the Boussinesq assumption is a standard approximation to the governing equations, since within an ocean basin, density anomalies rarely exceed 0.3% of the reference value. The Boussinesq approximation is employed throughout the ocean modelling community, achieving greater simplicity without appreciable loss of accuracy.

The modelled ocean is assumed to be in hydrostatic equilibrium. This balance between the vertical pressure gradient and gravity dominates at the scales of interest in this thesis, where the characteristic horizontal scale (L) of motion greatly exceeds the characteristic vertical scale (D). This assumption breaks down when D and L are comparable, for processes on scales that are not properly resolved in this study

(e.g convective plume formation, *Jones and Marshall*, 1993).

Interaction between the ocean and atmosphere is reduced to the prescription of a surface boundary condition. The simplest prescription applied below is a Newtonian relaxation on both the sea surface temperature, SST, and salinity, SSS:

$$\frac{\partial}{\partial t}SST = \frac{1}{\tau_T}(SST^* - SST), \tag{2.1}$$

$$\frac{\partial}{\partial t}SSS = \frac{1}{\tau_S}(SSS^* - SSS), \tag{2.2}$$

where $\tau_{T,S}$ are the restoring timescales and SST^*, SSS^* are the restoring profiles. The associated sensitivities, $\lambda_{T,S}$, (also called coupling coefficients or feedback factors) are given by

$$\lambda_T = \rho_0 C_p \Delta z_1 / \tau_T, \tag{2.3}$$

$$\lambda_S = \Delta z_1 / S_0 \tau_S, \tag{2.4}$$

where ρ_0, S_0 are reference values for the density and salinity respectively, C_p is the specific heat of sea water, and Δz_1 is the thickness of the upper ocean layer. SST relaxation (2.1) can be derived from the assumption that the ocean is in contact with an atmospheric equilibrium state (*Haney*, 1971) and is supported by the observation that the atmosphere drives SST anomalies on sub-annual timescales (*Davis*, 1976). SSS relaxation (2.2) is devoid of physical justification, but allows a realistic surface salinity distribution to be maintained. If SST and SSS match the restoring profiles, the surface thermohaline fluxes vanish. In the experiments configured below with a realistic basin geometry, surface fluxes of heat, freshwater and momentum are prescribed, but the restoring (2.1-2.2) is retained to prevent model drift.

2.4.3 Thermodynamics

The potential density field evolves nonlinearly in response to changes in salinity, S, and potential temperature, θ, following *Jackett and McDougall* (1995). Thermal expansion and haline contraction coefficients are assumed to be constant. Hereafter potential temperature/density is referred to as temperature/density. A simple representation of sea ice is included by imposing a lower limit on the model temperature, $\theta_{\min} = -1.9°\text{C}$. Excursions below this are reset to $\theta_{\min}$ and the inferred latent heat of fusion is incorporated into the local heat flux. The equation of state therefore remains valid throughout the region of θ-S space occupied by the model.

2.4.4 Mixing Parameterisations

Important physical processes occurring on sub-grid scales are not explicitly resolved and must be represented via relation to the large scale flow. In stably stratified regions, mixing of tracers is dominated by energetic, mesoscale eddies spawned through baroclinic instability. These eddies form near the Rossby Radius of Deformation, L_D, which depends on the stratification and the inverse planetary vorticity, and therefore decreases towards the poles (see *Chelton et al.*, 1998). On a $1° \times 1°$ grid, L_D is poorly resolved in the Tropics, and unresolved at high latitudes. An eddy parameterisation scheme must be incorporated to mimic the conversion of mean potential energy to eddy potential energy, and produce a realistic modelled state with a sensible distribution of tracers.

It has long been recognised that mixing in the ocean acts primarily along neutrally buoyant directions, i.e tangent to surfaces of locally defined potential density (*Iselin*, 1939; *Montgomery*, 1938), (see discussion in *Pedlosky*, 1996, chapter 4). However, early z-coordinate GCMs (e.g *Cox*, 1984) parameterised eddy stirring as a Fickian diffusion along geopotential surfaces. These simulations were plagued by spuriously large diapycnal transfers, the so-called "Veronis effect" (*Veronis*, 1975). Proper

inclusion of neutral mesoscale physics has led to important improvements including a better representation of water masses, thermocline gradients, surface heat fluxes and deep water formation (*Danabasoglu et al.*, 1994; *Danabasoglu and McWilliams*, 1995; *Hirst and McDougall*, 1996). Rotation of the diffusion tensor into alignment with the neutral surfaces (*Redi*, 1982) and introduction of an adiabatic mixing scheme for mesoscale eddies (*Gent and McWilliams*, 1990, hereafter GM) are thus recognised as two of the most important advances that have been made in the history of ocean modelling (*Griffies*, 2004).

The GM scheme simulates the removal of geostrophic shear via the growth of mesoscale eddies, reducing the potential energy of the mean state. It has been shown that this diffusion may be equivalently expressed as an eddy-induced transport (or "bolus") velocity (*Gent et al.*, 1995), in analogy to the Stokes drift in the theory of surface gravity waves (*Greatbatch*, 1998). The redistribution of tracers is thus achieved by the total "effective transport velocity" (*Plumb and Mahlman*, 1987), which is the sum of Eulerian mean and bolus contributions. In this study, *Redi* (1982) isopycnal diffusion is employed in conjunction with *Gent and McWilliams* (1990) isopycnal mixing in skew flux form (*Griffies*, 1998). For simplicity, the eddy mixing coefficient, κ_{GM}, is assumed constant (and positive) in all simulations below. It is noted that there is significant evidence for inverse cascades (associated with $\kappa_{\mathrm{GM}} < 0$) on submesoscales (*Waterman and Jayne*, 2011; *Venaille et al.*, 2011). In unstably stratified regions, mixing is achieved through the formation of convective plumes on horizontal scales $\leq$ 1 km (e.g. *Marshall and Schott*, 1999). Here, convection is parameterised by increasing the vertical diffusivity to 100 $\mathrm{m^2 s^{-1}}$ in regions with an unstable density profile. This rapidly eliminates static instability whilst avoiding numerical instabilities arising from instantaneous convective adjustment (*Cessi and Young*, 1996). Note that both convection and GM eddy mixing operate in regions of steep isopycnal slope. The presence of parameterised eddies can thus interfere with

deep convection and mixed layer formation unless carefully treated. Furthermore, the GM scheme is numerically problematic along steeply sloping density surfaces since the resulting, large bolus velocities can violate the CFL criterion (e.g *Durran*, 1999). To avoid this problem, the GM scheme is gently tapered as isopycnals steepen past a specified slope (1/100), following the scheme proposed by *Gerdes et al.* (1991).

The K-Profile Parameterization (KPP) scheme proposed by *Large et al.* (1994) is also employed to represent unresolved processes entailed in vertical mixing. In the present formulation, vertical mixing in the interior is governed by shear instability. The turbulent boundary layer is handled separately, following Monin-Obukhov similarity theory, and permits enhanced vertical mixing under the destabilizing influence of surface buoyancy forcing. Asymptotic matching of the surface and interior profiles allows interaction across the base of the turbulent boundary layer.

2.4.5 Numerical Details

Despite the inclusion of more sophisticated, isopycnal eddy parameterisations, simple horizontal and vertical diffusion of heat, salt and momentum is still required for numerical stability. Background viscous/diffusion parameters are selected to guarantee numerical stability under the chosen grid space and time step sizes following *Adcroft* (1995).[1] Tracer and momentum equations are evolved synchronously (although asynchronous time-stepping can offer accelerated convergence, it comes at the price of distorting wave propagation speeds (*Bryan*, 1984)).

[1]For example, under the Adams-Bashforth timestepping scheme used in the model, the stability constraint on the horizontal viscosity, ν_h, is $(4\ \nu_h \Delta t)/(\Delta x^2) < 0.3$. Consider the idealised model described in the following section, for which $\Delta t = 2000$ s and $min(\Delta x) = 111$ km. We must ensure $\nu_h \leq 4.6 \times 10^5$ m^{2}s^{-1}.

2.5 Model Configurations

As noted above, the numerical experiments in this thesis are performed using two configurations of the MITgcm. One configuration is a sector model with a reentrant channel, driven by idealised forcing profiles. This serves as an idealised Atlantic basin and is a useful starting point for testing the diagnostic tool developed in chapter 5. The second configuration is a global ocean with realistic bathymetry, driven by surface fluxes of freshwater, heat and momentum from reanalysis. The global model incorporates an additional scheme parameterising vertical mixing. Aside from this, the modelled dynamics differ little between the two configurations. Realistic geometry and forcing fields are favoured in chapter 3 for assessing global ocean teleconnection mechanisms. In the sections below, remaining details specific to each configuration will be discussed. A common approach to summarise the 3-dimensional circulation is by diagnosing overturning and barotropic streamfunctions (e.g. *Zika et al.*, 2012). We consider the 3-dimensional velocity field $\mathbf{u} = [u, v, w]$ within the domain bounded in longitude, x, latitude, y, and height, z, by (x_w, x_e), (y_s, y_n) and $(-H(x,y), \eta(x,y))$ respectively. To satisfy incompressibility, we define the barotropic streamfunction, ψ_{BT}, such that

$$\frac{\partial \psi_{\mathrm{BT}}}{\partial y} = -\int_{-H}^{\eta} u \, dz \quad ; \quad \frac{\partial \psi_{\mathrm{BT}}}{\partial x} = \int_{-H}^{\eta} v \, dz. \tag{2.5}$$

The Atlantic meridional overturning streamfunction, ψ_{AMOC}, is defined in an analogous manner such that

$$\frac{\partial \psi_{\mathrm{AMOC}}}{\partial y} = \int_{x_w}^{x_e} w \, dx \quad ; \quad \frac{\partial \psi_{\mathrm{AMOC}}}{\partial z} = -\int_{x_w}^{x_e} v \, dx. \tag{2.6}$$

The streamfunctions are diagnosed as follows

$$\psi_{\mathrm{BT}}(x,y) = \int_{y_s}^{y}\int_{-H}^{\eta} u(x,y,z)\,dz\,dy, \tag{2.7}$$

$$\psi_{\mathrm{AMOC}}(y,z) = \int_{-H}^{z}\int_{x_w}^{x_e} v(x,y,z)\,dx\,dz, \tag{2.8}$$

for each equilibrium state examined below.

2.5.1 Sector Model

The geometry of the sector model is shown in figure 2.1. The basin extends from 68°S to 68°N in latitude and 50° in longitude. The lateral boundaries are 2 grid points wide everywhere. The re-entrant channel extends from 66°S to 46°S in latitude. The depth of the basin is 5 km except at the east and west margin of the channel where one sill that is 2500 m deep and four grid points wide (in total) spans the zonally re-entrant latitude band, absorbing the momentum of the modelled Antarctic Circumpolar Current (ACC). The vertical is resolved by 20 levels of varying thickness increasing monotonically from 40 m at the surface to 500 m at depth. Remaining key model parameters are presented in table 1.

In this study the atmosphere is reduced to the prescription of a surface boundary condition. SST and SSS are restored to simple functions of latitude on time scales of 2 months and 6 months respectively. These profiles (shown in figure 2.2) capture the main features of the zonally averaged climatology for the Atlantic basin (*Antonov et al.*, 2006; *Locarnini et al.*, 2006). A westerly wind stress is applied to vary sinusoidally with latitude below 40°S, representing the mid-latitude atmospheric jet. The maximum wind stress is 0.2 N m^{-2}. In the remainder of the basin the wind stress is zero. In chapter 7 perturbations of this baseline case will be explored.

The model is initialised from an isohaline state. The initial temperature field is

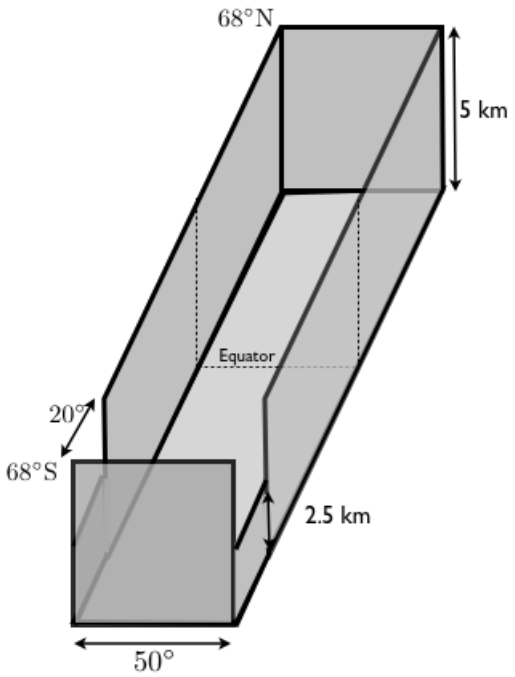

Figure 2.1: Model geometry employed for idealised calculations of the AMOC. The channel near the southern margin is zonally periodic and partially blocked to produce a modelled circumpolar current of comparable strength to the ACC.

TABLE 1: Sector model parameters

Upper Layer thickness	Δz_1	40 m
Horizontal viscosity	ν_h	10^4 m^2 s^{-1}
Vertical viscosity	ν_v	10^{-3} m^2 s^{-1}
Horizontal diffusivity	k_h	10^3 m^2 s^{-1}
Vertical diffusivity	k_v	3×10^{-5} m^2 s^{-1}
Thickness diffusivity	k_{GM}	10^3 m^2 s^{-1}
Maximum slope (GM)		10^{-2}
Reference density	ρ_0	1035 kgm^{-3}
Reference salinity	S_0	35 psu
Momentum time step	Δt_{mom}	2000 s
Tracer time step	Δt_{tracer}	2000 s
SST restoring timescale	τ_T	2 months
SSS restoring timescale	τ_S	6 months
SST coupling coefficient	λ_T	32 Wm^{-2}K^{-1}
SSS coupling coefficient	λ_S	7.3×10^{-8} ms^{-1} psu^{-1}
Max. wind stress (control run)	$\tau_{\max}$	0.2 N m^{-2}

horizontally homogeneous, decreasing monotonically from 21°C at the surface to 2°C in the abyss. Following integration over 3000 model years, no trends are discernible in the tracer and momentum fields and equilibrium is assumed. In steady state,

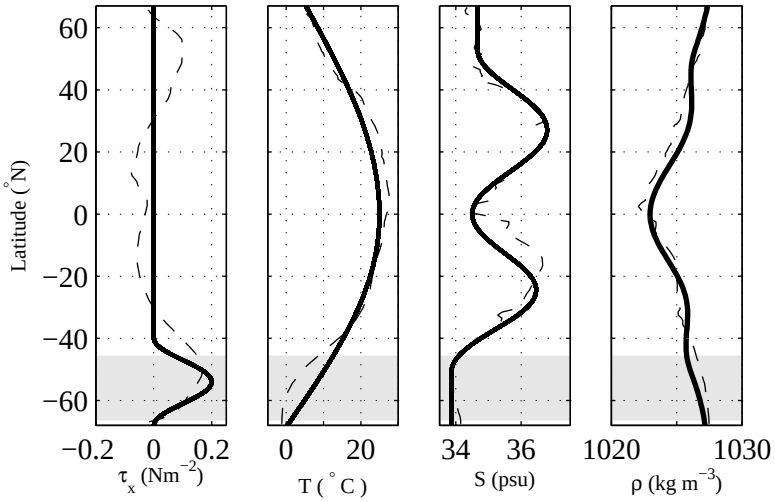

Figure 2.2: Idealised profiles (solid lines) of zonally averaged Atlantic climatology for (from left to right) zonal wind stress, sea surface temperature, sea surface salinity and sea surface density. Idealised profiles are based on NCEP/NCAR Reanalysis winds (*Kalnay et al.*, 1996) and thermohaline fields from the World Ocean Atlas (*Antonov et al.*, 2006; *Locarnini et al.*, 2006) (dashed lines). The reentrant latitudes are shaded grey.

the largest horizontal gradients in buoyancy are found at the surface where density is almost exactly prescribed by SST and SSS restoring. At depth, the buoyancy field is distorted so that the meridional buoyancy gradient is reversed in the northern hemisphere. Fluid flow is along buoyancy isolines except in the reentrant channel and adjacent to the eastern and western boundaries. Convective activity is concentrated along the northern and southern margins. Deep water predominantly forms in the north-east corner of the basin, returning south-westwards to join the deep western boundary jet.

The barotropic streamfunction, ψ_{BT}, is shown in figure 2.3. The westerly winds drive a strong barotropic transport of 100 Sv through the channel, and a weaker anticyclonic gyre to the north. The steady-state streamfunction for the meridional overturning circulation, ψ_{AMOC}, at the end of the control integration is shown in figure 2.4, where we examine contributions from the Eulerian, v, and bolus, $v*$, meridional velocities separately. The Eulerian AMOC (top panel) spans both hemispheres

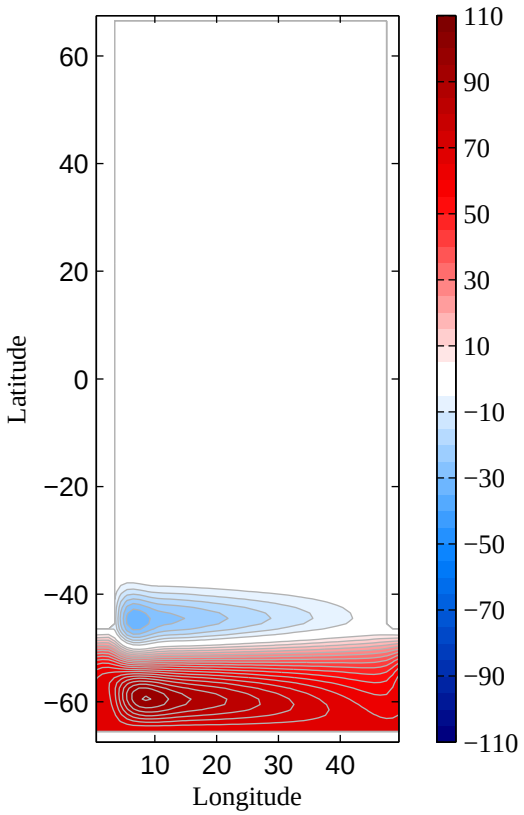

Figure 2.3: Barotropic streamfunction averaged over the final 10 years of the control run for the sector model. The contour interval is 5 Sv. The 0 Sv contour has been omitted. Positive/negative values correspond to clockwise/counterclockwise circulations.

with deep water formation near the northern margin. A wind-driven overturning cell occupies the reentrant channel, extending just below the depth of the sill where a zonal pressure gradient permits a geostrophic return flow. A well documented (*Danabasoglu et al.*, 1994) eddy-driven overturning largely cancels this wind-driven (or 'Deacon', *Doos and Webb*, 1994) cell in the modelled southern ocean (centre panel). The residual southern ocean overturning (bottom panel) peaks at 5.6 Sv near the mid-point of the channel. The residual MOC attains a maximum of 11.2 Sv near

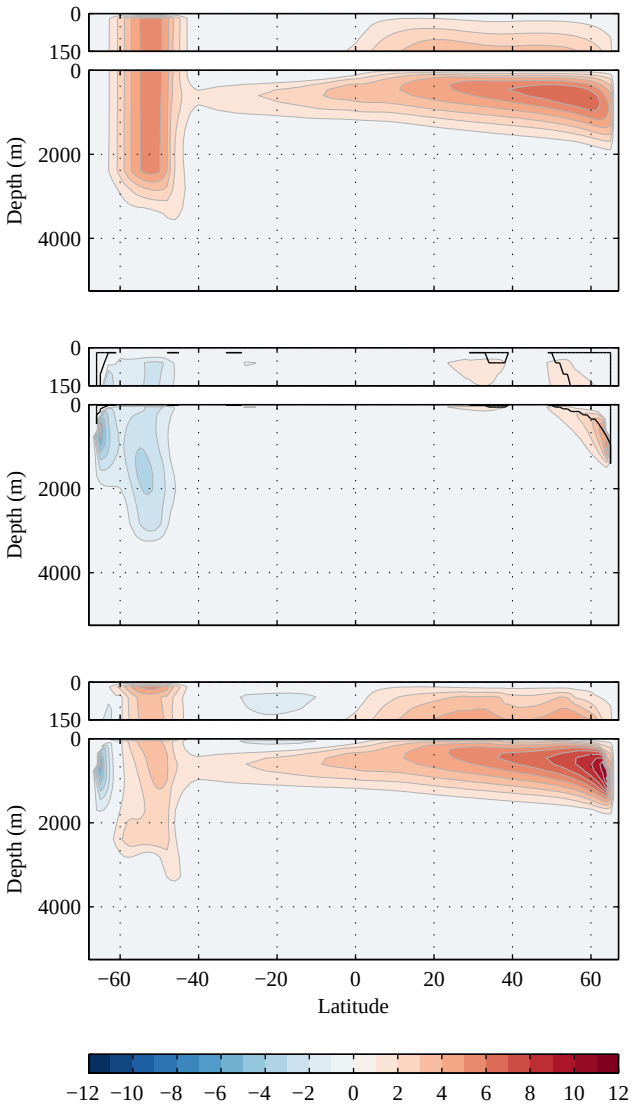

Figure 2.4: Eulerian mean (top), eddy-driven (centre) and residual (bottom) overturning streamfunctions averaged over the final 10 years of the control run. The residual overturning is computed from the total transport velocity. The contour interval is 1 Sv (10^6 m^3 s^{-1}). The 0 Sv contour has been omitted. Positive overturning indicates sinking northward of the upwelling region. Black contours overlaying the eddy-driven (centre) overturning enclose regions of active convective adjustment.

the northern margin, at a depth of 1165 m. A weaker counter-rotating cell with an associated volume flux of -1.4 Sv is confined near the surface at around 20°S.

In the ocean, the ACC connects the Atlantic with the Pacific and Indian Basins. Export of Antarctic Bottom Water (AABW) and the formation of a deep residual

Atlantic Overturning is thus sustained by the import of North Atlantic and Circumpolar Deep Waters (NADW and CDW). In this study, the modelled southern ocean is grossly limited in zonal extent and no attempt is made to represent interaction between multiple ocean basins. As a result, it is not possible to simulate a sustained deep residual overturning. The weak southern sinking cell visible in a narrow latitude band near the southern margin is a feeble manifestation of Antarctic Bottom Water (AABW) export from the real Southern Ocean.

It is also noted that the effect of the parameterised eddies is not confined to the vicinity of the reentrant channel. Instead, the eddies act to erode the steep isopycnal slope produced by surface buoyancy restoring near the northern margin. This is a technical artefact that is hard to avoid, but it is only problematic when the eddies slump the isopycnals to the extent that convection is inhibited. In figure 2.4 (centre panel) the black contours surround all areas that convectively adjust in steady state. The extension of convective adjustment northward of the latitudes occupied by parameterised eddies is important in permitting surface waters to sink and penetrate to depth.

2.5.2 Global Model

The bathymetry data in the global model is obtained from GEBCO. The domain is truncated below the poles to avoid violating the CFL criterion (e.g *Durran*, 1999) as the meridians converge. The vertical is resolved by 33 levels of varying thickness increasing monotonically from 10 m at the surface to 250 m at depth. Remaining key model parameters are presented in table 2. The model is driven by climatological surface fluxes of heat, freshwater and momentum, derived from the NCEP/NCAR Reanalysis II product (spanning the years 1979-2009 inclusive, *Kanamitsu et al.*, 2002). Raw monthly means are smoothly mapped onto the $1^\circ \times 1^\circ$ model grid using a cubic interpolation, before computing the climatological seasonal cycle. The

TABLE 2: Global model parameters

Upper layer thickness	Δz_1	10 m
Horizontal viscosity	ν_h	10^4 m^2 s^{-1}
Vertical viscosity	ν_v	10^{-3} m^2 s^{-1}
Horizontal diffusivity	k_h	10^2 m^2 s^{-1}
Vertical diffusivity	k_v	1×10^{-5} m^2 s^{-1}
Thickness diffusivity	k_{GM}	10^3 m^2 s^{-1}
Maximum slope (GM)		10^{-2}
Reference density	ρ_0	1035 kg m^{-3}
Reference salinity	S_0	35 psu
Momentum time step	Δt_{mom}	3600 s
Tracer time step	Δt_{tracer}	3600 s
SST restoring timescale	τ_T	2 months
SSS restoring timescale	τ_S	6 months
SST coupling coefficient	λ_T	32 Wm^{-2}K^{-1}
SSS coupling coefficient	λ_S	7.3 $\times 10^{-8}$ms^{-1} psu^{-1}

NCEP/NCAR Reanalysis II freshwater product accounts only for net precipitation; river runoff estimates are limited to the continental interior. We incorporate the runoff product from the Ocean Model Intercomparison Project (OMIP) into the model (see *Röske*, 2006). Linear interpolation onto the model grid is considered most suitable for runoff fields, avoiding generation of unphysical, negative values. The climatological seasonal cycle is then computed from the mean annual (365 day) cycle provided by OMIP. Finally, a correction is applied to both the heat and freshwater fluxes to ensure no net input over the annual cycle (figure 2.5).

The model is initialised to horizontally homogeneous temperature and salinity profiles based on hydrography. To prevent significant drift of SSS and SST, we relax the simulated profiles to climatology with a damping timescale of 6 and 2 months respectively. Restoration of the full depth temperature and salinity fields towards observed, climatological profiles is also imposed at the open portion of the northern margin. Following integration over 3000 model years no significant trends are discernible in the tracer and momentum fields and equilibrium is assumed.

The barotropic streamfunction, ψ_{BT}, at the end of the integration is shown in figure 2.6. The barotropic circulation is dominated by the vigorous ACC, attain-

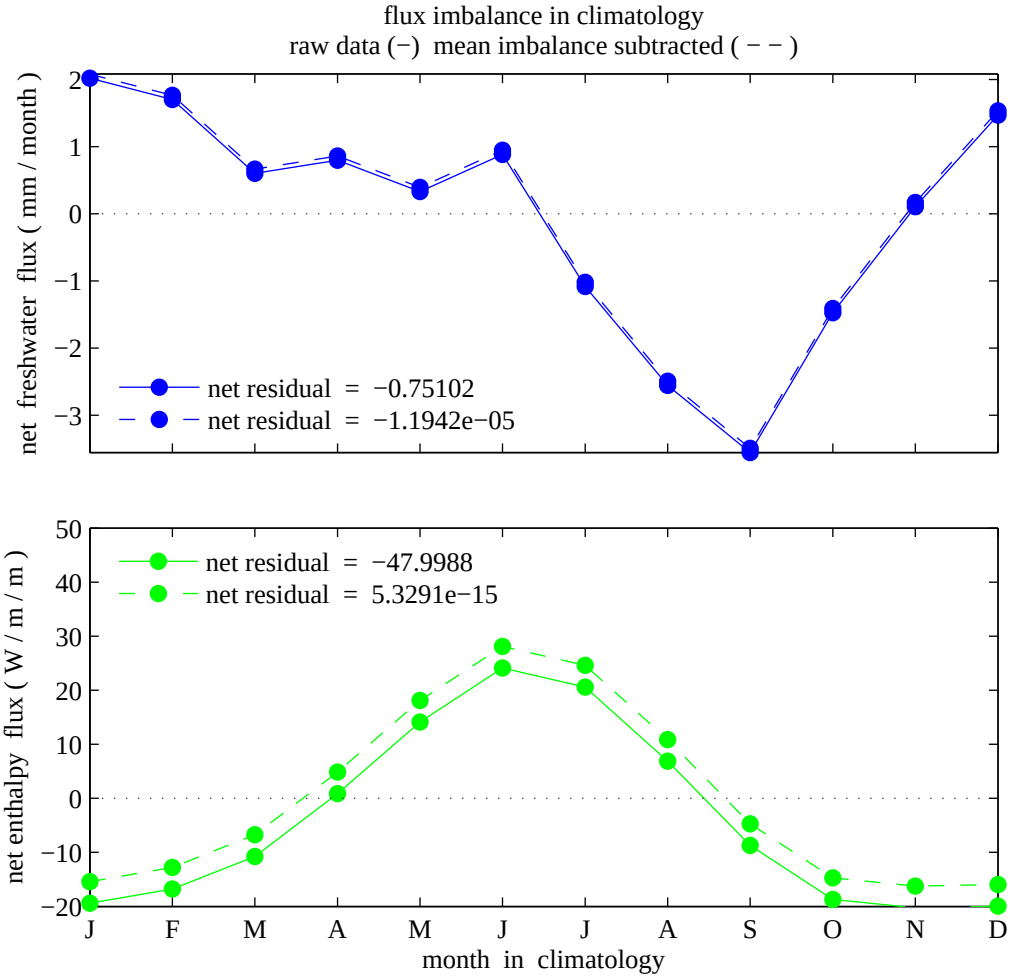

Figure 2.5: Flux corrections are applied to the climatological seasonal cycles in total freshwater (top) and total heat (bottom), to ensure no net input over the year. Residuals in the globally integrated climatologies (solid lines) are redistributed evenly over the annual cycle and ocean area to achieve closed climatologies (dashed lines) with which the model is forced. Separate contributions from shortwave and remaining radiative fluxes comprise the total heat flux; contributions from runoff and net precipitation comprise the total freshwater flux. In each case, the correction is applied to the largest flux component. Enthalpy and freshwater fluxes are defined to be positive acting upwards out of the ocean.

ing maximum eastward transports of 140 Sv. Subtropical and subpolar gyres attain transports of approximately 40 Sv. The residual meridional overturning streamfunc-

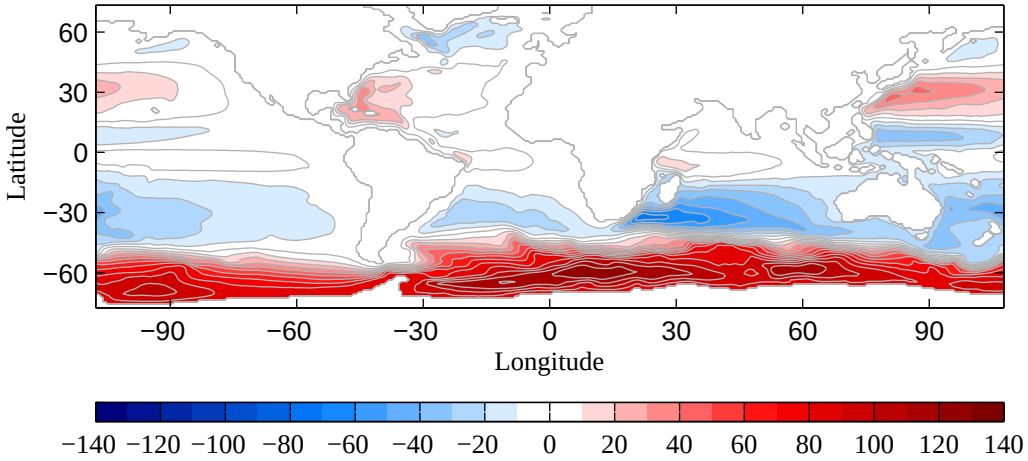

Figure 2.6: As for figure 2.3 but for the global model. The contour interval is 20 Sv.

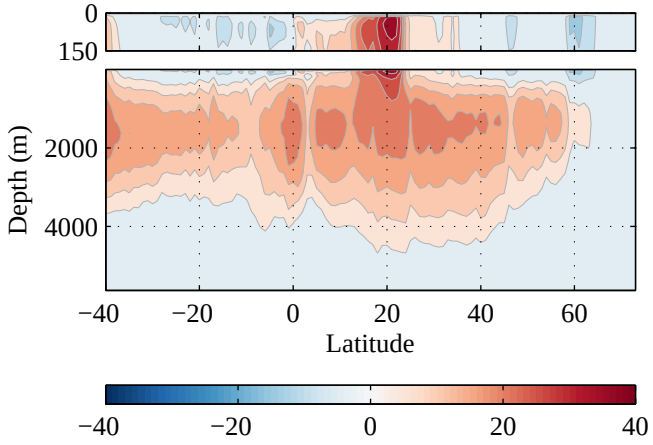

Figure 2.7: As for figure 2.4 but for the global model. The contour interval is 5 Sv.

tion, ψ_{AMOC} is shown in figure 2.7. The streamfunction describes net meridional overturning between the southern limit of the Atlantic basin and approximately 60°N. The maximum meridional volume flux of approximately 40 Sv is achieved in the upper ocean at 20°N. ψ_{AMOC} exhibits notable seasonal variability throughout the South Atlantic and in the subtropical North Atlantic. In the upper panel of figure

2.8, we plot a 20 year timeseries of monthly mean ψ_{AMOC} at 25°N and 1250 m depth at the end of the integration. The peak-to-peak amplitude of the seasonal cycle is approximately 7 Sv. The minimum occurs in February. The maximum occurs in November, although the seasonal cycle is characterised by a second local maximum in August. In figures 2.8a-d we show ψ_{AMOC} in February, May, August and November during the 3002nd model year. A strong seasonal signal is visible throughout the South Atlantic and in the subtropical North Atlantic. During the winter months ψ_{AMOC} describes a strong, interhemispheric overturning. Towards the spring (figure 2.8b) the overturning weakens before splitting into two distinct northern sinking cells in the summer (figure 2.8c). At this time, interhemispheric overturning is interrupted by a southern sinking cell extending to depth at the Equator. This reflects high frequency variability in the low latitude Ekman transport (e.g. *Jayne and Marotzke*, 2001). Despite these extreme changes in the structure of the low latitude ψ_{AMOC} on seasonal timescales, seasonal variations north of approximately 20°N are more closely described by a standing pattern; the velocities strengthen or weaken and their distribution through the column is almost seasonally invariant (figure 2.9).

The transport timeseries in figure 2.8 also indicates a decadal timescale of variability. In figure 2.10 we examine the inter-annual anomaly in ψ_{AMOC}. The amplitude of the interannual anomaly is small ($\sim$ 3 Sv) relative to the seasonal anomalies, but dominates variability at high northern latitudes where seasonality is small. In figures 2.10a-d it emerges that the interannual anomaly is advected equatorwards from high northern latitudes, generating a weak oscillation of the monthly mean ψ_{AMOC} at 25°N on decadal timescales.

Self-sustained interdecadal oscillations have been found in many ocean-only models of varying complexity, integrated under prescribed heat flux conditions (e.g. *Chen and Ghil*, 1995; *Greatbatch and Zhang*, 1995; *Winton*, 1996; *Cai et al.*, 1998; *Huck et al.*, 1999, 2001) and appear to rely on a phase difference between changes in the

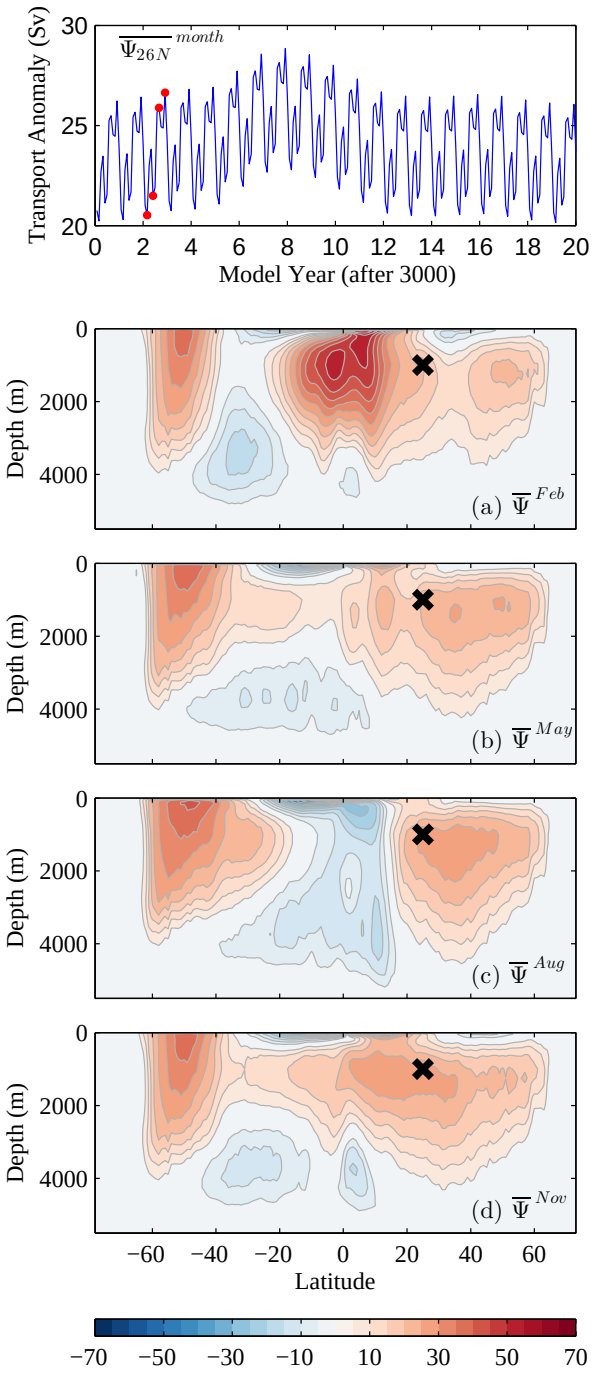

Figure 2.8: The upper panel shows the timeseries of the monthly mean AMOC at 25°N and 1250 m depth (black cross in panels (a)-(d)). Red dots indicate times for which the overturning is contoured in panels (a)-(d) (earliest to latest times respectively). The contour interval is 5 Sv. The 0 Sv contour has been omitted.

AMOC and the resulting temperature anomalies (*Te Raa and Dijkstra*, 2002; *Huck et al.*, 1999; *Colin de Verdiere and Huck*, 1999). By invoking the thermal wind argu-

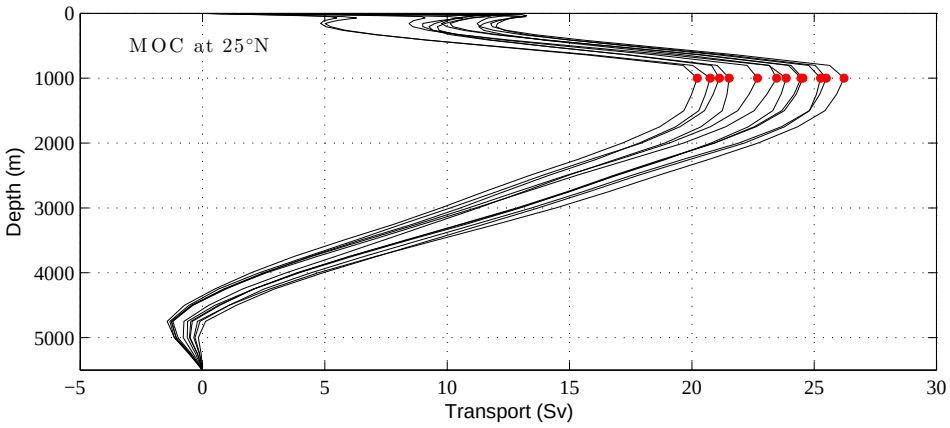

Figure 2.9: Vertical profiles of cumulative volume transport across 25°N, associated with the modelled AMOC. Profiles are based on monthly mean velocities for model year 3000. Red dots indicate the depth of the maximum volume flux, which is invariant across the seasonal cycle.

ment, a clear mechanism for the self-sustaining oscillation emerges. Following *Te Raa and Dijkstra* (2002), let us consider a warm anomaly in the interior, northern region of the basin. This generates a positive perturbation meridional temperature gradient, which induces a negative perturbation zonal overturning. This drives upwelling and downwelling on the eastern and western boundaries respectively, generating a positive perturbation zonal density gradient. The warm anomaly propagates westwards through the interior generating a negative perturbation zonal temperature gradient. This in turn induces a negative perturbation meridional overturning. This drives upwelling and downwelling to the north and the south respectively. Now a cold anomaly is established in the interior, northern region of the basin, and the opposite phase of the oscillation begins. This mechanism has been called a "thermal Rossby mode" (*Frankcombe et al.*, 2008) due to the analogy seen between Rossby waves propagating across the background potential vorticity gradient and thermal

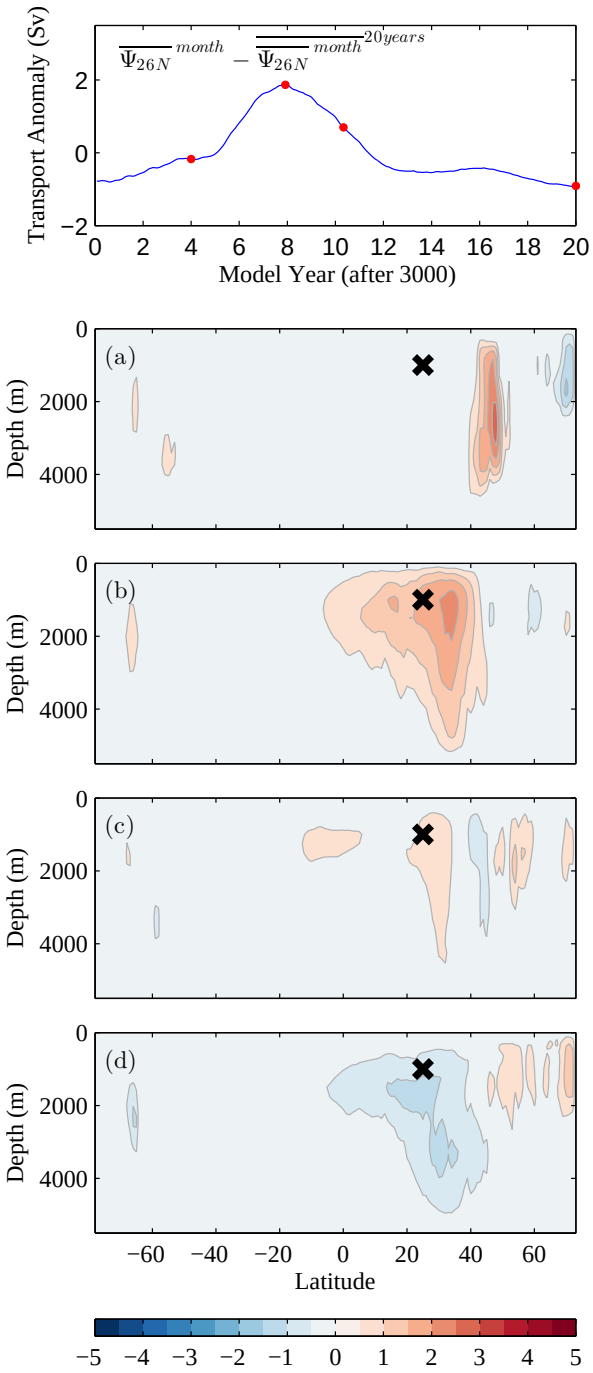

Figure 2.10: Inter-annual variability of the AMOC (Sv) computed as the difference of the monthly AMOC from the climatological seasonal cycle evaluated over the 20 year period. The upper panel shows the timeseries of inter-annual variability at 25°N and 1250 m depth (black cross in panels (a)-(d)). Red dots indicate times for which the inter-annual anomaly is contoured in panels (a)-(d) (earliest to latest times respectively). The contour interval is 0.5 Sv. The 0 Sv contour has been omitted.

anomalies propagating across the background temperature gradient above.

2.6 Summary

In this chapter, we have provided an introduction to the numerical framework that will be used in the following chapters of this thesis. Where necessary, we have explained chosen simplifications to the modelled dynamics. In the investigations that follow, two distinct model configurations are required. In chapters 3 and 4, a globally realistic model is favoured to more faithfully simulate teleconnection mechanisms present in the real ocean. Furthermore, we are interested in exploring the full structure of the mapping of atmospheric forcing anomalies onto the variability of the modelled ocean circulation. In chapters 6 and 7 we also require a simplified geometry for the first thorough implementation of a new diagnostic tool (derived in chapter 5) in a GCM.

It will be seen that an awareness of the variability in the background state is an import issue for the experiments in chapters 3 and 4. We have presented a brief analysis of the seasonal and lower frequency variability present in the globally realistic model configuration, identifying a decadal oscillation in the modelled North Atlantic. We suggest that the maintenance of this mode is consistent with the thermal Rossby mechanism discussed by *Huck et al.* (1999); *Te Raa and Dijkstra* (2002).

Chapter 3

Pathways and Timescales of AMOC Variability

3.1 Introduction

The ocean is a fluid possessing considerable memory due to large reservoir capacities, and slow propagation timescales. A well publicised example of this memory is associated with thermal inertia, causing a substantial lag of oceanic warming in response to increased greenhouse gas forcing (e.g. *Meehl et al.*, 2007). Slow propagation timescales are associated with the sluggish abyssal transports. A quick estimate of residence time for the global abyssal water mass can be made by dividing the volume of the world ocean ($\sim 3\times10^{18}$ m^3) by a representative value for the production rate (*Wunsch and Heimbach*, 2008). By assuming a production rate of 20 Sv, a reservoir time of approximately 5000 years is obtained. Spatially varying estimates can be found from passive tracer distributions (e.g. *Key et al.*, 2004; *Duplessy et al.*, 1991) and transit times analysis (e.g. *Haine et al.*, 2008; *Haine and Hall*, 2002).

The abyssal circulation can also adjust more rapidly on multi-decadal to centennial timescales through the propagation of ocean waves (*Kawase*, 1987). Similar

mechanisms have been invoked to elucidate the surface Atlantic response to thermohaline variability (e.g. *Johnson and Marshall*, 2002a; *Stammer*, 2008), the equilibration of the ACC (*Allison et al.*, 2011), and global ocean teleconnections (e.g. *Johnson and Marshall*, 2004; *Cessi and Otheguy*, 2003; *Greatbatch and Peterson*, 1996) on comparable timescales. As a result, regional changes in the ocean potentially result from the superposition of phenomena occurring long ago in distant regions (*Heimbach et al.*, 2011), rendering a mechanistic exploration of local AMOC variability a highly challenging task. This is particularly problematic in complex GCMs where attempts to identify causal mechanisms are often restricted to correlations that are only able to indicate mutual variability.

A powerful approach to determine the origins of oceanic variability is via the use of an adjoint sensitivity method (e.g. *Cacuci*, 1981). The adjoint provides the sensitivity of a chosen model diagnostic to model parameters and forcing fields throughout the model domain, as a function of forcing lead time, thus allowing the identification of causal chains. Below, we will use this approach to quantify the sensitivity of the monthly mean modelled AMOC to small amplitude anomalies in the historic local and remote atmospheric fluxes. Our focus is on the variability of the AMOC on seasonal to decadal timescales. The methodology will be described in detail in section 3.2. Below, a short review of some key studies relevant to our investigation will be presented.

3.1.1 Past Work

The first investigation of adjoint sensitivities in the ocean component of the MITgcm was presented by *Marotzke et al.* (1999), at a time when - within the climate research community - this approach was common only in meteorological applications (*Errico*, 1997). The authors focussed on the sensitivity of the annual mean meridional heat transport across 29°N in the Atlantic to small amplitude perturbations in hydrog-

raphy. By examining the changing spatial distribution of the sensitivity patterns as a function of time, they were able to identify analogous teleconnections in the adjoint framework to those present in the forward integration and explained by oceanic adjustment theory (e.g. *Kawase*, 1987). This was supported by the presentation of analytical solutions for adjoint Rossby and adjoint Kelvin waves in a later study by *Bugnion and Hill* (2006).

In idealised, coarse resolution ($4^\circ \times 4^\circ$) configurations of the MITgcm, Bugnion and co-authors (*Bugnion et al.*, 2006b; *Bugnion and Hill*, 2006) discussed the principal mechanisms by which the high latitude AMOC responds to wind and surface buoyancy forcing. Even in the presence of nonlinear (advective) processes, useful adjoint equilibrium sensitivities were derived for multi-centennial timescales. This is not an obvious result, since the adjoint provides information regarding linearized sensitivities and these may not approximate finite-amplitude sensitivities in the presence of nonlinear processes. A key finding by *Bugnion et al.* (2006b) is that the sensitivity patterns are highly dependent upon the thermohaline boundary conditions. Although the choice of boundary condition does not appear to affect the strength and structure of the equilibrated AMOC significantly, the sensitivity to surface forcing is notably reduced in the presence of restoring conditions on SSS and SST. The critical influence of the boundary conditions on the linear sensitivities is also stressed by *Bugnion et al.* (2006a). In a globally realistic geometry, the authors compare patterns of AMOC sensitivity to southern ocean wind stress under restoring, mixed, and flux boundary conditions. Pronounced AMOC sensitivity to wind stress, as proposed by *Toggweiler and Samuels* (1995) and *Gnanadesikan* (1999), is found only under restoring conditions.

The role of high latitude time-varying buoyancy forcing in the variability of the monthly mean AMOC has been pursued in an adjoint framework by *Czeschel et al.* (2010). In a higher resolution ($1^\circ \times 1^\circ$) globally realistic configuration of the MITgcm,

the authors detect advective feedbacks (not identified by *Bugnion et al.*, 2006a) that generate a damped decadal oscillation in the AMOC sensitivity to high latitude buoyancy fluxes. It is suggested that in any month, the mean AMOC may result from the cumulative effects of high latitude buoyancy anomalies applied over the previous 15-20 years. This would prevent the inference of trends in short observational AMOC time series.

Recently, *Heimbach et al.* (2011) have employed the adjoint to reveal key anomalies in temperature and salinity that may affect the annual mean meridional volume and heat transports associated with the AMOC in the sub-tropical North Atlantic. Their focus is on monthly to multi-decadal timescales. On monthly timescales, significant sensitivities are restricted to local disturbances. Within decadal timescales, anomalies in sub-surface temperature and salinity generated in remote parts of the global ocean, may be communicated to the subtropical North Atlantic and alter the AMOC. A key result is that notable differences are found between sensitivities for the meridional heat and volume transport associated with the AMOC.

Czeschel et al. (2012) investigated the seasonal variability of the monthly mean Florida Current transport using a numerical adjoint. The authors focus on the sensitivity of the transport to wind stress, clearly demonstrating the dominant role played by coastal wind forcing north of the Florida Strait. Significant memory to historic wind anomalies is limited to timescales less that a year. By multiplying the sensitivity patterns by realistic patterns of wind stress anomaly, the authors are able to reconstruct the observed annual cycle in the Florida Current Transport.

An important question in climate science is the extent to which predictability may be limited by rapid transient growth of anomalies, resulting from nonnormal dynamics of the system (e.g *Farrell and Ioannou*, 1996). A key extension to the work described above is the use of the adjoint to detect perturbations leading to the optimal excitation of the AMOC. Considerable progress in this area has been made by

Zanna and co-workers (*Zanna and Tziperman*, 2005, 2008; *Zanna et al.*, 2011, 2012) in idealized basin geometries. A key finding is that AMOC anomalies stimulated by deep perturbations in temperature and salinity may experience significant growth on sub-decadal timescales (7.5 years in *Zanna et al.*, 2011). Perturbations in upper ocean temperature and salinity are less efficient at exciting variability in the AMOC (*Zanna et al.*, 2012).

In summary, these studies provide great encouragement for further investigation of oceanic variability in the framework of a numerical adjoint. Sensitivity patterns elucidate teleconnection mechanisms which can be used to quantify the relative importance of local and remote anomalies in different hydrographic or forcing variables, occurring in the most recent or more historic past, in generating variability in the system. This has important implications for inferring trends from observational timeseries (*Czeschel et al.*, 2010) and also identifies key areas to target for future observation and modelling efforts (e.g *Heimbach et al.*, 2010, 2011).

3.1.2 Present Objectives

The aims of the present work are to explore the memory of the modelled AMOC to historic wind stress forcing and surface fluxes of heat and freshwater. Our focus is on seasonal to multi-decadal timescales. The work that follows may be viewed as an extension of the study by *Heimbach et al.* (2011), who restrict their discussion to the role played by temperature and salinity anomalies in the variability of the AMOC. We seek to present a thorough analysis of the propagation pathways and timescales that may link remote forcing regions to the subtropical Atlantic. Our focus on the subtropical AMOC is motivated be extensive past modelling and observational efforts at these latitudes.

3.2 Numerical Sensitivity Studies

An excellent and accessible introduction to the adjoint approach is provided by *Errico* (1997). His approach is followed in outlining the basic methodology here. It is helpful to briefly discuss the traditional approach to sensitivity analysis before presenting the adjoint methodology.

3.2.1 Traditional Sensitivity Studies

The evolution of the ocean state may be expressed concisely as follows

$$\mathbf{y} = m(\mathbf{x}), \tag{3.1}$$

where $\mathbf{x}$ is the initial state vector and m is a nonlinear operator that evolves the basic state, $\mathbf{x}$, to a new state, $\mathbf{y}$, at some later time. In the present case, m is our numerical model based on the discretised primitive equations. It follows that the state vector comprises the state variables (e.g. velocity components, temperature, salinity, sea surface elevation) discretised throughout the model domain.

In the present study, the processes setting the variability of the monthly mean AMOC across the RAPID array are of primary interest. In attempt to determine the relative importance of heat, freshwater and momentum fluxes, a possible approach could be to perturb some relevant aspect of the model input, (e.g the local wind stress) and re-run the model, examining the change in the model output, $\mathbf{y}$. We can envisage running an ensemble of perturbed experiments, changing different aspects of the surface forcing in each case, in attempt to constrain the key ingredients driving AMOC variability. This is the traditional approach to numerical investigation of sensitivity. It has been applied ubiquitously in model development, and subsequently to determine the impact of perturbed physics and quantify the uncertainty in model simulations. It forms the basis of numerical weather prediction. In a state of the

art ocean GCM, $\mathbf{x}$ may consist of $O(10^7)$ elements[1]. As a result, the number of possible perturbations at each time step is considerable, often requiring a very large ensemble to perform a comprehensive sensitivity study. In some applications (e.g. numerical weather prediction), the ensemble size can be minimised by using advanced mathematical tools to select the perturbed members that will span model phase space as efficiently as possible (e.g. singular vectors, *Barkmeijer et al.*, 1999). For other problems (e.g. future climate prediction), these techniques cannot be applied (*Frame et al.*, 2009) and massively distributed computing is required to conduct a useful ensemble experiment (e.g climate*prediction*.net, *Allen*, 1999).

Beyond the technical difficulties of implementing a large perturbed ensemble, a mechanistic interpretation of the ensemble output is also challenging. Each ensemble member, with a different perturbed input vector, $\mathbf{x} \rightarrow \mathbf{x} + \Delta\mathbf{x}$, is described by

$$\mathbf{y} + \Delta\mathbf{y} = m'(\mathbf{x} + \Delta\mathbf{x}). \tag{3.2}$$

The perturbed output state, $\mathbf{y} + \Delta\mathbf{y}$, arises from interactions between the basic state and the perturbation $(\mathbf{x}, \Delta\mathbf{x})$, and between the perturbation and itself $(\Delta\mathbf{x}, \Delta\mathbf{x})$. If the perturbation is 'large' then the nonlinear operator itself is altered $(m \rightarrow m')$ because the forward trajectory depends upon the model state. Consequently, the impact of the input perturbation, $\Delta\mathbf{x}$, is notoriously difficult to track through model space. Analysis of the ensemble output highlights mutual variability between input and output perturbations. However, it is non-trivial to confidently diagnose cause and effect along the entire model trajectory, from the application of the initial perturbation through to the evaluation of the final model state. Furthermore, we are usually interested in a few specific aspects of the climate system which are of noted importance (e.g global ocean heat content, Atlantic meridional heat flux,

[1]For example, consider the global GCM described in chapter 2. There are 5 prognostic variables (u, v, S, θ, η) which are evolved at $[nx \times ny \times nz] = [360 \times 152 \times 33]$ grid points.

ACC transport etc.). It is desirable then to focus our efforts on understanding all potential causes of variability in these few aspects, as opposed to the impact of one perturbation on the evolution of the entire climate state. For this, we turn to the adjoint model.

3.2.2 Adjoint Sensitivity Studies

To simplify matters, consideration can be restricted to perturbations that are 'small' ($\Delta\mathbf{x} \rightarrow \mathbf{x}'$) in the sense that the interactions between the perturbation and itself are negligible. The response of the linearized system is then approximated by a first-order Taylor series expansion

$$y'_\beta = \sum_\alpha \frac{\partial y_\beta}{\partial x_\alpha} x'_\alpha \; + \; O((x'_\alpha)^2), \tag{3.3}$$

where $y_\beta(t)$ is a particular element of the model output and the partial derivative is the Jacobian of the model, determined with respect to the input. Equation (3.3) is linear in the perturbation quantities and is therefore a linearized version of the original model. Note that the linearization is performed about the local model trajectory, which evolves through time and space. As a result, equation (3.3) is called the tangent linear model (TLM).

The TLM provides the linear sensitivity of the model output with respect to all model inputs. As noted above, there will typically be a small number of metrics, which are functions of the model output, $\mathcal{J}_n = f(\mathbf{y})$, that are of particular interest. For example, in the present study, the strength of the subtropical monthly mean AMOC is of primary interest. A suitable set of n objective (or "cost") functions could comprise 12 scalar values of the monthly mean maximum AMOC across 25°N:

$$\mathcal{J}_{1,2,...,12} = \overline{\psi_{25\mathrm{N}}}^{Jan}, \overline{\psi_{25\mathrm{N}}}^{Feb}, ..., \overline{\psi_{25\mathrm{N}}}^{Dec}. \tag{3.4}$$

Determining the sensitivity of each member of $\mathcal{J}_n$ to perturbations of the model state at the time of $\mathcal{J}$ evaluation is straightforward:

$$\mathcal{J}' = \sum_{\alpha} \frac{\partial \mathcal{J}}{\partial y_\alpha} y'_\alpha. \tag{3.5}$$

Of primary interest is the sensitivity of $\mathcal{J}$ to *all* earlier perturbations of the model state:

$$\mathcal{J}' = \sum_{\alpha} \frac{\partial \mathcal{J}}{\partial x_\alpha} x'_\alpha. \tag{3.6}$$

The challenge is to efficiently determine $\partial \mathcal{J}/\partial \mathbf{x}$ for all elements of $\mathbf{x}$ (i.e for each state variable, at every grid point, and each point in time). This is achieved via application of the chain rule for differentiation, allowing $\partial \mathcal{J}/\partial \mathbf{x}$ to be accessed indirectly from the product of more easily obtained gradients:

$$\frac{\partial \mathcal{J}}{\partial x_\beta} = \sum_{\alpha} \frac{\partial y_\alpha}{\partial x_\beta} \frac{\partial \mathcal{J}}{\partial y_\alpha}. \tag{3.7}$$

Equation (3.7) is called the adjoint model. Since the Jacobian in the TLM has been replaced with its transpose, the adjoint is often described as operating in reverse mode or backwards in time (whilst the TLM operates in forward mode or forwards in time). Equivalently, the TLM can be viewed as linearly transmitting perturbations through model space, whilst the adjoint model linearly transmits influence (figure 3.1) (*Giering and Kaminski*, 1998). *Heimbach et al.* (2011) refer to the adjoint model as a "dual GCM", mapping the propagation of information across the entire model domain, at all times.

The advantage of the adjoint approach to quantitative sensitivity study is now clear. Whilst the traditional (perturbed ensemble) approach informs the impact of one input perturbation on all model outputs, the adjoint approach reveals the linear sensitivity of a single objective function to all model inputs, elucidating the physical

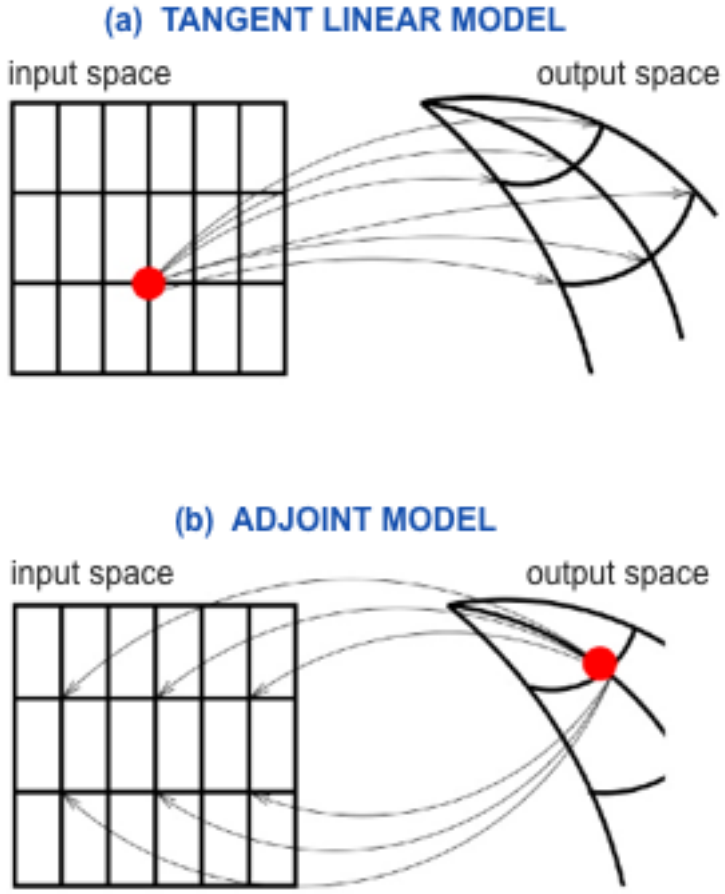

Figure 3.1: Schematic contrasting the (a) tangent linear and (b) adjoint models, (P Heimbach 2011, pers. comm.,). The TLM describes how a single input perturbation affects all model outputs. (b) The adjoint model describes the linear sensitivity of one output to all model inputs.

mechanisms connecting remote regions throughout the global domain. Applications of adjoint models extends beyond pure sensitivity studies to variational data assimilation, state estimation, model tuning and determination of singular vectors (see *Errico*, 1997, and references therein). Despite gaining recognition as powerful tools, they are grossly under-utilised in geophysical fluid dynamics, in part due to the difficulty in constructing an adjoint counterpart of a complex, nonlinear GCM. These issues will be briefly discussed below, before the experimental design used to explore the origins of subtropical AMOC variability is presented.

3.2.3 Obtaining the Adjoint

The development of a GCM can be split into three steps. We start by formulating the set of continuous differential equations that govern the geophysical system. Our next step is to select appropriate schemes to discretise these equations. Finally, a numerical algorithm is implemented to solve the discrete differential equations across the model domain. The adjoint model can be constructed after any of these three steps (*Giering and Kaminski*, 1998). In principal, all three approaches should yield identical gradients (linear sensitivities) in the absence of discontinuities (e.g. shocks) and in the limit of infinite grid resolution (*Giles and Pierce*, 2000).

Formulation of the adjoint model directly from the continuous governing equations (the "continuous approach") is discussed in detail by *Giles and Pierce* (1997). The authors construct the adjoint 2D Euler equations and find the solution is well posed for only a restricted set of objective functions ($\mathcal{J}_n$). Furthermore, the solution is subject to complications in enforcing the boundary conditions and subsequently constructing the discrete adjoint operators. As a result, the continuous approach is typically restricted to a simplified class of problems (*Giering and Kaminski*, 1998).

Formulation of the adjoint model from the discretised governing equations (the "fully-discrete approach") is achieved via the Lagrange multiplier method. Differentiating the Lagrange function with respect to the model variables provides the adjoint sensitivities. This approach has been followed by *Tziperman and Thacker* (1989) in constructing the adjoint model for the barotropic wind-driven gyre. It avoids the complicated construction of discrete adjoint operators, but - as for the continuous approach - requires extensive additional coding to generate a numerical adjoint. Any changes made to the discrete adjoint equations must be laboriously translated into the numerical code by hand. Furthermore, care must be taken to ensure that the solution retains numerically stable during linearization. As demonstrated by *Sirkes and Tziperman* (1997), numerical stability of the parent (forward)

finite discretisation does not guarantee stability of the adjoint finite discretisation.

These difficulties promote the use of the final approach: obtaining the adjoint model from the numerical code of the forward model. This approach is significantly aided by the recognition that a numerical model is simply a sequence of arithmetic operations. Differentiation of the entire code can therefore be achieved via a massive application of the chain rule. The establishment of simple rules for the differentiation of all elementary operations from which a numerical model may be composed (loops, read/write statements, assignments etc., see *Giering and Kaminski*, 1998, for worked examples and thorough discussion), encouraged exploration of automated adjoint model generation (although hand-coding has been used e.g. *Weaver et al.*, 2003). The result has been the development of powerful source-to-source transformation tools, capable of translating a program computing a function into a program computing the function and its derivative (see *Griewank*, 2000, and the community website www.autodiff.org for a list of active projects). These algorithmic differentiation (AD) tools are capable of operating on millions of lines of code, and have proved invaluable in the generation of adjoint counterparts of GCMs. They minimize the laborious and error-prone hand-coding of derivative code, making adjoint models accessible to the wider research community. Furthermore, model developers and users are relieved of the task of maintaining forward and adjoint models in exact consistency. Updates to the forward code should be incorporated into the adjoint upon application of AD.

As noted in chapter 2, the MITgcm has been developed in compatibility with the commercial AD tool TAF (Transformation of Algorithms in Fortran) developed by FastOpt (*Giering*, 2010). It follows that AD is invoked in the formulation of the adjoint model used in the sensitivity study in this chapter. Specifics of the experiment design will be described below. Firstly, it is noted that - for complex applications - adjoint generation is by no means fully automatic, and AD tools cannot be applied blindly. A few of the greatest technical challenges in obtaining a useful adjoint via

AD are illustrated in the following section.

3.2.4 Technical Challenges

For the computation of the transpose Jacobian in the adjoint model equation (3.7), variables are called in reverse order to that in which they are computed in the forward model. One of the greatest challenges in formulating an efficient adjoint model using AD relates to this reversed nature of the adjoint calculation. To ensure all local partial derivatives are available in reverse order, possible options are (1) to store all required variables to tape or (2) to recompute all required variables from scratch whenever they are required in the adjoint code. For large problems, option (1) is associated with enormous memory requirements, while option (2) is severely limited by a quadratic relation between required recomputations and CPU resource requirements (*Heimbach et al.*, 2002). Either approach, in pure form, is untenable and the problem is made tractable only by the insertion of a checkpointing scheme (first suggested by *Griewank*, 1992), balancing recomputation and storage demands. The MITgcm employs a 3-level checkpointing scheme, as illustrated in figure 3.2. The idea is to make the two outer checkpoint frequencies as coarse as possible (to avoid lengthly input/output (I/O) from tape), whilst not exceeding available RAM with the number of timesteps held in memory. In practice, these divisions are difficult to predict in advance, and the innermost level is maximised by trial and error.

For the AD tool to work efficiently, it is important that resources are assigned to store or recompute only those variables necessary in the computation of the local gradients in 3.7. The first step in reducing the work load of the tool is therefore for the user to specify a subset of variables (or "controls") which the gradient of the objective function is computed with respect to. Crucially, TAF can discriminate between active, passive and required variables in the code to be differentiated (*Giering*, 2010) and automatically insert many directives for I/O or recomputation where necessary.

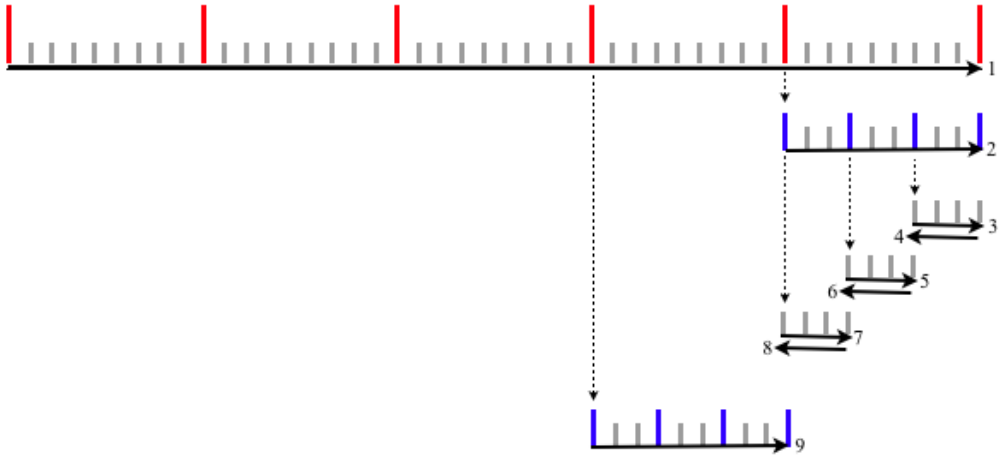

Figure 3.2: A 3-level hierarchical checkpointing scheme balances storage and recomputation demands, rendering the adjoint computationally tractable. (1) The full model trajectory is executed in forward mode and regular checkpoints (shown in red) are written to tape (every 9 timesteps in this example). At the end of the forward run, the objective function is evaluated. (2) The penultimate checkpoint is then read from tape and integrated to the end. Higher frequency regular checkpoints (shown in blue) are written to tape (every 3 timesteps in this example). (3) The penultimate inner checkpoint is read from tape and integrated to the end. Every timestep is stored in memory, allowing (4) computation of the adjoint back to the penultimate inner checkpoint. (5)-(8) This procedure is repeated until the adjoint has been computed over the final section of the outermost checkpoint level. (9) The procedure is repeated for the penultimate section of the outermost checkpoint level continuing until the adjoint of the full model trajectory has been computed. Note that only the outermost checkpoints (shown in red) are permanently stored. All other information is over-written (on tape or local memory). This schematic is adapted from *Heimbach et al.* (2002).

Problematic code structures exist, for which this step fails (see *Giering*, 2010, for discussion) and we found it necessary in places to insert store directives by hand (for example in DO-loops containing conditional assignments). Furthermore, proper generation of adjoint common blocks does not occur automatically and must often be kept in consistency with their forward model counterparts manually.

In conclusion, there is often a requirement for the user to understand how to use TAF directives, and develop a more detailed knowledge of the code. Exciting progress has recently been made towards truly automatic generation of adjoint models (*Farrell et al.*, 2012), although at this stage of development, these methods have yet to be

applied to complex GCMs.

3.3 Experiment Design

3.3.1 Model Configuration

The basic state about which the linear sensitivity study is performed is obtained from the global configuration of the MITgcm described in chapter 2 of this thesis. Important features to recall are: (1) surface forcing is applied as annually repeating cycles in climatological monthly mean fluxes of momentum, freshwater and heat. (2) SST/SSS relaxation to climatology is also applied to prevent model drift. (3) The equilibrated state exhibits significant variability on seasonal timescales (figure 2.8). (4) The equilibrated state exhibits only weak interannual variability (figure 2.10). This last point is highly desirable as we seek to perform the tangent linearisation about a stationary back ground state.

3.3.2 Objective Function Selection

The objective function, $\mathcal{J}$, can be any differentiable scalar measure of interest. In this chapter, $\mathcal{J}$ is chosen as the monthly mean maximum northward volume flux across 25°N. Since there is a notable seasonal cycle in the equilibrated model state (figure 2.8), 12 adjoint calculations are required to correctly diagnose the annual cycle using the adjoint. By increasing the length of the forward integration by 1 month for each experiment in turn, the definition of the costfunction is shifted from the January mean AMOC, $\mathcal{J}_1 = \overline{\psi_{25\mathrm{N}}}^{\,Jan}$, to the December mean AMOC, $\mathcal{J}_{12} = \overline{\psi_{25\mathrm{N}}}^{\,Dec}$. The seasonal cycle at 25°N is principally described by variations in the magnitude of the meridional velocity, v. There is little detectable shoaling/deepening of the turning point of the AMOC (figure 2.9). For this reason, the maximum overturning

is described as

$$\psi_{25\mathrm{N}} = \int_{x_w}^{x_e} \int_{z=-1250\ \mathrm{m}}^{0} v\ dz\ dx, \tag{3.8}$$

where $z = -1250$ m is the deepest point in the layer containing the turning point, for each member of $\mathcal{J}_n$.

3.3.3 Control Variables

The adjoint provides the gradient of the objective function, $\mathcal{J}$, with respect to all other variables in the model state vector. In this study, attention is focused on a small subset of controls: the net surface flux of heat (Q), freshwater ($E - P$), zonal momentum (τ^x), and meridional momentum (τ^y). SSS and SST restoring will also be considered later. Freshwater forcing from runoff is poorly represented in the forward model (see discussion in chapter 2). For this reason sensitivity to freshwater forcing will be assessed without the contribution from continental runoff. Net surface heat flux, Q, is defined here to exclude the contribution from shortwave radiation. In the forward model, the shortwave flux is handled separately from the latent, sensible and longwave heat fluxes due to its unique ability to penetrate below the surface layer. This distinction is retained in the adjoint investigation.

3.3.4 Adjoint Model Execution

Following the equilibration of the global model (described in chapter 2) TAF is invoked to transform the code into derivative form. As illustrated in figure 3.2, the checkpointing scheme entails 3 complete passes of the model trajectory in forward mode and 1 pass in reverse mode. For the current application a reverse pass is approximately 2.5 times slower than a forward pass. Consequently, the computational requirements involved in the execution of the adjoint model are a factor 5.5 times larger than for a standard forward integration. For the current model configuration

and available resources, adjoint experiments of 15-20 (model) years are at the limit of computational tractability.

No discussion has yet been given to the limitations of the adjoint. The usefulness of the linear sensitivity information it provides is founded on the assumption that the tangent linearisation about the nonlinear model trajectory is applicable. This not only restricts consideration to small amplitude perturbations in non-eddying regimes (*Lea et al.*, 2000), but also confines the study to a finite timespan. For now, it is noted that 15-20 year timeseries of linear sensitivity will be evaluated but might not be meaningful in their entirety. This point will be revisited later.

One further issue arises from the inclusion of highly nonlinear and discontinuous parameterisation schemes, such as GM and KPP, in the forward model. It is notoriously difficult to linearize these schemes without introducing unacceptable levels of noise into the numerical adjoint. For example, the adjoint of the KPP scheme contains an unstable term (see the discussion in *Hoteit et al.*, 2005). The complication in using GM in conjunction with KPP arises from having to match eddy stirring to convective mixing in regions of steep isopycnal slope. Although some choices of tapering schemes are less problematic than others (Patrick Heimbach, personal communication), the simplest way of avoiding potential noise problems is to neglect both KPP and GM altogether in the adjoint calculation. To obtain an exact linearisation, these schemes must also be omitted from the parent (forward) model. However, important interior mixing and boundary heat flux processes are then absent from the basic state. Below, GM and KPP are retained in the forward model and omitted from the adjoint solution. This choice will be revisited at the end of the chapter.

3.4 Numerical Experiment Results

I start by examining the pure sensitivity information, which reveals pathways and dynamical mechanisms that are potentially important in setting the variability of

$\overline{\psi_{25\mathrm{N}}}^{month}$. It is natural to discuss sensitivity distributions with increasing lead time from the point at which the objective function is analysed. This reversal of the time axis allows adjoint waves to be examined as moving away from the causal impulse (see *Bugnion and Hill*, 2006). As a result, propagation pathways observed in the forward model are traversed in the opposite direction in the adjoint framework. Following *Heimbach et al.* (2011), adjoint analogues of physics seen in the forward model are referred to below as "dual" effects.

The objective function is evaluated during the first month of the adjoint calculation, which is referred to as "t = -1 month" in the figure captions or "a lead time of 1 month" in the text. For example, if the costfunction is the January mean AMOC, $\overline{\psi_{25\mathrm{N}}}^{Jan}$, the sensitivity at a lead time of 2 months refers to the impact of forcing anomalies applied during the previous December.

In this section, the adjoint sensitivity distributions are displayed using a logarithmic contour spacing to highlight the propagation pathways. We are not aware that this approach has been taken in previous studies. Only the largest amplitude sensitivities will be discussed in detail. To simplify the discussion, all sensitivities shown in this section are for $\overline{\psi_{25\mathrm{N}}}^{Jan}$. Sensitivity dependence on the seasonality of the background hydrography will be addressed later in the chapter.

3.4.1 Key Regions and Propagation Pathways

Sensitivity to Surface Momentum Fluxes

In figure 3.3 snapshots of AMOC sensitivity to zonal wind stress, $\partial\overline{\psi_{25\mathrm{N}}}^{month}/\partial\tau^x$, are shown. For comparison, the same fields are redrawn with a constant contour interval in figure 3.4. At a lead time of 1 month (figure 3.3a), significant sensitivity to zonal wind stress is mainly confined to the North Atlantic basin. The pattern is dominated by a broad, zonally-uniform band of negative sensitivity extending across the basin width at 25°N. It is suggested that the latitudinal extent of this section of negative sensitivity may reflect coherence of the barotropic response (or "external mode" circulation, *Lee and Marotzke*, 1998) at 25°N, over 5-10 degrees of latitude.

An increase in the westerly wind stress, τ^x, of 1 Nm^{-2} within this band would lead to a decrease in $\overline{\psi_{25\mathrm{N}}}^{Jan}$ by approximately 0.5 Sv in the following month (figure 3.4a). This is consistent with Ekman theory, which dictates that the ageostrophic meridional mass flux is related to the orthogonal wind stress as follows

$$V_{EK} = -\frac{\tau^x}{\rho_0 f}, \tag{3.9}$$

where ρ_0 is the reference density and f is the Coriolis parameter. Integrating across the width of one grid cell at 25°N, a westerly wind of 1 Nm^{-2} in any grid box along the section leads to a southward surface transport of ≈ 0.4 Sv.

At short lead times, notable negative sensitivities also extend along most of the eastern boundary from 25°N to the Equator. A band of positive sensitivity occupies the western boundary region from 25°N to the Flemish Cap. The zonal asymmetry of these boundary-intensified sensitivities highlights the importance of Kelvin waves in the rapid adjustment of the AMOC as follows. In the northern hemisphere, on the eastern boundary of the ocean basin, a westerly wind drives offshore divergence along coastlines orientated from NW-SE and onshore convergence along coastlines

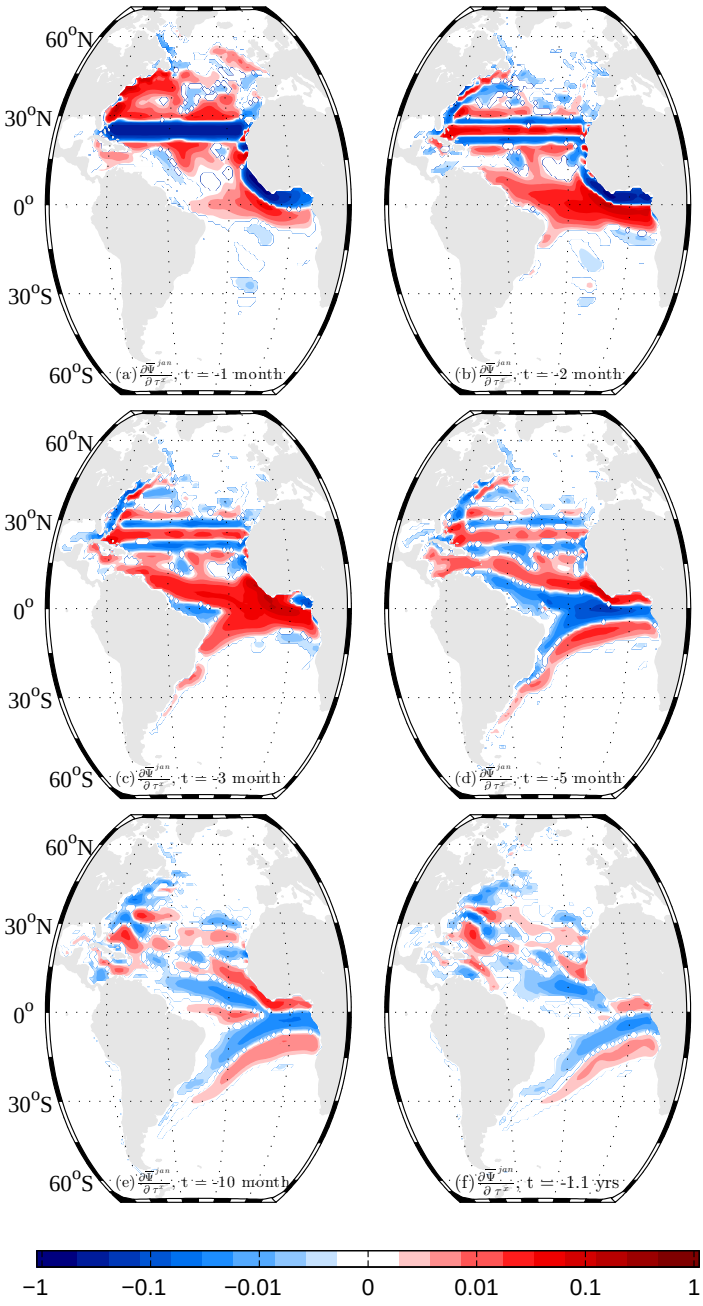

Figure 3.3: Linear sensitivity of $\overline{\psi_{25N}}^{Jan}$ to zonal wind stress at a lead time of (a) 1 month, (b) 2 months, (c) 3 months, (d) 5 months, (e) 10 months and (f) 1.1 years. The colour scale is logarithmic. Absolute magnitudes smaller than 0.001 Sv/Nm^{-2} have been set to 0 Sv/Nm^{-2}. Positive sensitivity indicates that a strengthening of the eastward wind at the specified lead time increases the overturning at 25°N.

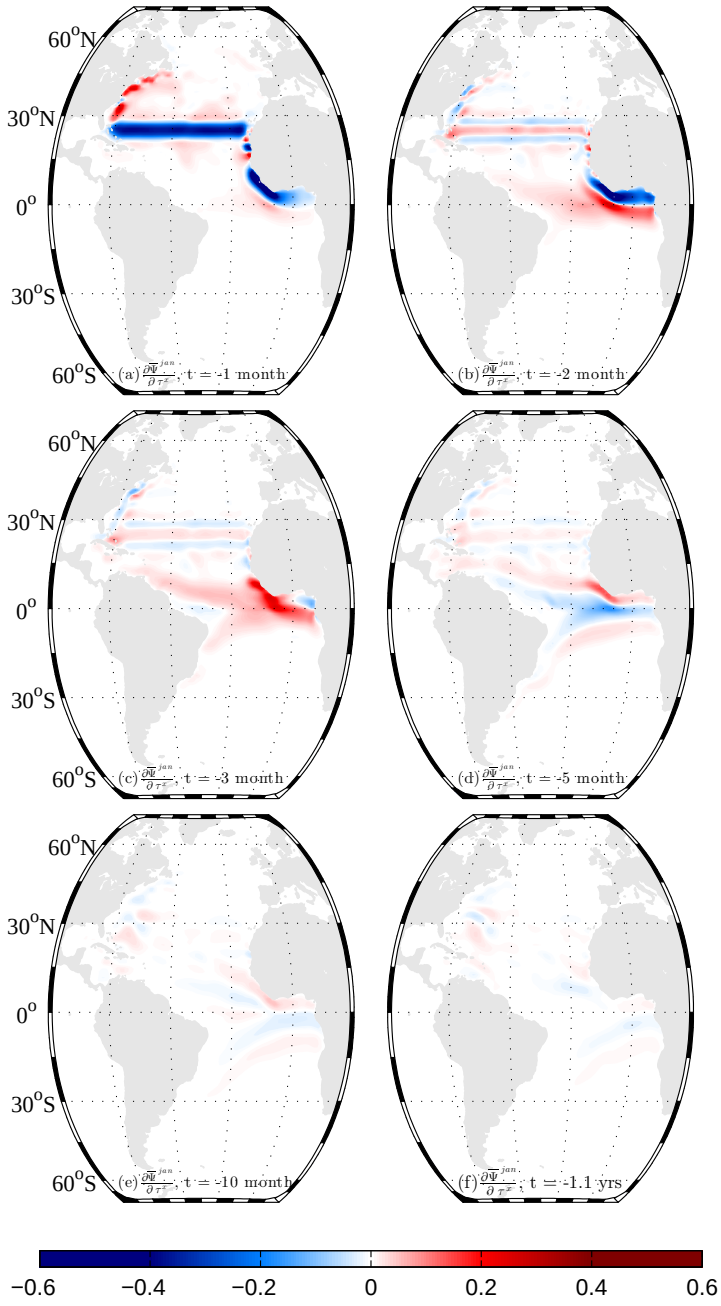

Figure 3.4: As for figure 3.3 but with a linear colour scale.

orientated from SW-NE. The opposite is true on the western boundary. As a result, westerlies drive offshore divergence along the majority of the east coast of the US and the west coast of Africa from Cape Verde to the Gulf of Guinea. Internal

Kelvin waves, appearing to travel at speeds of $\sim$1 ms^{-1} in the model, communicate the resultant negative pressure anomalies cyclonically around the basin[1]. Pressure anomalies generated anywhere in the upstream coastal wave guides within $\sim$3000 km of 25°N, can thus perturb the AMOC on timescales of 1 month.

On the western side of the basin, negative pressure anomalies strengthen the zonal pressure gradient and the upper ocean northward transport by geostrophic balance:

$$\mathbf{u} = \frac{1}{\rho f}\hat{k} \times \nabla p, \tag{3.10}$$

where $\hat{k}$ is a unit vector in the vertical, ∇ is the gradient vector and p is the pressure. This results in positive sensitivity between 25°N and the Flemish Cap. On the eastern boundary the opposite is true, resulting in negative sensitivity between 25°N and the Gulf of Guinea.

At a lead time of 2 months (figure 3.3b), a signature of the fast barotropic response is still visible around the latitude of the objective function, although the sensitivity centred across 25°N is now positive and flanked by sensitivity bands of alternating sign, spread over approximately 15° of latitude. The physics responsible for this distribution is not immediately obvious. It is seen to recur in the surface buoyancy flux sensitivities (figures 3.8 and 3.10) at short lead times and can be explored using a forward sensitivity experiment. The control integration is extended for 2 months from the start of December in the final year, with a positive perturbation to the December zonal wind stress at 25°N, as shown in figure 3.5a. The wind anomaly generates a dipole of free surface displacement, centred about the axes of anomalous forcing (figure 3.5c-d), with sea level elevated to the south. This signal appears to be communicated rapidly through the western sub-basin (i.e to the west of the Mid-Atlantic Ridge (MAR)) by barotropic Rossby waves. Conservation of

[1]Since the total Coriolis force deflects the flow to the right (left) in the northern (southern) hemisphere, the pressure anomaly can only be sustained adjacent to the boundary if the Kelvin wave travels with the coast to the right (left).

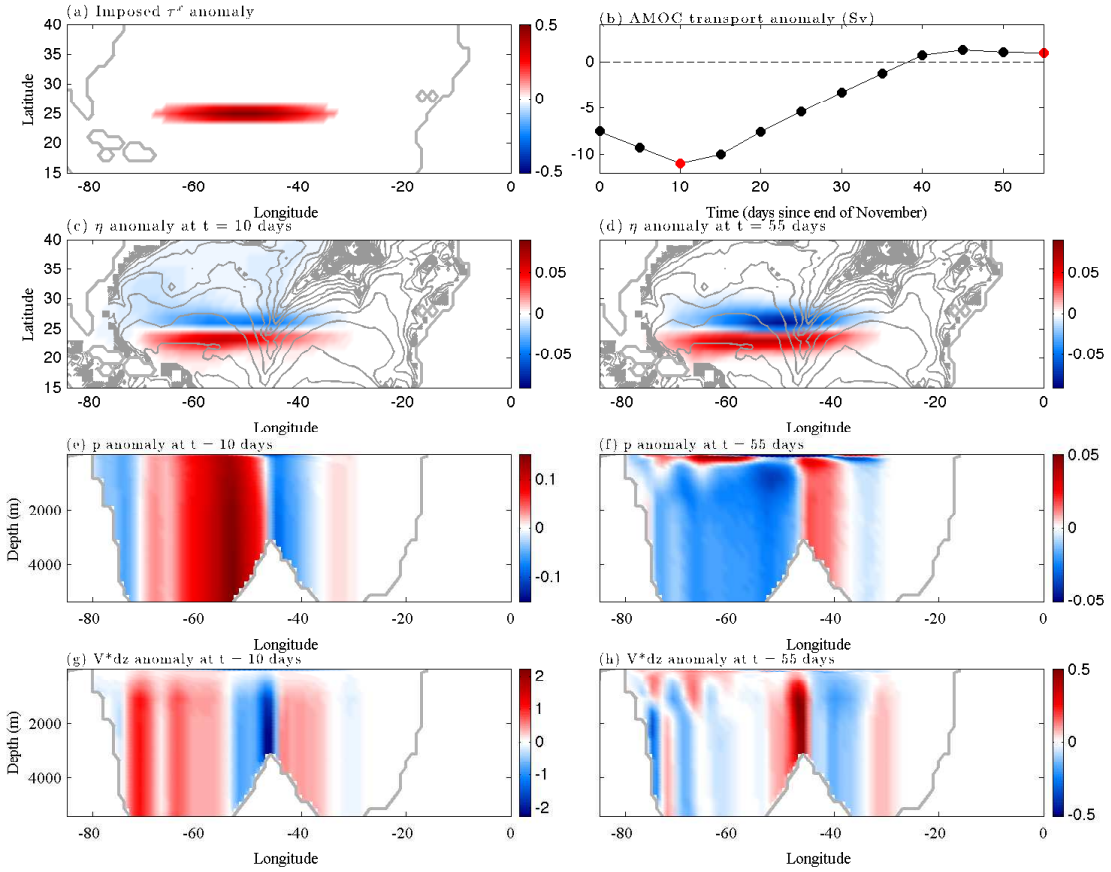

Figure 3.5: (a) Applied December eastward wind stress anomaly (Nm^{-2}), serving as a simple representation of the interior sensitivity pattern in figure 3.3b. Resulting anomalies in the free surface displacement (m), pressure ($\mathrm{m}^2\mathrm{s}^{-2}$) at 25°N, and meridional mass transport ($\mathrm{m}^2\mathrm{s}^{-1}$) at 25°N are shown in panels (c)-(h) for day 10 (left column) and day 55 (right column) of the integration. In panels (c)-(d), contours of constant f/H are shown in grey. Thick grey contours in panels (a),(e)-(h) delineate the ocean floor. The $\overline{\psi_{25\mathrm{N}}}^{Jan}$ transport anomaly (Sv) is plotted in panel (b).

potential vorticity (PV) results in topographic steering, so that the barotropic signal is communicated along contours of constant f/H. As the ridge is approached (H decreases), the waves are steered towards the Equator (decreasing f). As the waves move off the ridge (H increases) onto the abyssal plane, steering is towards higher latitudes (increasing f). PV conservation by the westward propagating waves thus results in negative/positive pressure anomalies arriving on the eastern/western flank of the MAR at 25°N during the first month (December) of the integration. The neg-

ative pressure gradient established across the ridge crest (figure 3.5e) is equilibrated by a southward anomalous geostrophic transport (figure 3.5g) and an associated weakening of the AMOC by 11 Sv on the 10th day of the integration (figure 3.5b). By the 2nd month of the integration (January), the negative pressure anomaly has propagated around the f/H saddle associated with the MAR, arriving at 25°N in the western sub-basin from the south, and spreading westward. The spreading signal is further modified by the excitation of slower, baroclinic Rossby waves propagating westward from the western flank of the MAR (*Barnier*, 1988). This reversal of the zonal pressure gradient (figure 3.5f) generates an anomalous northward geostrophic transport over the ridge crest (figure 3.5h) and a strengthening of the AMOC during the 2nd month of the integration. The net result of the December wind stress anomaly is an increase of approximately 0.5 Sv in the January mean AMOC. This is in good, quantitative agreement with the linear sensitivities (figure 3.4b). Note that the imposed eastward wind anomaly need not extend across the MAR to generate an AMOC strengthening at short lead times. As suggested in figure 3.3b, it can be applied at almost any location across the section, since topographic steering will ensure that a positive perturbation zonal pressure gradient is established during the following month.

The subtle details of the interaction between the MAR and propagating Rossby waves are beyond the scope of the present study, but have been explored at length using WKB theory (*Straub*, 1994; *Hallberg*, 1997; *Tailleux and McWilliams*, 2000, 2002; *Tailleux*, 2004, 2006; *Killworth and Blundell*, 1999; *Killworth*, 2003a,b) and the reader is referred to *Marshall* (2011) for a useful discussion. Relevant to the analysis above is the detection of localized transfers of energy between wave modes over abrupt changes in bathymetry (*Hallberg*, 1997). Recently, *Marshall* (2011) derived an integral constraint to explain why this modal interaction must occur. It emerges that a net radiative flux of upper layer thickness into a closed f/H

contour on one side of the ridge is almost immediately re-radiated on the opposite side of the ridge. This apparent topographic short cut, the "Rossby wormhole", must be achieved by conversion between wave modes and the generation of transient barotropic circulations around the f/H contour.

Within a lead time of 2 months, the final notable feature is a band of positive sensitivity, emanating from the subtropical west african coast and crossing to the western side of the basin in the Equatorial waveguide. Here dual coastal Kelvin waves are shed to the north and south (figure 3.3b). With a further increase in lead time (figures 3.3c-d) these dual Kelvin waves continue to propagate northwards/southwards in the respective hemispheres, shedding eastward propagating dual Rossby waves into the ocean interior. Low latitude dual Rossby waves show a notable equatorward tilt towards the eastern boundary due to the dual Beta effect (dual Rossby wave phase is eastward and fastest at the Equator). The emergence of the tropics as a key pathway for dual Rossby wave propagation - not visible in the sensitivity patterns at higher latitudes - is consistent with the adjoint sensitivities presented by *Galanti and Tziperman* (2003); *Kohl* (2005); *Heimbach et al.* (2011). Long Rossby waves are damped in transit by viscous dissipation but may amplify along the baroclinically unstable equatorward flanks of the subtropical gyres.

At a lead time of 2 months, dual Rossby wave generation is also visible on the Eastern US Seaboard. Here, the positive band of sensitivity - occupying the coastal waveguide at short lead times - propagates offshore and a band of negative sensitivity sits adjacent to the coast (figure 3.3d-f). By a lead time of 10 months however, the amplitude of the sensitivities has diminished significantly. By a lead time of 1.1 years, the sensitivities are vanishingly small relative to their amplitude during the month of the objective evaluation.

Sensitivity distributions to meridional wind stress, $\partial\overline{\psi_{25\mathrm{N}}}^{\,month}/\partial\tau^y$, reveal similar rapid teleconnections to those discussed above. At lead times shorter than 2 months

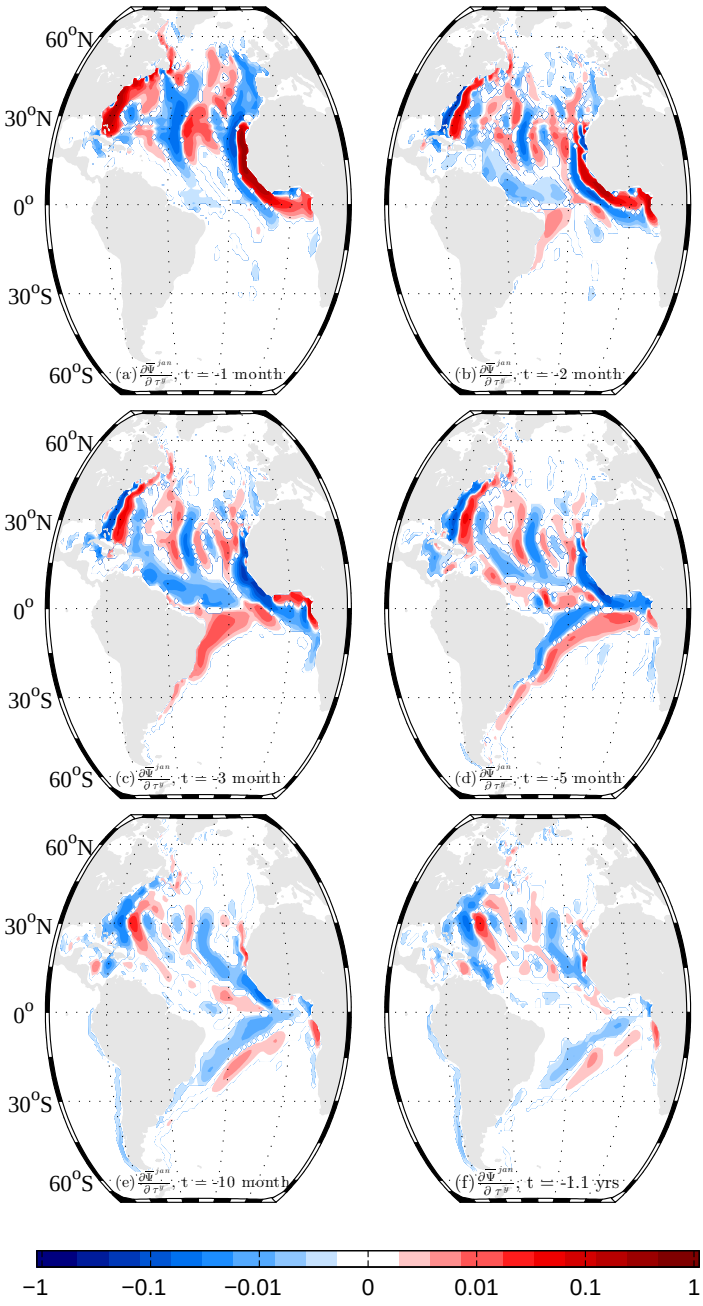

Figure 3.6: As for figure 3.3 but for sensitivity to meridional wind stress, τ^y. Positive sensitivity indicates that a strengthening of the northward wind at the specified lead time increases the overturning at 25°N.

(figures 3.6a-b), large amplitude positive sensitivities are concentrated in the coastal wave guides to the north (south) of the section, on the west (east) side of the basin

respectively. In the northern hemisphere, southerly winds drive offshore (onshore) surface transport on the western (eastern) basin margin. The resulting enhancement of the cross-basin zonal pressure gradient is accompanied by a strengthening in the interior northward transport, by geostrophic balance (3.10).

A dipole of weaker sensitivity is also visible straddling the MAR around 25°N at short lead times (figure 3.6a). Considering a wind stress anomaly that matches this sensitivity pattern (i.e replace positive (negative) sensitivity with southerly (northerly) wind), the result is a strengthening of the AMOC by a local enhancement of the zonal pressure gradient across the crest of the MAR. This is confirmed with a forward sensitivity experiment (figure 3.7). The control experiment is integrated for one month from the beginning of January, with a perturbation to the January meridional wind stress, as shown in figure 3.7a. The anomalous Ekman velocity generates dipoles of surface displacement, centred about the axes of anomalous forcing (figure 3.7b). As seen for the zonal wind stress experiment above (figure 3.5c), the signal generated on the western flank of the MAR is rapidly communicated westward by long, barotropic Rossby waves following contours of f/H. This results in the positive pressure signal generated at the base of the MAR spreading approximately westward, while the negative anomaly generated upslope is deflected polewards. The signal generated on the eastern flank is unable to cross the MAR at 25°N, but must take a more contorted route south-westwards around the f/H saddle. Positive zonal pressure gradients are generated across the majority of the eastern sub-basin, directly beneath the positive wind stress anomaly, and slightly eastwards of the negative anomaly (figure 3.7c). As above, there is evidence for conversions between barotropic and baroclinic modes. In general, negative zonal pressure gradients are established directly beneath the negative wind stress anomaly and slightly eastwards of the positive anomaly. The meridional velocity adjusts geostrophically to balance these perturbation pressure gradients. The zonal integral of the meridional

mass flux (figure 3.7d) reveals that the perturbed AMOC is described by an anomalous northward (southward) volume flux above (below) 4000 m. The net result is an average AMOC increase of approximately 0.5 Sv during the single month (January) of integration. This is in good quantitative agreement with the linear sensitivities (figure 3.6a).

With increased lead time, the amplitude of the sensitivities decay and slower pathways emerge through the ocean interior. As for the zonal wind stress, meridional wind stress anomalies applied in the vicinity of the section, the neighbouring upstream coastal waveguides, the equatorial wave guide, and the equatorward flanks of the subtropical gyres have the largest impact on the monthly mean transport variability. At no time do wind stress anomalies outside the Atlantic Basin appear significant for the seasonal variability of the AMOC at 25°N. It is also suggested that wind anomalies in the south-east and north-east Atlantic are unimportant for AMOC seasonality at 25°N. In a forward sense, anomalies generated in these locations can only reach 25°N after first crossing the basin via long Rossby waves, to then travel equatorwards in the western boundary waveguides. The signal is damped during the basin crossing, achieved over a period that increases toward the poles (*Chelton and Schlax*, 1996). Furthermore, geostrophy of the Kelvin wave, eventually generated on the western boundary, dictates that the associated pressure anomaly must decrease in magnitude as the Kelvin wave moves equatorward. After passing through the equatorial region, the signal cannot re-amplify with poleward migration in the eastern boundary wave guide due to the leakage of Rossby waves into the interior (*Johnson and Marshall*, 2002a). This point is critical in severely limiting the potential for anomalies generated south of the Equator to affect the transport at 25°N.

Sensitivity to surface buoyancy forcing

In figures 3.8-3.9 snapshots of AMOC sensitivity to net upward surface heat flux (ignoring the shortwave contribution), $\partial\overline{\psi_{25\mathrm{N}}}^{Jan}/\partial Q$, are shown. At short lead times (figure 3.8a-c), many of the fast pathways already discussed in the context of AMOC sensitivity to wind stress are visible. At a lead time of 1 month (figure 3.8a) positive (negative) sensitivities occupy the neighbouring upstream coastal waveguide on the western (eastern) boundary. A heat flux perturbation matching this distribution (i.e net surface cooling (warming) on the western (eastern) boundary) and communication of the resulting anomalies by dual coastal Kelvin waves, generates an upper ocean negative perturbation density gradient across 25°N on monthly timescales. This is accompanied by a strengthening of the interior northward transport, by thermal wind balance:

$$\frac{\partial \mathbf{u_g}}{\partial z} = -\frac{g}{\rho_0 f}\hat{k} \times \nabla\rho. \tag{3.11}$$

At a lead time of 2 months (figure 3.8b), the negative sensitivity on the eastern boundary crosses the basin in the equatorial wave guide and sheds dual coastal Kelvin waves in the South American waveguides. These in turn shed eastward propagating dual Rossby waves, clearly visible at a lead time of 10 months (figure 3.8c), by which time dual coastal Kelvin waves have communicated the positive sensitivity on the eastern US seaboard around the Labrador and Irminger basins. At this time, dual Rossby wave trains also emerge at around 15°N and 30°N. Although dual Rossby propagation is notable within the subtropics, the wave train at 30°N makes little progress eastwards. It is likely that this is due to Doppler shifting by the dual subtropical gyre circulation.

With a further increase in lead time, all processes continue as previously discussed; dual Kelvin waves advance through the coastal wave guides, and dual Rossby waves advance eastwards through the interior, with faster phase speeds towards the

equator (figure 3.8d). However, in marked contrast with the wind stress sensitivities presented above, the sensitivities to buoyancy forcing do not decrease monotonically with increased lead time. Instead, decadal timescales are generated by advective processes linking 25°N to high northern latitudes.

Decadal variability of the AMOC has been investigated using an adjoint modelling approach by *Czeschel et al.* (2010). The authors identify buoyancy forcing over the high latitude North Atlantic as the potential driver of a decadal oscillation in the subtropical AMOC, yielding the counter-intuitive result that high latitude warming can cause an eventual strengthening of the AMOC. Defining stages of this oscillatory mode are shown (from the present study) in figure 3.9. Strong seasonality is visible in the buoyancy sensitivities, so all fields shown correspond to heat flux anomalies applied in the same month.

At a lead time of 6 years (figure 3.9a), positive sensitivity amplifies notably in the subpolar gyre and Greenland-Iceland-Norwegian (GIN) Seas (see also figure 3.8d) and travels southwards, advected by the dual western boundary jet, into the Gulf of Mexico. The wave train emanating from near 25°N on the western boundary extends right across the basin to western europe, where a region of negative sensitivity is established. As the lead time increases to 9 years (figure 3.9b), the sensitivity intensifies in the North Atlantic basin and the positive sensitivity on the western boundary is advected further southwards in the dual North Brazil Current. It is implied that ocean cooling almost anywhere in the North Atlantic western boundary current system or subpolar gyre interior would lead to an increase in $\overline{\psi_{25\mathrm{N}}}^{month}$, 9 years later. Heat gain by the ocean right on the eastern boundary, between the Mediterranean and the northern margin of the model, further supports AMOC strengthening when applied at this lead time.

By a lead time of 11 years (figure 3.9c), discrete patches of negative sensitivity, visible in the Labrador Sea and Irminger Current at shorter lead times (figures 3.9a-

b), amplify and spread (by eastwards propagation of dual Rossby waves) to occupy a large part of the subpolar gyre. Positive sensitivity now occupies the north-eastern Atlantic coastal wave guides. It is implied that after a period of approximately 10 years, $\overline{\psi_{25\mathrm{N}}}^{month}$ responds in the opposite sense to a perturbation zonal density gradient at high northern latitudes. As lead time increases towards 15 years (figures 3.9d-f), the region of negative sensitivity is spread, by the dual Gulf Stream and dual Rossby waves, to fill most of the northwest Atlantic basin. The sensitivity distribution at a lead time of 15 years (figure 3.9f) is approximately in anti-phase with the sensitivity distribution at a lead time of 9 years (figure 3.9b),

The sensitivity patterns appear consistent with the self-sustaining "thermal Rossby" mode discussed by *Te Raa and Dijkstra* (2002) and *Huck et al.* (1999). However, as discussed by *Czeschel et al.* (2010), other physical mechanisms are at play that affect the oscillation. Most notably, thermal anomalies established on the east coast of the North Atlantic stimulate baroclinic Rossby waves which (in a forward sense) propagate westwards towards the Gulf Stream and are subsequently advected into the subpolar gyre to alter the high latitude zonal density gradient. In the adjoint framework, this mechanism is most clearly seen with lead times increasing from 3 to 11 years (figures 3.8d-3.9c). Positive sensitivity in the subpolar gyre (figure 3.8d) is advected southwards by the dual Gulf stream, detaching from the coast near Florida (figure 3.9a) and propagating north-eastwards towards Europe (figures 3.9b-3.9c) in a dual Rossby wave train along the southern flank of the separated western boundary jet. The identification of this pathway and our interpretation of the dual teleconnection is consistent with *Czeschel et al.* (2010) and supported by sea surface height observations (*Fu*, 2004).

An interesting feature in the sensitivity patterns to buoyancy forcing at increased lead times (figure 3.9) is the suggested importance of buoyancy forcing over the region occupied by the Agulhas retroflection (figure 3.9). In the real ocean, eddies shed

by this system act as the dominant supplier of warm and salty waters entering the Atlantic to form the upper limb of the AMOC. This leakage is not well represented at the current model resolution, however it has been identified as a potential contributor to AMOC variability on decadal timescales in high resolution modelling studies (*Biastoch et al.*, 2008). Intriguingly, the sensitivity is stationary at lead times of a decade and longer, in close agreement with the sensitivity patterns to 3-dimensional temperature and salinity fields presented by *Heimbach et al.* (2011). The authors hypothesize that this stationarity is due to prolonged periods of persistent recirculation without significant leakage.

The patterns of sensitivity to surface heat, $\partial\overline{\psi_{25\mathrm{N}}}^{\,month}/\partial Q$, and freshwater fluxes, $\partial\overline{\psi_{25\mathrm{N}}}^{\,month}/\partial(E-P)$, are very similar at lead times exceeding 1 month (figures 3.8-3.11). The notable distinction during the month of cost function evaluation (compare figures 3.8a and 3.10a) is due to the formulation of the continuity equation. Following *Huang* (1993), freshwater fluxes in the present study are treated as a source of volume in the continuity equation (as opposed to a virtual salt flux), directly influencing the sea surface height, η, (see *Campin et al.*, 2004). It follows that the global ocean salt content is exactly conserved, whilst total ocean mass may change. The associated change in volume is then redistributed rapidly around the globe by barotropic Kelvin waves with a speed of approximately 200 ms^{-1} in the deep ($H \sim 4$ km) ocean (e.g. *Stepanov and Hughes*, 2006; *Lorbacher et al.*, 2012). Surface heat fluxes also alter the ocean volume by perturbing the near-surface density field. However, the volume source due to thermal expansion of the water column is neglected in the model[2]. It follows that the fast global barotropic response is absent from the heat flux sensitivities.

A forward experiment confirms that the sensitivity pattern in figure 3.10a, is set

[2]This simplification is supported by *Greatbatch* (1994), who estimates that the maximum seasonal range in steric expansion is an order of magnitude smaller than the seasonal variation in η driven by freshwater fluxes. The resulting Goldsbrough-Stommel circulation (e.g see *Huang*, 2010, chapter 5) induced by thermal expansion is therefore negligible relative to that induced by $E-P$.

by the barotropic teleconnections described above. The control experiment is integrated for one month from the beginning of January, with a perturbation of -0.5 Sv to the January $E - P$ field (i.e volume gain) in the North Atlantic. The perturbation is distributed smoothly over a $12° \times 12°$ area centred on 30.5°W and 40.5°N. Barotropic adjustment rapidly communicates the signal to the western boundary and southwards in the western boundary waveguide (figure 3.12a-b). The signal then propagates across the Equator and into the eastern boundary wave guides, which in turn shed barotropic Rossby waves into the interior (figure 3.12c-d). The signal enters the Pacific via the Indian ocean which adjusts in an analogous manner to the Atlantic (figure 3.12e-h). The perturbation is radiated across the global ocean within 12 days (figure 3.12h).

Since the extra volume is added north of the section, the signal arrives at 25°N in the western boundary waveguide, generating a negative cross-basin perturbation pressure gradient and weakening the northward geostrophic transport. The interior adjusts so that a return (northward) transport is generated over the MAR. If the perturbation is applied south of the section, the signal will reach 25°N on the eastern boundary. This leads to (1) the change in sign about the latitude of the objective function, (2) smaller sensitivities to the south of the section since all perturbations to the south must pass through the "equatorial buffer" (*Johnson and Marshall*, 2002a).

This analysis is consistent with a recent simulation of rapid barotropic sea level rise in response to ice sheet melting (*Lorbacher et al.*, 2012). On imposing a 0.1 Sv freshwater perturbation around the perimeter of Greenland (or Antarctica), the authors demonstrate that the global ocean experiences sea level rise within 7-8 days. Despite this fast response, inter-basin gradients in the perturbed sea level remain (as also seen in figure 3.12).

To conclude, we note that strong sensitivity to freshwater forcing is found in

the subtropical gyres of both hemispheres at lead times exceeding a decade (figure 3.11). The suggestion is that salty anomalies, generated by increased low-latitude evaporation, are advected towards the North-East Atlantic, where they support a positive perturbation zonal density gradient. Interestingly, the subtropics do not play a significant role in the thermal Rossby mode present in the surface heat flux sensitivities (figure 3.9). We hypothesize that this discrepancy is due to stronger damping of SST anomalies relative to SSS anomalies imposed in the model.

3.4.2 AMOC Memory to Wind and Buoyancy Variability

An estimate of the memory of $\overline{\psi_{25\mathrm{N}}}^{month}$ to surface fluxes of buoyancy and momentum can be made by examining the evolution of linear sensitivity in a particular part of the basin. As shown in the previous section, the subpolar Atlantic is an important centre of action for freshwater and heat flux variability. Conversely, significant sensitivity to wind stress variations is restricted to the vicinity of 25°N and the local coastal waveguides. In figures 3.13a-b, the sensitivity to surface heat and freshwater fluxes is shown integrated over the subpolar gyre. In figures 3.13c-d the sensitivity to zonal and meridional wind is integrated over the western boundary region on the Eastern US Seaboard, north of the objective latitude. As identified above, a strong barotropic response dominates the initial response of $\overline{\psi_{25\mathrm{N}}}^{month}$ to perturbed fluxes of momentum and freshwater, but is absent from the accumulated heat flux sensitivities (figure 3.13a). Seasonal variability is visible in all surface flux sensitivities, for all 12 months of costfunction evaluation. Seasonality is most notable for the sensitivities to surface buoyancy forcing. However, despite the dominance of the wind stress sensitivities by the initial barotropic response, close inspection of figures 3.13c-d reveals that seasonality is still detectable across the wind stress sensitivity timeseries.

Consistent with the analysis by *Czeschel et al.* (2010), the subtropical AMOC is associated with oscillatory sensitivity to the surface buoyancy forcing in the subpolar

North Atlantic. We perform our subpolar gyre integral to allow direct comparison of the amplitude and period of the oscillation in 3.13a with that in figure 1 of *Czeschel et al.* (2010). Note that the surface heat flux is defined to be positive into the ocean in *Czeschel et al.* (2010), at odds with our definition. To prevent ambiguity, we introduce the notation "cold phase" ("warm phase") to denote lead times when cooling (warming) over the subpolar gyre would lead to an eventual increase in the AMOC. Although our analyses are consistent in producing an initial cold phase, followed by a warm phase at increased lead times, there are notable differences in the amplitude and period of the oscillations. In the present study, the oscillation has a period of approximately 10 years. We resolve only one full cycle of the oscillation. The maximum absolute amplitude of both cold and warm phases of sensitivity is approximately 6.5 $\times 10^{-3}$ Sv/Wm^{-2}. *Czeschel et al.* (2010) are able to derive a 40 year long sensitivity timeseries resolving two full cycles of the oscillation. In contrast to the present analysis, they observe a notable damping of the oscillation with increased lead time. The maximum absolute amplitude of their initial cold phase is 2.0 $\times 10^{-3}$ Sv/Wm^{-2}. Their subsequent (with increased lead time) warm phase achieves an amplitude of only 0.8 Sv/Wm^{-2}. Furthermore, damping of the oscillation with increased lead time is accompanied by a reduction in period.

Czeschel et al. (2010) note that the damping is highly sensitive to the formulation of the boundary condition on SSS/SST. On repeating their analysis with fixed heat fluxes in place of SST restoring, the sensitivities were amplified by up to 100%. This result is supported by *Bugnion et al.* (2006a,b) who show that the modelled overturning exhibits greater sensitivity to surface buoyancy forcing under mixed or fixed flux boundary conditions than under relaxation boundary conditions.

In the present study, we employ a relaxation timescale of 6 months on SSS, allowing for increased persistence of surface buoyancy anomalies relative to *Czeschel et al.* (2010) who employ a relaxation timescale of 3 months. This is consistent with

weaker damping of the high-latitude oscillatory sensitivity in the present study, although this may not fully explain the discrepancy in both the amplitude and phase of oscillation. A substantial body of work (see *Dijkstra et al.*, 2006, and references therein) have explored generation of internal modes of oceanic variability on decadal timescales. As discussed in chapter 2, these oscillatory modes rely on a phase difference between changes in the AMOC and the resulting temperature anomalies. These modes have been found under a broad range of conditions (*Colin de Verdiere and Huck*, 1999; *Huck et al.*, 1999), but threshold behaviour has been shown to exist (*Huck et al.*, 2001; *Te Raa and Dijkstra*, 2002), and the modes may vanish in the presence of strong atmospheric damping and/or large horizontal mixing of heat for example. These studies suggest that closer comparison of model parameters would be also be useful in helping to diagnose the discrepancy between our results and those of *Czeschel et al.* (2010).

3.4.3 Importance of Seasonality in the Background State

To investigate the importance of seasonality in the background hydrography, the timeseries of accumulated sensitivity shown in figure 3.13 are realigned with the corresponding month in the calendar year. The month in which the seasonal maximum sensitivity occurs is assessed for every year of the 12 month ensemble. It emerges that $\overline{\psi_{25\mathrm{N}}}^{month}$ is most sensitive to wind stress anomalies applied over the Eastern US Seaboard in autumn; high latitude buoyancy anomalies are most effective when applied in winter and spring (figure 3.14). As expected, the seasonal peak in buoyancy sensitivity coincides with the seasonal peak in mixed layer depth. Consistent with observations, the modelled mixed layer depth deepens during winter and shoals during summer, attaining a maximum depth of ∼500 m over the subpolar gyre in February. Surface salinity and temperature anomalies are thus rapidly communicated to depth and shielded from future damping by atmosphere-ocean interaction.

3.4.4 Importance of Nonlinear Dynamics

Finally, we turn to examine the validity of the linear sensitivities examined in this chapter. This depends critically upon whether the tangent linear model is an accurate representation of perturbation growth in the GCM. As discussed above, the linearization is only representative for perturbations of a sufficiently small amplitude. The precise definition of 'small' depends upon the linearity of the background state; increased nonlinearity in the underlying dynamics reduces the permissible size of the imposed perturbation. Furthermore, any finite amplitude perturbation - however small - in the fully nonlinear model will eventually experience exponential growth due to nonlinear interaction between various scales (*Lorenz*, 1963). For this reason, there exists a finite time period over which our linear sensitivities remain meaningful.

In a coarse resolution ($4^\circ \times 4^\circ$) configuration of the MITgcm, *Bugnion et al.* (2006b) derived linear sensitivities that remain valid over multi-centennial timescales. At higher ($1^\circ \times 1^\circ$) resolution, this timescale is reduced to 15-20 model years (*Czeschel et al.*, 2010). At eddy-resolving resolutions, useful adjoint gradients have only been obtained by assuming the background state is at rest (*Czeschel et al.*, 2012). Even in this case, the rapid emergence of strongly nonlinear dynamics restricts application of the adjoint to timescales of a few months.

We determine the timescales over which the linear sensitivities remain relevant by running an ensemble of four forward integrations in which the atmospheric heat, freshwater, zonal wind stress and meridional wind stress is perturbed in isolation. The design of the ensemble members is based on the analysis in figure 3.13. Specifically, the four ensemble members (a-d) are forced with the full surface flux climatologies and (a) heat flux anomalies of 10 Wm^{-2} over the subpolar region, (b) freshwater flux anomalies of 1×10^{-7} ms^{-1} over the subpolar region, (c) zonal wind stress anomalies of 1 Nm^{-2} over the western boundary region, (d) meridional wind stress anomalies of 1 Nm^{-2} over the western boundary region. The coordinates of the

subpolar and western boundary regions are defined in the caption of figure 3.13. A similar procedure was followed by *Czeschel et al.* (2010). For each member, a time-series of anomalous $\overline{\psi_{25\mathrm{N}}}^{month}$ is compared to that generated by projecting the forcing anomaly imposed in the forward run onto patterns of linear sensitivity (not shown). Consistent with *Czeschel et al.* (2010), we find that the linear sensitivities provide a meaningful description of the nonlinear system on timescales of approximately 15 years. Note that this is the maximum length of most of the adjoint experiments.

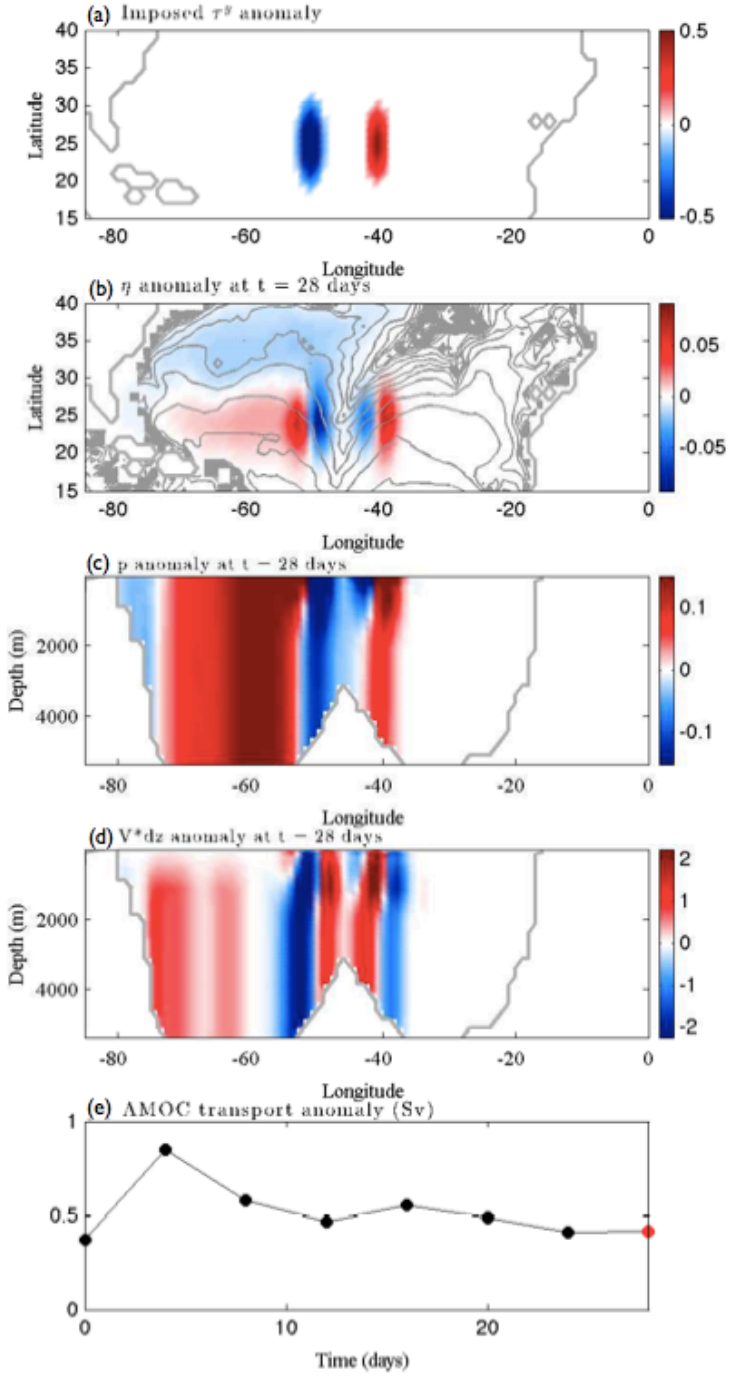

Figure 3.7: (a) Applied January northward wind stress anomaly (Nm^{-2}) serving as a simple representation of the sensitivity dipole in figure 3.6a. Resulting anomalies in the free surface displacement (m), pressure ($\mathrm{m}^2\mathrm{s}^{-2}$) at 25°N, and meridional mass transport ($\mathrm{m}^2\mathrm{s}^{-1}$) at 25°N are shown in panels (b)-(d) respectively for day 28 of the integration. Thick grey contours in panels (c)-(d) delineate the ocean floor. In panel (b), contours of constant f/H are shown in grey. The $\overline{\psi_{25\mathrm{N}}}^{Jan}$ transport anomaly (Sv) is plotted in panel (e).

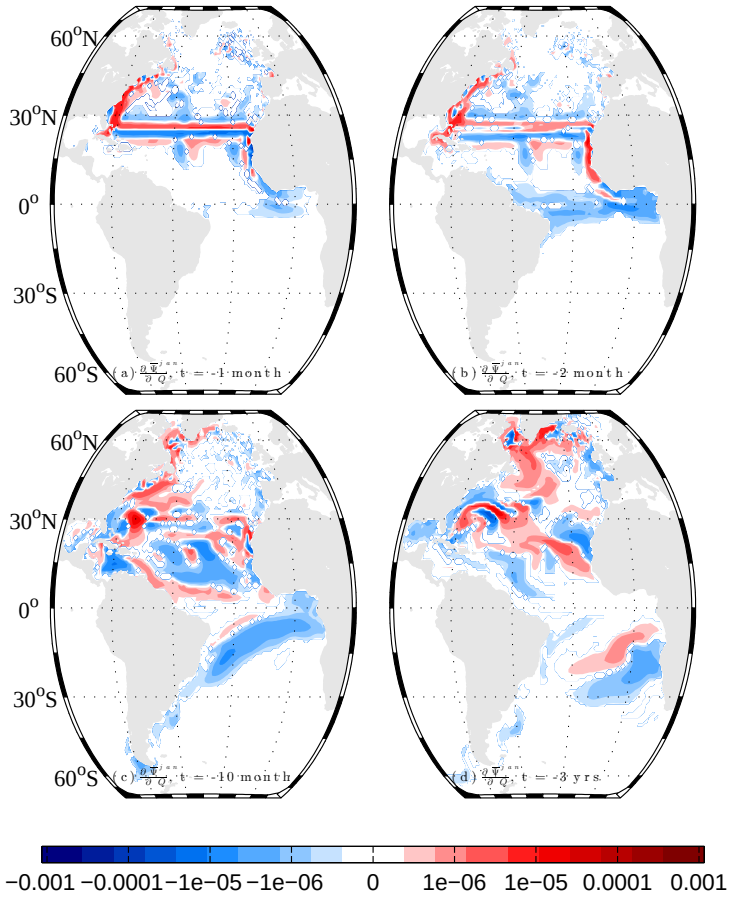

Figure 3.8: Linear sensitivity of $\overline{\psi_{25\mathrm{N}}}^{Jan}$ to net surface heat flux (Q, excluding short wave radiation) at a lead time of (a) 1 month, (b) 2 months, (c) 10 months, and (d) 3 years. The contour spacing is logarithmic and absolute magnitudes less than 1e-7 Sv/Wm^{-2} have been set to 0 Sv/Wm^{-2}. Positive sensitivity indicates that heat loss to the atmosphere at the specified lead time increases the overturning at 25°N.

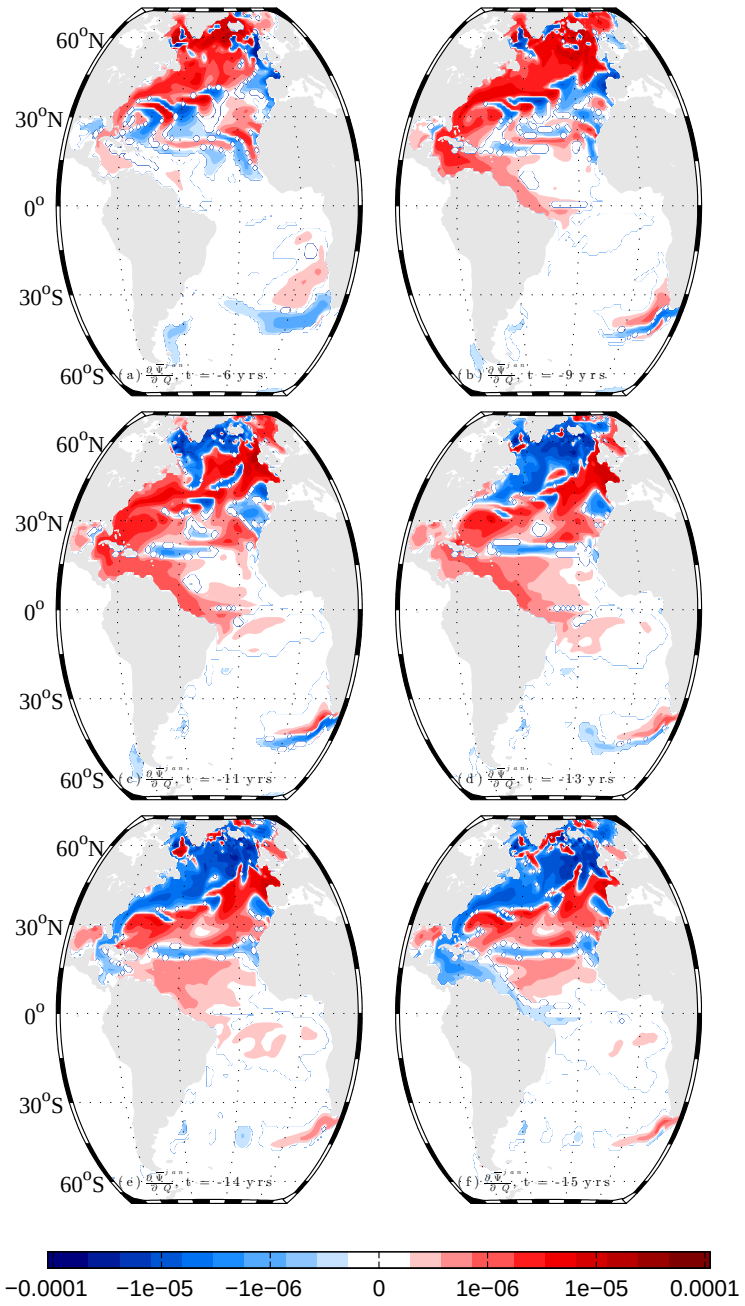

Figure 3.9: As for figure 3.8 but for lead times of (a) 6 years, (b) 9 years, (c) 11 years, (d) 13 years, (e) 14 years and (f) 15 years.

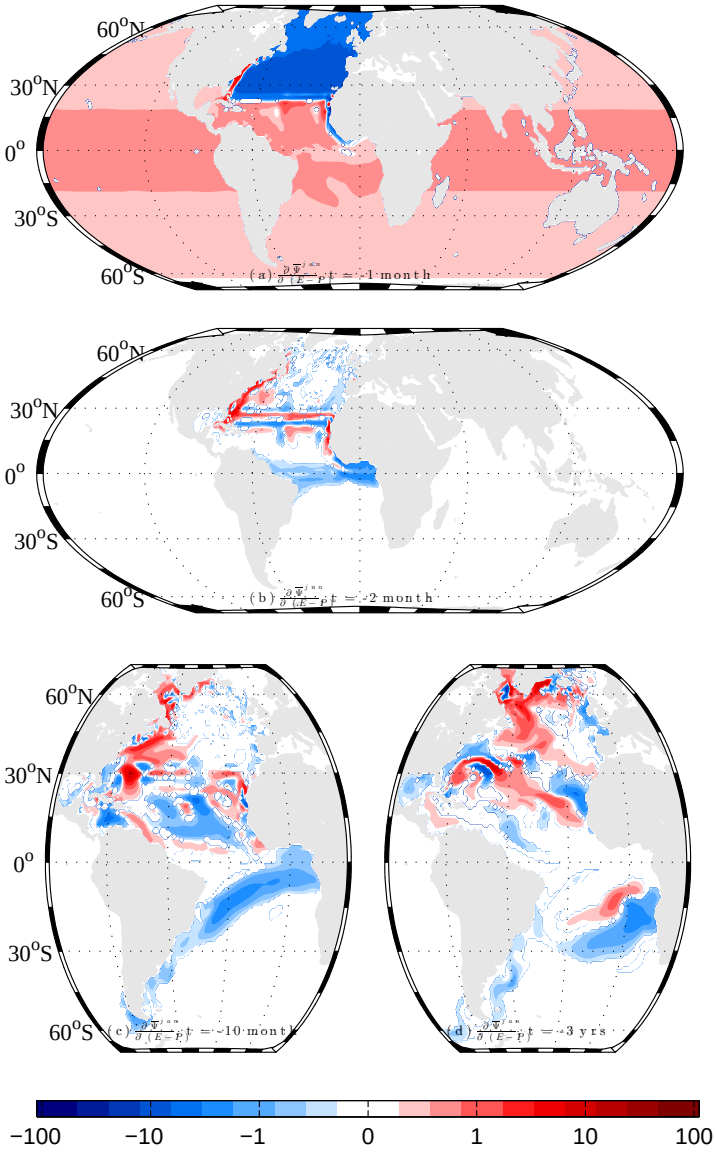

Figure 3.10: Linear sensitivity of $\overline{\psi_{25\mathrm{N}}}^{Jan}$ to net surface freshwater flux (E-P, excluding runoff) at a lead time of (a) 1 month, (b) 2 months, (c) 10 months, and (d) 3 years. The contour spacing is logarithmic and absolute magnitudes less than 0.1 Sv/ms^{-1} have been set to 0 Sv/ms^{-1}. Positive sensitivity indicates that a increased freshwater loss to the atmosphere at the specified lead time increases the overturning at 25°N.

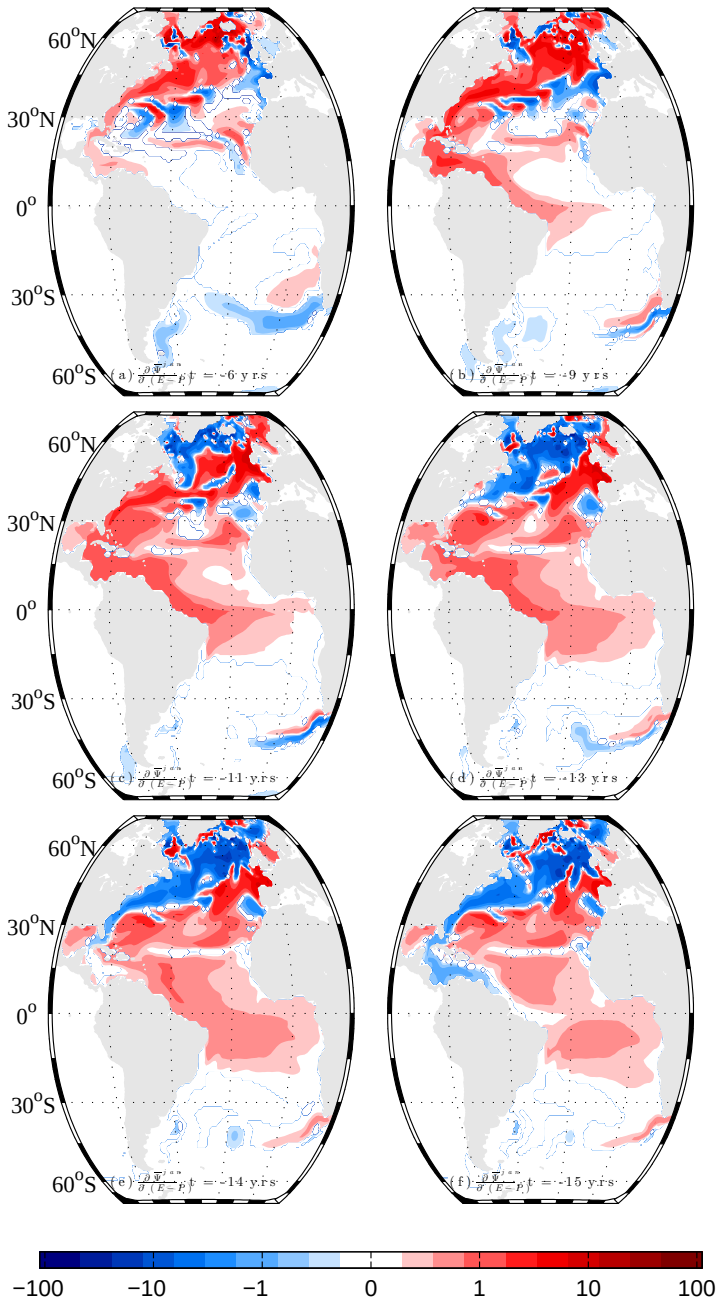

Figure 3.11: As for figure 3.10 but for lead times of (a) 6 years, (b) 9 years, (c) 11 years, (d) 13 years, (e) 14 years and (f) 15 years.

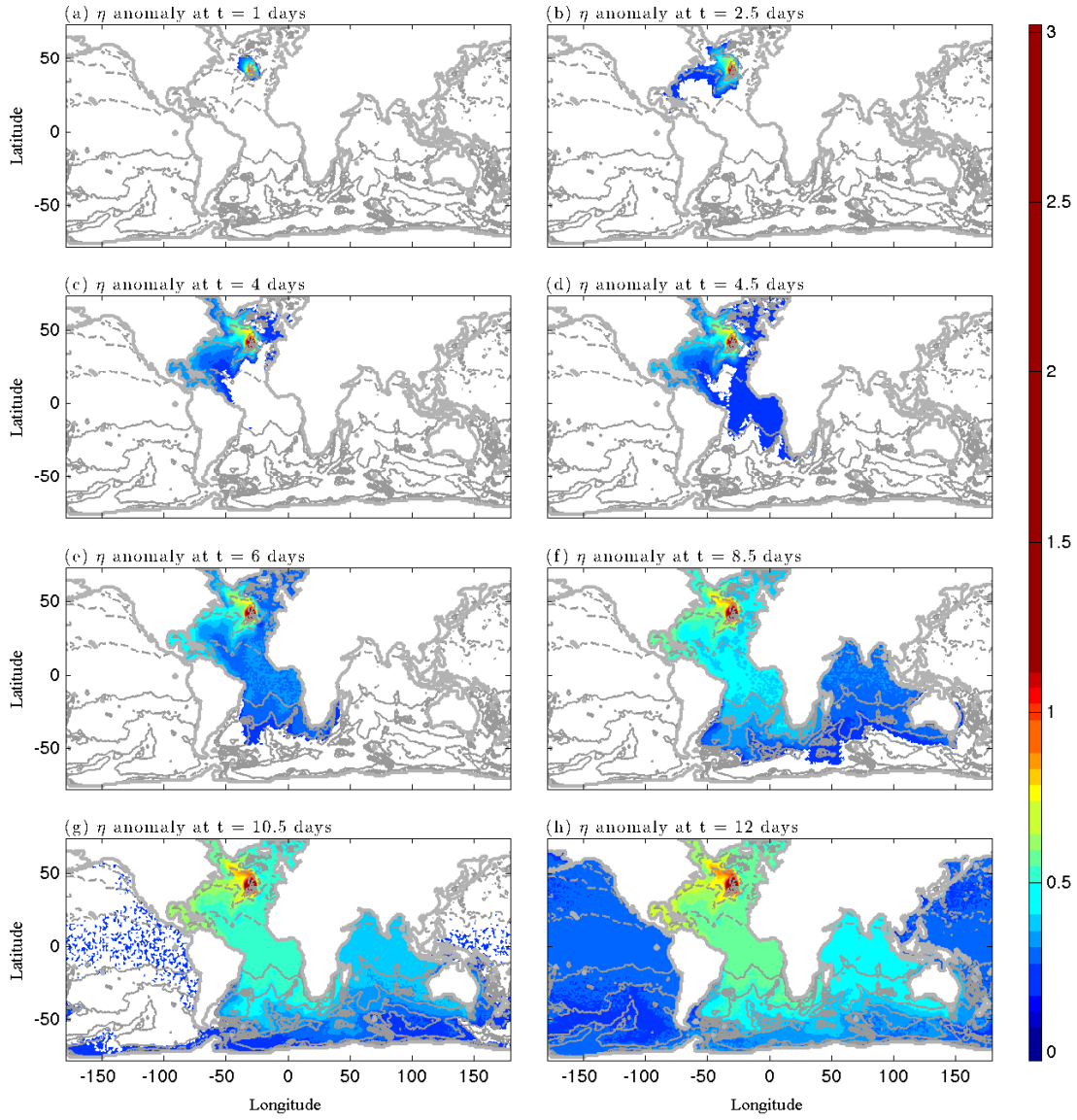

Figure 3.12: Surface displacement anomaly (m), following a freshwater flux input perturbation of 0.5 Sv in the North Atlantic at 30.5°W, 40.5°N. Anomalies are shown for day 1, 2.5, 4, 4.5, 6, 8.5, 10.5 and 12 of the integration in panels (a)-(h) respectively. Contours of f/H are shown in grey with an interval of 2×10^{-9} $s^{-1}m^{-1}$. White areas indicate 0 m surface displacement.

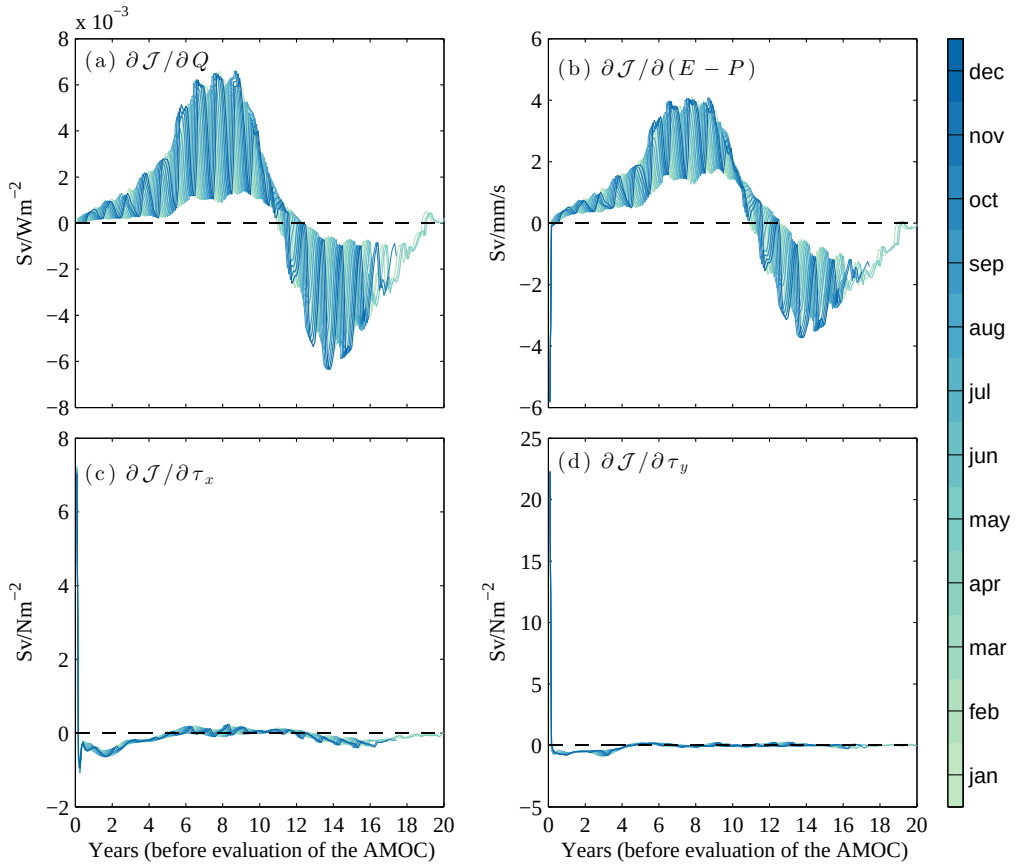

Figure 3.13: Time series of integrated linear sensitivity of $\mathcal{J} = \overline{\psi_{25\mathrm{N}}}^{\,month}$ to (a) surface heat flux, (b) surface freshwater flux, (c) zonal wind stress, (d) meridional wind stress. Colours correspond to the *month* in which $\overline{\psi_{25\mathrm{N}}}^{\,month}$ is defined (each requiring a separate adjoint experiment which is run for between 15 and 20 model years). The sensitivities to buoyancy fluxes (a,b) are integrated over the subpolar gyre (-90°W:10°E , 45°N:70°N). Sensitivities to momentum fluxes (c,d) are integrated over a section of the western boundary (-82°W:-55°W , 25°N:48°N). Both heat and freshwater fluxes are positive upwards. Zonal (meridional) wind stress is positive eastwards (northwards). Positive sensitivity thus indicates that (a) ocean cooling, (b) ocean salinification, or strengthening of the (c) westerly or (d) southerly winds leads to an increase in $\overline{\psi_{25\mathrm{N}}}^{\,month}$.

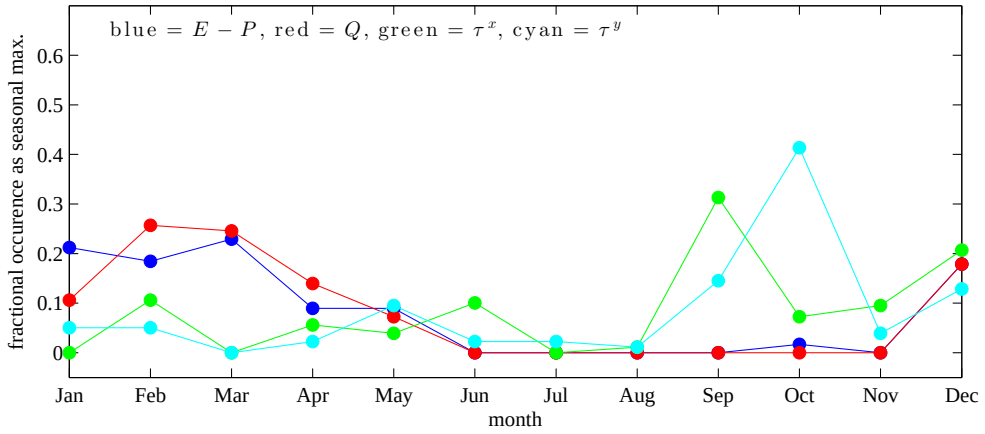

Figure 3.14: Estimated location of the peak amplitude in the seasonal cycles of accumulated sensitivity shown in figure 3.13. Colours correspond to different forcing fields, as indicated by the key. For example, data shown (in red) for surface heat fluxes is derived from the timeseries in figure 3.13a. For each forcing field, the absolute seasonal maximum is computed across the full 12 month ensemble using a 14 year timeseries of sensitivity for each member (i.e 168 annual cycles).

3.5 Conclusions and Discussion

In this chapter, we have explored the sensitivity of the monthly mean AMOC at 25°N, $\overline{\psi_{25\mathrm{N}}}^{month}$, to global surface fluxes of buoyancy and momentum. Our approach has been to use a numerical adjoint to explore the mechanisms by which forcing anomalies may propagate (through space and time) to perturb the subtropical AMOC. We have set out to present a full assessment of the teleconnections that may influence $\overline{\psi_{25\mathrm{N}}}^{month}$ on 1 month to 15 year timescales (the endpoints of our adjoint experiment). We are not aware that the initial barotropic signal in the linear sensitivities has been explored in previous AMOC-related adjoint investigations. We have tried to include these fast pathways in our discussion above and we found it was often useful to conduct a few forward perturbation experiments, in order to better understand the physics. On longer timescales, many teleconnections are recognisable as dual analogues of mechanisms in the forward model (e.g Kelvin waves, Rossby waves and Gulf Stream advective pathways). We find strong evidence in support of basin mode teleconnection mechanisms (*Cessi and Louazel*, 2001; *Johnson and Marshall*, 2002b) and a role played by the "Equatorial buffer" (*Johnson and Marshall*, 2002a).

It emerges that $\overline{\psi_{25\mathrm{N}}}^{month}$ remembers wind stress anomalies applied in the vicinity of 25°N for a few months, but possesses multi-decadal memory to buoyancy forcing over the high latitude North Atlantic. Consistent with *Czeschel et al.* (2010), we suggest that this oscillation is sustained as a "thermal Rossby" mode (*Huck et al.*, 1999; *Te Raa and Dijkstra*, 2002), modified by baroclinic Rossby waves generated at the eastern boundary. In the heat flux sensitivity patterns, this mode appears confined to the North Atlantic basin. In the freshwater flux sensitivities, the subtropical gyre in the southern hemisphere acts as a source of buoyancy anomalies, supplied to the North-East Atlantic on decadal timescales.

In the present study, we find no indication that this high latitude oscillation is damped with increased lead time. Although we are only able to examine one complete

period of oscillation, a tentative inference is that high latitude buoyancy anomalies can project onto repeat cycles of the basin mode with equal vigor. We might expect that SSS and SST restoring, viscous dissipation and/or horizontal mixing of heat and salt would lead to a damping of this mode, as found by *Czeschel et al.* (2010). We suggest that restoration of SSS to climatology may be the key cause of the damping clearly visible in the first complete period of their oscillation. Determination of (1) the exact dependence of the decay time on the restoring timescale and (2) the precise physics setting the phase of the oscillation, are important avenues for future work. Related to this issue is the need to determine (3) the role played by the variability present in the parent forward model from which the adjoint model is derived.

On timescales of less than 15 years, $\overline{\psi_{25\mathrm{N}}}^{month}$ appears almost completely insensitive to small amplitude forcing anomalies applied outside the Atlantic basin. A notable exception is in the Agulhas retroflection region, where historic buoyancy forcing at lead times of 10 years and longer appears important. The generation of decadal AMOC variability by Agulhas leakage is consistent with high resolution modelling studies (*Biastoch et al.*, 2008). The physics responsible for this signal at the present coarse resolution requires further investigation.

3.5.1 Limitations

The sensitivities presented in this chapter describe the linearized response of $\overline{\psi_{25\mathrm{N}}}^{month}$, and are meaningful only when considering small amplitude perturbations in the surface forcing fields. Furthermore, the linearization restricts application of the adjoint method to coarse resolution, non-eddy resolving models. Although *Czeschel et al.* (2012) have applied the adjoint in an eddying regime, the rapid emergence of strongly nonlinear dynamics restricts application of the adjoint to timescales of a few months. It is considered that eddies play an important role in the dynamics of the AMOC, for example by mediating exchanges between the sub-polar and sub-tropical gyres,

and between the Indian and Atlantic basins. It is non-trivial to estimate how the inclusion of eddies may alter the picture provided by the linear sensitivity analysis. The possibility of extracting useful sensitivity information from adjoint ensembles has been investigated by *Lea et al.* (2000). The authors conclude that meaningful ensemble statistics cannot be derived for complex systems, such as the GCM used in our investigation. Related to this issue is the necessary absence of a fully interactive atmosphere in our investigation.

In addition to neglecting eddies and realistic atmosphere-ocean interaction, it was found that we had to deactivate GM and KPP parameterisation schemes to obtain a useful adjoint model. As a result, important mixing and boundary heat flux processes are absent from the linearized state. Furthermore, both schemes were retained in the parent forward model and it is difficult to determine whether an inexact adjoint about a realistic model trajectory yields more/less useful sensitivity information than an exact adjoint about a less realistic trajectory.

We have discussed the important role played by the high latitude North Atlantic in generating AMOC variability on decadal timescales. However, a key issue in the present investigation is the absence of an Arctic basin in our model. Instead, exchange at the northern margin of our domain is parameterised by a full-depth restoring of temperature and salinity to climatology. This is problematic for two reasons. Firstly, we miss important high latitude physics; we expect the AMOC to be sensitive to atmospheric fluxes over the Arctic basin since they play a role in freshwater export into the North Atlantic. Secondly, it has been shown that climatological datasets provide a poor representation of the overflow hydrography, which can grossly affect the volume and heat flux associated with the modelled AMOC (*Döscher et al.*, 1994) and modelled ocean heat content variability (*Zhai et al.*, 2011).

We have identified the important role of fast teleconnections via boundary waveg-

uides. However, the propagation of trapped waves may be hindered somewhat in coarse resolution models (*Greatbatch and Peterson*, 1996). Furthermore, the speed of the trapped waves is model dependant and the timescales identified here may be altered at higher resolutions (*Marshall and Johnson*, 2013).

A final limitation to note is that the adjoint is formulated about a model state that exhibits a decadal mode of variability (figure 2.10). It is important to determine if the sensitivities change significantly when the tangent linearisation is performed about a different portion of the model state. Furthermore, it is important to attempt to extend the adjoint experiments to longer timescales. For the present study, this was computationally unfeasible. However, our adjoint sensitivity timeseries terminate at a length of 15 years, before we detect significant failure in our assumption of linearity. As a result, we have not extracted the full information regarding sensitivity to more historic forcing, that may be accessible through our adjoint model.

3.5.2 Implications

The sensitivity distributions presented in this chapter reveal potentially important centres of action, where perturbations in the surface fluxes of heat, freshwater and momentum may stimulate anomalies in the monthly mean AMOC across 25°N. However, we must recall that - as stated by equation (3.6) - sensitivities need to be co-located (in time and space) with forcing anomalies to actually perturb the objective function:

$$\mathcal{J}' = \frac{\partial \mathcal{J}}{\partial x_\beta} x'_\beta.$$

It follows that distributions of pure sensitivity, $\partial\mathcal{J}/\partial x_\beta$, might not correspond to significant regions of actual influence. To illustrate this point, it is useful to briefly assess the expected variability in the surface forcing fields of interest in this study. In figure 3.15, the standard deviation of the surface fluxes of buoyancy and momentum are shown for the NCEP Reanalysis II product. The largest amplitude variability in

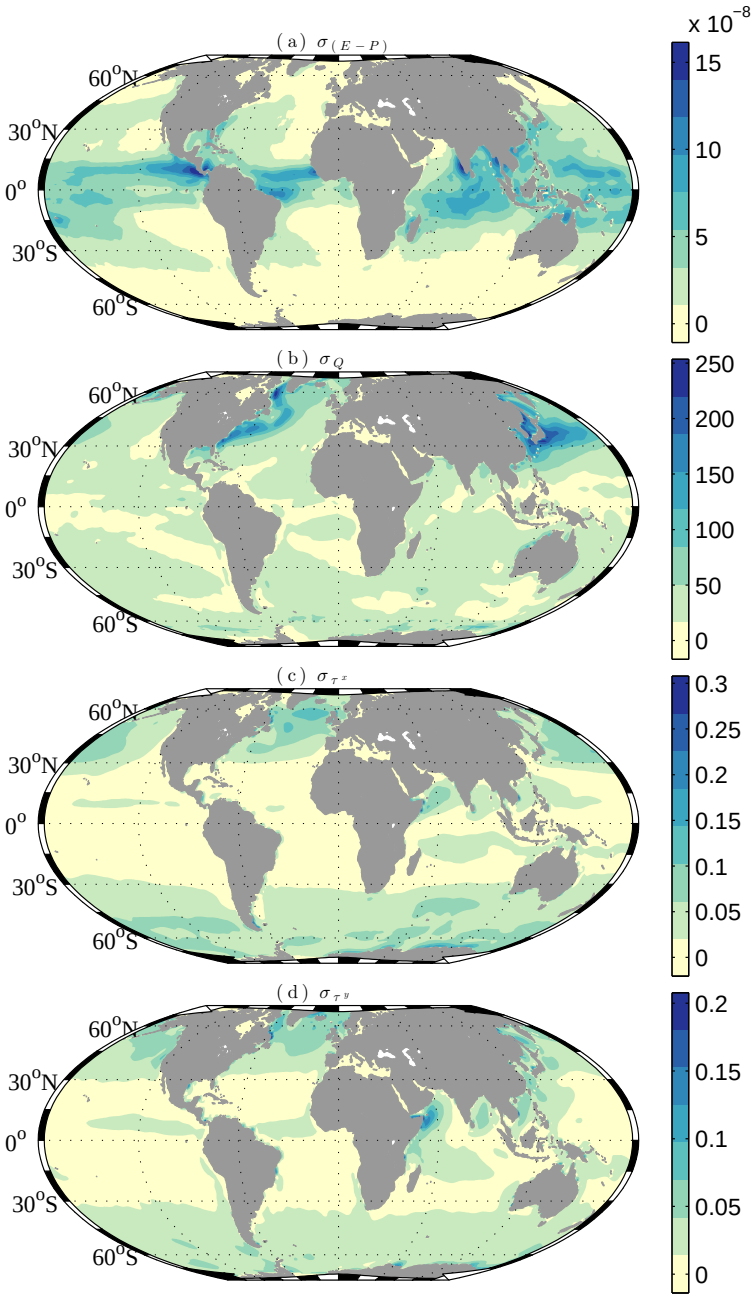

Figure 3.15: Standard deviation of surface (a) freshwater flux (ms^{-1}, excluding runoff), (b) heat flux (Wm^{-2}, excluding shortwave radiation), (c) zonal wind stress (Nm^{-2}) and (d) meridional wind stress (Nm^{-2}), from the NCEP Reanalysis II product (1979-2010).

$\boldsymbol{\tau}$ is found over the mid-latitude storm tracks, displaced from the coastal waveguides and the basin interior near 25°N where the wind stress sensitivities are largest (figures 3.3 and 3.6). Although large anomalies in Q may be expected along the path of the Gulf Stream and the subpolar gyre (figure 3.15b), large anomalies in $E - P$ are concentrated within the ITCZ, where linear sensitivity to $E - P$ appears negligible at some lead times (figures 3.10-3.11).

This discussion stimulates the investigation in the next chapter, in which our key aim is to compute the expected amplitude of the AMOC response.

Chapter 4

Origins of Modelled AMOC Variability

4.1 Introduction

Following immediately from the work presented in chapter 3, we now investigate the projection of forcing anomalies onto regions of notable sensitivity.

4.1.1 Present Objectives

The principal aims of the present work are to establish the extent to which we may use the adjoint to:

1. Quantify the relative contribution of the climatological seasonal cycles in surface fluxes of heat, freshwater and momentum to the seasonal cycle of the modelled AMOC at 25°N.

2. Assess the potential for interannual anomalies in surface fluxes of heat, freshwater and momentum to contribute to seasonal variability of the modelled AMOC at 25°N.

3. Assess the potential for interannual anomalies in surface fluxes of heat, freshwater and momentum to generate interannual to decadal variability of the modelled AMOC at 25°N.

4.2 Origins of Modelled AMOC Variability

It is helpful to recall that we accounted for strong seasonality in the background model state by performing 12 adjoint experiments, achieving an ensemble of sensitivity timeseries for costfunctions defined across the months of the calendar year. Timeseries of transport anomaly are now estimated by multiplying linear sensitivities by corresponding forcing fields and integrating across the global domain.

We divide each full forcing field, $F(x, y, t)$, into a climatological seasonal cycle, $F_c(x, y, m)$ where $m = jan, ..., dec$, and interannual anomalies about this climatology, $F'(x, y, t)$. We choose the forcing fields from the NCEP Reanalysis II product, so that the climatologies, $F_c = Q_c, (E - P)_c, \tau_c^x, \tau_c^y$, are the very same fields employed in the equilibration of the forward model, about which the adjoint experiments were performed.

4.2.1 Estimated AMOC Variability

In the previous chapter, we noted that - despite the presence of nonlinear dynamics in the forward model - the linear sensitivities remain valid for timescales of at least 15 years. Following this, we start by using 15 year timeseries of linear sensitivity to estimate expected variability in the AMOC at 25°N. We start by estimating the expected seasonal cycle, which we denote as $\psi_c(m)$. To illustrate the correct alignment of sensitivities with F_c, let us consider the calculation of the December AMOC climatology, $\psi_c(dec)$, as shown in figure 4.1.

We start by projecting F_c onto the sensitivity for lead times of 1-12 months

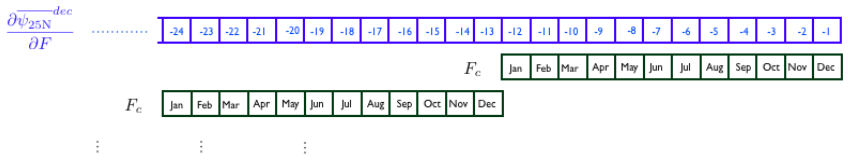

Figure 4.1: Sensitivities (blue, with lead times shown in months) are multiplied by corresponding forcing climatologies (black) at every gridpoint and integrated across the globe. Sensitivity of the December mean transport at a lead time of 1 month, 13 months,....,169 months is multiplied by the forcing climatology in December. Sensitivity at a lead time of 2 months, 14 months,...,170 months is multiplied by the forcing climatology in November etc. Only the first two years of the projection are shown here. Averaging the transport time series over the full 15 year projection yields the mean December transport, $\psi_c(12)$, resulting from 15 year memory to climatological forcing.

where, following the convention defined in section 3.4, a lead time of 1 month in this example corresponds to forcing during the most recent December. Integrating over the global domain yields 12 transport values. Integrating in time yields the net $\psi_c(dec)$ resulting from AMOC memory of one year. The net $\psi_c(dec)$ resulting from AMOC memory of two years is obtained by also projecting F_c onto sensitivity for lead times of 13-24 months and accumulating over all lead time, as shown in figure 4.1. To account for 15 year memory, F_c is projected onto consecutive years of increasing lead time until the full 15 year sensitivity timeseries has been spanned. Repeating the analysis for the remaining 11 costfunctions yields the full seasonal cycle, $\psi_c(jan, ..., dec)$, shown in figure 4.2b.

The climatological seasonal cycle in surface heat flux, Q_c, drives a peak-to-peak seasonal cycle of 7 Sv, with a maximum in August and a minimum in December. The climatological seasonal cycle in zonal and meridional wind stress make a lesser contribution. τ_c^x and τ_c^y each force a peak-to-peak cycle of $\sim$4 Sv. Interestingly, these cycles are in approximate anti-phase; τ_c^y acts to reinforce (weaken) the modelled AMOC in the northern hemisphere summer (winter), whilst τ_c^x acts in the opposite sense. The climatological seasonal cycle in freshwater forcing, $(E-P)_c$, makes a negligible contribution to ψ_c. The net seasonal cycle has a peak-to-peak amplitude

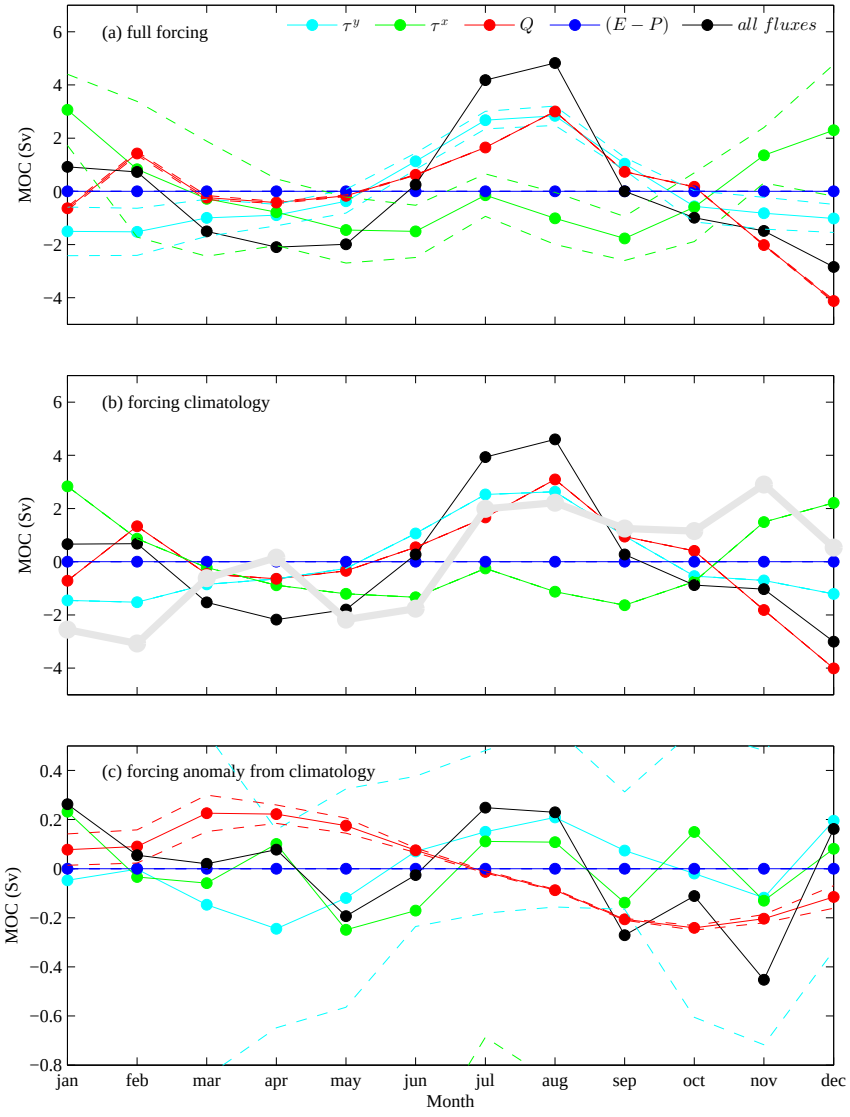

Figure 4.2: Mean AMOC seasonal cycle computed from projecting linear sensitivities onto (a) full surface flux fields, (b) climatological seasonal cycles in surface fluxes and (c) forcing anomalies from climatology (note the change in axis limits here). Net seasonal cycles from wind and surface buoyancy forcing combined are shown in black. Dashed lines indicate one standard deviation about the mean (lying beyond the axis limits for τ^x, τ^y in (c)). The seasonal cycle in the modelled $\overline{\psi_{25\mathrm{N}}}^{month}$ is shown by the thick grey line in (b).

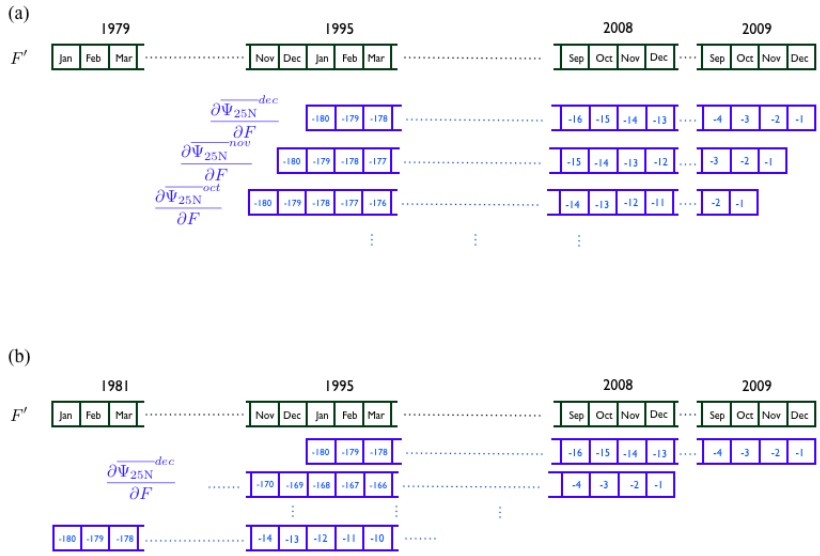

Figure 4.3: Sensitivities (blue, with lead times shown in months) are multiplied by corresponding forcing fields (black) at every gridpoint, to yield timeseries of monthly mean AMOC transport anomaly, ψ'. Integration in time then yields the net ψ' in any month resulting from forcing applied over the previous 15 years. In panel (a) projection of sensitivities onto anomalies to compute the transport in December, November and October 2009 is illustrated. In panel (b) we illustrate how all December transport anomalies spanning 1995 to 2009 inclusive are computed from projecting distinct periods of Reanalysis forcing onto the 15 year long sensitivity timeseries.

of approximately 7.5 Sv with a maximum (minimum) in August (December).

Here we recall that the forcing climatologies, F_c, are the same fields used to establish the model state about which the linear sensitivity information has been derived. By projecting F_c, onto the corresponding sensitivity patterns, we expect to retrieve the AMOC seasonal cycle present in the forward experiment. This is shown by the thick grey line in figure 4.2b. Little notable correspondence is seen between the modelled seasonal cycle and ψ_c constructed from the linear sensitivities. It may be inferred that, in our model, historic forcing applied at lead times of greater than 15 years is critically important in setting the seasonal variability of the subtropical AMOC. This will be confirmed shortly.

We estimate expected interannual variability in the subtropical AMOC by projecting interannual forcing anomalies, $F' = Q', (E-P)', \tau^{x\prime}, \tau^{y\prime}$, onto the sensitivity

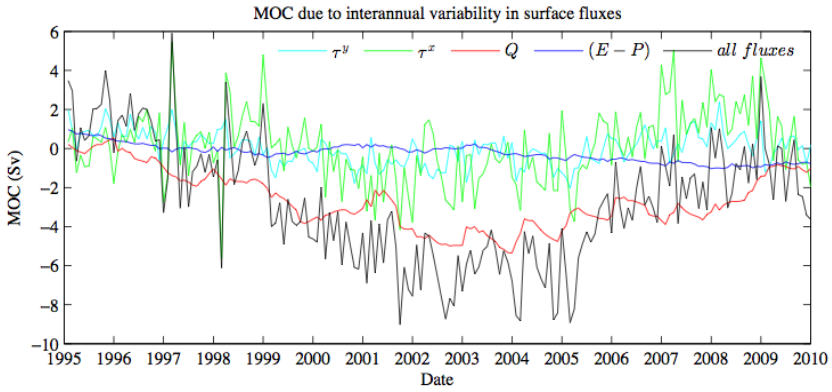

Figure 4.4: Anomalies in $\overline{\psi_{25\mathrm{N}}}^{month}$ associated with forcing anomalies, F', about the climatological seasonal cycle, F_c. Transport anomalies are computed using the adjoint approach so that in any month, the AMOC anomaly is the net result of F' applied over the previous 15 years.

patterns. The correct alignment of F' onto corresponding sensitivity for lead times of 1-180 months is illustrated in figure 4.3. The resultant timeseries of 1995-2010 AMOC transport anomaly, ψ', is shown in figure 4.4. ψ' generated by Q' ranges between -5.4 Sv and 1.1 Sv. ψ' generated by $\tau^{x\prime}$ and $\tau^{y\prime}$ ranges between -5.6 Sv and 5.5 Sv, and -2.0 Sv and 2.4 Sv respectively and exhibits significant variability on subannual timescales. Interestingly, $(E-P)'$ is ineffectual in perturbing the monthly mean AMOC at 25°N (associated anomalies are $O(10^{-3})$ Sv).

Notable low frequency AMOC variability is also visible in the 1995-2010 timeseries of ψ'. This is driven principally by Q', which makes a negative contribution to the AMOC through almost the entire period assessed. Interestingly, strong seasonality in this timeseries is notable for the period 2003-2006, which prompts an investigation of the potential contribution of Q' to ψ_c. The mean seasonal cycle driven by interannual anomalies in the forcing fields, F', from 1995-2009 inclusive, is shown in figure 4.2c. The seasonal cycle driven by the full surface forcing, $F = F_c + F'$, is shown in figure 4.2a for comparison. In both panels, the standard deviation about the computed mean is also shown (dashed lines). The mean seasonal cycle driven by F' is an order of magnitude smaller than that driven by F_c for all forcing fields. Furthermore,

the analysis of mean AMOC seasonality driven by F' is only meaningful for the interannual anomalies in surface heat flux, Q'. The interannual variation in wind-driven ψ' is so large that $\tau^{y\prime}$ and $\tau^{x\prime}$ do not make a consistent contribution to any particular phase of seasonality. This is consistent with the rapid decay of AMOC sensitivity to increasingly historic wind stress, diagnosed in the previous chapter. In contrast to the buoyancy-driven ψ', the wind-driven ψ' results overwhelmingly from the wind forcing during the prior few months (see figure 3.13). We therefore expect wind stress to dominate high frequency AMOC variability whilst the impact of buoyancy anomalies is smoothed over multi-annual periods, acting to redden the spectrum of AMOC variability.

4.2.2 Temporal Origins of AMOC Variability

Finally, we explore the relative importance of recent and historic forcing in setting variability of the modelled AMOC on seasonal to decadal timescales. The computation of the mean seasonal cycle, ψ_c, due to F_c and F' is repeated, gradually reducing the length of the sensitivity timeseries from the full 15 years, shown in figure 4.2, to 1 month. This is equivalent to truncating the assumed memory of the AMOC (to surface forcing) from 15 years to 1 month.

In figure 4.5 we plot ψ_c driven by each F_c as a function of assumed AMOC memory. Historic heat fluxes are shown to contribute significantly to the computed ψ_c; truncating the AMOC memory from 15 years to 1 month can alter the estimated transport anomaly by up to 6.3 Sv (figure 4.5b). In contrast, historic wind forcing is relatively unimportant; reducing the assumed memory of the AMOC from 15 years to 1 month alters the transport anomaly by less than 2.5 Sv and 1.4 Sv for τ^y and τ^x respectively (figure 4.5c-d). This is consistent with the analysis in the previous chapter of this thesis, where we showed that the AMOC exhibits decadal memory to high latitude buoyancy forcing, whilst significant memory to wind stress is confined

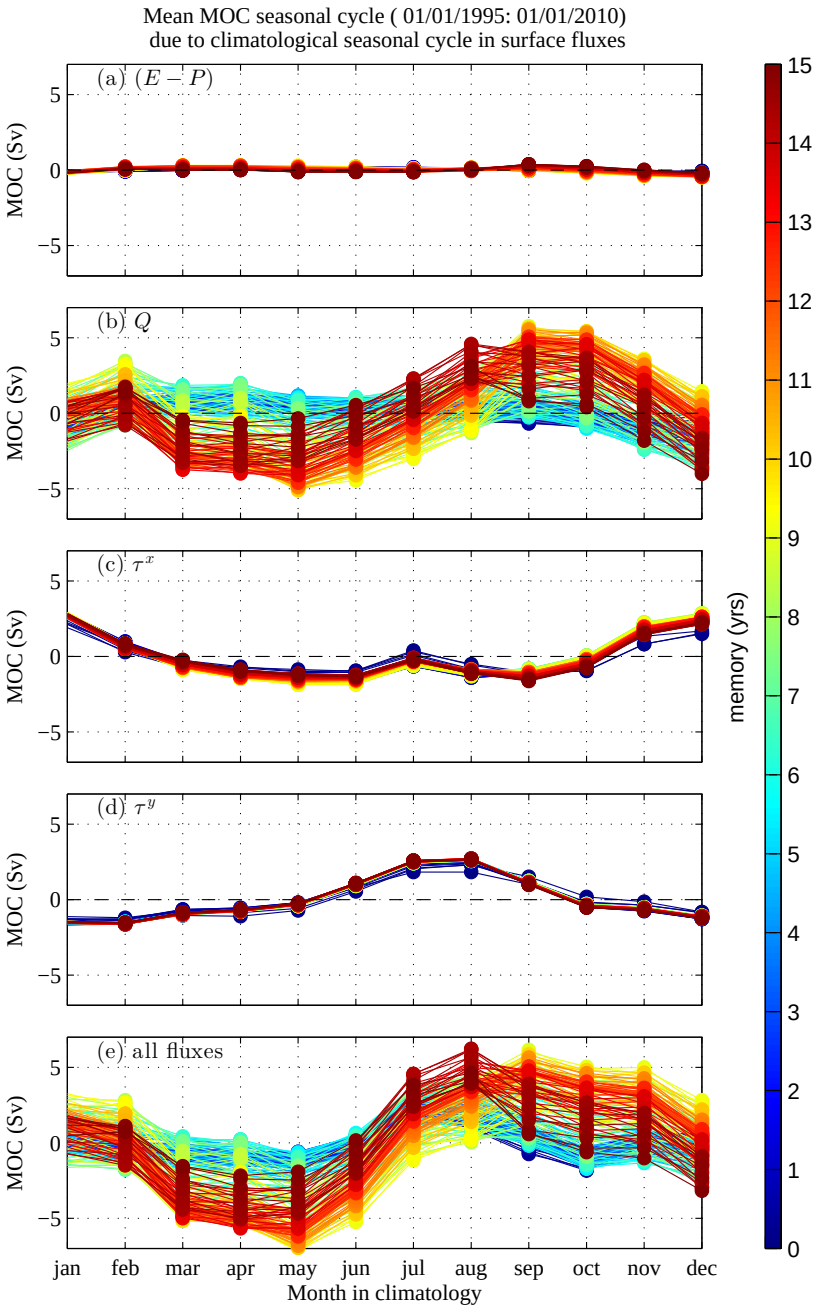

Figure 4.5: Seasonal cycle, ψ_c, in the modelled AMOC computed by projecting linear sensitivities onto the corresponding seasonal climatology in (a) surface freshwater flux, (b) surface heat flux, (c) zonal wind stress, (d) meridional wind stress and (e) all of the above fluxes combined. Colour indicates the length of AMOC memory considered in computing ψ_c.

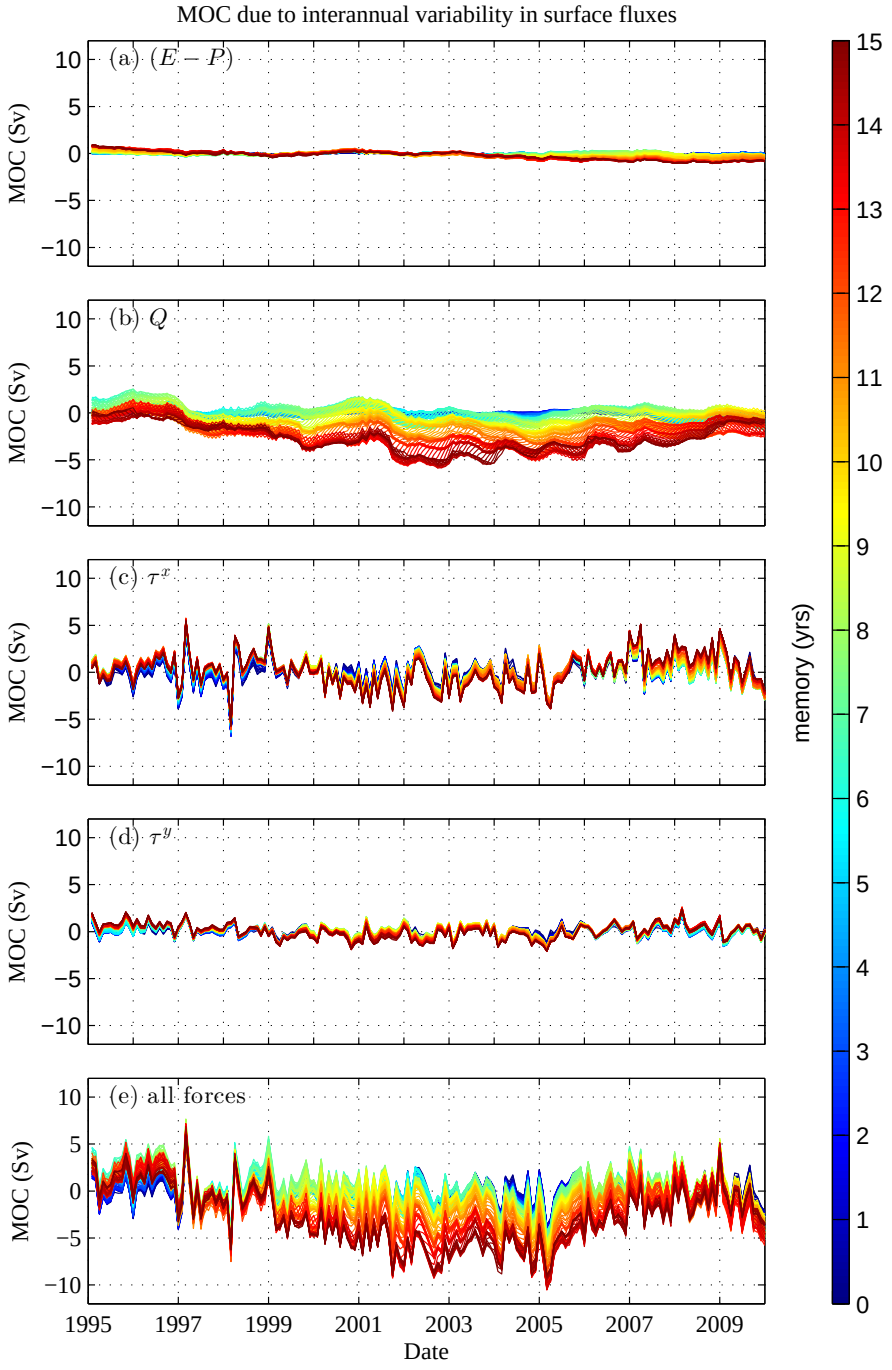

Figure 4.6: As for figure 4.4, but for AMOC memory truncated gradually from 15 years to 1 month. Colour indicates the length of assumed memory considered in computing ψ'.

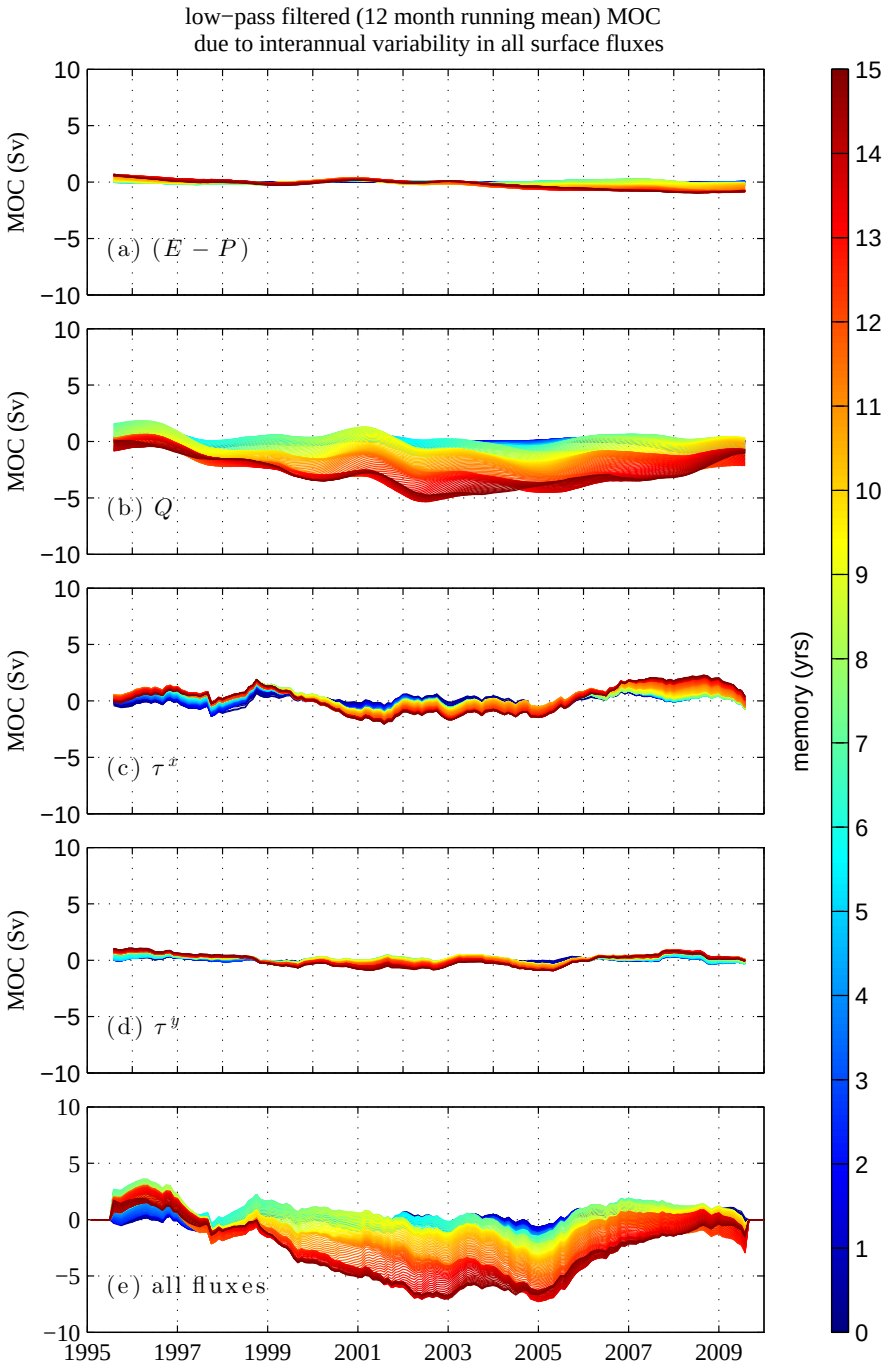

Figure 4.7: Low frequency variability in the modelled AMOC as a function of memory, computed by projecting interannual anomalies, F', onto the corresponding linear sensitivities and low-pass filtering the resultant transport timeseries with a 12 month running mean. Colour indicates the length of memory considered in computing ψ'.

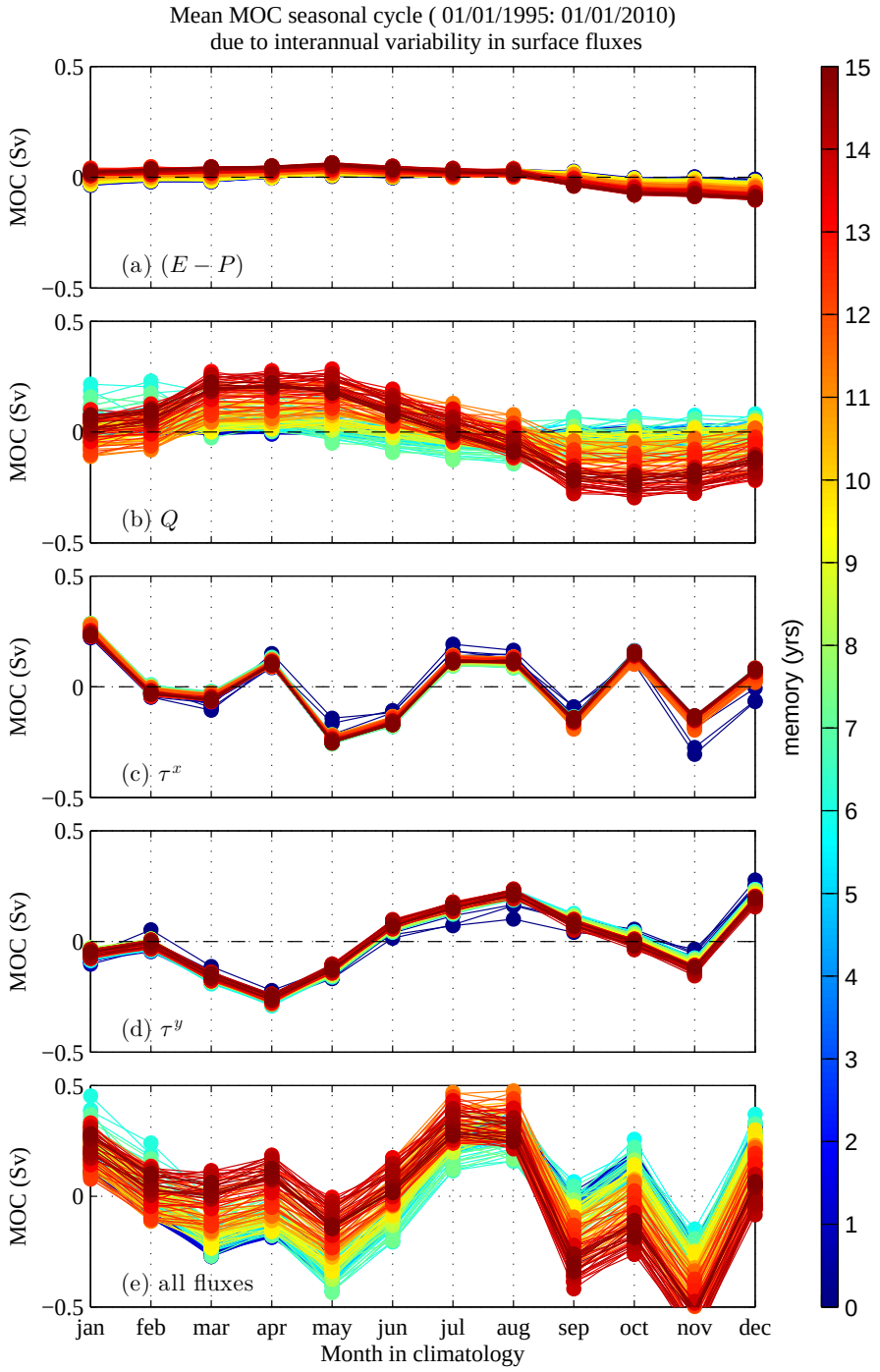

Figure 4.8: As for figure 4.5, but for ψ_c computed by projecting linear sensitivities onto corresponding interannual forcing anomalies, F'. Colour indicates the length of AMOC memory considered in computing ψ_c.

to one year.

The analysis is repeated for the full timeseries of ψ' in figure 4.6 (low-pass filtered timeseries are shown in figure 4.7). Surprisingly, historic interannual wind forcing anomalies, $\tau^{x\prime}$ and $\tau^{y\prime}$, are not negligible, but for some time periods, alter the estimated transport anomaly by approximately 2 Sv (figures 4.6c-d). Historic interannual heat flux anomalies, Q', also contribute significantly to the computed ψ'; truncating the assumed memory from 15 years to 1 month can alter the estimated transport anomaly by approximately 5 Sv (figure 4.6b). We suggest that this coherent response is excited by low frequency variations in Q' associated with the North Atlantic Oscillation (NAO) (projecting onto the decadal mode observed in the AMOC sensitivity to surface buoyancy forcing).

In figure 4.8b, we show that historic Q' also contributes significantly to the computed ψ_c; truncating the AMOC memory from 15 years to 1 month can alter the estimated transport by up to 0.4 Sv. As for ψ_c driven by Q_c (figure 4.5b), we can detect that increased memory does not lead to a simple amplification of the seasonal cycle. For memory of only a few years, it is not clear if a robust seasonal cycle exists. Furthermore, it appears that the peak-to-peak amplitude in ψ_c driven by Q_c may actually decrease as the assumed memory is extended beyond about 12 years. To show this more clearly, we examine the convergence of the peak-to-peak amplitude of ψ_c with increased memory in figure 4.9. The seasonal cycle from wind stress forcing (figures 4.9c-d) asymptotes a fixed amplitude of approximately 5 Sv on increasing the assumed AMOC memory from 1 month to 1 year. However, the seasonal cycle resulting from heat flux forcing does not converge over our 15 year experiment (figure 4.9b). Increasing the assumed memory from 0 to 9 years leads to a gradual increase in amplitude of the seasonal cycle from 2 to 10 Sv. Furthermore, there is a notable shift in the phase of the seasonal cycle when the assumed memory is increased beyond 7 years.

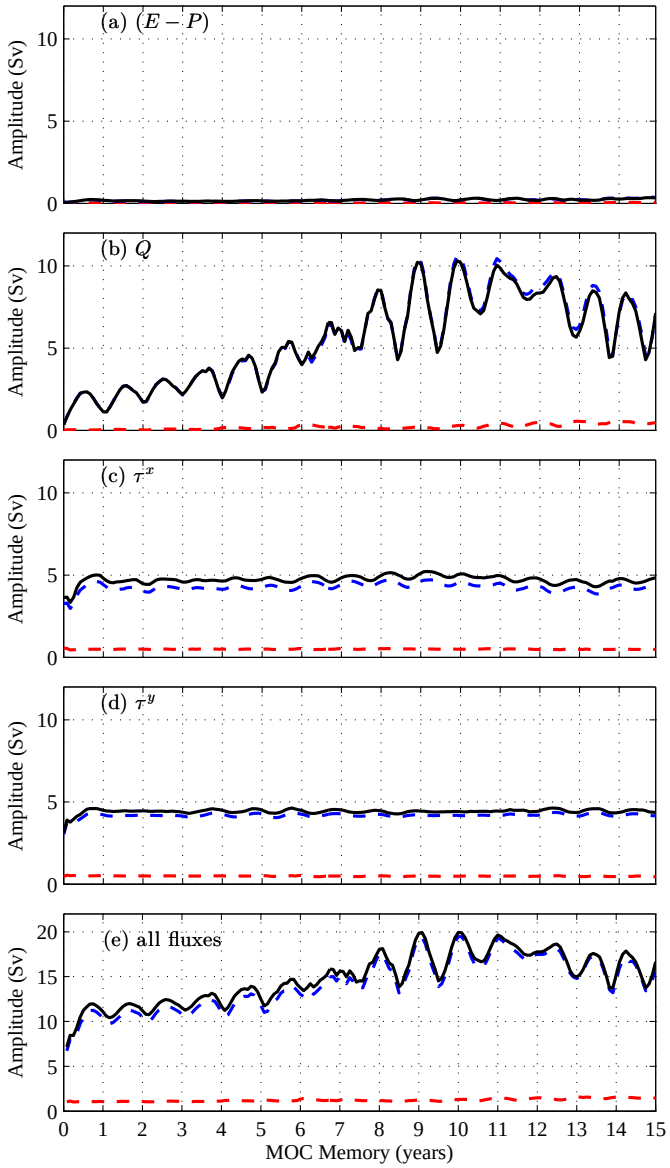

Figure 4.9: Peak-to-peak amplitude (Sv) of the seasonal cycle in the modelled AMOC as a function of ocean memory (years). The seasonal cycle is constructed by projecting (a) freshwater fluxes, (b) net surface heat flux, (c) zonal wind stress, (d) meridional wind stress and (e) all of the fluxes combined onto the corresponding linear sensitivities. AMOC seasonality driven by the full surface flux (F, solid black) has been separated into the climatological seasonal cycle (F_c, dashed blue) and the interannual anomaly (F', dashed red).

4.3 Conclusions and Discussion

In this chapter, we have estimated the expected variability in the monthly mean AMOC at 25°N on sub-seasonal to decadal timescales. Our approach has been to project forcing fields from the NCEP Reanalysis II product onto the linear sensitivity patterns presented in the previous chapter. We have examined variability driven by forcing climatology, F_c, and interannual anomalies about this climatology, F', separately. By accounting for long term (15 year) memory of the AMOC to surface fluxes of buoyancy and momentum, we deduce that Q_c, τ_c^x and τ_c^y combine to drive a net seasonal cycle characterised by a peak-to-peak amplitude of 7.5 Sv, with a maximum (minimum) in August (December). The net seasonal cycle is dominated by the contribution from Q_c. Due to the ocean's short term memory to small perturbations in wind forcing, $\tau^{x\prime}$ and $\tau^{y\prime}$ do not have significant potential to contribute to a robust seasonal cycle. However, Q' does drive a robust seasonal cycle with a peak-to-peak amplitude of 0.4 Sv. Interestingly, this is in approximate anti-phase with that driven by Q_c. We may speculate that - in areas where heat fluxes project successfully onto sensitive regions - Q' is principally described by a standing pattern of amplification/reduction in Q_c. This encourages closer inspection in future work.

We find that significant low frequency variability in the monthly mean AMOC at 25°N may be generated by Q'. Our analysis suggests that for the period 1996-2010, Q' has acted to weaken the subtropical AMOC by up to 5.4 Sv. $\tau^{x\prime}$ and $\tau^{y\prime}$ may also make a (lesser) contribution to generating low frequency variability, but they are most notable for driving large transient anomalies in the subtropical AMOC (O(10 Sv) and O(4 Sv) respectively, between consecutive months).

Freshwater forcing makes a negligible contribution to variability in the monthly mean AMOC at 25°N on all timescales. This finding is consistent with numerical investigations of CO_2 induced AMOC weakening performed by *Thorpe et al.* (2001); *Gregory et al.* (2005); *Mikolajewicz and Voss* (2000), which highlight the dominant

role of surface heat fluxes over freshwater fluxes in a range of atmosphere-ocean GCMs. In the present study, we expect that the impotence of $(E-P)'$ is partly due to their confinement to the ITCZ (figure 3.15), whilst large amplitude sensitivities to $E-P$ are concentrated in the North Atlantic (figure 3.11).

Our final - and perhaps most important - conclusion is that we are unable to reconstruct modelled seasonality in the subtropical AMOC using the full 15 year timeseries of linear sensitivities presented in chapter 3.

4.3.1 Limitations

The main caveats of the linear sensitivity study have been discussed in the previous chapter (section 3.5.1), where it was also noted that we were unable to extend all members of our adjoint ensemble beyond a length of 15 years, due to computational restrictions. In this chapter, we have shown that historic forcing, occurring at lead times exceeding 15 years, is essential for reconstructing seasonal variability in the modelled AMOC.

An additional limitation is that the results presented in this chapter are dependent upon both the model and the reanalysis forcing employed. Reanalysis products are notoriously poor at simulating small scale features in the curl and divergence of the wind field (*Chelton et al.*, 2004). Such features are common around the coast due to abrupt changes in orography and the land-sea temperature contrast. However, significant sensitivities to wind anomalies are found within the coastal waveguides near 25°N (section 3.4.1). We acknowledge that we may be missing an important contributor to the total variability of the AMOC, by poorly resolving the coastal wind field.

The issues discussed here prevent a direct comparison of our transport estimates with recent observations from the monitoring array at 26.5°N. Indeed, we did not even attempt to simulate the observed seasonal cycle in the subtropical AMOC

in our forward model (causes of the disagreement between observed and simulated seasonality is discussed by *Balan Sarojini et al.*, 2011, for an ensemble of coupled climate models). Instead our efforts were invested in a mechanistic investigation of variability in the subtropical AMOC.

4.3.2 Implications

Recent analysis suggests the observed seasonality in the AMOC at 25°N, with a peak-to-peak amplitude of 6.7 Sv, is dominated by seasonality in the wind stress curl immediately adjacent to the eastern boundary (*Chidichimo et al.*, 2010). QuikSCAT observations show that this seasonality in the wind curl has persisted with little change in amplitude and phase since the beginning of the record in 1999 (*Kanzow et al.*, 2010). As a result, it has been suggested that forcing from previous years does not contribute significantly to the seasonality of the AMOC. Furthermore, the authors suggest that the seasonal cycle observed in a 48 month long timeseries is likely to be "representative of much longer intervals" (*Kanzow et al.*, 2010).

However, the latest data have shown that a clear seasonal cycle is absent in the sixth year of measurement (see figure 1.3). Instead, a dramatic (negative) excursion of the AMOC is notable in the winter of 2009/2010, which has yet to be explained. Above, we have shown that $\tau^{x\prime}$ can generate transient anomalies in the monthly mean AMOC of $O(10$ Sv), suggesting that linear sensitivity studies could be useful in probing the potential for transient reversals of the AMOC. Furthermore, our inability to reconstruct the modelled seasonal cycle, even when accounting for atmospheric forcing over the past 15 years, firmly supports the argument that the AMOC should be viewed as the time-integrated response to a long history of prior forcing (*Wunsch*, 2012). We suggest that great caution must be taken in drawing strong inferences from short observational datasets.

Chapter 5

Rotational Momentum Balance of the MOC: Introduction and Analytics

5.1 Introduction

5.1.1 Motivation

At large scales in the ocean, the pressure gradient appears in the dominant steady state force balances in both horizontal and vertical directions (geostrophic and hydrostatic balance respectively). Evolution of the flow is driven by small deviations from this balanced state. This motivates re-formulation of the governing momentum equations in terms of vorticity (e.g. *Pedlosky*, 1987; *Vallis*, 2006) so that the pressure gradient is entirely eliminated. The vorticity framework is used in the formulation of many of our conceptual models, including some of the cornerstones of classical ocean circulation theory (e.g. *Sverdrup*, 1947; *Stommel*, 1948; *Stommel and Arons*, 1960).

Alternatively, we may consider the rotational momentum equation in which the forcing responsible for the acceleration of the flow regime is also isolated. It will

be shown that the same pointwise balance occurs between equivalent terms in the rotational momentum and vorticity equations. However, the rotational momentum framework offers the advantage of describing the circulation in terms of simple force balances, in place of more complex vorticity sources and sinks.

Furthermore, in the hydrostatic limit, a three-dimensional rotational force is readily decomposed into a depth-integrated force, which is described by a horizontal force function, and overturning forces, which are described by two overturning force functions, allowing a clean separation between the buoyancy dominated (overturning) and wind dominated (depth-integrated) circulations. In this chapter, it will be shown that these scalar force functions allow some mechanisms of MOC generation to be assessed analytically. In chapter 6 we will show that the force functions represent powerful diagnostics for visualising the three-dimensional momentum balance in ocean models.

5.1.2 Past Work

The derivation of the rotational momentum framework has been published in *Marshall and Pillar* (2011) (hereafter MP11), where we also present analytical and numerical solutions to some classical problems in physical oceanography, instilling confidence in our approach. Both authors contributed to the development of the framework and the analysis of the three-dimensional rotational momentum budget for an idealised meridional overturning circulation. The full mathematical derivation will be presented in the following section and the numerical solution of the meridional overturning will be further explored in the next chapter of this thesis.

The analytical solutions in MP11 were derived by David Marshall and are consequently not presented in this thesis. The numerical solution for the barotropic wind-driven gyre in MP11 was presented by the author for examination in an undergraduate thesis (*Pillar*, 2007), and is likewise not reproduced below. It is helpful

however, to briefly discuss a few reassuring and surprising results provided by the investigation. For example, the analytically derived force functions for barotropic Rossby waves demonstrate that the beta effect is the unambiguous cause of westward phase propagation. The role of the Coriolis force in westward intensification is significantly less clear if one considers the full force, everywhere directed at a right angle to the velocity vector. The numerically derived force functions for a barotropic wind-driven gyre also confirm the key role of the beta effect in westward intensification and - additionally - in inhibiting the separation of the western boundary jet, consistent with the integral vorticity analyses presented by *Marshall and Tansley* (2001) and *Munday and Marshall* (2005). Further expectations are confirmed in clearly demonstrating the existence of pointwise Sverdrup balance in the gyre interior, and the dominant role of the rotational inertial force in extending the recirculation subgyre away from the western boundary. Most interestingly, the rotational momentum analysis reveals the contrasting influence of the viscous force upon changing from a free-slip to a no-slip boundary condition. Under free-slip conditions, the rotational viscous force is confined to the western boundary layer, following contours of relative vorticity. In contrast, under no-slip boundary conditions the viscous damping extends across the entire basin (see MP11 for a full discussion). The provision of new dynamical insights into a well-established problem encourages further exploration in the rotational momentum framework. The remainder of this chapter contains work led by the author since starting her doctorate degree.

5.1.3 Present Aims

The aim in this chapter is to present a simple tool to elucidate the force balance governing the strength and structure of the large-scale ocean circulation, with a particular focus on the MOC. We aim to derive mechanisms of MOC generation analytically where possible, setting the scene for the diagnosis of the force balance

governing the circulation in an OGCM in the following chapter of this thesis.

5.1.4 Chapter Outline

This chapter is organised as follows. In section 5.2, the rotational momentum approach is fully derived. This is an expanded and extended form of that presented in MP11, and includes a proper treatment of the boundary conditions on the force function in arbitrary domains. In section 5.3 analytical solutions are presented for overturning components of the force function. Mechanisms responsible for the generation of meridional overturnings are discussed. A new analytical scaling is derived that relates the MOC to the depth-integrated meridional density gradient (MDG). Finally, in section 5.4, the diagnostic tool is reviewed, limitations of the design are identified and results from the analytical investigation are summarized.

5.2 Methodology

The incompressible (or Boussinesq) Navier-Stokes equation in primitive variable form may be expressed as follows:

$$\rho_0 \frac{\partial \mathbf{u}}{\partial t} + \nabla p = \sum \mathbf{F}, \tag{5.1}$$

$$\nabla \cdot \mathbf{u} = 0, \tag{5.2}$$

$$\mathbf{u} = \mathbf{u_b} \quad \text{on the boundary}, \tag{5.3}$$

where $\mathbf{u} = [u, v, w]$ is the 3-dimensional velocity field, t is time, p is pressure, ρ_0 is a reference density, and $\mathbf{F} = [F^x, F^y, F^z]$ is the contribution from any one momentum source, sink or redistribution term (including inertia). Here consideration is restricted to domains with impermeable boundaries:

$$\hat{n} \cdot \mathbf{u_b} = 0, \tag{5.4}$$

where $\hat{n}$ is a unit vector normal to the boundary. Equation (5.1) indicates two distinct responses of an incompressible (or Boussinesq) fluid, such as the ocean, to an applied force. The forcing, $\mathbf{F}$, generates a local acceleration, $\partial\mathbf{u}/\partial t$, and a nonlocal response by establishing a pressure gradient force, ∇p, to maintain non-divergence of the resultant motion and to satisfy the kinematic boundary condition. To illustrate this, consider the effect of a zonal force reversing with latitude in a rectangular basin (figure 5.1). High pressure is established in the north-east and south-west corners of the basin. Low pressure is established in the north-west and south-east corners. The resultant pressure gradient force simply acts to remove fluid from/return fluid to the boundary. The sum of the applied force and the pressure gradient force drives a purely rotational acceleration.

5.2.1 Vorticity - Vector Potential Formulation

To satisfy the continuity equation (5.2) the velocity may be rewritten as

$$\mathbf{u} = \nabla \times \mathbf{\Psi}. \tag{5.5}$$

Adopting terminology from electromagnetic theory, $\mathbf{\Psi} = [\Psi^x, \Psi^y, \Psi^z]$ is called the vector potential (e.g *Durney and Johnson*, 1969) and serves as the 3-dimensional analog of the streamfunction, ψ, in 2-dimensional regimes. However, the vector

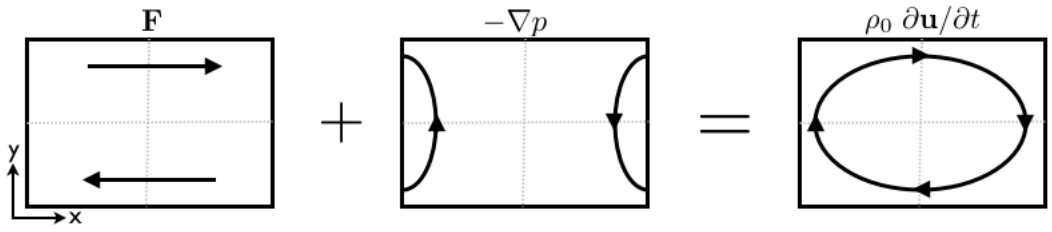

Figure 5.1: Schematic illustrating the response of a Boussinesq fluid to an applied zonal force, $\mathbf{F}$. The net acceleration, $\rho_0\partial\mathbf{u}/\partial t$, is the sum of the applied force, $\mathbf{F}$ and the pressure gradient forces, ∇p.

potential is not uniquely defined since the gradient of any scalar field may be added to $\boldsymbol{\Psi}$ without altering its curl. Examining the vorticity, $\boldsymbol{\omega} = [\omega^x, \omega^y, \omega^z]$, indicates that an additional constraint must be imposed on the divergence of the vector potential, $\boldsymbol{\Psi}$, to determine a unique expression:

$$\boldsymbol{\omega} = \nabla \times \nabla \times \boldsymbol{\Psi} = \nabla(\nabla \cdot \boldsymbol{\Psi}) - \nabla^2 \boldsymbol{\Psi}. \tag{5.6}$$

Imposing the Coulomb gauge will remove all invariance and yield a Poisson equation relating $\boldsymbol{\omega}$ to $\boldsymbol{\Psi}$:

$$\nabla \cdot \boldsymbol{\Psi} = 0, \tag{5.7}$$

$$\boldsymbol{\omega} = -\nabla^2 \boldsymbol{\Psi}. \tag{5.8}$$

The condition of no-normal flow must be satisfied on the boundary:

$$\hat{n} \cdot \nabla \times \boldsymbol{\Psi} = \boldsymbol{\Psi} \cdot \nabla \times \hat{n} - \nabla \cdot (\hat{n} \times \boldsymbol{\Psi}) = 0, \tag{5.9}$$

(from equation 5.4) and the continuity equation ($\nabla \cdot \mathbf{u} = 0$, and hence $\nabla \cdot \boldsymbol{\omega} = 0$, $\nabla \cdot \boldsymbol{\Psi} = 0$) must be enforced globally. Without loss of generality (5.9) may be satisfied by setting

$$\hat{n} \times \boldsymbol{\Psi} = \mathbf{0}, \tag{5.10}$$

on the boundary. Combining this condition with the imposed gauge yields two Dirichlet conditions and one Neumann condition on the components of $\boldsymbol{\Psi}$. For example, for an eastern/western bounding wall (5.10) implies $\Psi^z = \Psi^y = 0$, and $\partial \Psi^x / \partial x = 0$ follows from (5.7) . To proceed, the aim is to recast the vector potential into physically intuitive components and to break the three-dimensiona elliptic equation (5.8) into more tractable problems for each of these components in isolation.

5.2.2 Barotropic and Overturning Potentials

The 3-dimensional vector force function is now written in terms of horizontal, $\mathbf{\Psi}_h = [\Psi^x, \Psi^y]$, and vertical, Ψ^z, parts where the latter is further decomposed into depth-averaged ("barotropic") and depth-dependent ("baroclinic") contributions:

$$\begin{aligned} \mathbf{\Psi} &= \mathbf{\Psi}_h(x,y,z) + \Psi^z(x,y,z)\hat{k}, \\ &= \mathbf{\Psi}_h(x,y,z) + \Psi_{\mathrm{BT}}(x,y)\hat{k} + \Psi_{\mathrm{BC}}(x,y,z)\hat{k}, \end{aligned} \tag{5.11}$$

satisfying

$$\Psi_{\mathrm{BT}} = \frac{1}{H}\int_{-H}^{0} \Psi^z \, dz, \tag{5.12}$$

$$\Psi_{\mathrm{BC}} = \Psi^z - \Psi_{\mathrm{BT}}. \tag{5.13}$$

The superscript z on the barotropic and baroclinic components has been dropped to simplify notation. The surface is found at $z = 0$. $-H(x,y) < 0$ is the depth of the ocean floor. By definition the baroclinic mode vanishes when integrated over the full depth of the basin:

$$\int_{-H}^{0} \Psi_{\mathrm{BC}} \, dz = 0. \tag{5.14}$$

Substituting the new expression for $\mathbf{\Psi}$ back into the gauge (5.7), the baroclinic vector potential is shown to scale as an order aspect ratio smaller than the horizontal velocity potential:

$$\nabla \cdot \mathbf{\Psi} = \nabla \cdot \mathbf{\Psi}_h + \frac{\partial \Psi_{\mathrm{BT}}}{\partial z} + \frac{\partial \Psi_{\mathrm{BC}}}{\partial z} = 0, \tag{5.15}$$

$$|\Psi_{\mathrm{BC}}| \sim |\mathbf{\Psi}_h|\frac{D}{L}, \tag{5.16}$$

where L and D are characteristic lengths in the horizontal and vertical directions respectively. Equation (5.16) implies that in hydrostatic regimes ($D < L$), vertical

shear in the velocity field is principally described by the horizontal vector potential. This scaling may now be used to simplify the elliptic problem for the vorticity, $\boldsymbol{\omega}$. We start by eliminating Ψ_{BC} from the expression for the horizontal velocity:

$$\begin{aligned}
\boldsymbol{u}_h &= (\nabla \times \boldsymbol{\Psi})_h && (5.17)\\
&= \left(\frac{\partial \Psi^z}{\partial y} - \frac{\partial \Psi^y}{\partial z}\right)\hat{\imath} - \left(\frac{\partial \Psi^z}{\partial x} - \frac{\partial \Psi^x}{\partial z}\right)\hat{\jmath}, && (5.18)\\
&= \left(\frac{\partial \Psi^z}{\partial y}\hat{\imath} - \frac{\partial \Psi^z}{\partial x}\hat{\jmath}\right) + \left(\frac{\partial \Psi^x}{\partial z}\hat{\jmath} - \frac{\partial \Psi^y}{\partial z}\hat{\imath}\right), && (5.19)\\
&= -\hat{k} \times \nabla_h \Psi^z + \hat{k} \times \frac{\partial \boldsymbol{\Psi}_h}{\partial z}, && (5.20)\\
&= -\hat{k} \times \nabla_h \Psi_{\mathrm{BT}} - \hat{k} \times \nabla_h \Psi_{\mathrm{BC}} + \hat{k} \times \frac{\partial \boldsymbol{\Psi}_h}{\partial z}. && (5.21)
\end{aligned}$$

The scaling in (5.16) suggests

$$\nabla_h \Psi_{\mathrm{BC}} \sim |\boldsymbol{\Psi}_h| \frac{D}{L^2} \sim \left|\frac{\partial \boldsymbol{\Psi}_h}{\partial z}\right| \frac{D^2}{L^2}. \tag{5.22}$$

Substituting this into (5.21)

$$\boldsymbol{u}_h = -\hat{k} \times \nabla_h \Psi_{\mathrm{BT}} + \hat{k} \times \frac{\partial \boldsymbol{\Psi}_h}{\partial z}\left(1 + O\left(\frac{D^2}{L^2}\right)\right). \tag{5.23}$$

Note that the $O(D^2/L^2)$ term is not necessarily aligned with $\hat{k} \times \partial \boldsymbol{\Psi}_h / \partial z$. However, in the hydrostatic limit ($D^2/L^2 \ll 1$) the amplitude of this term is relatively small, so that - regardless of its direction - it makes a negligible contribution to $\boldsymbol{u}_h$. The baroclinic part of the vector potential, Ψ_{BC}, may therefore be neglected when solving for the horizontal velocity. The three-dimensional elliptic problem may now be

simplified as follows:

$$\begin{aligned}
\boldsymbol{\omega}_h &= -\nabla^2 \boldsymbol{\Psi}_h = -\frac{\partial^2 \boldsymbol{\Psi}_h}{\partial x^2} - \frac{\partial^2 \boldsymbol{\Psi}_h}{\partial y^2} - \frac{\partial^2 \boldsymbol{\Psi}_h}{\partial z^2} && (5.24)\\
&= -\frac{|\boldsymbol{\Psi}_h|}{L^2} - \frac{\partial^2 \boldsymbol{\Psi}_h}{\partial z^2}, && (5.25)\\
&= -\frac{D^2}{L^2}\frac{\partial^2 |\boldsymbol{\Psi}_h|}{\partial z^2} - \frac{\partial^2 \boldsymbol{\Psi}_h}{\partial z^2}, && (5.26)\\
&= -\frac{\partial^2 \boldsymbol{\Psi}_h}{\partial z^2}\left(1 + O\left(\frac{D^2}{L^2}\right)\right). && (5.27)
\end{aligned}$$

To eliminate Ψ_{BC} from the vertical vorticity equation, the expression for ω^z is integrated over the full depth of the column, reducing the three-dimensional elliptic problem for Ψ^z to a two-dimensional problem for the dominant, barotropic component:

$$\nabla_h^2 \Psi_{\mathrm{BT}} = -\frac{1}{H}\int_{-H}^{0} \omega^z \, dz, \tag{5.28}$$

from (5.14). This is a vast improvement on (5.8). In the hydrostatic limit ($D^2/L^2 \ll 1$) the 3-dimensional elliptic problem for the full vorticity, $\boldsymbol{\omega}$, has been reduced to the solution of two second order ordinary differential equations:

$$\begin{aligned}
\nabla^2 \Psi^x \approx \frac{\partial^2 \Psi^x}{\partial z^2} &= -\omega^x, && (5.29)\\
\nabla^2 \Psi^y \approx \frac{\partial^2 \Psi^y}{\partial z^2} &= -\omega^y, && (5.30)
\end{aligned}$$

and a two-dimensional Poisson equation for the barotropic component of the force function (5.28).

Our final step is to recast the horizontal components of the vector potential into rescaled barotropic and overturning modes. This step is taken in an effort to generate a trio of scalars exhibiting closed contours in the orthogonal planes of the coordinate system, thus describing depth-integrated, meridional overturning and zonal overturning circulations (for latitude-longitude-depth coordinates), providing

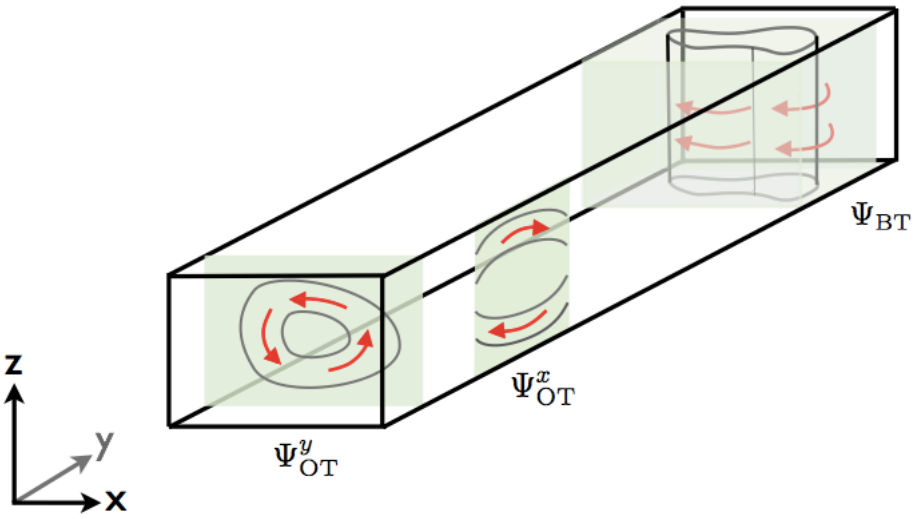

Figure 5.2: Schematic illustrating the decomposition of the vector potential into depth-independent barotropic and depth-dependent overturning components.The velocity parallels contours of constant potential with a strength inversely proportional to the contour spacing. Red arrows indicate the sense of rotation for positive values of potential.

a simple but complete description of the three-dimensional flow. The overturning vector potential, $\boldsymbol{\Psi}_{\mathrm{OT}} = [\Psi^x_{\mathrm{OT}}, \Psi^y_{\mathrm{OT}}]$, is now introduced by setting:

$$\boldsymbol{\Psi} = \boldsymbol{\Psi}_{\mathrm{OT}} + (\boldsymbol{\Psi}_h - \boldsymbol{\Psi}_{\mathrm{OT}}) + \Psi_{\mathrm{BT}}\hat{k}, \tag{5.31}$$

where $\boldsymbol{\Psi}_{\mathrm{OT}}$ is defined to vanish on the top and bottom boundaries

$$\boldsymbol{\Psi}_{\mathrm{OT}}(z=0) \;=\; \boldsymbol{\Psi}_{\mathrm{OT}}(z=-H) \;=\; \mathbf{0}, \tag{5.32}$$

since closed overturning circulations are sought. The depth-varying shear (curvature) in the three-dimensional horizontal vector potential, $\boldsymbol{\Psi}_h$, should be fully contained within the new overturning component, $\boldsymbol{\Psi}_{\mathrm{OT}}$. This is achieved by setting

$$\boldsymbol{\Psi}_h - \boldsymbol{\Psi}_{\mathrm{OT}} = cz, \tag{5.33}$$

where c is a constant, so that any residual between $\mathbf{\Psi}_h$ and $\mathbf{\Psi}_{\mathrm{OT}}$ scales linearly with depth and can thus be expressed as a weighted barotropic contribution. At the bottom boundary:

$$\mathbf{\Psi}_h(z=-H) - \mathbf{\Psi}_{\mathrm{OT}}(z=-H) = -cH. \tag{5.34}$$

Substituting c back into (5.33)

$$\mathbf{\Psi}_h \;=\; \mathbf{\Psi}_{\mathrm{OT}} - \frac{z}{H}\mathbf{\Psi}_h(z=-H), \tag{5.35}$$

using (5.32). To determine the exact relationship between $\mathbf{\Psi}_{\mathrm{OT}}$ and $\mathbf{\Psi}_h$, the correct treatment of $\mathbf{\Psi}_h$ on the bottom boundary must be considered. Here, the unit normal is given by

$$\hat{n} = \frac{\hat{k} + \nabla_h H}{\sqrt{1^2 + |\nabla_h H|^2}}. \tag{5.36}$$

Substituting into the kinematic boundary condition ($\mathbf{\Psi} \times \hat{n} = \mathbf{0}$)

$$\begin{aligned}
\mathbf{\Psi} \times (\hat{k} + \nabla_h H) &= \mathbf{0},\\
-(\hat{k} \times \mathbf{\Psi}) \;-\; (\nabla_h H \times \mathbf{\Psi}) &= \mathbf{0},\\
-\hat{k} \times (\hat{k} \times \mathbf{\Psi}) \;-\; \hat{k} \times (\nabla_h H \times \mathbf{\Psi}) &= \mathbf{0},\\
(-\hat{k}\cdot\mathbf{\Psi})\hat{k} + (\hat{k}\cdot\hat{k})\mathbf{\Psi} \;-\; (\hat{k}\cdot\mathbf{\Psi})\nabla_h H + (\hat{k}\cdot\nabla_h H)\mathbf{\Psi} &= \mathbf{0},\\
-\Psi^z\hat{k} + \mathbf{\Psi} \;-\; \Psi^z\nabla_h H &= \mathbf{0}.
\end{aligned}$$

In the hydrostatic limit this simplifies to

$$\mathbf{\Psi}_h\left[1 + O\left(\frac{D^2}{L^2}\right)\right] = \Psi_{\mathrm{BT}}\nabla_h H \qquad (\text{at } z=-H). \tag{5.37}$$

Substituting (5.37) into (5.35) completes the definition of $\mathbf{\Psi}_{\mathrm{OT}}$:

$$\mathbf{\Psi}_h = \mathbf{\Psi}_{\mathrm{OT}} - \frac{z}{H}\Psi_{\mathrm{BT}}\nabla_h H. \tag{5.38}$$

The overturning potentials are described by the same second order differential equations (5.29)-(5.30) as the components of $\mathbf{\Psi}_h$:

$$\frac{\partial^2 \Psi^x_{\mathrm{OT}}}{\partial z^2} = -\omega^x, \tag{5.39}$$

$$\frac{\partial^2 \Psi^y_{\mathrm{OT}}}{\partial z^2} = -\omega^y. \tag{5.40}$$

Integrating twice with respect to z

$$\Psi^x_{\mathrm{OT}} = \int_{-H}^{z}\left(\int_{-H}^{z}\left(\frac{\partial v}{\partial z} - \frac{\partial w}{\partial y}\right)\,dz + c_1\right)\,dz. \tag{5.41}$$

$$\Psi^y_{\mathrm{OT}} = \int_{-H}^{z}\left(\int_{-H}^{z}\left(\frac{\partial w}{\partial x} - \frac{\partial u}{\partial z}\right)\,dz + c_2\right)\,dz. \tag{5.42}$$

The integration constants, $c_{1,2}$, are chosen to ensure the overturning vanishes when integrating over the full depth:

$$\Psi^x_{\mathrm{OT}} = \int_{-H}^{z}\left(\int_{-H}^{z}\left(\frac{\partial v}{\partial z} - \frac{\partial w}{\partial y}\right)\,dz - \overline{\int_{-H}^{z}\left(\frac{\partial v}{\partial z} - \frac{\partial w}{\partial y}\right)\,dz}^{z}\right)\,dz,$$

$$\Psi^y_{\mathrm{OT}} = \int_{-H}^{z}\left(\int_{-H}^{z}\left(\frac{\partial w}{\partial x} - \frac{\partial u}{\partial z}\right)\,dz - \overline{\int_{-H}^{z}\left(\frac{\partial w}{\partial x} - \frac{\partial u}{\partial z}\right)\,dz}^{z}\right)\,dz,$$

where $\overline{}^{z}$ indicates a vertical average over the full range of z. In the hydrostatic limit, it may be expected that horizontal shear of the vertical velocity, $O(W/L)$, is negligible relative to vertical shear in the horizontal velocity, $O(V/D)$, since $D < L$

and $W < V$. It follows that away from latitudes of intense vertical motion

$$\Psi^x_{\mathrm{OT}} \approx \int_{-H}^{z} (v - \overline{v}^z)\ dz, \tag{5.43}$$

$$\Psi^y_{\mathrm{OT}} \approx -\int_{-H}^{z} (u - \overline{u}^z)\ dz. \tag{5.44}$$

Combined with the barotropic potential, Ψ_{BT}, these scalars provide a complete description of the 3-dimensional flow field. This description is useful in dividing potentially complex flow fields into overturning and depth-integrated components (figure 5.2). It will later be shown that this provides a natural separation between the buoyancy-driven and wind-driven flow regimes. The full velocity is described by $\mathbf{u} = \nabla \times \mathbf{\Psi}$, where

$$\mathbf{\Psi} = \left(\Psi^x_{\mathrm{OT}} - \frac{z}{H}\Psi_{\mathrm{BT}}\frac{\partial H}{\partial x}\right)\hat{\imath} + \left(\Psi^y_{\mathrm{OT}} - \frac{z}{H}\Psi_{\mathrm{BT}}\frac{\partial H}{\partial y}\right)\hat{\jmath} + \Psi_{\mathrm{BT}}\hat{k}, \tag{5.45}$$

retaining the directional superscripts on the components of $\mathbf{\Psi}_{\mathrm{OT}}$ to prevent ambiguity. The x-component of the velocity potential, $\mathbf{\Psi} \cdot \hat{\imath} = \Psi^x$, describes circulations about the x-axes. It must therefore be possible to show that the MOC streamfunction, ψ_{AMOC}, is given by the basinwide integral of Ψ^x. For completeness, this will briefly be confirmed below.

5.2.3 Relating the MOC and Velocity Potential

The meridional overturning streamfunction is given by the integral of the meridional velocity, v, across the depth and full width of the basin ($x_w \leq x \leq x_e$):

$$\psi_{\mathrm{AMOC}} = \int_{-H}^{z}\int_{x_w}^{x_e} v\ dx\ dz. \tag{5.46}$$

Substituting for $v = (\nabla \times \mathbf{\Psi}) \cdot \hat{\jmath}$

$$\psi_{\mathrm{AMOC}} = \int_{-H}^{z} \int_{x_w}^{x_e} \left(\frac{\partial \Psi^x}{\partial z} - \frac{\partial \Psi_{\mathrm{BT}}}{\partial x} \right) dx\, dz, \tag{5.47}$$

$$= \int_{-H}^{z} \int_{x_w}^{x_e} \left(\frac{\partial \Psi^x_{\mathrm{OT}}}{\partial z} - \frac{\Psi_{\mathrm{BT}}}{H} \frac{\partial H}{\partial x} - \frac{\partial \Psi_{\mathrm{BT}}}{\partial x} \right) dx\, dz, \tag{5.48}$$

$$= \int_{x_w}^{x_e} \left([\Psi^x_{\mathrm{OT}}]^z_{-H} - \left[\frac{z}{H} \Psi_{\mathrm{BT}} \frac{\partial H}{\partial x} \right]^z_{-H} \right) dx - z[\Psi_{\mathrm{BT}}]^{x_e}_{x_w}. \tag{5.49}$$

Recalling that $\mathbf{\Psi}_{\mathrm{OT}}(z = -H) = \mathbf{0}$ the expected result is achieved up to the boundary values on Ψ_{BT}, which have yet to be determined:

$$\psi_{\mathrm{AMOC}} = \int_{x_w}^{x_e} \mathbf{\Psi} \cdot \hat{\imath}\, dx - z[\Psi_{\mathrm{BT}}]^{x_e}_{x_w}. \tag{5.50}$$

In this framework, the MOC thus comprises two distinct modes; the "vertical shears" component Ψ^x_{OT}, and the rescaled barotropic or "external mode" component $z/H\ \Psi_{\mathrm{BT}}\ \partial H/\partial x$ (following notation introduced by *Lee and Marotzke*, 1998). Note that the latter is dependent upon the presence of depth-integrated flow over bathymetric variations in the x-direction. We expect the external mode to be important where boundary jets impinge on the continental slope (see figure 5.3) and where the zonal component of wind-driven gyres pass over topographic variations (as demonstrated by *Lee and Marotzke*, 1998).

5.2.4 Boundary Condition on the Barotropic Velocity Potential

The final step in completing the velocity decomposition into overturning and external modes is the derivation of the correct treatment of Ψ_{BT} on the lateral boundary. Here, the lateral boundary describes any land mass blocking the horizontal flow by

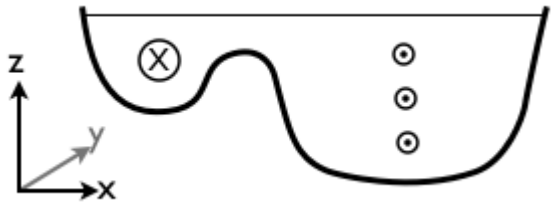

Figure 5.3: Consider a slow, southward flow in the interior of an ocean basin, returned northwards in a relatively shallow channel adjacent to the western boundary. Zonal integration produces a meridional overturning with northward volume transport in the depth range occupied by the channel, and southward volume transport at greater depths.

outcropping at the surface. In terms of the velocity potential, the horizontal velocity is given by

$$\begin{aligned} \mathbf{u}_h &= \left(\frac{\partial \Psi_{\mathrm{BT}}}{\partial y} - \frac{\partial \Psi^y}{\partial z}\right)\hat{\imath} - \left(\frac{\partial \Psi_{\mathrm{BT}}}{\partial x} - \frac{\partial \Psi^x}{\partial z}\right)\hat{\jmath}, \qquad (5.51) \\ &= \left(\frac{\partial \Psi_{\mathrm{BT}}}{\partial y} - \frac{\partial \Psi^y_{\mathrm{OT}}}{\partial z} + \frac{\Psi_{\mathrm{BT}}}{H}\frac{\partial H}{\partial y}\right)\hat{\imath} - \left(\frac{\partial \Psi_{\mathrm{BT}}}{\partial x} - \frac{\partial \Psi^x_{\mathrm{OT}}}{\partial z} + \frac{\Psi_{\mathrm{BT}}}{H}\frac{\partial H}{\partial x}\right)\hat{\jmath}. \end{aligned}$$

From the kinematic boundary condition ($\hat{n}\cdot\mathbf{u} = \hat{n}\cdot(\nabla\times\boldsymbol{\Psi}) = 0$), it emerges that $H\Psi_{\mathrm{BT}}$ is constant along the lateral boundary:

$$\frac{\partial}{\partial y}(H\Psi_{\mathrm{BT}}) = 0 \quad \text{on east/west boundaries,} \qquad (5.52)$$

$$-\frac{\partial}{\partial x}(H\Psi_{\mathrm{BT}}) = 0 \quad \text{on north/south boundaries,} \qquad (5.53)$$

using equations (5.43)-(5.44). If one single lateral boundary encompasses the domain, the choice of constant $H\Psi_{\mathrm{BT}}$ is arbitrary. However, if the domain is multiply connected with N discrete bounding segments, there are $N-1$ unknown boundary values to constrain. The necessary constraints may be found by imposing that the

depth integrated velocity also vanishes normal to the boundary:

$$\frac{\partial}{\partial y}(H\Psi_{\mathrm{BT}}) = \int_{-H}^{0} u\, dz \quad \text{on east/west boundaries,} \tag{5.54}$$

$$-\frac{\partial}{\partial x}(H\Psi_{\mathrm{BT}}) = \int_{-H}^{0} v\, dz \quad \text{on north/south boundaries.} \tag{5.55}$$

The solution method for Ψ_{BT} is as follows. An arbitrary value is chosen for Ψ_{BT} on one boundary. Since the horizontal velocity is known everywhere, from this starting point integration of (5.54) and/or (5.55) along lines connecting all boundary segments in the global domain provides the remaining boundary values. The elliptic problem (5.28) can then be inverted to provide Ψ_{BT} throughout the domain interior. This will be illustrated in the next chapter, where numerical solutions for Ψ_{BT} will be presented in an idealised configuration of a GCM.

5.2.5 Rotational Momentum Equation

The decomposition presented above holds for any rotational vector field where $D/L < 1$ is satisfied. It immediately follows that an identical decomposition may be written for the rotational component of the forcing fields driving the evolution of the (purely rotational) velocity. The forcing terms, $\mathbf{F}$, in the momentum equation (5.1) may be written as the linear superposition of purely rotational and purely divergent parts using the Helmholtz decomposition:

$$\left(\rho_0 \frac{\partial \mathbf{u}}{\partial t} + \nabla p\right)\Big|_{\mathbf{F}} = \mathbf{F}_{\mathrm{rot}} + \mathbf{F}_{\mathrm{div}}, \tag{5.56}$$

where

$$\nabla \cdot \mathbf{F}_{\text{rot}} = 0, \tag{5.57}$$

$$\nabla \times \mathbf{F}_{\text{div}} = \mathbf{0}, \tag{5.58}$$

introducing the notation $\Big|_{\mathbf{F}}$ to denote association with a particular forcing field, $\mathbf{F}$. Since the velocity, $\mathbf{u}$, is purely rotational by (5.2), only the purely rotational forcings project onto the local momentum tendency. In the Eulerian reference frame the divergent forcing generates a pressure gradient which simply acts to return (remove) fluid to (from) the impermeable boundaries, ensuring continuity of the resultant motion.

$$\nabla p\Big|_{\mathbf{F}} = \mathbf{F}_{\text{div}}. \tag{5.59}$$

The pressure gradient thus complicates the interpretation of the force balance responsible for the evolution of the flow regime, motivating the formation of the "rotational momentum" equation in which the pressure gradient is entirely absent:

$$\frac{\partial \mathbf{u}}{\partial t}\bigg|_{\mathbf{F}} = \frac{\mathbf{F}_{\text{rot}}}{\rho_0} = \nabla \times \mathbf{A}, \tag{5.60}$$

satisfying (5.57). $\mathbf{A}$ is termed the "force function" and is analogous to the vector potential, $\mathbf{\Psi}$, used to describe the purely rotational velocity field. The kinematic boundary condition on the velocity field, $\hat{n} \cdot \mathbf{u} = 0$, translates into an equivalent condition on the force function:

$$\hat{n} \cdot (\nabla \times \mathbf{A}) = 0. \tag{5.61}$$

It follows from (5.45) that

$$\mathbf{A} = \left(\mathrm{A}^{x}_{\mathrm{OT}} - \frac{z}{H} \mathrm{A}_{\mathrm{BT}} \frac{\partial H}{\partial x} \right) \hat{\imath} \; + \; \left(\mathrm{A}^{y}_{\mathrm{OT}} - \frac{z}{H} \mathrm{A}_{\mathrm{BT}} \frac{\partial H}{\partial y} \right) \hat{\jmath} \; + \; \mathrm{A}_{\mathrm{BT}} \hat{k}, \tag{5.62}$$

where the barotropic and overturning components of $\mathbf{A}$ are described by a set of equations that are analogous to (5.28), (5.39)-(5.40) derived for $\mathbf{\Psi}$:

$$\nabla_h^2 \mathrm{A_{BT}} = -\frac{1}{\rho_0 H} \int_{-H}^{0} (\nabla \times \mathbf{F}) \cdot \hat{k} \, dz, \tag{5.63}$$

$$\frac{\partial^2 \mathrm{A_{OT}^x}}{\partial z^2} = -\frac{1}{\rho_0} (\nabla \times \mathbf{F}) \cdot \hat{\imath}, \tag{5.64}$$

$$\frac{\partial^2 \mathrm{A_{OT}^y}}{\partial z^2} = -\frac{1}{\rho_0} (\nabla \times \mathbf{F}) \cdot \hat{\jmath}. \tag{5.65}$$

The forces controlling the evolution of the vertical shear and external mode circulations may now be examined separately:

$$\frac{\partial \mathbf{\Psi}_{\mathrm{OT}}}{\partial t} = \sum \mathbf{A}_{\mathrm{OT}}, \tag{5.66}$$

$$\frac{\partial \Psi_{\mathrm{BT}}}{\partial t} = \sum \mathrm{A_{BT}}. \tag{5.67}$$

The overturning and barotropic force functions must be solved subject to the same boundary conditions as their corresponding components of $\mathbf{\Psi}$. From (5.32), the overturning force function, $\mathbf{A}_{\mathrm{OT}}$, is also defined to vanish on the top and bottom boundaries:

$$\mathbf{A}_{\mathrm{OT}}(z = 0) = \mathbf{A}_{\mathrm{OT}}(z = -H) = \mathbf{0}. \tag{5.68}$$

Determination of the lateral boundary condition on $\mathrm{A_{BT}}$ is presented in the next section. Combining (5.50) and (5.66)-(5.67), the tendency of the MOC due to any particular forcing can be determined by integrating the associated zonal overturning force function across the basin:

$$\left.\frac{\partial \psi_{\mathrm{AMOC}}}{\partial t}\right|_{\mathbf{F}} = \int_{x_w}^{x_e} \left.\mathbf{A}\right|_{\mathbf{F}} \cdot \hat{\imath} \, dx \; - \; z \left[\left.\mathrm{A_{BT}}\right|_{\mathbf{F}} \right]_{x_w}^{x_e}. \tag{5.69}$$

This is an extremely useful expression for the analysis of numerical output from complex GCMs. At any point in the domain, in the Eulerian frame of reference, the adjustment of the MOC can be unambiguously attributed to the responsible forcing term. The rotational momentum balance maintaining the MOC can thus be easily assessed at each and every point in time and space.

5.2.6 Boundary Condition on the Barotropic Force Function

Determination of the Dirichlet boundary condition on the barotropic force function, $\mathrm{A_{BT}}$, proceeds along similar lines to that for the barotropic velocity potential, Ψ_{BT}, presented in section (5.2.4). The kinematic condition of constant $H\Psi_{\mathrm{BT}}$ translates into the equivalent condition that $H\mathrm{A_{BT}}$ is constant on the lateral boundaries. As before, additional constraints can be found from imposing that the depth-integrated rotational force (projecting on to the depth-integrated velocity) vanishes. In terms of the force function, the full horizontal force is given by

$$\begin{aligned}\frac{\mathbf{F}_h}{\rho_0} &= \left(\left(\frac{\partial \mathrm{A_{BT}}}{\partial y} - \frac{\partial \mathrm{A}^y_{\mathrm{OT}}}{\partial z} + \frac{\mathrm{A_{BT}}}{H}\frac{\partial H}{\partial y}\right)\hat{\imath} \;-\; \left(\frac{\partial \mathrm{A_{BT}}}{\partial x} - \frac{\partial \mathrm{A}^x_{\mathrm{OT}}}{\partial z} + \frac{\mathrm{A_{BT}}}{H}\frac{\partial H}{\partial x}\right)\hat{\jmath} \;+\; \frac{\nabla_h p}{\rho_0}\right)\Bigg|_{\mathbf{F}}, \\ &= \left(\hat{k}\times\frac{\partial \mathbf{A}_{\mathrm{OT}}}{\partial z} \;-\; \hat{k}\times\nabla_h \mathrm{A_{BT}} \;-\; \frac{\mathrm{A_{BT}}}{H}\hat{k}\times\nabla_h H \;+\; \frac{\nabla_h p}{\rho_0}\right)\Bigg|_{\mathbf{F}}.\end{aligned}$$

Integrating over the full depth of the column and rearranging

$$\hat{k}\times\nabla_h(H\mathrm{A_{BT}}) = -\frac{1}{\rho_0}\int_{-H}^{0}(\mathbf{F}_h - \nabla_h p)\,dz. \tag{5.70}$$

The obvious way to proceed would be to solve for the pressure field, p, by inverting the three-dimensional elliptic problem for $\mathbf{F}_{\mathrm{div}}$:

$$\nabla\cdot\mathbf{F} = \nabla\cdot\mathbf{F}_{\mathrm{div}} = \nabla^2 p\Big|_{\mathbf{F}}, \tag{5.71}$$

subject to the Neumann boundary condition

$$\hat{n} \cdot \nabla p \Big|_{\mathbf{F}} = \hat{n} \cdot \mathbf{F}, \tag{5.72}$$

(from $\hat{n} \cdot \mathbf{u} = 0 \implies \hat{n} \cdot \mathbf{F}_{\text{rot}} = 0$). However, inversion of the three-dimensional elliptic problem (5.71) is challenging unless the problem is carefully preconditioned. This issue is avoided in the MITgcm's pressure solve (*Marshall et al.*, 1997b) by splitting p into barotropic and baroclinic contributions

$$p_{\text{BT}}(x,y) = \frac{1}{H} \int_{-H}^{0} p(x,y,z)\, dz, \tag{5.73}$$

$$p_{\text{BC}}(x,y,z) = p(x,y,z) - p_{\text{BT}}(x,y). \tag{5.74}$$

The baroclinic pressure, p_{BC}, can easily be obtained from hydrostatic balance for the buoyancy force:

$$p_{\text{BC}} \Big|_{\text{buoyancy}} = \int_{-H}^{z} -\rho g\, dz, \tag{5.75}$$

and is zero for all remaining forces. Substituting into (5.70)

$$\frac{\rho_0}{H}\, \hat{k} \times \nabla_h \left(H \text{A}_{\text{BT}} \Big|_{\mathbf{F}} \right) - \nabla_h p_{\text{BT}} \Big|_{\mathbf{F}} = -\frac{1}{H} \int_{-H}^{0} \left(\mathbf{F}_h - \nabla_h p_{\text{BC}} \Big|_{\mathbf{F}} \right) dz. \tag{5.76}$$

Taking the horizontal divergence forms a two-dimensional elliptic problem for p_{BT}

$$\nabla_h^2 p_{\text{BT}} \Big|_{\mathbf{F}} = \frac{1}{H} \nabla_h \cdot \int_{-H}^{0} \left(\mathbf{F}_h - \nabla_h p_{\text{BC}} \Big|_{\mathbf{F}} \right) dz, \tag{5.77}$$

which can be solved subject to the condition that the depth-integrated rotational forcing must vanish normal to the boundary:

$$\hat{n} \cdot \nabla_h p_{\mathrm{BT}} \Big|_{\mathbf{F}} = \frac{1}{H} \hat{n} \cdot \int_{-H}^{0} \left(\mathbf{F}_h - \nabla_h p_{\mathrm{BC}} \Big|_{\mathbf{F}} \right) \, dz. \tag{5.78}$$

It is now possible to determine the Dirichlet condition on the barotropic force function, $\mathrm{A_{BT}}$. Firstly, the 2-dimensional elliptic problem (5.77) is inverted to obtain p_{BT}, subject to the Neumann boundary condition (5.78). $\mathrm{A_{BT}}$ is then found from the components of (5.76):

$$\frac{\partial}{\partial y} \left(H \mathrm{A_{BT}} \Big|_{\mathbf{F}} \right) = \frac{1}{\rho_0} \left(\int_{-H}^{0} \left(F^x - \frac{\partial p_{\mathrm{BC}}}{\partial x} \Big|_{\mathbf{F}} \right) \, dz - H \frac{\partial p_{\mathrm{BT}}}{\partial x} \Big|_{\mathbf{F}} \right), \tag{5.79}$$

$$\frac{\partial}{\partial x} \left(H \mathrm{A_{BT}} \Big|_{\mathbf{F}} \right) = -\frac{1}{\rho_0} \left(\int_{-H}^{0} \left(F^y - \frac{\partial p_{\mathrm{BC}}}{\partial y} \Big|_{\mathbf{F}} \right) \, dz - H \frac{\partial p_{\mathrm{BT}}}{\partial y} \Big|_{\mathbf{F}} \right). \tag{5.80}$$

An arbitrary value for $\mathrm{A_{BT}}$ is chosen on one boundary. Integration of (5.79) and/or (5.80) along lines connecting all boundary segments in the global domain provides the remaining boundary values.

5.3 New Analytical Results

The principal focus of this chapter (and the two that follow) is the determination of the momentum balance setting the strength and structure of the MOC, motivating a preliminary examination of the structure of $\mathrm{A}^x_{\mathrm{OT}}$ from analytical solutions of equation (5.69), not presented in MP11. Here, it is helpful to write the forcing terms in a general form of the governing momentum equation (5.1) explicitly, so that the contribution of each term to the generation of meridional overturnings may be examined. Expanding $\mathbf{F}$ into individual contributions from inertia, Coriolis, buoyancy,

wind, viscosity and friction respectively:

$$\rho_0 \frac{\partial \mathbf{u}}{\partial t} + \nabla p = -\rho_0 \mathbf{u} \cdot \nabla \mathbf{u} \; - \; \rho_0 f \hat{k} \times \mathbf{u} \; - \; g\rho' \hat{k} \; + \; \frac{\boldsymbol{\tau}}{d_{ek}} \; + \; \rho_0 \mu \nabla^2 \mathbf{u} \; - \; \rho_0 r \mathbf{u}, \quad (5.81)$$

where $f(y)$ is the Coriolis parameter, g is gravity, $\rho'(x, y, z)$ is a density anomaly with reference to some background value, ρ_0. $\boldsymbol{\tau}(x, y)$ is the wind stress felt from the surface to a depth $z = d_{ek}$. For simplicity, it has been assumed that momentum dissipation is achieved by Laplacian diffusion and linear drag, where μ and r are the associated constant coefficients.

Analytical solutions to the external mode of the MOC, $z/H \; \Psi_{\mathrm{BT}} \partial H/\partial x$, are not derived below. We will recall that the external mode may contribute significantly to the MOC (if strong horizontal currents pass over zonally varying bathymetry) when we interpret the results below.

5.3.1 Generation of Overturning Circulations

Away from the ocean margins, the large scale ocean circulation is in thermal wind balance (e.g *Vallis*, 2006) . Horizontal gradients in the density field can thus be maintained in steady-state by vertical shear in the orthogonal geostrophic velocity. The overturning circulations associated with this prevailing balance between Coriolis and buoyancy forces are now examined in the rotational momentum framework. Substituting the Coriolis term for $\mathbf{F}$ in the two-dimensional ODEs for $\mathbf{A}_{\mathrm{OT}}$ (5.64)-(5.65):

$$\frac{\partial^2 \mathbf{A}_{\mathrm{OT}}}{\partial z^2} = -f \frac{\partial \mathbf{u}}{\partial z}. \quad (5.82)$$

Following the solution method presented above for $\boldsymbol{\Psi}_{\mathrm{OT}}$, (5.82) is integrated twice with respect to z, and the constant of integration is chosen so that $\mathbf{A}_{\mathrm{OT}}$ vanishes on

the top and bottom boundaries of the domain. In component form:

$$\left.\mathrm{A}^x_{\mathrm{OT}}\right|_{\mathrm{Coriolis}} = -f \int_{-H}^{z} u - \overline{u}^z \, dz, \tag{5.83}$$

$$\left.\mathrm{A}^y_{\mathrm{OT}}\right|_{\mathrm{Coriolis}} = -f \int_{-H}^{z} v - \overline{v}^z \, dz, \tag{5.84}$$

where $\overline{}^z$ indicates a vertical average over the full range of z. The generation of a vertical shears mode of the MOC, Ψ^x_{OT}, by the Coriolis force is therefore achieved by tilting of planetary vorticity, f, into the local $y-z$ plane by depth-integrated vertical shear of the full zonal velocity (5.66). Substituting the buoyancy term for $\mathbf{F}$ in (5.64)-(5.65):

$$\frac{\partial^2 \mathbf{A}_{\mathrm{OT}}}{\partial z^2} = -g\hat{k} \times \nabla\rho'. \tag{5.85}$$

Without loss of generality, in the presence of planetary rotation, the thermal wind equation can be used to express the buoyancy force function in terms of the geostrophic velocity $\mathbf{u_g}$:

$$\frac{\partial^2 \mathbf{A}_{\mathrm{OT}}}{\partial z^2} = f\frac{\partial \mathbf{u_g}}{\partial z}. \tag{5.86}$$

Note that this relation may be invoked without making the assumption that the flow is in geostrophic balance. Proceeding as above,

$$\left.\mathrm{A}^x_{\mathrm{OT}}\right|_{\mathrm{buoyancy}} = f \int_{-H}^{z} u_g - \overline{u_g}^z \, dz, \tag{5.87}$$

$$\left.\mathrm{A}^y_{\mathrm{OT}}\right|_{\mathrm{buoyancy}} = f \int_{-H}^{z} v_g - \overline{v_g}^z \, dz. \tag{5.88}$$

Generation of a vertical shears mode, $\Psi^x_{\rm OT}$, by the buoyancy force is achieved by tilting of planetary vorticity, f, into the local $y-z$ plane by depth-integrated vertical shear of the geostrophic zonal velocity.

5.3.2 Ageostrophic Maintenance of the MOC

In the hydrostatic limit, overturning circulations forced by the Coriolis and buoyancy forces should be of equal and opposite magnitude unless deviations from geostrophy occur. For a flat-bottomed basin - for which the external mode vanishes - the MOC may be viewed as a residual overturning

$$\left.\frac{\partial \Psi^x_{\rm OT}}{\partial t}\right|_{\rm residual} = \left.{\rm A}^x_{\rm OT}\right|_{\rm Coriolis} + \left.{\rm A}^x_{\rm OT}\right|_{\rm buoyancy} = -f \int_{-H}^{z} (u_{ag} - \overline{u_{ag}}^z)\ dz, \qquad (5.89)$$

generated by tilting of planetary vorticity, f, into the $y-z$ plane by vertical shear of the ageostrophic zonal velocity (figure 5.4). This description of the MOC forms a close analogy with an atmospheric front, whose maintenance is achieved by cross-frontal secondary circulations (e.g *Holton*, 2004). It is interesting to also note that an interhemispheric MOC requires that the vertical shear in u_{ag} changes sign with f at the Equator.

In steady state, the residual overturning will be balanced by overturnings generated by wind, frictional, viscous and inertial effects. Simple expressions are easily obtained for the wind and friction forms given in (5.81), which are derived below for completeness. Substituting the wind forcing term for $\mathbf{F}$ in (5.64)-(5.65)

$$\frac{\partial^2 \mathbf{A}_{\rm OT}}{\partial z^2} = -\frac{1}{\rho_0 d_{ek}} \hat{k} \times \frac{\partial \boldsymbol{\tau}}{\partial z}, \qquad (5.90)$$

and proceeding as before, it is found that MOC generation is achieved by shear in the zonal component of the wind-driven Ekman velocity, $\mathbf{u}_{ek} = [u_{\rm ek}, v_{\rm ek}]$, tilting

planetary vorticity into the $y-z$ plane:

$$\mathrm{A}^{x}_{\mathrm{OT}}\Big|_{\mathrm{wind}} = f\int_{-H}^{z}(u_{ek}-\overline{u_{ek}}^{z})\ dz, \tag{5.91}$$

$$\mathrm{A}^{y}_{\mathrm{OT}}\Big|_{\mathrm{wind}} = f\int_{-H}^{z}(v_{ek}-\overline{v_{ek}}^{z})\ dz. \tag{5.92}$$

Substituting the linear friction for $\mathbf{F}$ in (5.64)-(5.65):

$$\frac{\partial^2 \mathbf{A}_{\mathrm{OT}}}{\partial z^2} = r\boldsymbol{\omega}, \tag{5.93}$$

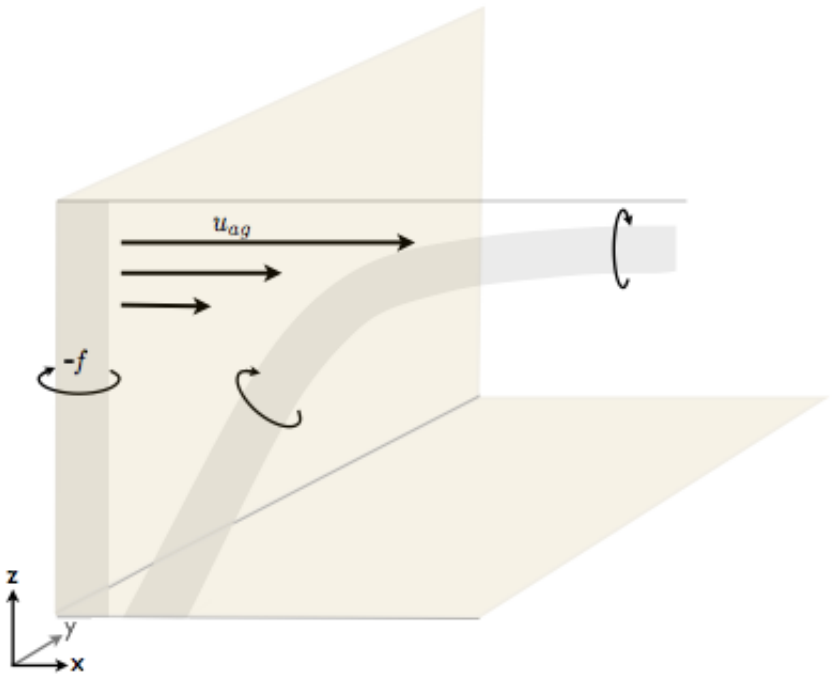

Figure 5.4: Generation of large scale meridional overturning is accomplished near the impermeable boundaries, where the Coriolis force vanishes and vertical shear in the resultant ageostrophic zonal velocity, u_{ag}, tilts planetary vorticity into the $y-z$ plane.

and proceeding as before, linear friction is seen to directly oppose MOC generation:

$$\mathrm{A}^x_{\mathrm{OT}}\Big|_{\mathrm{friction}} \approx -r\Psi^x_{\mathrm{OT}}, \tag{5.94}$$

$$\mathrm{A}^y_{\mathrm{OT}}\Big|_{\mathrm{friction}} \approx -r\Psi^y_{\mathrm{OT}}, \tag{5.95}$$

as expected.

Simple analytical expressions for the viscous and inertially driven meridional overturnings are more challenging to derive. For completeness, the force functions for each are written below, although they are at present no more insightful than their corresponding terms in the vorticity equation. The expressions for the inertial force function

$$\mathrm{A}^x_{\mathrm{OT}}\Big|_{\mathrm{inertia}} = \int_{-H}^{z} \left(\int_{-H}^{z} (\mathbf{u}\cdot\nabla)\omega^x - (\boldsymbol{\omega}\cdot\nabla)u \; dz \; - \; \overline{\int_{-H}^{z} (\mathbf{u}\cdot\nabla)\omega^x - (\boldsymbol{\omega}\cdot\nabla)u \; dz}^{z} \right) dz, \tag{5.96}$$

$$\mathrm{A}^y_{\mathrm{OT}}\Big|_{\mathrm{inertia}} = \int_{-H}^{z} \left(\int_{-H}^{z} (\mathbf{u}\cdot\nabla)\omega^y - (\boldsymbol{\omega}\cdot\nabla)v \; dz \; - \; \overline{\int_{-H}^{z} (\mathbf{u}\cdot\nabla)\omega^y - (\boldsymbol{\omega}\cdot\nabla)v \; dz}^{z} \right) dz, \tag{5.97}$$

indicate that rotational inertia generates a meridional overturning via advection and stretching of pre-existing zonal relative vorticity, ω^x, and tilting of meridional and vertical relative vorticity into the $y-z$ plane. Rotational viscous forcing acts to locally diffuse vorticity down gradient ($\mu > 0$):

$$\mathrm{A}^x_{\mathrm{OT}}\Big|_{\mathrm{viscosity}} = -\mu \int_{-H}^{z} \left(\int_{-H}^{z} \nabla^2\omega^x \; dz - \overline{\int_{-H}^{z} \nabla^2\omega^x \; dz}^{z} \right) dz, \tag{5.98}$$

$$\mathrm{A}^y_{\mathrm{OT}}\Big|_{\mathrm{viscosity}} = -\mu \int_{-H}^{z} \left(\int_{-H}^{z} \nabla^2\omega^y \; dz - \overline{\int_{-H}^{z} \nabla^2\omega^y \; dz}^{z} \right) dz. \tag{5.99}$$

It may act as a source or sink of meridional overturning circulation depending on the curvature of ω^x.

To conclude, it is important to recall that analytical solutions have not been considered for the external mode component of the MOC. In this section we have shown that, in a flat bottom basin, MOC generation is due to tilting of planetary vorticity by ageostrophic forcings. The latter are expected to be significant in the Ekman layer and at the boundaries, where the Coriolis force vanishes to satisfy the kinematic boundary condition and large gradients are established in the velocity field. However, in a basin with realistic bathymetry, the external mode contribution may also be significant, especially at the basin margins, where horizontal jets impinge on the continental slope. Consequently, the simple vorticity tilting argument, illustrated in figure 5.4, is not a full description of MOC generation.

5.4 Discussion and Conclusions

5.4.1 Rotational Momentum Framework: Summary

In this chapter, we have revisited the momentum balance of the large-scale ocean circulation. When a force is applied to a Boussinesq fluid, the fluid is accelerated both locally by the applied force and remotely by the pressure gradients established to maintain non-divergence of the resultant motion and to satisfy the no-normal-flow boundary conditions. The net acceleration is described by a rotational force, uniquely determined by a Helmholtz decomposition of the applied force into its rotational and divergent components, along with the kinematic boundary condition that the rotational force should vanish normal to solid boundaries.

A key advantage of the approach is that, if two terms balance pointwise in the vorticity equation, then the equivalent two terms balance pointwise in the rotational momentum equation. This allows for vorticity descriptions of the dynamics to be

readily reinterpreted in terms of rotational force balances. This provides an alternative interpretation of the forces driving the large-scale overturning circulation.

In the hydrostatic limit, we have shown that the rotational forces can be further decomposed into a depth-integrated horizontal component and two overturning components, each of which is described by scalar force functions. Since the velocity field is also nondivergent and satisfies the same no-normal-flow boundary condition, precisely the same decomposition can be applied to the velocity field. This is useful as a diagnostic tool for two reasons: (i) it provides a rigorous dynamical approach for decomposing the circulation and associated momentum balances into depth-integrated and overturning components, and (ii) it is far easier to visualize scalar fields (streamfunctions and force functions) than vector fields (velocities and forces).

5.4.2 Limitations

A key assumption in the development of the rotational momentum framework presented above is that the ocean is a Boussinesq fluid in hydrostatic balance at all times. As discussed in chapter 2, the Boussinesq assumption is not restrictive. The hydrostatic assumption however, prevents motions on the submesoscale ($L \leq 10$ km), such as convective instabilities and frontal circulations, from being examined within the rotational momentum framework as it is set out in this chapter. Although we have not discussed eddy momentum fluxes in the analysis above, we should note that we are able to determine the contribution of mesoscale eddies (for which 10 km$< L \leq 100$ km) to the rotational momentum budget. This would be a valuable extension to the present work.

The rotational momentum framework provides an Eulerian view of the flow regime. Although this choice is highly practical, it is important to remember that the components of the velocity potential, Ψ, describe the projection of the three-

dimensional flow field into the local latitude-depth, longitude-depth or latitude-longitude plane. Contoured velocity potentials must not be interpreted as particle pathways.

5.4.3 Analytical Solutions Summary

We have presented anaytical solutions for the vertical shears component, Ψ^x_{OT}, of the overturning. We propose that the geostrophic Atlantic MOC may be viewed in part as a residual overturning, generated by tilting of planetary vorticity in to the latitude-depth plane by depth-integrated vertical shear of the ageostrophic zonal velocity. Analytical solutions were not presented for the external mode component of the MOC, which depends more intricately on the geometry of the domain. This component will be large where strong horizontal flows pass over bathymetric variations in the east-west direction, for example on the western margin of the basin, where the boundary currents impinge on the continental slope.

Chapter 6

Rotational Momentum Balance of the MOC: Numerical Modelling Experiments

6.1 Introduction

6.1.1 Present Aims

Following results presented by MP11 and in the previous chapter of this thesis, the principal aims of the work presented here are to:

1. determine the force balance governing the overturning in an idealised OGCM by computing the force functions defined in the previous chapter of this thesis;

2. extend the analysis to complex geometries and determine the relative importance of vertical shears and external modes of the AMOC.

6.2 Idealised Modelling Studies

We start by assessing the rotational momentum budget governing the three dimensional circulation in the highly idealised reentrant channel model presented in chapter 2. We present solutions below for the scalar components of the velocity potential, $\mathbf{\Psi}$, and force function, $\mathbf{A}$, at the final timestep of the integration. Our particular focus is on the dynamics of the modelled Atlantic meridional overturning, ψ_{AMOC}. In the previous chapter we saw that meridional (zonal) overturning circulations are described by the zonal (meridional) component of the vector potential:

$$\begin{aligned} \mathbf{\Psi} \cdot \hat{\imath} &= \Psi^{x}_{\mathrm{OT}} - \frac{z}{H}\Psi_{\mathrm{BT}}\frac{\partial H}{\partial x}, \\ \mathbf{\Psi} \cdot \hat{\jmath} &= \Psi^{y}_{\mathrm{OT}} - \frac{z}{H}\Psi_{\mathrm{BT}}\frac{\partial H}{\partial y}. \end{aligned} \tag{6.1}$$

In this chapter, we will refer to an overturning volume flux in the local $y-z$ ($x-z$) plane as the MOC (ZOC):

$$\begin{aligned} \mathrm{MOC} &= \Delta x \ \mathbf{\Psi} \cdot \hat{\imath}, \\ \mathrm{ZOC} &= \Delta y \ \mathbf{\Psi} \cdot \hat{\jmath}, \end{aligned} \tag{6.2}$$

where Δx (Δy) is the grid cell width (length). We reserve the notation AMOC (AZOC) to describe the zonal (meridional) integral of $\mathbf{\Psi} \cdot \hat{\imath}$ ($\mathbf{\Psi} \cdot \hat{\jmath}$) across the full width (length) of the modelled Atlantic basin. Careful consideration was given to the proper discretisation of the rotational momentum terms to (i) achieve an accurate decomposition and (ii) facilitate comparison of the relevant terms with ψ_{AMOC}. Key details of the calculation are now reviewed below.

6.2.1 Technical Details

To compute the components of the velocity potential, $\mathbf{\Psi}$, the curl of the velocity field (the relative vorticity, $\boldsymbol{\omega} = [\omega^x, \omega^y, \omega^z]$), must be determined. The MITgcm evolves

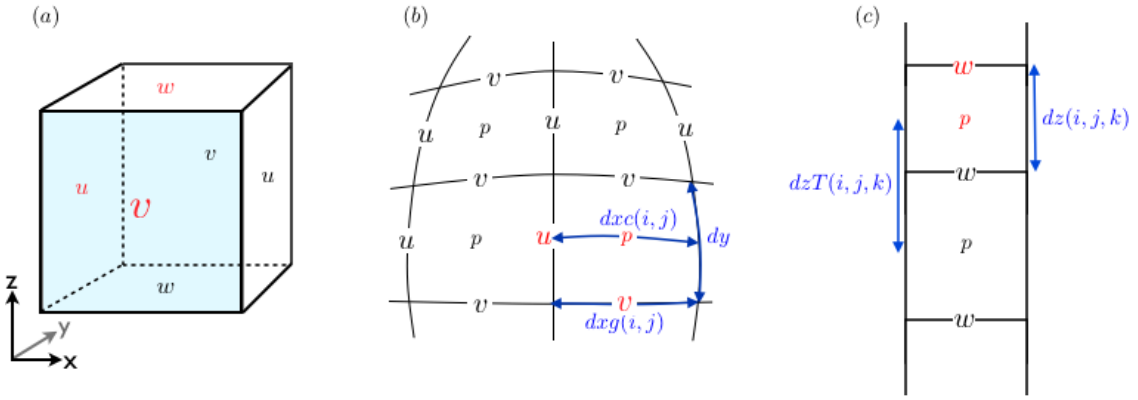

Figure 6.1: (a) C-grid staggering of the velocity components, $[u, v, w]$, in the MITgcm. Pressure, p, and all other tracers are located at the cell centre. $u(i, j, k), v(i, j, k)$, $w(i, j, k)$ and $p(i, j, k)$ are shown in red. The model convention is that i and j indices increase in the positive x and y directions respectively. The k index increases in the negative z direction. The horizontal and vertical grid spacings are shown (in blue) in (b) and (c) respectively.

the velocity components on a staggered grid (figure 6.1) and there are numerous options for the precise positioning of the curl. To achieve the greatest possible accuracy, all choices are made to remain in close consistency with the discretisation algorithms implemented in the prognostic model. Given this, $\boldsymbol{\omega}$ is computed as the circulation per unit area, so that the components are positioned as indicated in figure 6.2. Since $\boldsymbol{\omega}_h$ must be integrated twice with respect to z to determine $\boldsymbol{\Psi}_{\mathrm{OT}}$, the selected discretisation ensures the AMOC will be co-located with ψ_{AMOC}, in the latitude-depth plane. Furthermore, following our discussion in the previous chapter, we expect ocean adjustment to occur in the viscous boundary layers and seek to determine Ψ^x_{OT} as close to the boundary as possible. This is particularly critical for the present grid resolution, which exceeds the deformation radius, L_D, at high latitudes. The east and west boundaries are met at u velocity points. By assessing ω^x as shown in figure 6.2, we can hope to resolve ageostrophic dynamics in the rotational momentum analysis.

On performing the vertical integrals, we are careful to account for partial cell representation of bathymetry. However, it is important to note that the modelled

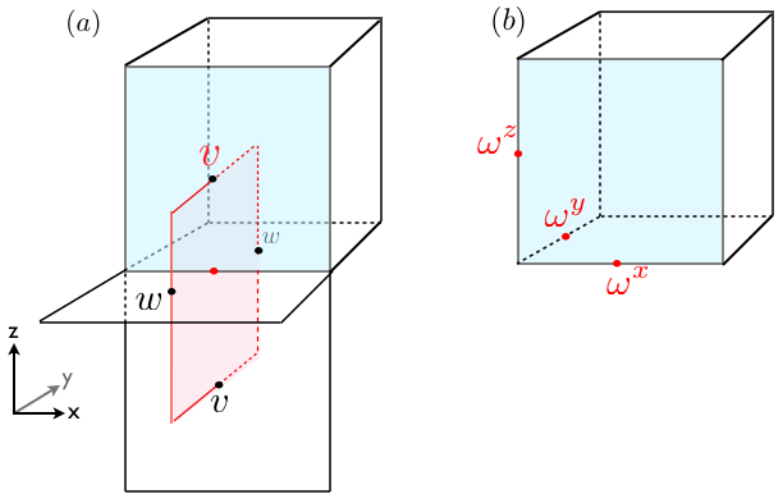

Figure 6.2: The curl is computed as the circulation divided by the enclosed area, (a) shown here for the zonal vorticity, ω^x, where $v(i,j,k)$ is shown in red. The C-grid staggering of all components of $\boldsymbol{\omega}$ is shown in (b) for $\omega^x(i,j,k), \omega^y(i,j,k)$, and $\omega^z(i,j,k)$.

displacement of the free surface, η, is linearized and does not appear in flux computations in the MITgcm (i.e the tracer content between the reference and displaced surface is ignored). As a result, it is neglected in the computation of the velocity potential. The final locations of the vertical shears components of the velocity potential, $[\Psi^x_{\rm OT}, \Psi^y_{\rm OT}]$, are shown in figure 6.3.

Calculation of the vertical shears component of the force function, $[\mathrm{A}^x_{\rm OT}, \mathrm{A}^y_{\rm OT}]$, is identical to the methodology presented above for $[\Psi^x_{\rm OT}, \Psi^y_{\rm OT}]$, except that we compute the curl of the momentum tendencies, $\mathbf{F}$, in place of the curl of the velocity field, $\mathbf{u}$. The horizontal momentum tendencies, $\mathbf{F}_h = [F^x, F^y]$, in the prognostic model are co-located with their corresponding velocity components. All horizontal momentum tendencies are computed online. Since the model is hydrostatic, the vertical momentum tendency, F^w, from the buoyancy force is not handled on the w point, and is instead computed diagnostically. To avoid interpolating density, ρ, from the cell centre onto w, we exploit hydrostatic balance to express ρ in terms of pressure,

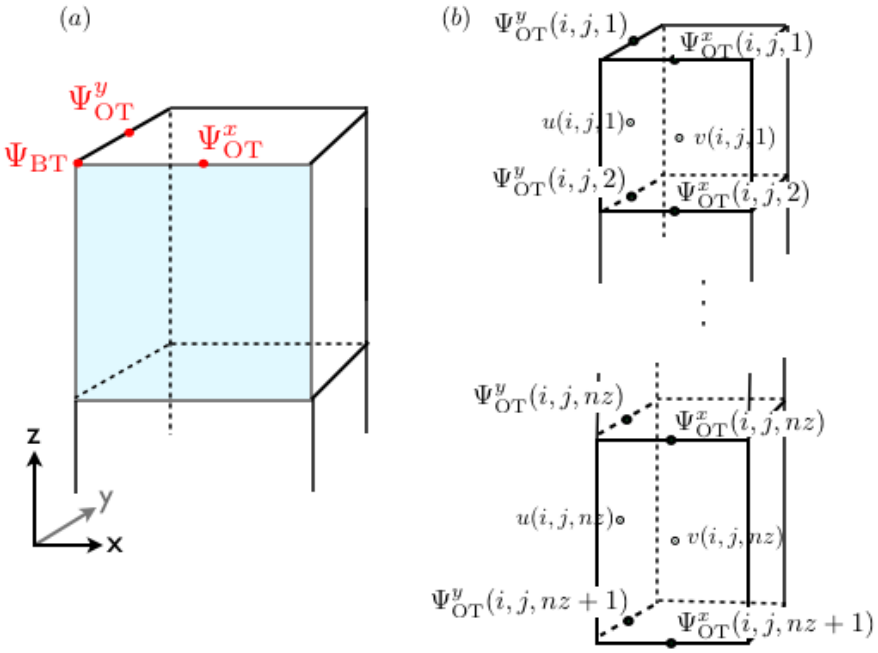

Figure 6.3: C-grid staggering of the barotropic and overturning components of the velocity potential. (a) $\Psi^x_{\rm OT}(i,j,k), \Psi^y_{\rm OT}(i,j,k)$ and $\Psi_{\rm BT}(i,j)$ are shown in red for comparison with the location of $\mathbf{u}(i,j,k)$ and $\boldsymbol{\omega}(i,j,k)$ in figures 6.1a and 6.2. (b) $\Psi^x_{\rm OT}(i,j,1)$ is half a cell above $v(i,j,1)$ and co-located with the MOC streamfunction, $\psi_{\rm AMOC}$.

p, (as in our analytical investigation of $\mathbf{A}_{\rm OT}\Big|_{\rm buoyancy}$ in section 5.3.1):

$$\mathbf{F}\Big|_{\rm buoyancy} = -g\rho\hat{k} = \frac{\partial p}{\partial z}\hat{k}, \tag{6.3}$$

and the components of $\mathbf{A}_{\rm OT}\Big|_{\rm buoyancy}$ are computed as follows

$$\mathrm{A}^x_{\rm OT}\Big|_{\rm buoyancy} = -\frac{1}{\rho_0}\int_{-H}^{z}\left(\frac{\partial p}{\partial y} - \overline{\frac{\partial p}{\partial y}}^{z}\right)\,dz, \tag{6.4}$$

$$\mathrm{A}^y_{\rm OT}\Big|_{\rm buoyancy} = \frac{1}{\rho_0}\int_{-H}^{z}\left(\frac{\partial p}{\partial x} - \overline{\frac{\partial p}{\partial x}}^{z}\right)\,dz, \tag{6.5}$$

at the desired location (figure 6.3). To compute the horizontal pressure gradient, $\nabla_h p$, across the boundaries, we ensure that the kinematic boundary condition is

satisfied, i.e acceleration across the impermeable coastlines by any other forcing terms must be cancelled by $\nabla_h p$:

$$\hat{n} \cdot \nabla_h p = \hat{n} \cdot \left(\sum \mathbf{F}_h - \nabla_h p \right). \tag{6.6}$$

Although the volume changes associated with the displacement of the linear free surface are not taken into consideration, it is important to include the contribution of the surface height gradients to the horizontal pressure gradient.

Finally, we recall that the components of the velocity potential (force function), as defined in chapter 5, inform a sense of circulation as indicated in figure 5.2. We define positive $\mathbf{\Psi} \cdot \hat{\jmath}$ ($\mathbf{A} \cdot \hat{\jmath}$) to correspond to anti-clockwise circulations about the y-axis. We will refer to positive $\mathbf{\Psi} \cdot \hat{\jmath}$ as an "western sinking cell". This is in recognition of the existence of sinking to the west of upwelling for cells described by $\mathbf{\Psi} \cdot \hat{\jmath} > 0$. The description is not restricted to cells with sinking adjacent to the western boundary. Similarly, we will refer to positive $\mathbf{\Psi} \cdot \hat{\imath}$ as a "northern sinking cell". This terminology will also be adopted when examining the force functions and discussing the acceleration of a particular sense of overturning.

6.2.2 Momentum Closure

Before proceeding to examine the rotational momentum balance governing the modelled circulation, it is important to check that all momentum tendency terms, $\mathbf{F}$, have been correctly extracted from the model at the final timestep. As an example, all zonal momentum tendencies in the surface model layer are shown in figure 6.4. The dominant balance is between the Coriolis, pressure gradient and wind forcing (figures 6.4a-c), with a smaller contribution made by dissipation and inertia at the lateral boundaries and within the reentrant channel (figures 6.4d-e). The net forcing (figure 6.4f) almost exactly matches the computed velocity tendency (figure 6.4g).

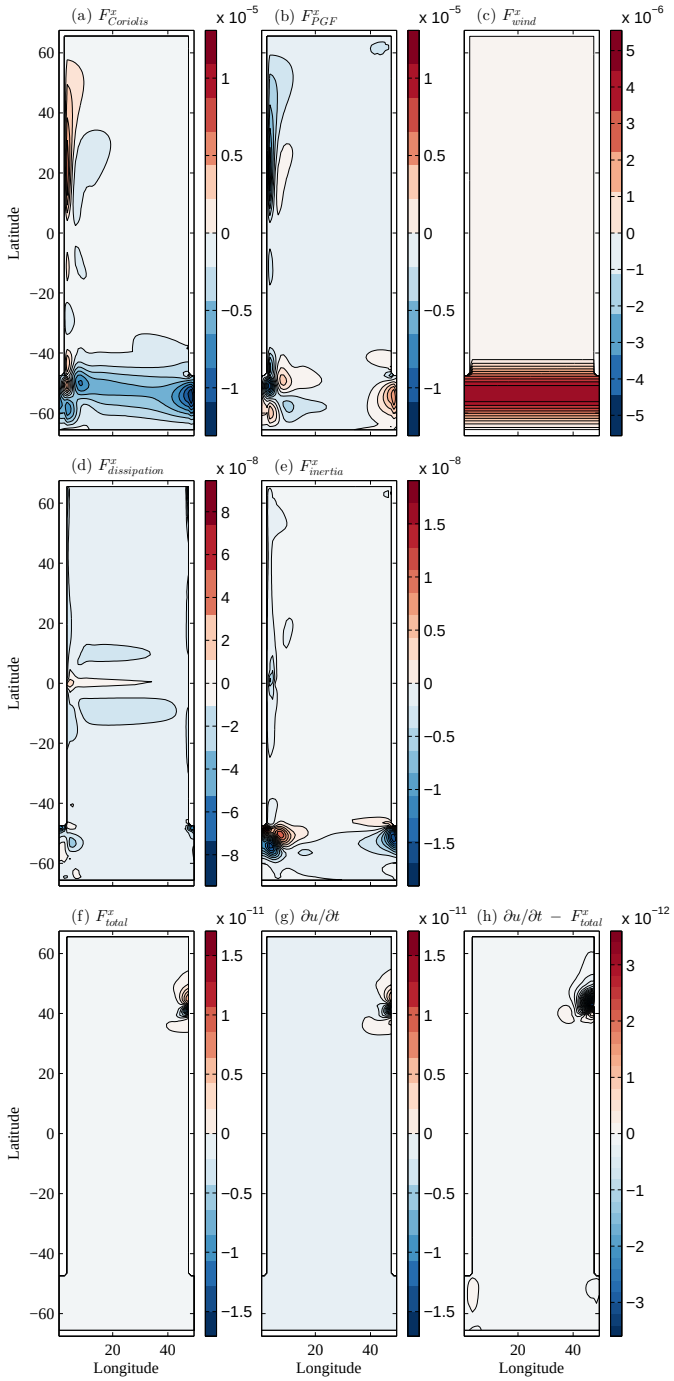

Figure 6.4: Instantaneous zonal momentum tendency (ms^{-2}) in the surface model layer at the end of the integration due to (a) Coriolis, (b) pressure gradient, (c) wind, (d) dissipation, and (e) inertial forcing. The net forcing, measured velocity tendency, and difference between the two are shown shown in panels (f), (g), and (h) respectively.

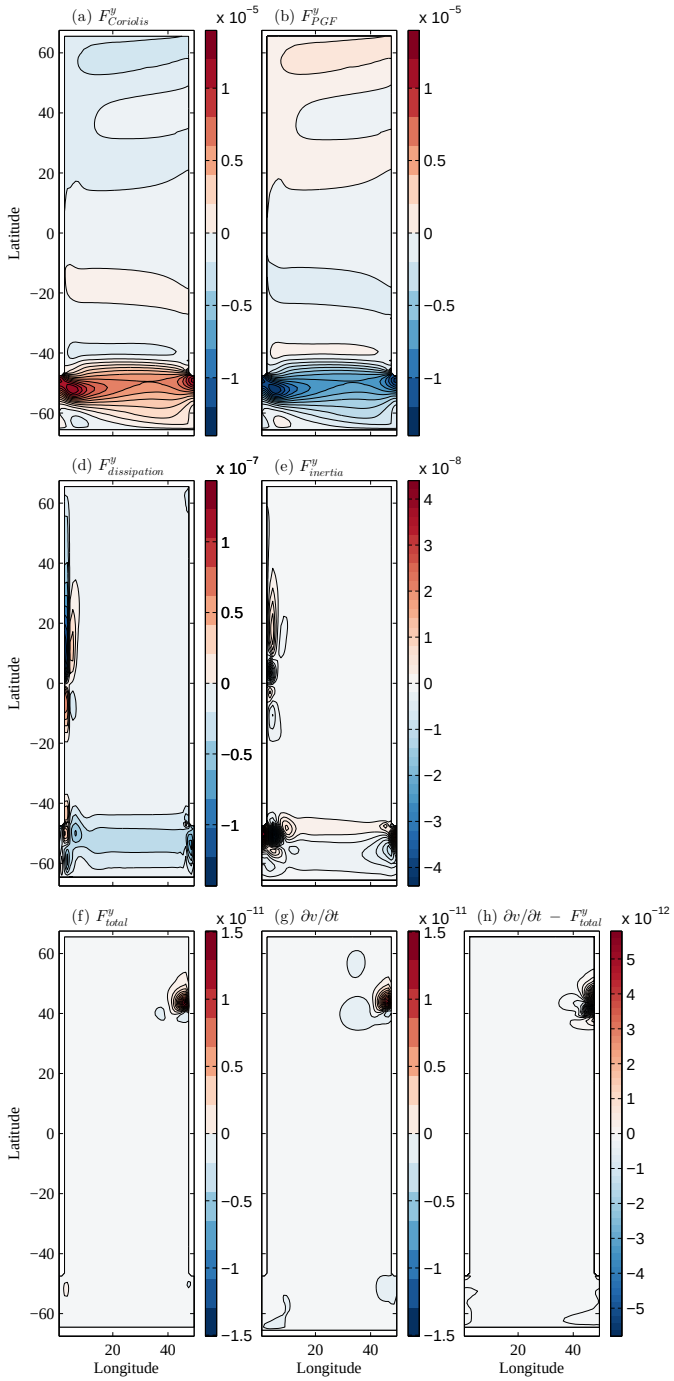

Figure 6.5: As for figure 6.4 but for the instantaneous meridional momentum tendency. Panel (c) is omitted as the wind forcing is identically zero.

The error in the calculation of the momentum tendencies (figure 6.4h) is an order of magnitude smaller than the modelled acceleration and can most likely be attributed

to the time-staggered nature of the Adams-Bashforth timestepping scheme (*Campin*, 2010). This is found to be true when the analysis is repeated for all remaining model layers and for the meridional momentum budget (shown for the surface layer in figure 6.5), providing reassurance that all full momentum forcings have been accurately computed. We are now ready to examine the instantaneous rotational momentum budget at the end of the model integration and expect rotational momentum closure if the components of the force function, $\mathbf{A}$, are computed accurately.

6.2.3 Analysed State

The Atlantic meridional overturning, Atlantic zonal overturning and barotropic streamfunctions (ψ_{AMOC}, ψ_{AZOC}, and ψ_{BT} respectively) in the final timestep of the model integration are shown in figures 6.6a, 6.7a and 6.8a respectively. The Eulerian acceleration of ψ_{AMOC}, ψ_{AZOC}, and ψ_{BT} is shown in figures 6.6b, 6.7b and 6.8b respectively.

Our primary interest is to elucidate the rotational momentum balance governing the modelled ψ_{AMOC}. We start by decomposing the full horizontal velocity field into vertical shears and external mode components of local overturning. Although our focus is on meridional overturning circulations ($\mathbf{\Psi} \cdot \hat{\imath}$), we also present solutions to zonal overturning circulations ($\mathbf{\Psi} \cdot \hat{\jmath}$) below. It will be shown that the zonal overturning is helpful in interpreting the generation of the meridional overturning.

6.2.4 Vertical Shear Modes

In figure 6.9 the MOC vertical shears component, Ψ^x_{OT}, is shown integrated across the width of one grid cell, at a selection of latitude-depth cross-sections through the basin. Significant vertical shear in the meridional velocity is concentrated within the vicinity of the western boundary. Consequently, Ψ^x_{OT} is found to be largest here (figures 6.9a-b), achieving a maximum amplitude at 3.5°E (figure 6.9b), just outside the viscous boundary layer. Here, a northern sinking cell extends from approximately 30°S to

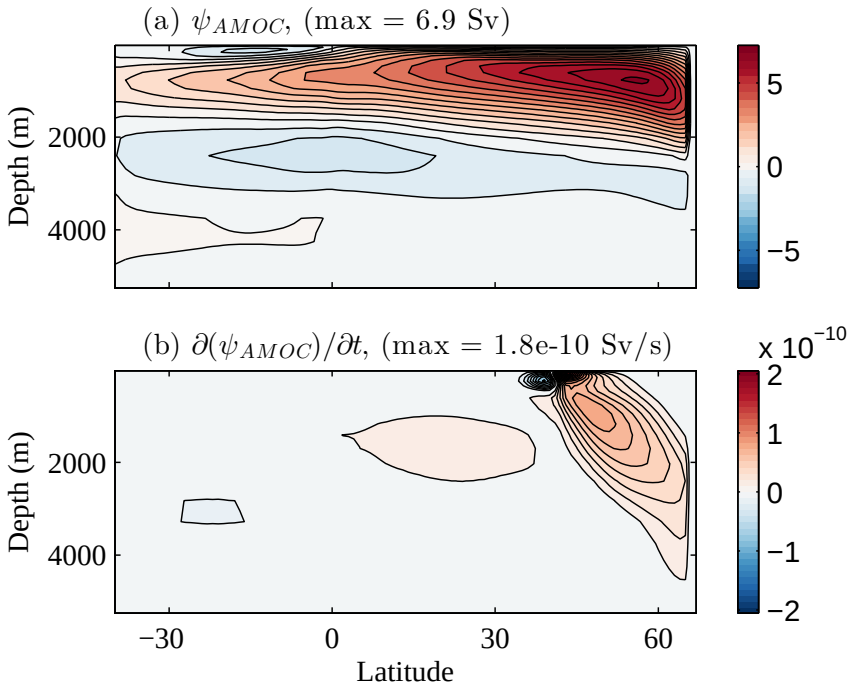

Figure 6.6: (a) AMOC streamfunction, ψ_{AMOC}, and (b) acceleration of the AMOC streamfunction, $\partial\psi_{\mathrm{AMOC}}/\partial t$, in the final timestep of the idealised model integration. The contour interval is 0.5 Sv in (a) and 1×10^{-11} Sv s^{-1} in (b). The 0 contour has been omitted. Positive values indicate sinking to the north.

60°N, achieving a maximum volume transport of 2.6 Sv. Near 40°N, Ψ^x_{OT} extends to a depth of 4 km. This is a signature of the western intensified return flow, emanating from the northern sinking region and moving southwards at depth. Moving towards the Equator, the northern sinking cell shoals and two counter-rotating cells emerge, straddling the Equator at 2 km depth, and near the surface at 10°S. In the reentrant channel, a southern sinking cell achieves a volume transport of 1.7 Sv and is flanked by a weaker counter-rotating cell to the north. Towards the basin interior (figures 6.9c-e), Ψ^x_{OT} decays rapidly everywhere and remains small on reaching the eastern boundary (figure 6.9f). The exception is in the reentrant channel, where an intense northern sinking cell achieves a volume transport of 1.0 Sv at 47.5°E, flanked by a

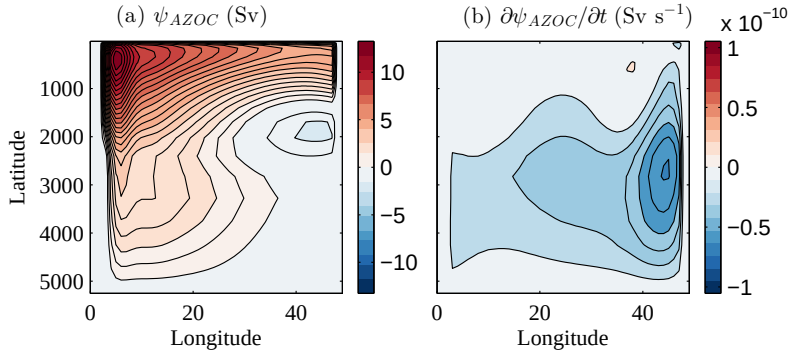

Figure 6.7: (a) AZOC streamfunction, ψ_{AZOC}, and (b) acceleration of the AZOC streamfunction, $\partial\psi_{\mathrm{AZOC}}/\partial t$, in the final timestep of the idealised model integration. This describes net zonal overturning north of the reentrant latitudes. The contour interval is 0.5 Sv in (a) and 1×10^{-11} Sv s^{-1} in (b). The 0 contour has been omitted. Positive values indicate sinking to the east.

weaker counter-rotating cell to the north.

In figure 6.10 the ZOC vertical shears component, Ψ^{y}_{OT}, is shown integrated across the length of a grid cell, at a selection of longitude-depth cross sections through the basin. At the northern margin (figure 6.10, upper left panel) the ZOC spans the basin width within the upper 1 km, with a narrow sinking region confined to the north-east corner of the basin. At 63.5°N, just south of the viscous boundary layer, the ZOC attains a maximum volume flux of 0.7 Sv. Moving southwards towards the Equator (figure 6.10, second row), the ZOC weakens and contracts into the upper-west corner of the longitude-depth section, where the largest vertical shear in the zonal velocity is concentrated. South of 30.5°N, a western sinking cell is a notable feature on the western boundary, positioned below the eastern sinking cell. Nearing the Equator, this cell contracts significantly to occupy only the surface layers. South of the Equator (figure 6.10, third row), the western sinking cell deepens and becomes eastern intensified. Within the reentrant channel (figure 6.10, bottom row) a strong ZOC associated with the modelled ACC spans the width of the basin. In the centre

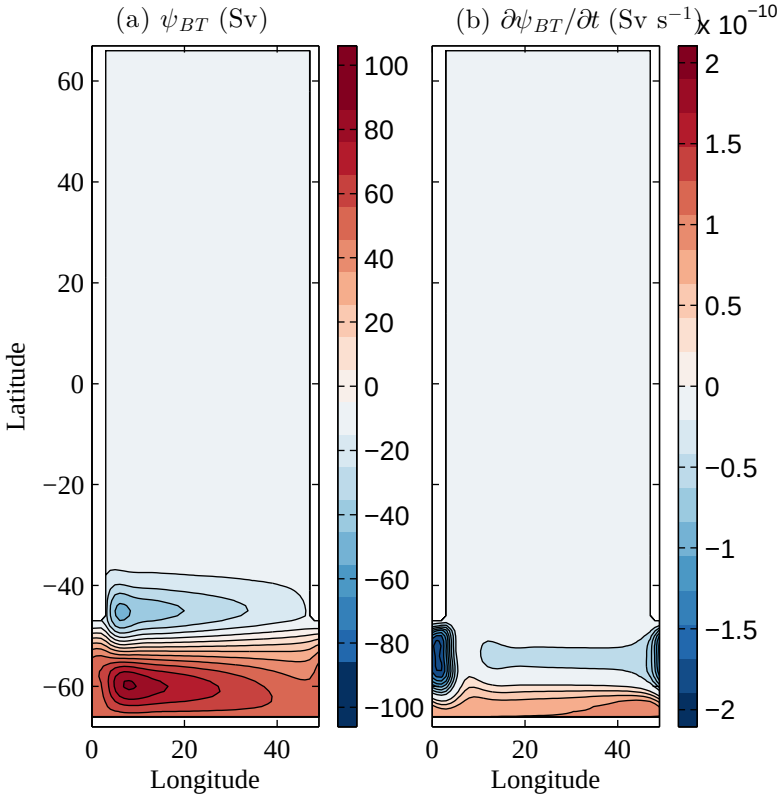

Figure 6.8: (a) Barotropic streamfunction, ψ_{BT}, and (b) acceleration of the barotropic streamfunction, $\partial\psi_{\mathrm{BT}}/\partial t$, in the final timestep of the idealised model integration. The contour interval is 10 Sv in (a) and 2×10^{-11} Sv s^{-1} in (b). The 0 contour has been omitted. Positive values indicate clockwise circulations looking down onto the $x-y$ plane.

of the channel (figure 6.10, bottom row, middle panel) the ZOC closes in a zonally periodic sense, and has two distinct maxima of 5.0 Sv immediately upstream and downstream of the sill.

6.2.5 External Modes

As the depth-integrated circulation (figure 6.8a) passes over the sill in the reentrant channel, an external mode of the MOC is generated. In figure 6.11 we plot the MOC external mode, $z/H\ \Psi_{\mathrm{BT}}\ \partial H/\partial x$, integrated across one grid cell in the two

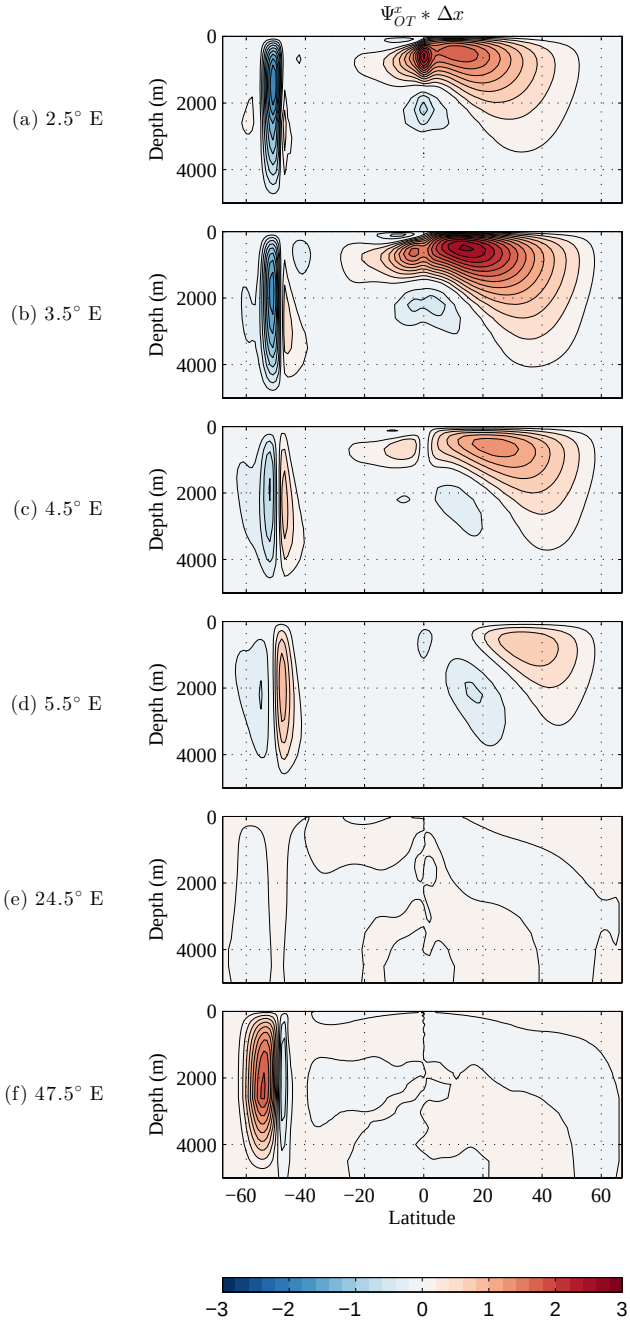

Figure 6.9: Zonal component of the vertical shears velocity potential, Ψ^x_{OT}, integrated across one grid cell width at the indicated longitudes. The upper (lower) panel shows the potential integrated across the cell adjacent to the western (eastern) boundary. The contour interval is 0.2 Sv for the top four panels and 0.1 Sv for the lower two panels. The 0 Sv contour has been omitted. Positive values indicate sinking to the north.

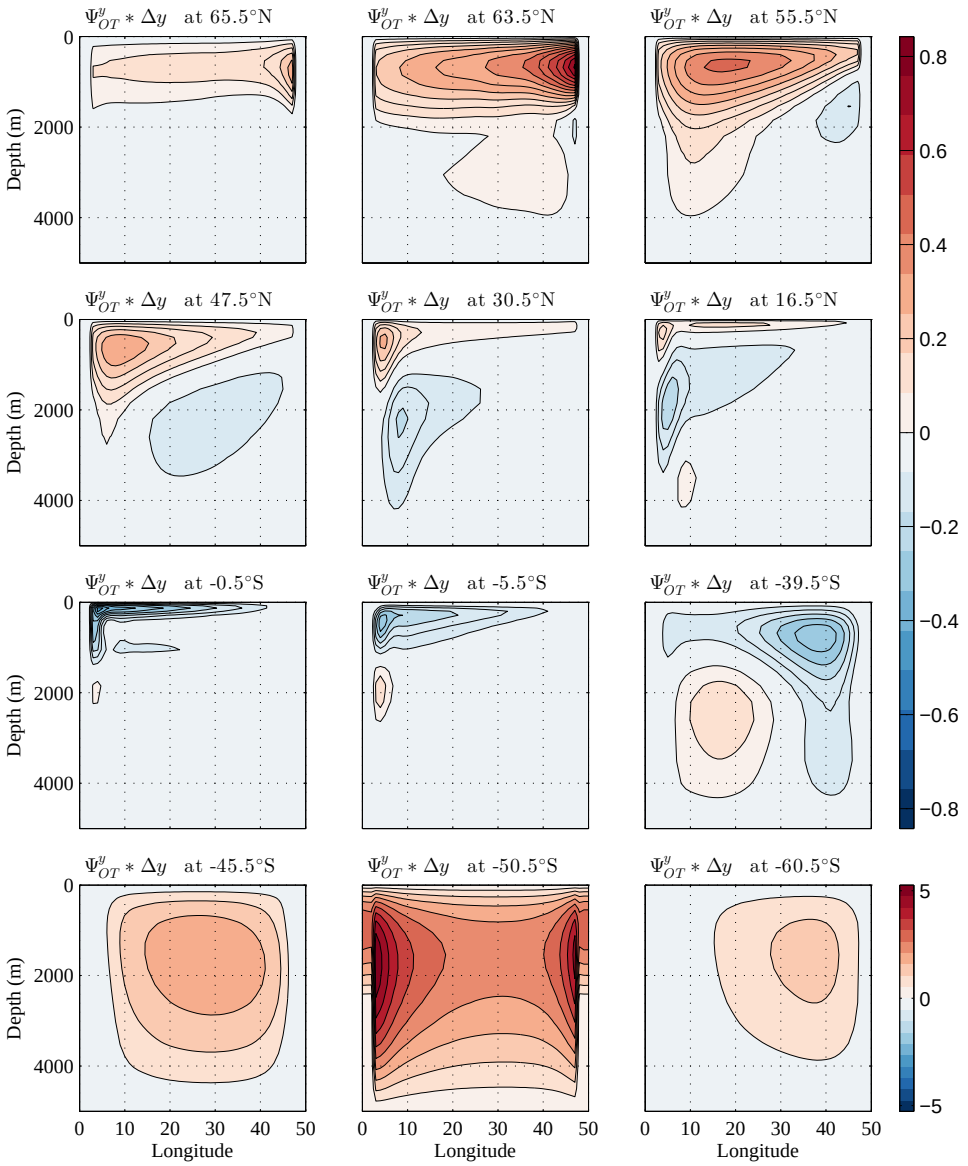

Figure 6.10: Meridional component of the vertical shears velocity potential, Ψ^y_{OT}, integrated across one grid cell length at the indicated latitudes. The top left (bottom) right panel shows the potential in the grid cell adjacent the northern (southern) boundary. The contour interval is 0.05 Sv in the upper three rows and 0.5 Sv in the bottom row. The 0 Sv contour has been omitted. Positive values indicate sinking to the east.

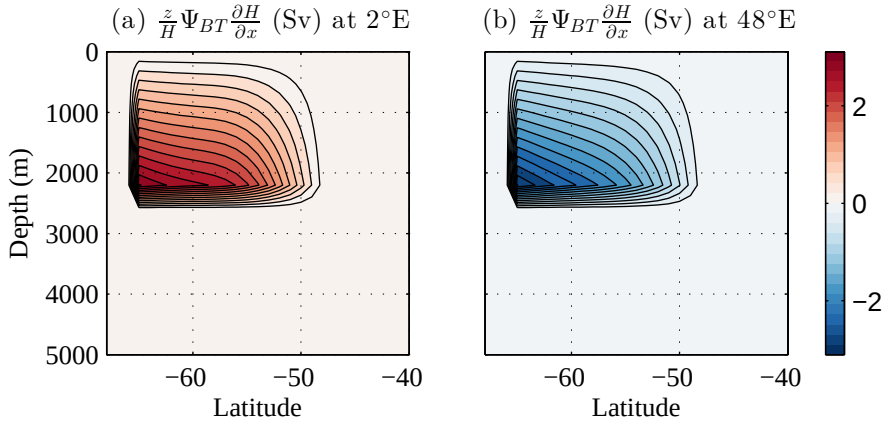

Figure 6.11: Zonal component of the external overturning mode, $z/H\ \Psi_{\mathrm{BT}}\ \partial H/\partial x$, integrated across one grid cell width at the longitudes adjacent to the sill. The contour interval is 0.2 Sv. The 0 Sv contour has been omitted. Positive values indicate sinking to the north.

latitude-depth planes on the eastern (figure 6.11a) and western (figure 6.11b) edge of the sill. These circulations are almost equal and opposite (combined there is a weak residual northern sinking MOC of 0.2 Sv). This is expected as $\partial H/\partial x$ at 48°E is simply the negative of $\partial H/\partial x$ at 2°W and since the sill spans only 4° of longitude, Ψ_{BT} is almost identical at the two locations.

Away from the sill, the bathymetry is uniform and the external mode is zero. The external mode does not project onto ψ_{AMOC}. Similarly, the absence of north-south variations in bathymetry ensure that an external mode cannot project onto the ZOC.

6.2.6 AMOC Summary

The vertical shears component of the velocity potential, $\mathbf{\Psi}_{\mathrm{OT}}$, fully describes the overturning circulation north of the reentrant channel. By integrating Ψ^x_{OT} across the full width of the basin, we recover ψ_{AMOC} (compare figures 6.6a and 6.12a). In figures 6.12b-d we divide the zonal integral into contributions from the basin interior and the viscous boundary layers. The boundary layer integrals are performed across

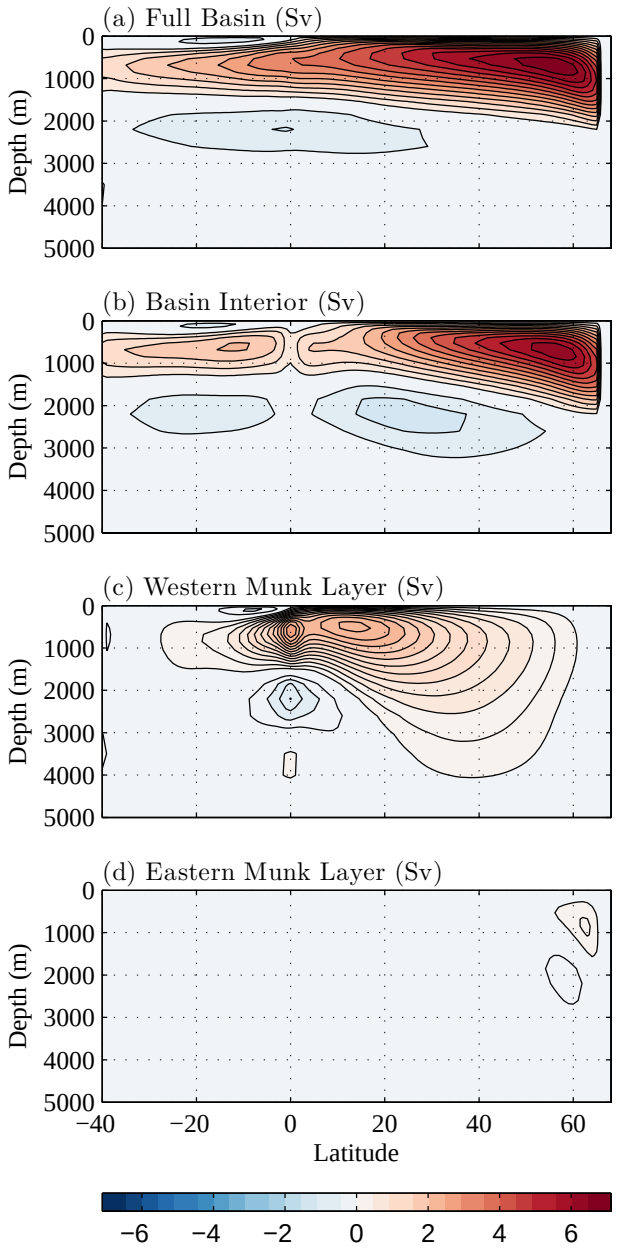

Figure 6.12: Zonal component of the vertical shears velocity potential, Ψ^x_{OT}, integrated across (a) the full basin width, (b) the basin interior, (c) the western boundary Munk layer, and (d) the eastern boundary Munk layer. The contour interval is 0.5 Sv for (a) and (b), and 0.2 Sv for (c) and (d). The 0 Sv contour has been omitted.

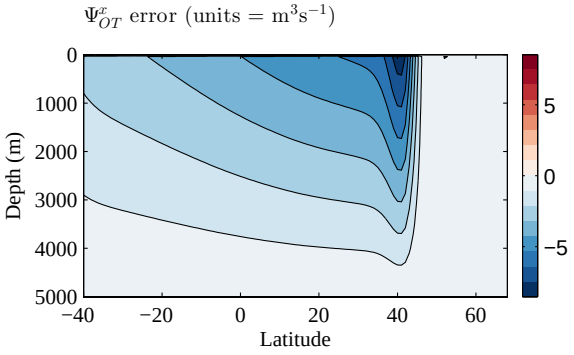

Figure 6.13: Error in Ψ^x_{OT}, computed as the difference between ψ_{AMOC}, and the basinwide integral of Ψ^x_{OT}. The contour interval is 1 m^{3}s^{-1}. We consider only the region north of the reentrant channel. Negative values indicate that Ψ^x_{OT} underestimates the northern sinking meridional overturning.

the full basin width, multiplying Ψ^x_{OT} by an exponential weighting function with a range of 0 to 1. For example, the western boundary layer contribution is computed as

$$\int_{x_w}^{x_w+\delta_M} \Psi^x_{\mathrm{OT}}\, dx = \int_{x_w}^{x_e} e^{-x/\delta_M}\, \Psi^x_{\mathrm{OT}}\, dx, \tag{6.7}$$

where x is the distance from the western boundary and, following *Munk* (1950), $\delta_M = \sqrt[3]{\nu_h/\beta}$ is the width of the viscous boundary layer. δ_M spans 2.5 grid cells at high latitudes and 0.7 grid cells at the Equator. Despite the narrow extent of the viscous boundary layers, the western boundary layer makes a significant contribution to the basin-wide northward volume flux at low latitudes. At high latitudes, ψ_{AMOC}, is mainly accomplished away from the boundaries by the interior velocity field.

To quantify the error in our calculation of the vertical shears velocity potential, the difference between ψ_{AMOC} and $\int \Psi^x_{\mathrm{OT}}\, dx$ is shown in figure 6.13. The maximum amplitude of the residual is -7.6 m^{3}s^{-1}, i.e $O(10^6)$ times smaller than ψ_{AMOC}. Spatial coherence in the error field suggests that improvements could be made to our discrete algorithms involved in the computation of Ψ^x_{OT}. For now, we accept the error as shown, noting that it makes a negligible difference to the total volume flux.

In this section, we have presented numerical solutions to the vertical shears, $\mathbf{\Psi}_{\mathrm{OT}}$, and external mode, $z/H\ \Psi_{\mathrm{BT}}\ \nabla_h H$, components of the velocity potential. By examining the scalar potentials, the three-dimensional circulation is easily visualised. We now demonstrate that an analysis of the corresponding scalar force functions makes a mechanistic interpretation of the three-dimensional circulation more tractable.

6.2.7 Generation of the AMOC and ZMOC

As described by the vertical shears rotational momentum equations (5.66) components of the vertical shears force function, $[\mathrm{A}^x_{\mathrm{OT}}, \mathrm{A}^y_{\mathrm{OT}}]$, project on to the local acceleration of the corresponding component of the vertical shears velocity potential, $[\Psi^x_{\mathrm{OT}}, \Psi^y_{\mathrm{OT}}]$. By solving for $[\mathrm{A}^x_{\mathrm{OT}},\ \mathrm{A}^y_{\mathrm{OT}}]$ associated with each and every force present, the processes setting the strength and structure of the three-dimensional circulation in the modelled Atlantic basin, mapped by $[\Psi^x_{\mathrm{OT}}, \Psi^y_{\mathrm{OT}}]$ in the previous section, and summarised by the 2-dimensional streamfunctions, ψ_{AMOC} and ψ_{ZMOC}, will be revealed.

Generation of MOC Vertical Shear Modes

We start by examining MOC generation by the zonal component of the vertical shears force function, $\mathrm{A}^x_{\mathrm{OT}}$. It is helpful to split our discussion to consider the main basin and the reentrant channel separately, since within the reentrant channel anomalously vigorous overturnings are found.

In figure 6.14, the zonal overturning force function, $\mathrm{A}^x_{\mathrm{OT}}$, integrated across one grid cell, is shown for the buoyancy and Coriolis forces at a selection of longitudes (identical to the selection in figure 6.9), for the region north of the reentrant channel. In the previous chapter, we showed analytically that $\mathrm{A}^x_{\mathrm{OT}}\Big|_{\mathrm{Coriolis}} \left(\mathrm{A}^x_{\mathrm{OT}}\Big|_{\mathrm{buoyancy}}\right)$ describes MOC generation via tilting of planetary vorticity, f, into the $y-z$ plane by vertical shear in the zonal (zonal geostrophic) velocity. A notable result in figure 6.14

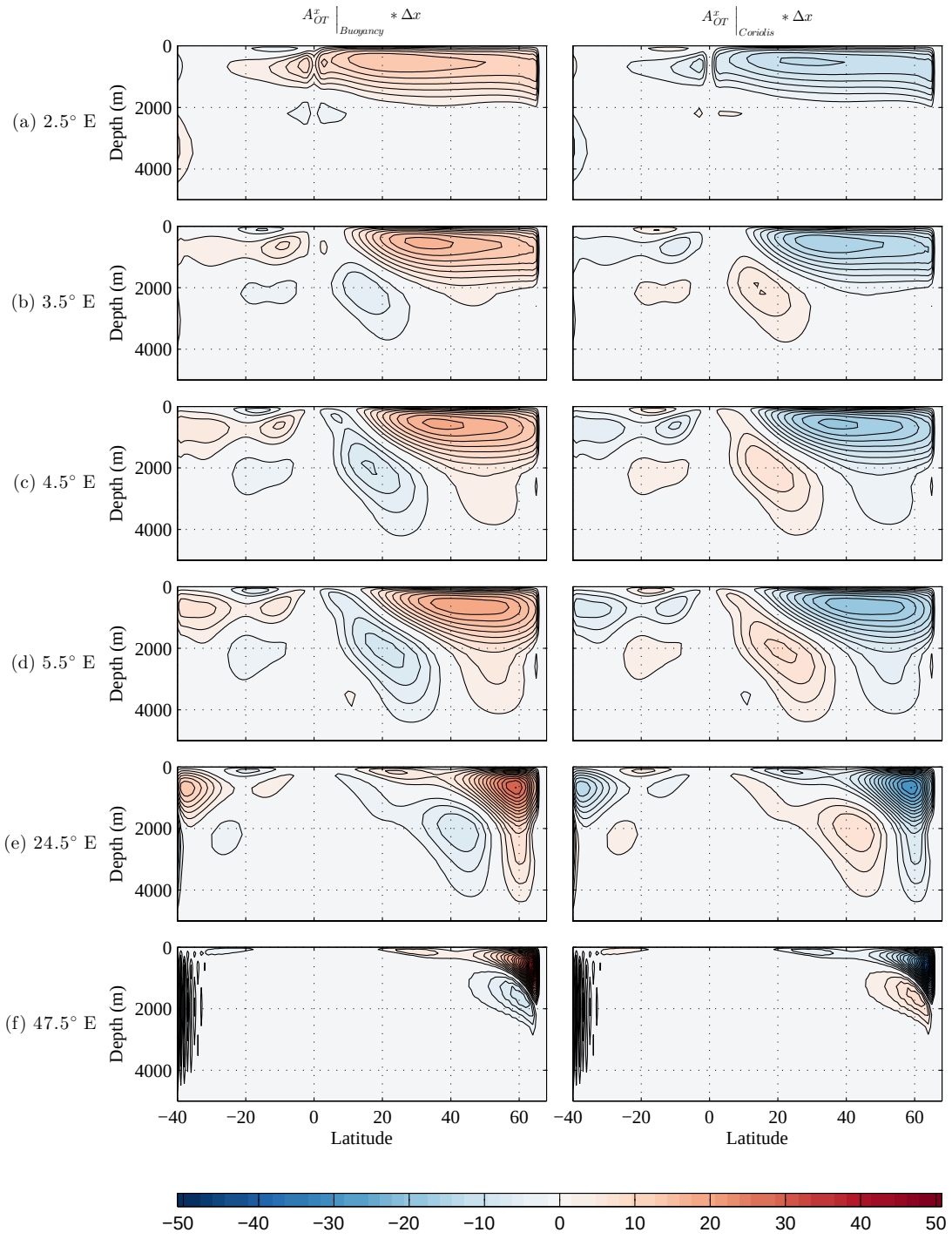

Figure 6.14: Zonal component of the overturning force function, A^x_{OT}, integrated across one grid cell width for buoyancy (left column) and Coriolis (right column) forces at the indicated longitudes. The contour interval is 2 m^3s^{-2}. The 0 m^3s^{-2} contour has been omitted. As for the corresponding component of the velocity potential, Ψ^x_{OT}, positive values indicate sinking to the north.

is that $\mathrm{A}^x_{\mathrm{OT}}\Big|_{\mathrm{Coriolis}}$ and $\mathrm{A}^x_{\mathrm{OT}}\Big|_{\mathrm{buoyancy}}$ are almost exactly equal and opposite throughout the domain, indicating pointwise thermal wind balance in the rotational momentum equation. Even within the western (figure 6.14, top row) and eastern (figure 6.14, bottom row) boundary layers, the force functions are comparable, indicating that the zonal velocity is approximately geostrophic here.

Adjacent to the western boundary (figure 6.14, top row), the rotational buoyancy force accelerates a MOC between the surface and a depth of 2 km, with sinking at the northern margin and upwelling between the Equator and 25°S. The interhemispheric nature of this cell suggests that the vertical shear in the zonal velocity changes sign with f at the Equator, as identified in the analysis of Ψ^y_{OT} (figure 6.10, compare the middle two rows). The qualitative similarity between this buoyancy-driven northern sinking cell and the basinwide streamfunction, ψ_{AMOC} (6.6a), is striking, and will be explored thoroughly in the next chapter.

Moving eastwards into the basin interior, the northern sinking cell driven by the rotational buoyancy force contracts into the Northern Hemisphere, intensifying towards the northern margin. A weaker, counter-rotating cell is established to the south, consistent with the structure of the ZOC presented in figure 6.10. On reaching the eastern boundary (figure 6.14f), the only remaining signature of a deep MOC is confined north of 45°N. This is in stark contrast with the buoyancy-driven overturning on the western boundary.

At all longitudes profiled in figure 6.14 - with the exception of the western boundary layer - a notable shoaling of the overturning cells is visible as the Equator is approached. As f diminishes towards the Equator, it becomes harder for deep meridional overturnings to be generated by the weak zonal abyssal currents. The MOC therefore contracts towards the surface layers where the only shear flows large enough to act on vanishingly small planetary vorticity are found.

Meridional overturnings driven by dissipation and inertia (figure 6.15) are signifi-

cantly smaller than those driven by the rotational Coriolis and buoyancy forces, and are confined to the viscous boundary layers. On the western boundary dissipation drives an interhemispheric MOC with upwelling to the north. The strong similarity between the shape of the rotational dissipative forcing and the (counter-rotating) overturning velocity potential, Ψ^x_{OT} (figure 6.9), at 2.5°E suggests that dissipation at the western boundary is predominantly achieved by bottom friction, which is parameterised as a linear drag mechanism, acting directly against the flow everywhere. On the eastern boundary, MOC generation by rotational dissipation is small and confined to the far northern corner of the basin. MOC generation by rotational inertia is an order of magnitude smaller than generation by rotational dissipation, and appears insignificant in the pointwise rotational momentum balance of the modelled MOC. However, it is interesting to note that - in contrast to all other rotational forces - MOC generation by inertia tends to be largest in the vicinity of the Equator. In section 5.3.2 we showed that overturnings driven by inertia depend upon the existence of relative vorticity. Consequently, rotational inertia may play a dominant role in achieving an Equatorial crossing of the northern sinking cell, as the rotational Coriolis and buoyancy forces vanish with f, and rotational dissipation acts to oppose the flow.

In steady state, the residual between the rotational Coriolis and buoyancy forces (figure 6.16, left column) must balance the MOC driven by rotational inertia and dissipation combined (figure 6.15), north of the reentrant channel. The residual $\mathrm{A}^x_{\mathrm{OT}}$ is shown in figure 6.16 (right column). Net acceleration is $O(1 \times 10^{-5}\ \mathrm{m^3\ s^{-2}})$ in the vicinity of the lateral boundaries, achieving a maximum in the north-east corner of the basin. In the interior, the net acceleration is small. In figure 6.17 we quantify the error in our calculation of $\mathrm{A}^x_{\mathrm{OT}}$, by differencing the basinwide integral of the residual $\mathrm{A}^x_{\mathrm{OT}}$ (figure 6.17a) from the Eulerian acceleration of ψ_{AMOC} (figure 6.17b). The error (figure 6.17c) is small everywhere except adjacent to the northern margin

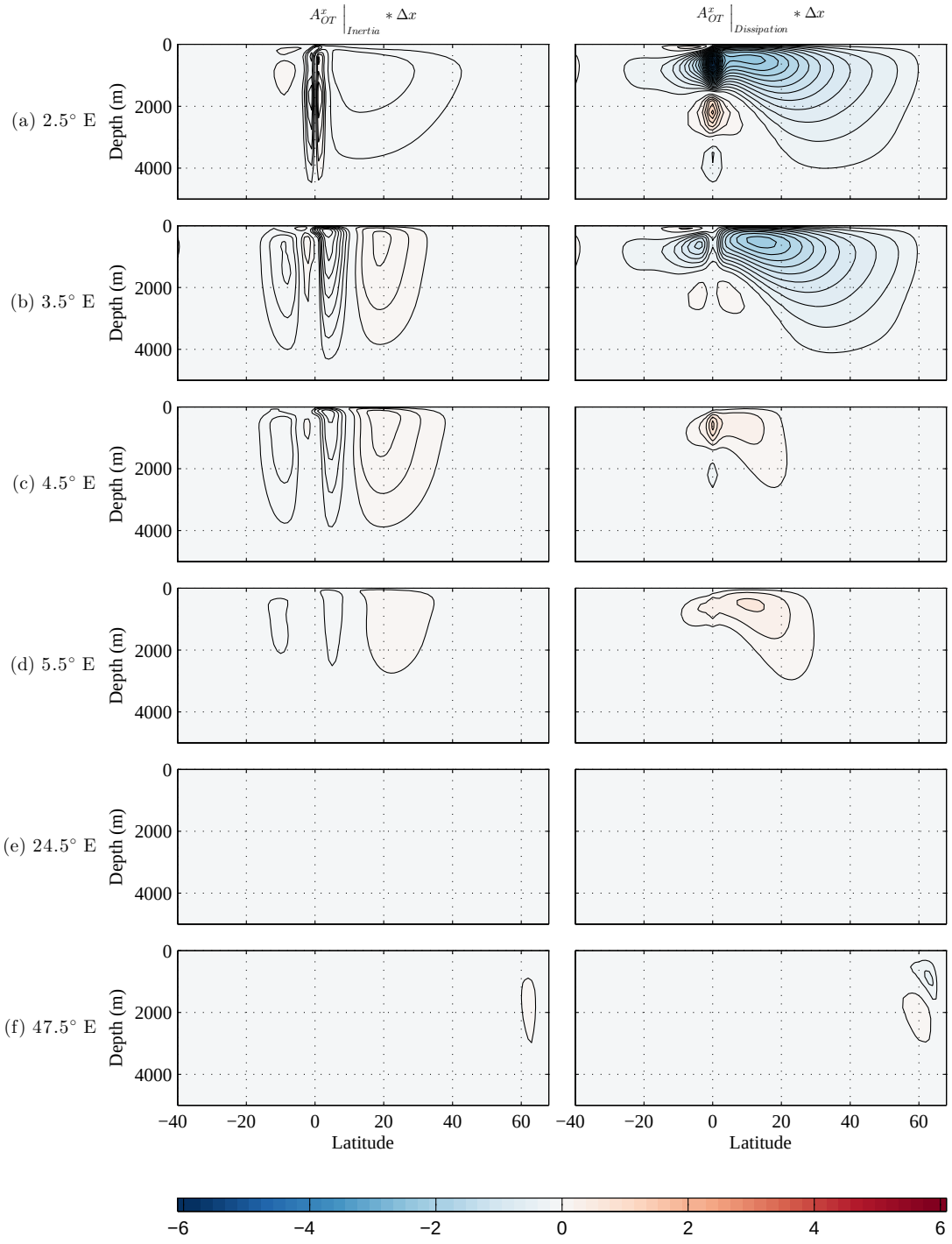

Figure 6.15: As for figure 6.14 but for inertial (left column) and dissipation (right column) forces at the indicated longitudes. The contour interval is 0.2 m^3s^{-2} for dissipation and 0.02 m^3s^{-2} for inertia. The 0 m^3s^{-2} contour has been omitted.

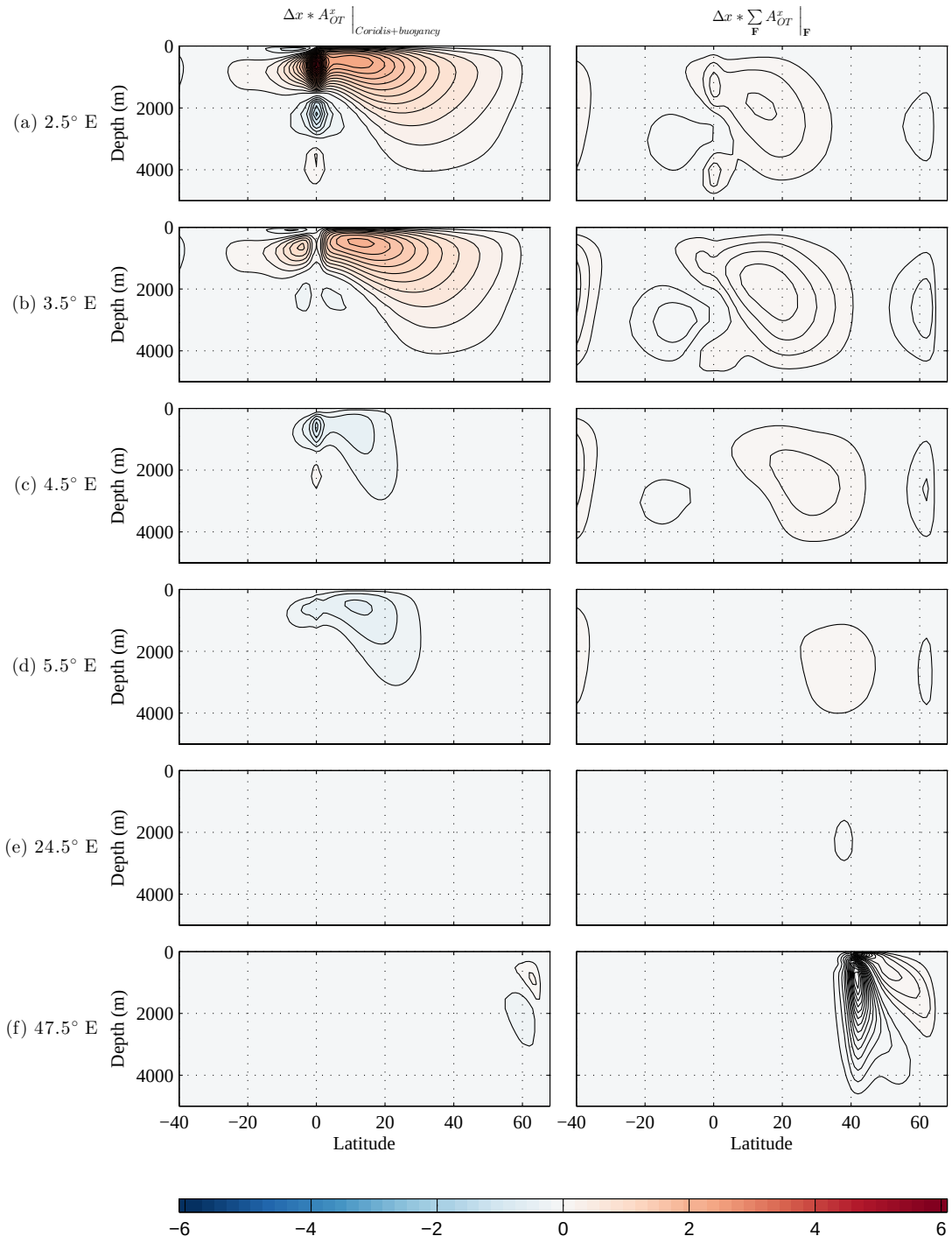

Figure 6.16: As for figure 6.14 but for Coriolis and buoyancy forces combined (left column) and for Coriolis, buoyancy, inertial and dissipation forces combined (right column) at the indicated longitudes. The contour interval is 0.2 m^3s^{-2} for the left column and $1e^{-6}$ m^3s^{-2} for the right column. The 0 m^3s^{-2} contour has been omitted.

and within a few degrees of 40°N. Here, we recall that a small residual was detected in the full meridional momentum budget (figure 6.5h), most likely attributable to the multistep Adams-Bashforth timestepping algorithm. To determine whether the incomplete closure in the rotational momentum budget can be explained by the residual in the full momentum budget,

$$F^y\Big|_{\text{AB-residual}} = \frac{\partial v}{\partial t} - \sum F^y, \tag{6.8}$$

we compute $\mathrm{A}^x_{\mathrm{OT}}$ associated with $F^y\Big|_{\text{AB-residual}}$. The result, $\mathrm{A}^x_{\mathrm{OT}}\Big|_{\text{AB-residual}}$, is consistent with the evaluated error in $\mathrm{A}^x_{\mathrm{OT}}$ (compare figures 6.17c and 6.18a). If we correct the sum of all force functions to include $\mathrm{A}^x_{\mathrm{OT}}\Big|_{\text{AB-residual}}$ (figure 6.18b), the new error is $O(10^2)$ smaller than the local tendency of ψ_{AMOC} (figure 6.18c). Furthermore, the new error compares qualitatively to the error in Ψ^x_{OT} (figure 6.13).

Finally, we briefly repeat the analysis presented above for the latitudes spanned by the reentrant channel. Here, the rotational buoyancy force drives a vigorous southern sinking cell, opposed by an almost equal and opposite forcing from rotational Coriolis (figure 6.19, first and second columns). Due to the extreme strength of the wind-driven zonal jet in the reentrant channel, the tendency of the meridional volume flux associated with these terms is an order of magnitude larger than that in the zonally-bounded basin to the north. However, the purely zonal winds (generating a meridional Ekman velocity) cannot directly project onto the vertical shears component of the MOC (which requires a nonzero zonal Ekman velocity). Ageostrophic generation of the MOC by rotational dissipation and inertia is confined to the boundary layers (figure 6.19, third and fourth columns). As for the region north of the channel, the residual between the Coriolis and buoyancy driven overturnings is balanced by an almost equal and opposite MOC tendency forced by dissipation and inertia combined (figure 6.20). The net MOC tendency inferred from

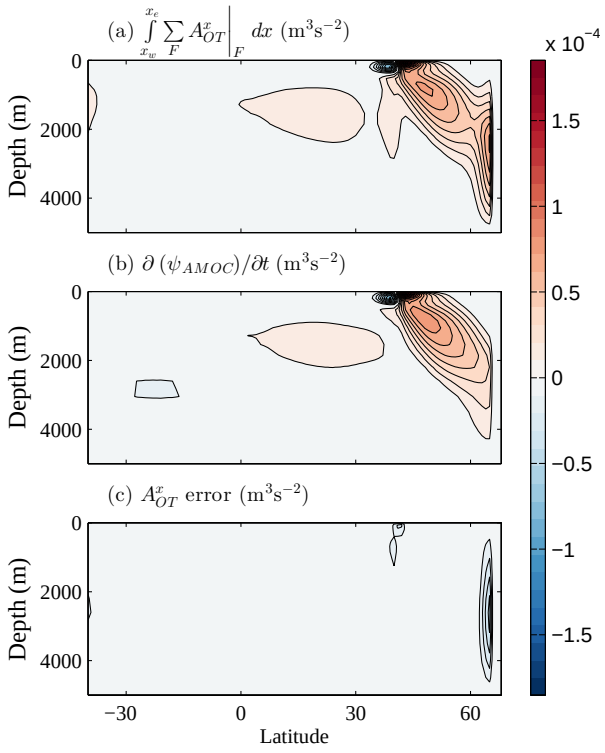

Figure 6.17: By subtracting (a) the basinwide integral of the residual $\mathrm{A}^x_{\mathrm{OT}}$ from (b) the net acceleration of ψ_{AMOC} we quantify (c) the error in our calculation of $\mathrm{A}^x_{\mathrm{OT}}$. The contour interval is $1{\times}10^{-5}$ m^3 s^{-1}. The 0 m^3 s^{-1} contour has been omitted.

the residual force function in the reentrant channel is $O(1e^{-5}$ m^3 s$^{-2})$. As above, this is in agreement with the modelled MOC tendency in the channel when adjusted to incorporate $\mathrm{A}^x_{\mathrm{OT}}\Big|_{\text{AB-residual}}$ (not shown).

Generation of ZOC Vertical Shear Modes

We now examine ZOC generation by the meridional component of the vertical shears force function, $\mathrm{A}^y_{\mathrm{OT}}$. In figures 6.21 and 6.22 $\mathrm{A}^y_{\mathrm{OT}}$, integrated along one grid cell, is shown for buoyancy and Coriolis forces respectively, at a selection of latitudes (identical to the selection in figure 6.10). In the previous chapter (section 5.3.1), we showed that $\mathrm{A}^y_{\mathrm{OT}}\Big|_{\text{Coriolis}}$ $\left(\mathrm{A}^y_{\mathrm{OT}}\Big|_{\text{buoyancy}}\right)$ describes ZOC generation via tilting of the planetary vorticity, f, into the $x-z$ plane by vertical shear in the meridional

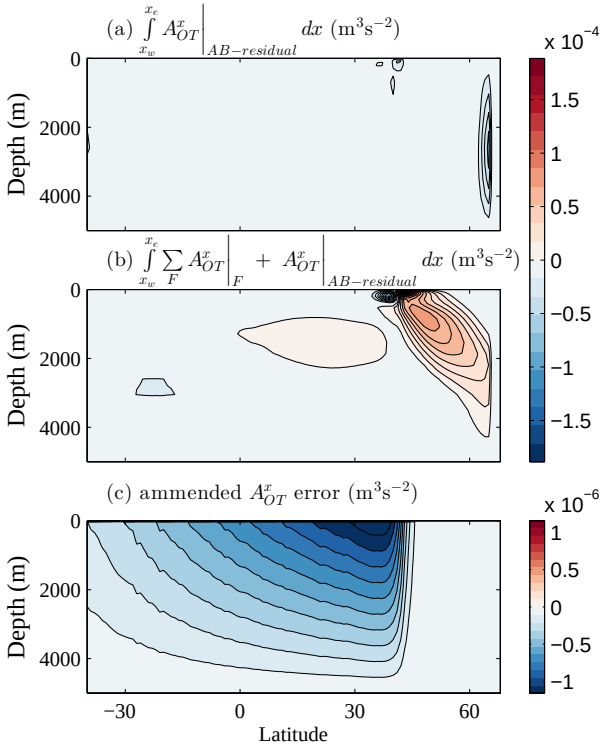

Figure 6.18: The apparent error in our computation of $\mathrm{A}^x_{\mathrm{OT}}$ (figure 6.17) can be explained by the incomplete closure of the full momentum equation. By computing (a) the zonal integral of the force function associated with $F^y\Big|_{\text{AB-residual}}$, and (b) adding it to the total force function associated with all properly resolved terms, the tendency in ψ_{AMOC} (figure 6.17b) is almost exactly recovered. (c) The ammended error is computed as the adjusted force funcion in (b) differenced from the tendency of ψ_{AMOC}. The contour interval is $1{\times}10^{-5}$ m^3 s^{-1} in (a) and (b), and $1{\times}10^{-7}$ m^3 s^{-1} in (c). The 0 m^3 s^{-1} contour has been omitted.

velocity (meridional geostrophic velocity). A notable result in figures 6.21 and 6.22 is that $\mathrm{A}^y_{\mathrm{OT}}\Big|_{\text{Coriolis}}$ and $\mathrm{A}^y_{\mathrm{OT}}\Big|_{\text{buoyancy}}$ are almost exactly equal and opposite north of the reentrant latitude band. The structure of both force functions here can be understood by examining Ψ^x_{OT} in figure 6.9.

In the vicinity of the northern margin, the rotational buoyancy force drives a western sinking ZOC (figure 6.21, top row), which is qualitatively comparable to the overturning velocity potential here (figure 6.10), but rotating in the opposite sense.

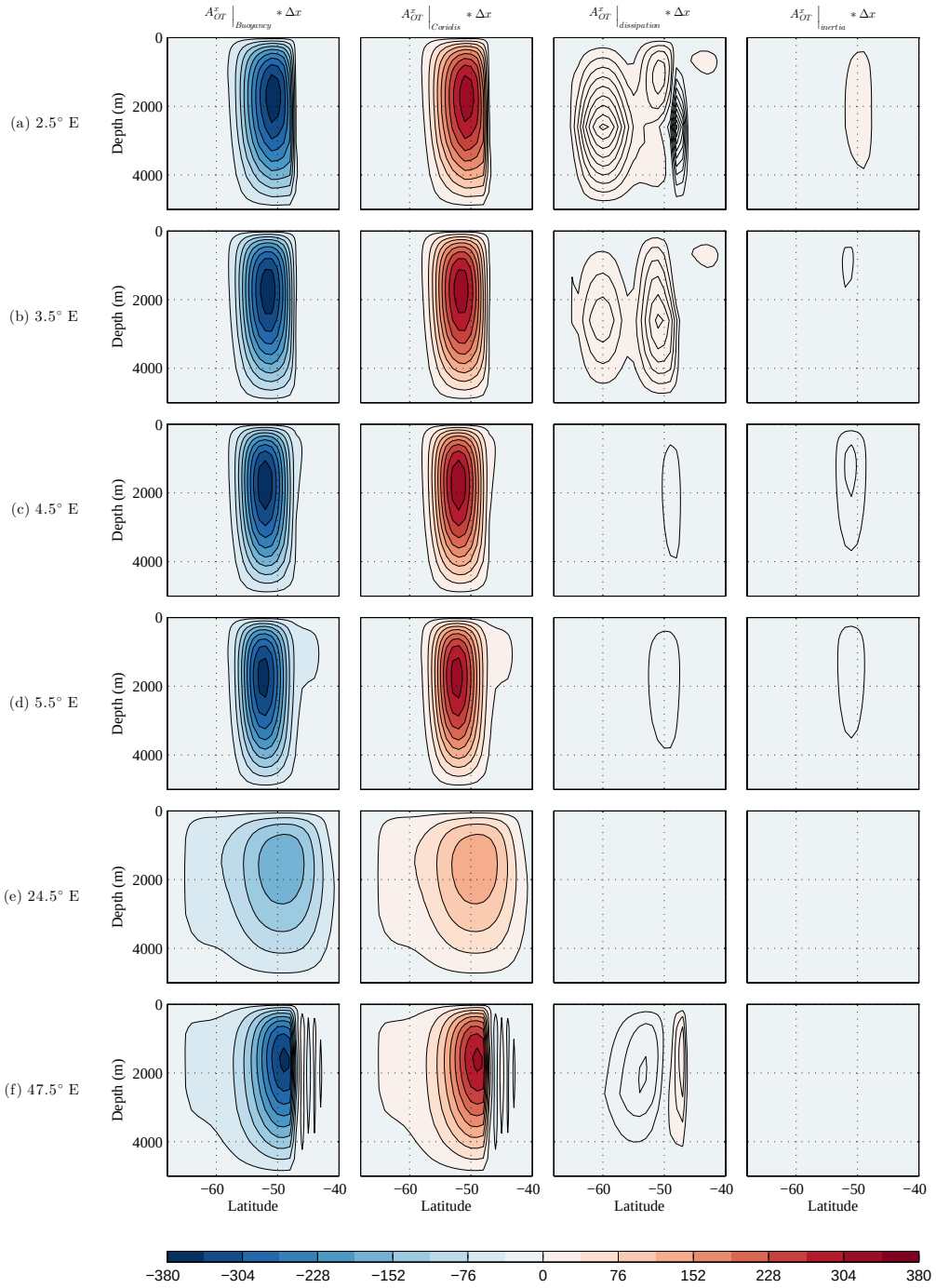

Figure 6.19: As for figure 6.14 but for buoyancy, Coriolis, dissipation and inertial forces (left to right columns) in the reentrant channel, at the indicated longitudes. The contour interval is 40 m^3s^{-2} for Coriolis and buoyancy, 0.2 m^3s^{-2} for dissipation and 0.02 m^3s^{-2} for inertia. The 0 m^3s^{-2} contour has been omitted.

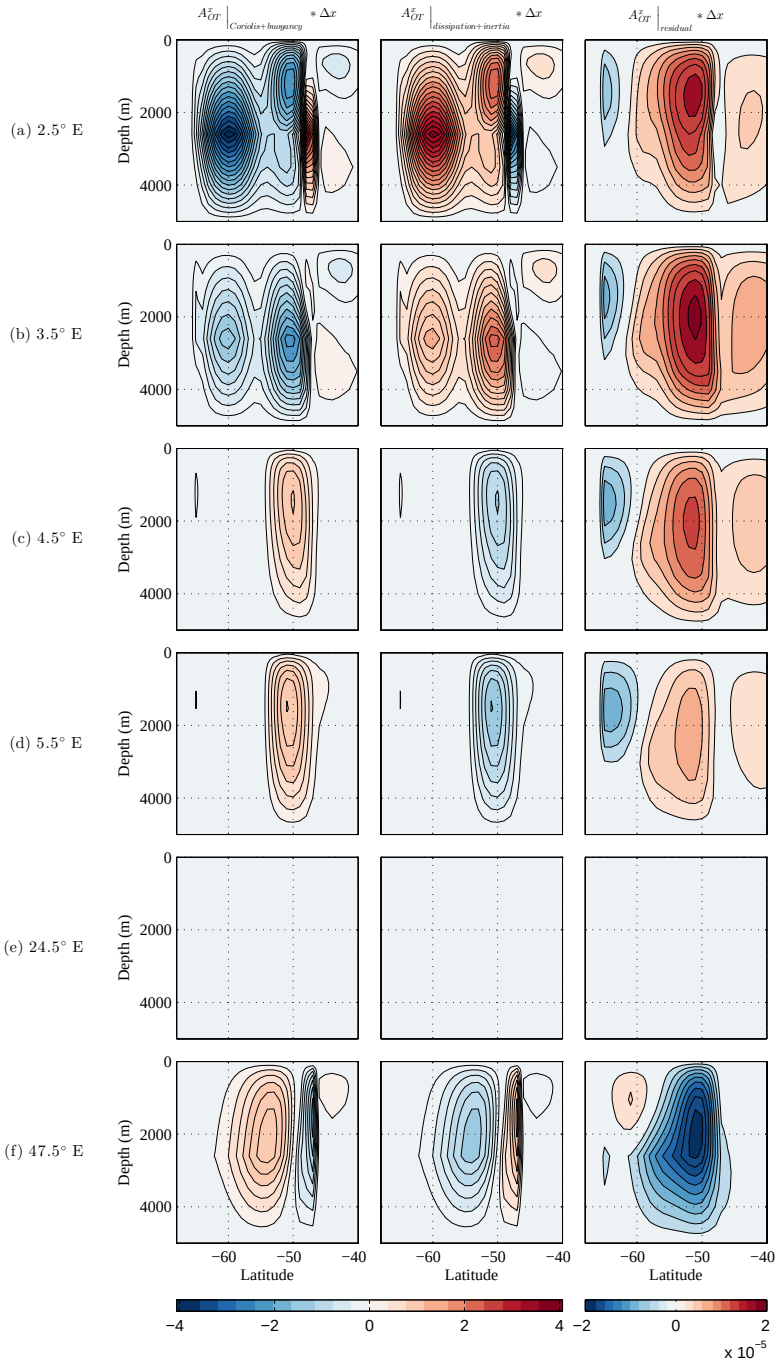

Figure 6.20: As for figure 6.14 but for Coriolis and buoyancy forces combined (left column), inertia and dissipation combined (middle column) and Coriolis, buoyancy, inertial and dissipation forces all combined (right column) at the indicated longitudes. The contour interval is 0.2 m^3s^{-2} for the left and middle column and $2e^{-6}$ m^3s^{-2} for the right column. The 0 m^3s^{-2} contour has been omitted.

Moving towards the Equator, (figure 6.21, top two rows), a counter-rotating cell is established at greater depths, where the vertical shear in the meridional velocity reverses (see Ψ^x_{OT} in figure 6.9). As f diminishes, both cells contract towards the western boundary, where the largest shear in the meridional velocity is found.

Even in the vicinity of the boundary jets, cancellation between the ZOC driven by the Coriolis and buoyancy forces is almost exact. In the vorticity framework, the maintenance of density gradients by the thermal wind is viewed as a balance between baroclinic vorticity production - acting to slump density surfaces - and counter-production by tilting of planetary vorticity by the geostrophic flow (e.g *Pedlosky*, 1987). In the rotational momentum framework, we see here that examination of the force functions provides an entirely complementary view of the large scale dynamics and allows us to clearly visualise how the boundary current system remains propped up against the western margin.

At the Equator, the ZOC driven by the rotational Coriolis and buoyancy forces vanishes (figures 6.21-6.22, third row). Within the reentrant channel the rotational forcing is twice as strong as in the basin to the north, due to the presence of wind forcing. At all reentrant latitudes, two counter rotating cells straddle the sill, caused by the reversal of the local MOC across the step change in bathymetry (see Ψ^x_{OT} in figure 6.9).

Within the reentrant channel (figures 6.21 and 6.22, bottom rows), there are notable deviations from pointwise thermal wind balance in the rotational momentum equation. In the absence of zonal barriers, a zonal pressure gradient cannot be sustained, and the meridional velocity is not in geostrophic balance above the sill. This affects the vertical shear in the geostophic velocity field throughout the water column. Differences between $\mathrm{A}^y_{\mathrm{OT}}\Big|_{\mathrm{buoyancy}}$ and $\mathrm{A}^y_{\mathrm{OT}}\Big|_{\mathrm{Coriolis}}$ extend from the surface to depth.

The ZOC driven by the wind field is confined to the reentrant channel. In section

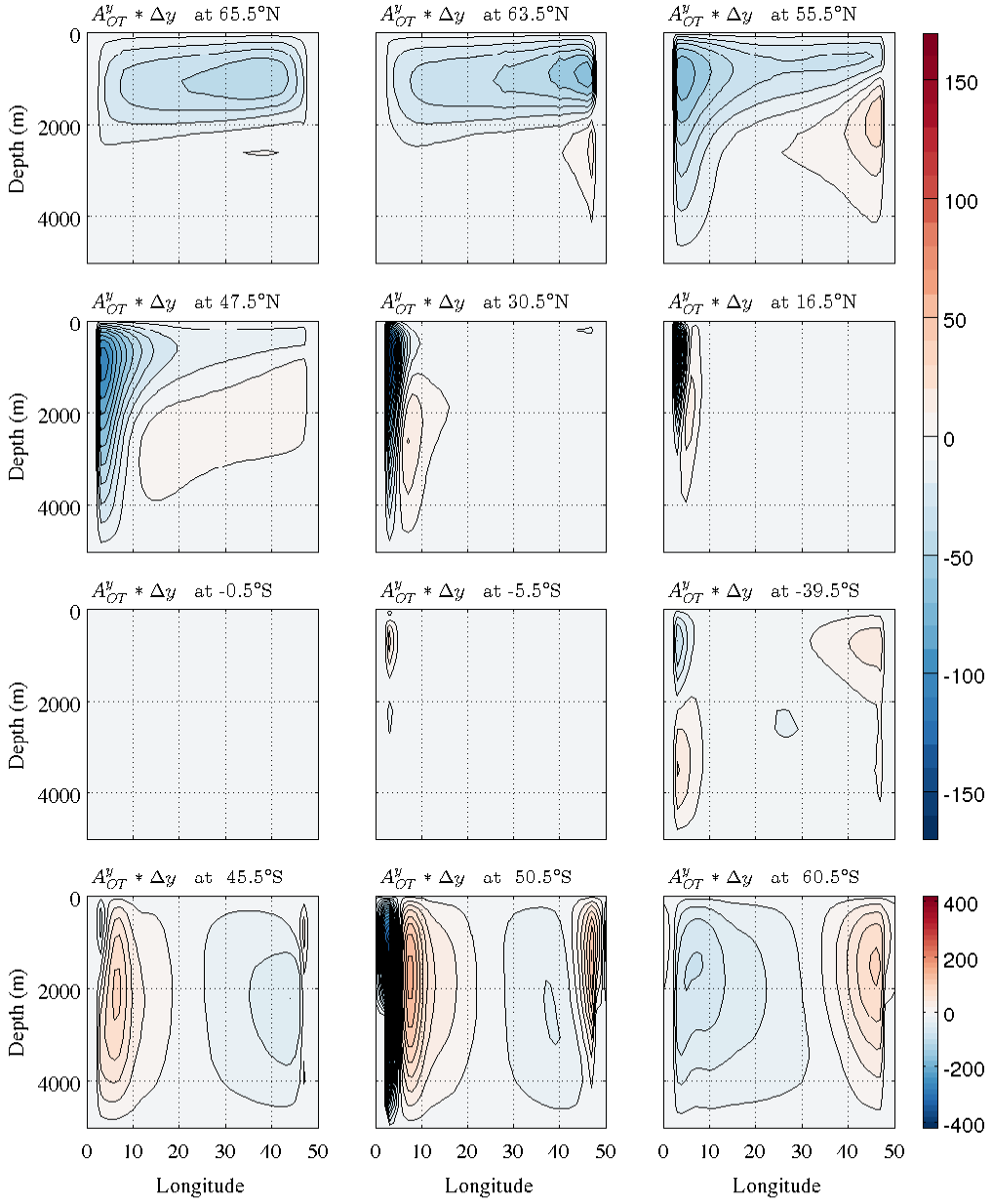

Figure 6.21: As for figure 6.10 but for the meridional component of the overturning force function, A^y_{OT}, associated with the buoyancy force. The contour interval is 10 m^3s^{-2} north of the reentrant channel (upper three rows) and 20 m^3s^{-2} within the reentrant channel (bottom panel). The 0 m^3s^{-2} contour has been omitted.

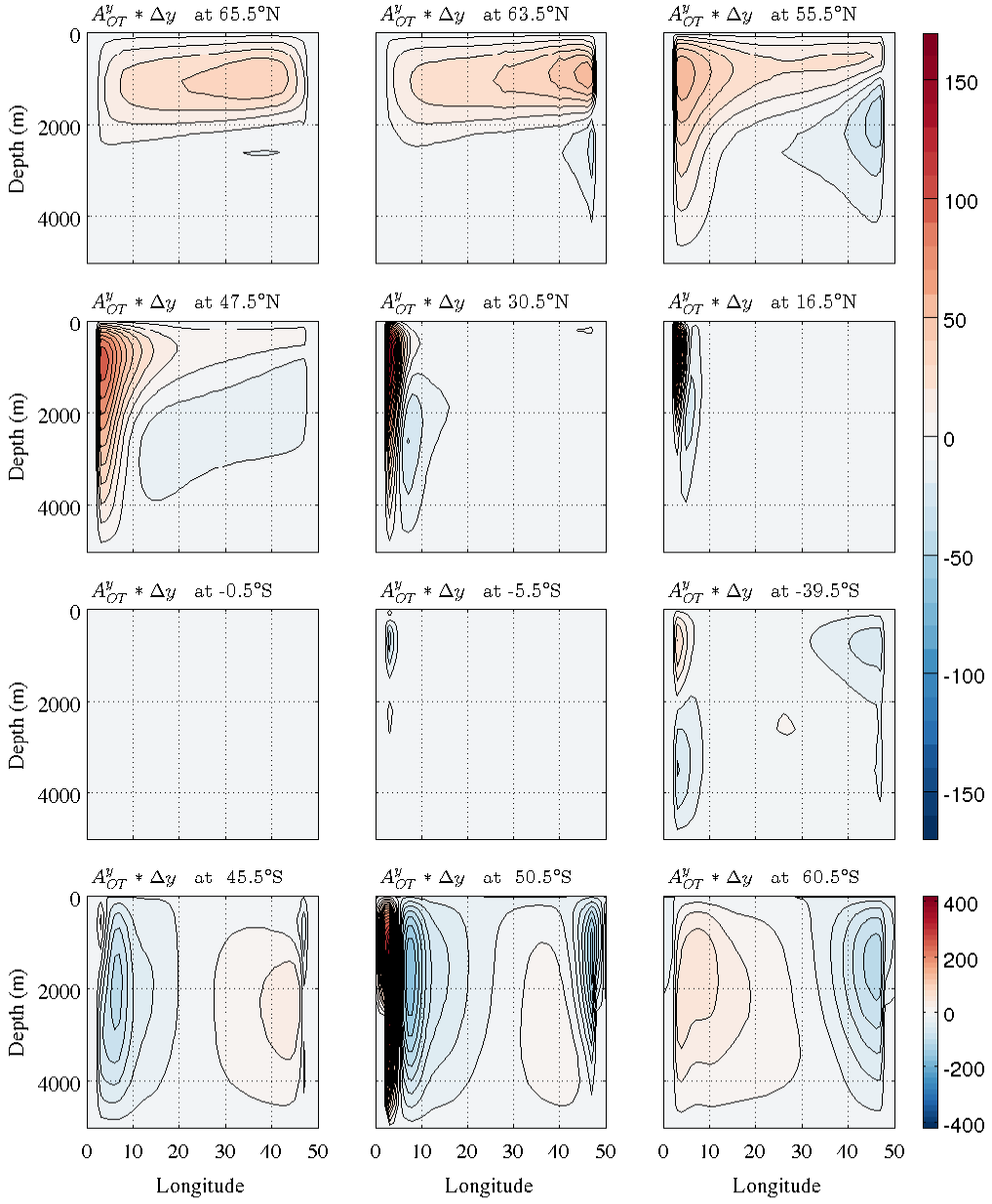

Figure 6.22: As for figure 6.10 but for the meridional component of the overturning force function, A^y_{OT}, associated with the Coriolis force. The contour interval is 10 m^3s^{-2} north of the reentrant channel (upper three rows) and 20 m^3s^{-2} within the reentrant channel (bottom panel). The 0 m^3s^{-2} contour has been omitted.

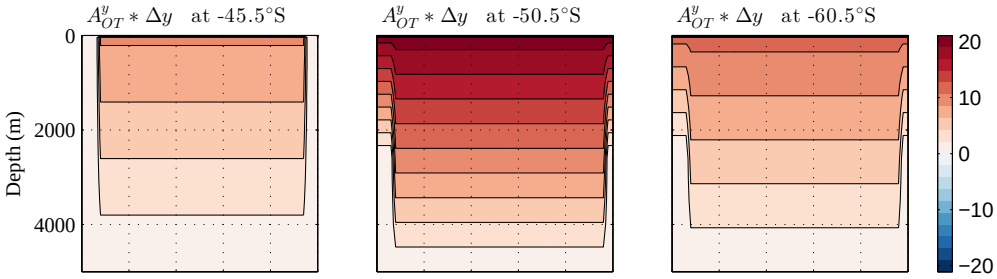

Figure 6.23: As for figure 6.10 but for $\mathrm{A}^y_{\mathrm{OT}}\Big|_{\mathrm{wind}}$, and showing only the selection of reentrant latitudes (elsewhere $\mathrm{A}^y_{\mathrm{OT}}\Big|_{\mathrm{wind}} = 0$). The contour interval is 2 $\mathrm{m}^3\mathrm{s}^{-2}$. The 0 $\mathrm{m}^3\mathrm{s}^{-2}$ contour has been omitted.

5.3.2, we showed that ZOC generation by the wind is described in part by tilting of f into the $x - z$ plane by vertical shear in the meridional Ekman velocity. This produces a positive ZOC, which is closed in a zonally-reentrant sense. It is perhaps inappropriate to diagnose a ZOC here, but it is shown for completeness in figure 6.23.

Zonal overturnings driven by dissipation and inertia (figure 6.24-6.25) are 2-3 orders of magnitude smaller than those driven by rotational Coriolis and buoyancy forces and are confined to the viscous boundary layers and the interior reentrant latitudes. Combined, they almost cancel the net ZOC driven by rotational Coriolis, buoyancy and wind forces combined. The residual $\mathrm{A}^y_{\mathrm{OT}}$ is shown in figure 6.26. As for the MOC, the inferred net acceleration of the ZOC is $O(1 \times 10^{-5})$ $\mathrm{m}^3\mathrm{s}^{-1}$ in the vicinity of the boundaries. The net acceleration is also large in the reentrant latitude band. The maximum is found in the north-east corner of the basin, again indicating that the virtual forcing from the Adams-Bashforth timestepping algorithm should be incorporated into the rotational momentum analysis.

In analogy to our correction for $\mathrm{A}^x_{\mathrm{OT}}$, we compare the meridional integral of the

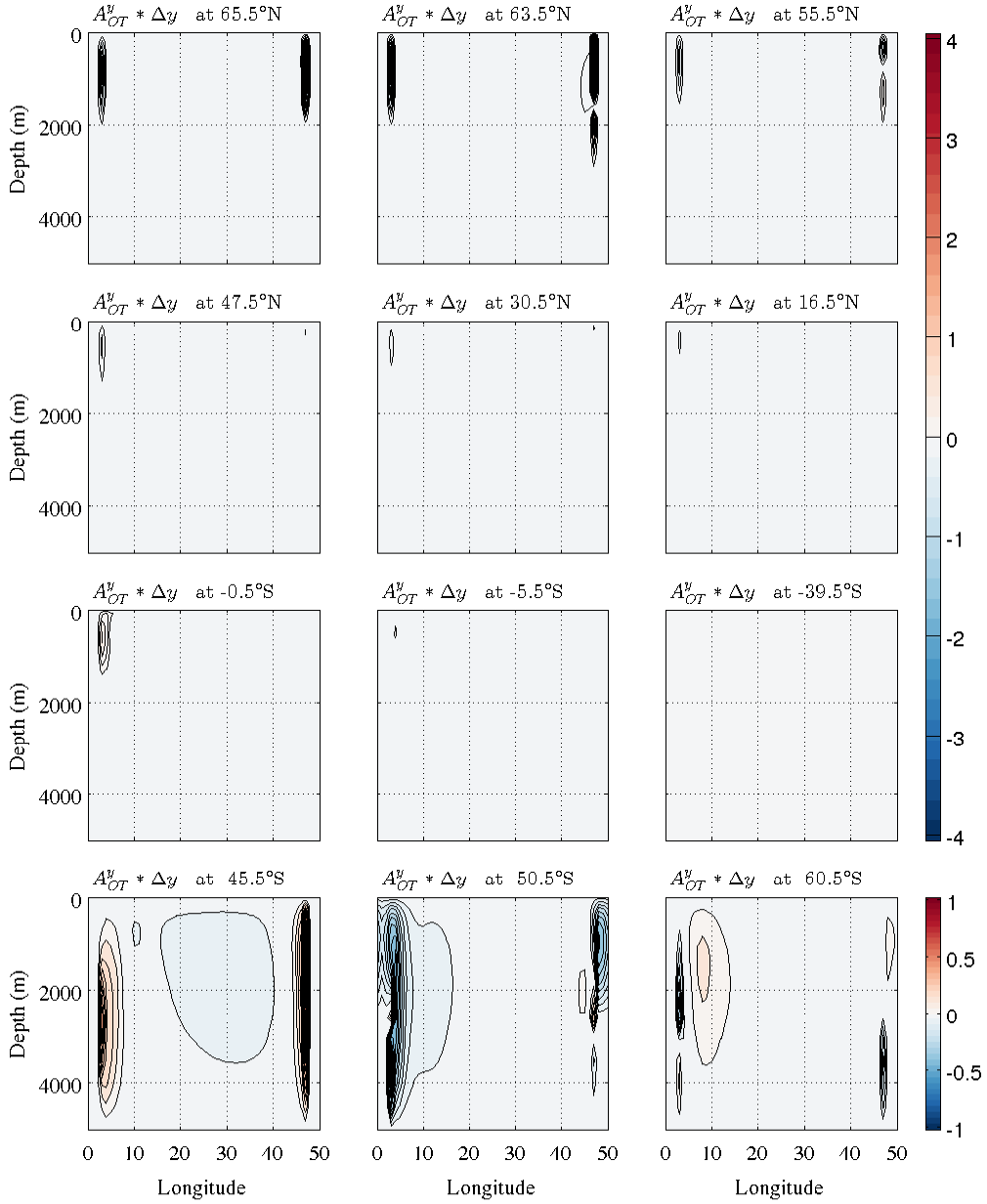

Figure 6.24: As for figure 6.10 but for the meridional component of the overturning force function, A^y_{OT}, associated with the dissipation force. The contour interval is 0.1 m^3s^{-2} north of the reentrant channel (upper three rows) and 0.05 m^3s^{-2} within the reentrant channel (bottom panel). The 0 m^3s^{-2} contour has been omitted.

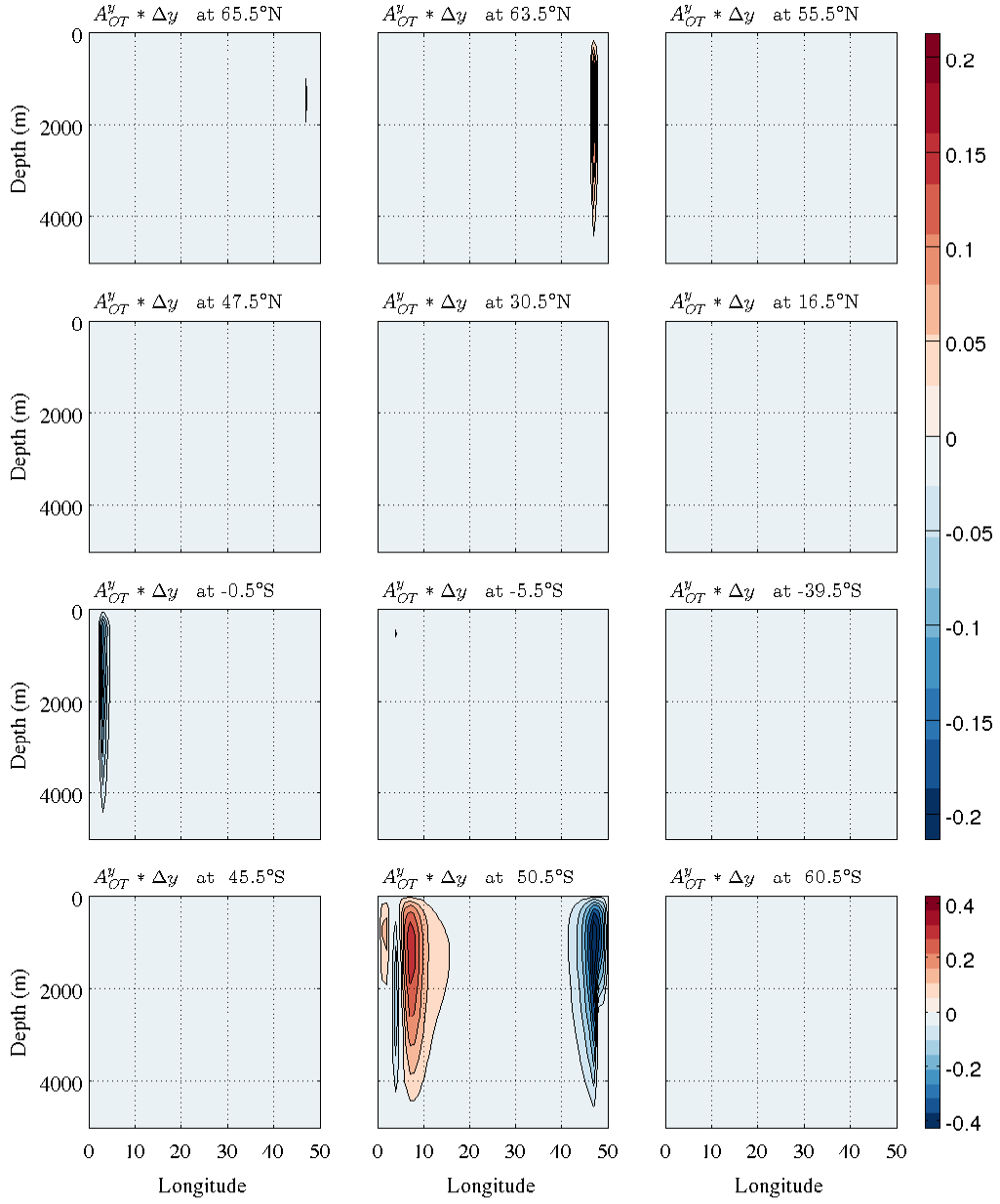

Figure 6.25: As for figure 6.10 but for the meridional component of the overturning force function, A^y_{OT}, associated with the inertial force. The contour interval is 0.025 m^3s^{-2} north of the reentrant channel (upper three rows) and 0.05 m^3s^{-2} within the reentrant channel (bottom panel). The 0 m^3s^{-2} contour has been omitted.

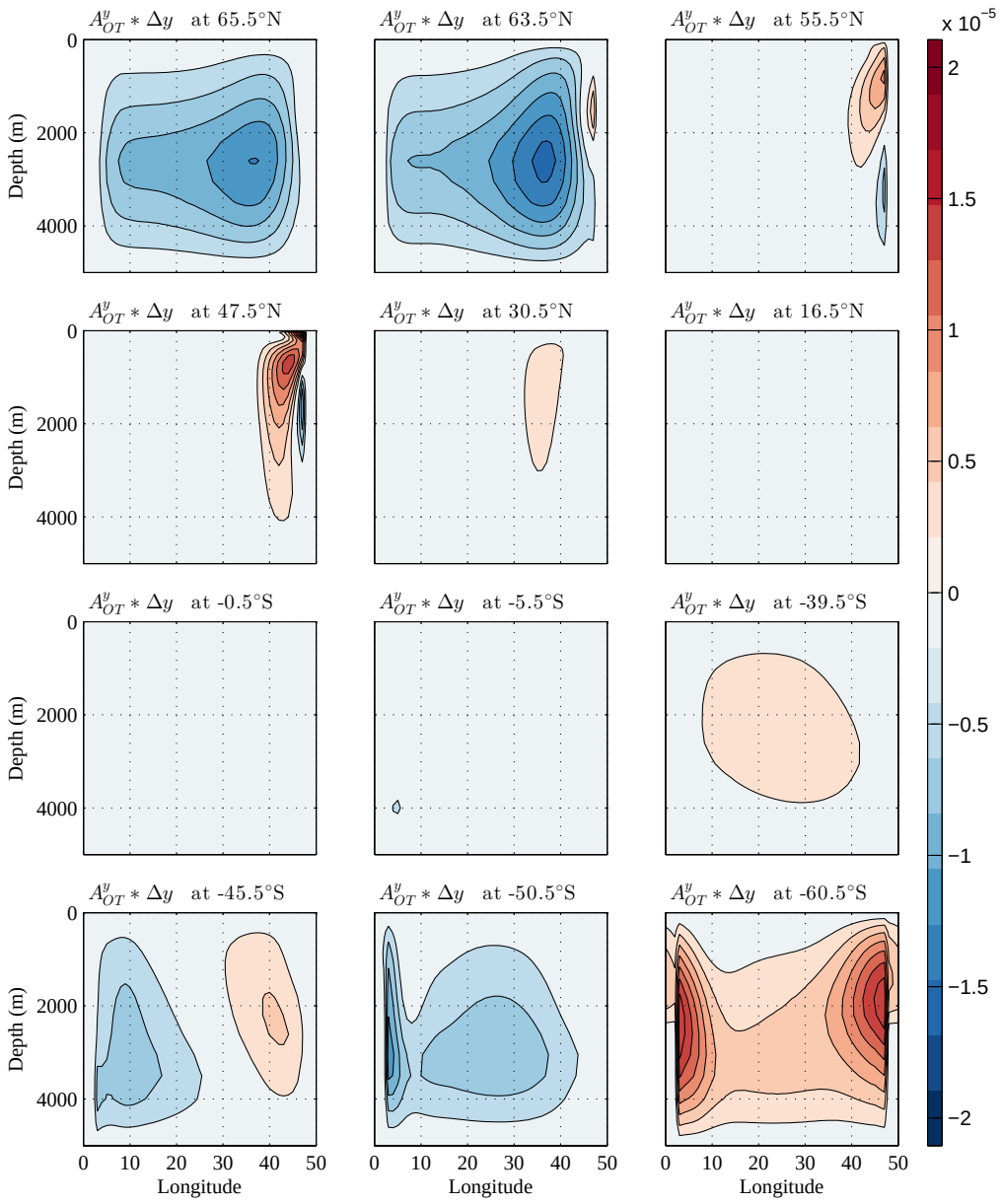

Figure 6.26: As for figure 6.10 but for the residual meridional component of the overturning force function, A^y_{OT}, from Coriolis, buoyancy, inertial, dissipation and wind forces combined. The contour interval is 2e−6 m^3s^{-2}. The 0 m^3s^{-2} contour has been omitted.

residual A^y_{OT} (figure 6.27a) with the modelled tendency of ψ_{AZOC} (figure 6.27b). The

apparent error in $\mathrm{A}^{y}_{\mathrm{OT}}$ (figure 6.27c) is matched by $\mathrm{A}^{x}_{\mathrm{OT}}\Big|_{\text{AB-residual}}$ (figure 6.28a). On accounting for this source term, the corrected total ZOC generation (figure 6.28b) is consistent with the modelled tendency of ψ_{AZOC}. The ammended error (figure 6.28c) is an order of magnitude smaller than the net acceleration of ψ_{AZOC} (figure 6.27b).

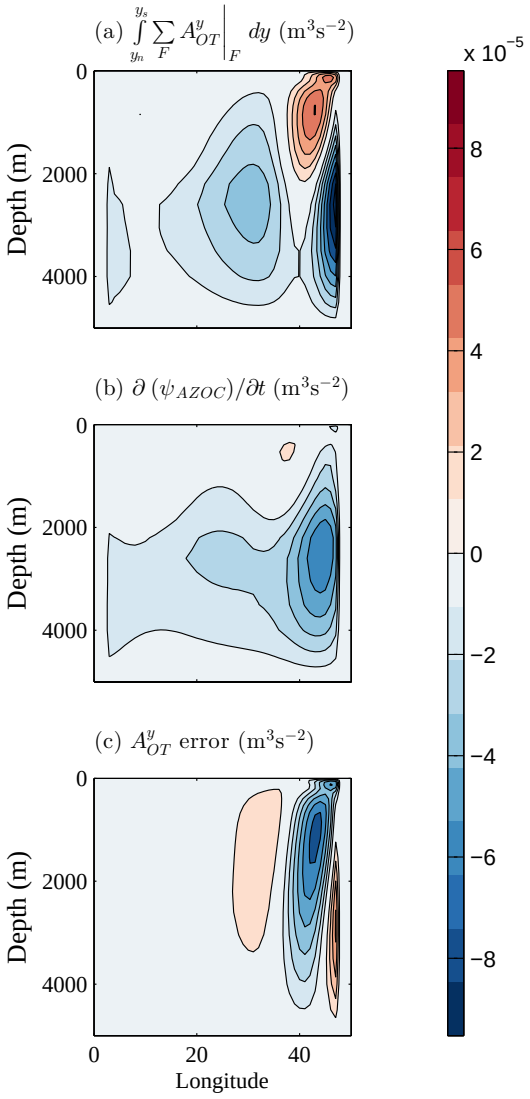

Figure 6.27: By subtracting (a) the meridional integral of the residual $\mathrm{A}^y_{\mathrm{OT}}$ from (b) the net acceleration of ψ_{AZOC} we quantify (c) the error in our calculation of $\mathrm{A}^y_{\mathrm{OT}}$. The contour interval is $1{\times}10^{-5}$ m^3 s^{-1}. The 0 m^3 s^{-1} contour has been omitted.

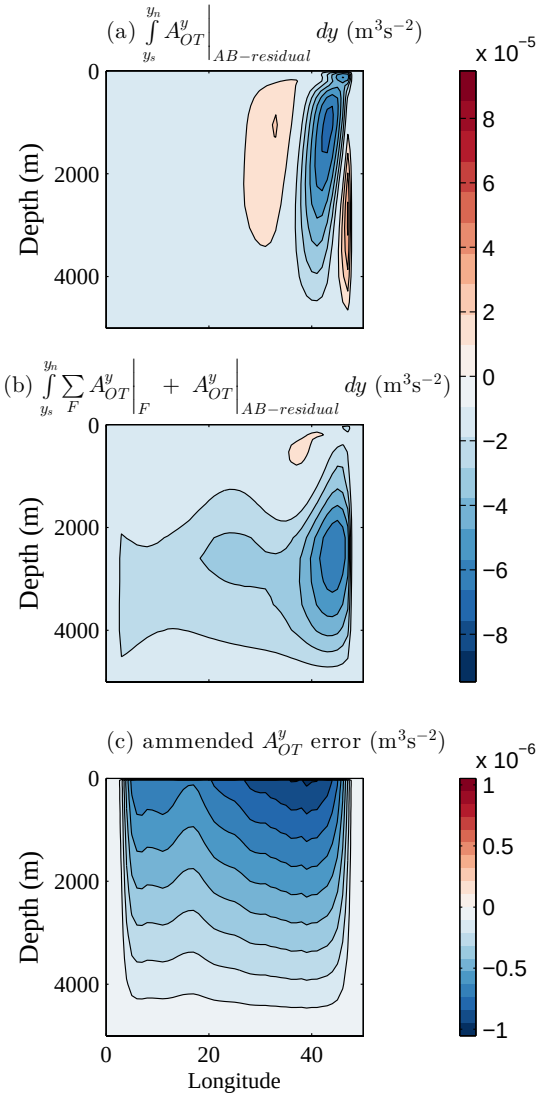

Figure 6.28: The apparent error in our computation of A^y_{OT} (figure 6.27) can be explained by the incomplete closure of the full momentum equation. By computing (a) the meridional integral of the force function associated with $F^y\Big|_{\text{AB-residual}}$, and (b) adding it to the total force function associated with all properly resolved terms, the tendency in ψ_{AZOC} (figure 6.27b) is almost exactly recovered. (c) The ammended error is computed as the adjusted force funcion in (b) differenced from the tendency of ψ_{AZOC}. The contour interval is 1×10^{-5} m^3 s^{-1} in (a) and (b), and 1×10^{-7} m^3 s^{-1} in (c). The 0 m^3 s^{-1} contour has been omitted.

6.3 Extension to Complex Global Geometries

The rotational momentum analysis presented above is now repeated in a global, realistic model geometry. Although it is of great interest to examine the rotational momentum balance of the global ocean circulation, our focus is on the dynamics governing the AMOC, and the following analysis is restricted to the Atlantic basin accordingly. The key aims for the remainder of this chapter are to:

1. determine the relative contribution of vertical shears and external modes to the total ψ_{AMOC} in a realistic Atlantic basin with heterogeneous bathymetry;

2. elucidate the force balances maintaining the vertical shears mode of ψ_{AMOC} in a realistic basin.

The model is the global configuration of the MITgcm presented in chapter 2 and employed in the linear sensitivity studies in chapters 3-4. Results shown below are from the final timestep of the 3000 year integration. The technicalities entailed in the computation of the force function and velocity potential are identical to those presented above. However, the determination of the Dirichlet condition on the barotropic velocity potential, Ψ_{BT}, and barotropic force function, A_{BT}, is considerably more challenging in the globally realistic, multiply connected domain. For this reason, it was non-trivial to compute the rotational momentum balance of the modelled external mode and this topic is reserved for future work. The determination of the cross-boundary pressure gradient merits a brief discussion below, as it hopefully lays the foundations for proceeding to solve for Ψ_{BT} and A_{BT} in the future.

6.3.1 Technical Details

The presence of numerous and irregular discrete bounding segments encourages automatic detection of coastal cells and distinct bounding curves. Distinguishing coastal

cells with the boundary lying to the north, south, east or west is critical for the computation of the cross-boundary pressure gradient, on which the buoyancy overturning force function depends. This is easily achieved by defining a mask, $m(x, y, z)$, from the bathymetry dataset, assigning land cells a value of 0, and ocean cells a value of 1. Subtracting the mask at each grid cell $m(i, j, k)$, from the neighbouring cell one degree to the east, $m(i + 1, j, k)$, yields 0 over the open ocean and continental interior, -1 in coastal cells with boundaries to the east and 1 in coastal cells with boundaries to the west. Similarly, subtracting $m(i, j, k)$ from the mask one degree to the north, $m(i, j + 1, k)$, yields -1 in coastal cells with boundaries to the north and 1 in coastal cells with boundaries to the south. The analysis for model level 1 is shown in figure 6.29.

This analysis is straightforward, but is presented here as it is fundamentally important in the rotational momentum analysis and illustrates how the existing code may easily be implemented in different configurations and at higher resolutions of the MITgcm.

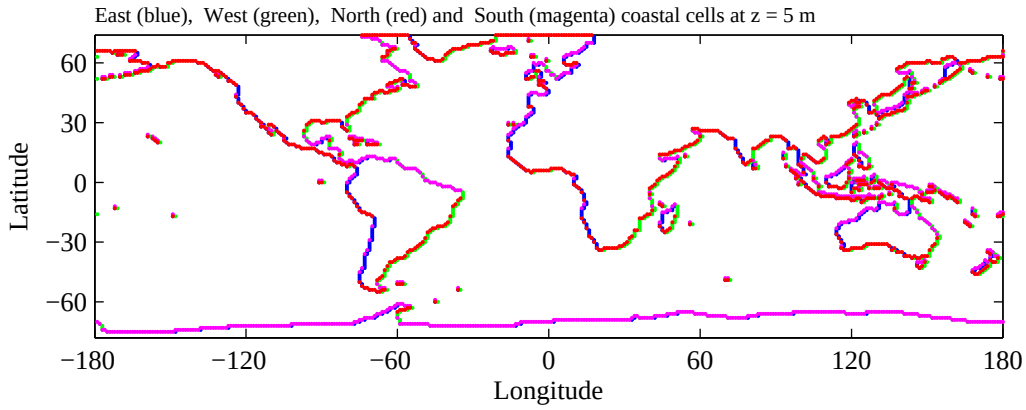

Figure 6.29: Automated identification of coastal cells neighbouring eastern (blue), western (green), northern (red) and southern (magenta) boundaries, shown here for model level 1 ($z = 5$ m).

6.3.2 Momentum Closure

Before proceeding to examine the rotational momentum balance governing the modelled circulation, it is important to check that all momentum tendency terms, **F**, have been correctly extracted from the model at the final timestep. As an example, all zonal and meridional momentum tendencies in the surface model layer are shown in figures 6.30 and 6.31. The dominant balance is between the Coriolis, pressure gradient, wind and dissipation forces (panels (a)-(d) in both figures). A smaller contribution is made by the inertial force at the Equator and in the modelled ACC, where velocity gradients are large (panel (e) in both figures). The net forcing (panel (f) in both figures) almost exactly matches the computed tendency (panel (g) in both figures). The non-closure of the full momentum budget (panel (h) in both figures) is an order of magnitude smaller than the modelled acceleration and - as for the idealized model - can be attributed to the multistep nature of the time-stepping scheme (*Campin*, 2010). As before, we expect rotational momentum closure if the components of the force function, **A**, are computed accurately and incorporate the error in the full momentum budget.

6.3.3 Analysed State

The instantaneous ψ_{AMOC}, ψ_{AZOC}, and ψ_{BT} are shown in figures 6.32a, 6.33a and 6.34a respectively, with the associated Eulerian acceleration shown in panel (b) in each case. The net meridional overturning volume flux is described by an interhemispheric northern sinking cell, with a turning depth near 2 km, achieving a maximum transport of 27.5 Sv. The net zonal overturning volume flux is described by an eastern sinking cell in the upper 2 km between 50°W and the eastern margin, overlying a western sinking cell that occupies the basin at depth. The barotropic streamfunction is dominated by the modelled ACC and gyre circulations. As for the idealised model, we start our discussion of the the rotational momentum budget by decomposing the

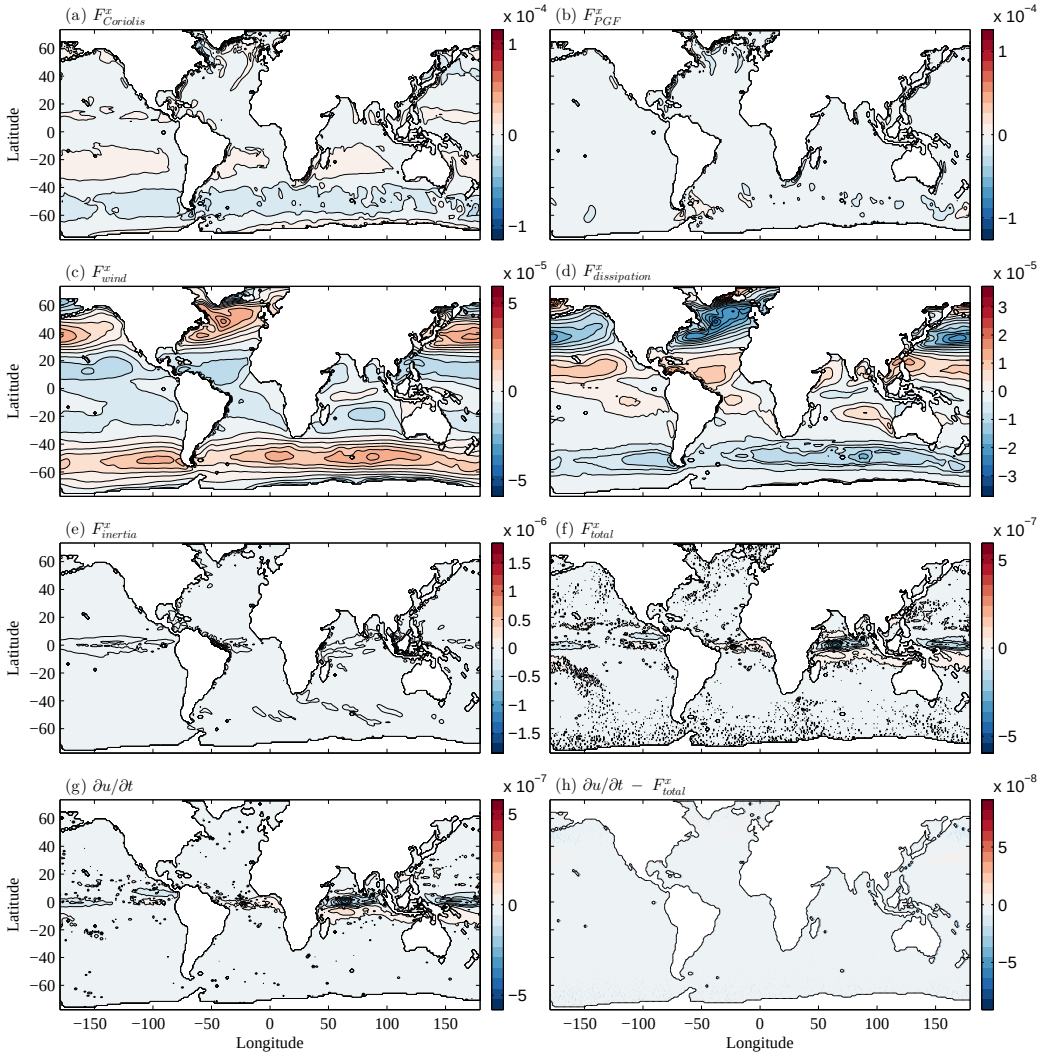

Figure 6.30: Instantaneous zonal momentum tendency (ms^{-2}) in the surface model layer at the end of the integration due to (a) Coriolis, (b) pressure gradient, (c) wind, (d) dissipation, and (e) inertial forcing. The net forcing, measured velocity tendency, and difference between the two are shown in panels (f), (g), and (h) respectively.

full velocity field into vertical shear and external modes of local overturning.

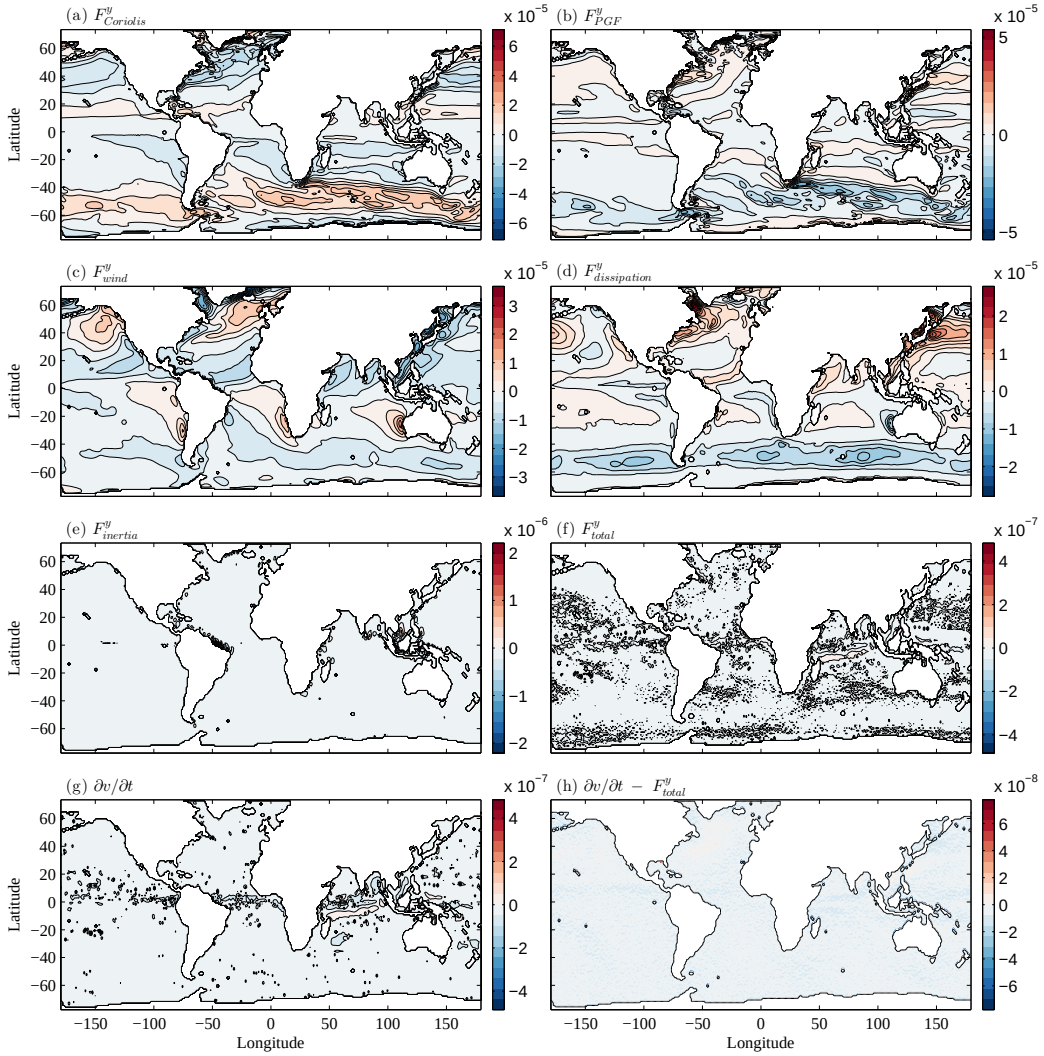

Figure 6.31: Instantaneous meridional momentum tendency (ms^{-2}) in the surface model layer at the end of the integration due to (a) Coriolis, (b) pressure gradient, (c) wind, (d) dissipation, and (e) inertial forcing. The net forcing, measured velocity tendency, and difference between the two are shown in panels (f), (g), and (h) respectively.

6.3.4 MOC Overturning and External Modes

MOC Vertical Shear Mode

In figures 6.35-6.39, the MOC vertical shears component, Ψ^x_{OT}, is shown integrated across one grid cell width, at a selection of $x-y$ cross-sections through the Atlantic basin. The greatest meridional mass transports are achieved in the western boundary

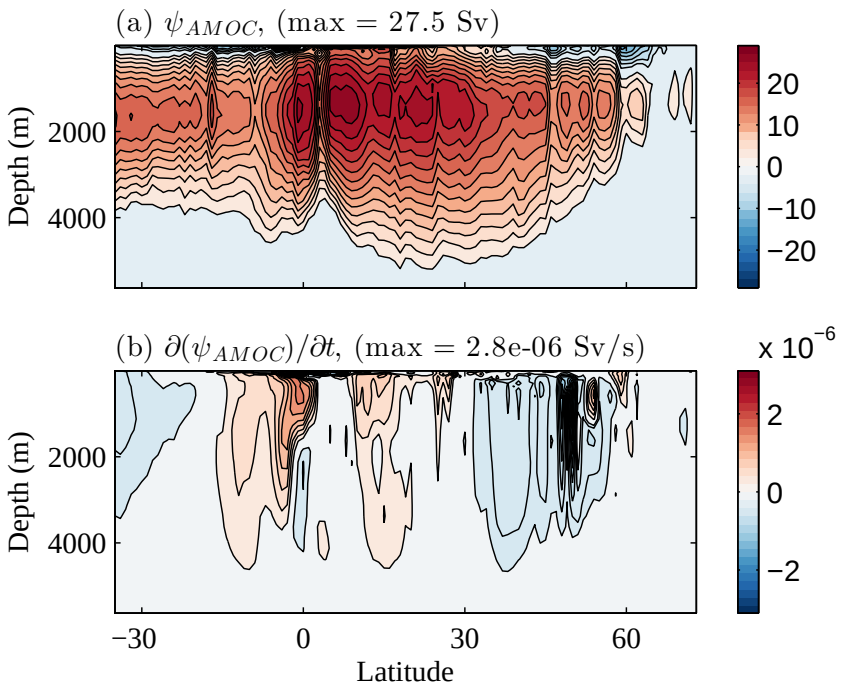

Figure 6.32: (a) AMOC streamfunction, ψ_{AMOC}, and (b) acceleration of the AMOC streamfunction, $\partial\psi_{\mathrm{AMOC}}/\partial t$, in the final timestep of the global model integration. The contour interval is 2 Sv in (a) and 1×2^{-7} Sv s^{-1} in (b). The 0 contour has been omitted. Positive values indicate sinking to the north.

current system (figures 6.35 and 6.37). Fast northward currents at the surface overlie a sluggish return flow at depth, leading to northern sinking cells at all locations crossed by the Gulf Stream, Antilles, and North Brazil currents. These cells have a turning point at around 1 km depth and achieve a volume flux of approximately 8 Sv (across each degree of longitude).

Moving towards the ocean interior (figure 6.36), northern sinking cells are still found at latitudes occupied by the boundary jets, whilst southern sinking cells emerge in the regions occupied by the anticyclonic subtropical gyre. As the Gulf Stream separates and follows a more north-eastward trajectory, the volume flux in the $y-z$ plane diminishes to approximately 2 Sv per degree of longitude, and remains near

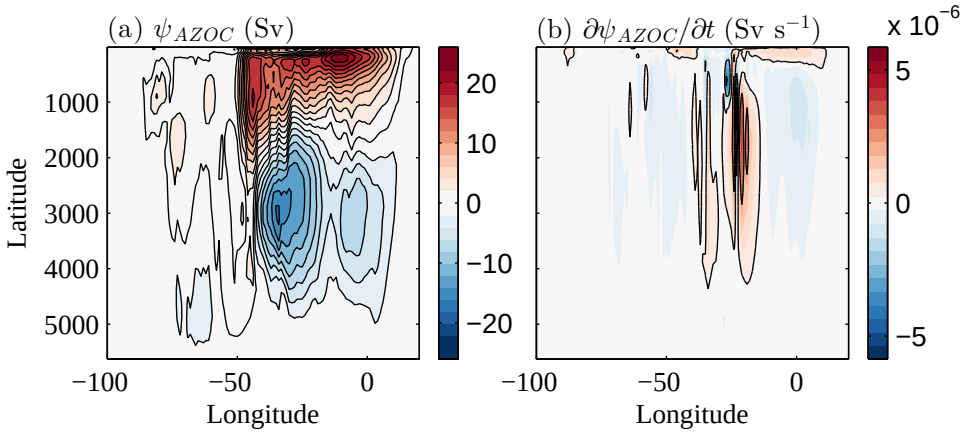

Figure 6.33: (a) AZOC streamfunction, ψ_{AZOC}, and (b) acceleration of the AZOC streamfunction, $\partial\psi_{\mathrm{AZOC}}/\partial t$, in the final timestep of the global model integration. The contour interval is 2 Sv in (a) and 2×10^{-7} Sv s^{-1} in (b). The 0 contour has been omitted. Positive values indicate sinking to the east.

this amplitude throughout the remainder of the basin (figures 6.38-6.39).

Upon reaching the Mid-Atlantic Ridge (figure 6.38), the meridional overturning fragments into a complex distribution of counter-rotating cells, which can be distinguished as signatures of the large scale flow as follows. At the northern limit of the $y-z$ planes shown in figure 6.38, the modelled East Greenland and Irminger Currents are met. The East Greenland Current flows south-westwards near the surface, driving a southern sinking cell in the vicinity of 60°N. Where the northward-flowing limb of the Irminger Current is met near the surface (figure 6.38l), a northern sinking cell is established at this latitude. The surface-intensified northern sinking cell visible at a latitude of 30°N at -30.5°W (figure 6.38m, and shifting northward through panels n-p) is a signature of the modelled North Atlantic Drift. The southern sinking cell just to the south, extending from near the surface to 4 km depth, is associated with the anticyclonic subtropical gyre. The poleward flowing Equatorial currents drive northern and southern sinking cells in their respective hemispheres. Finally,

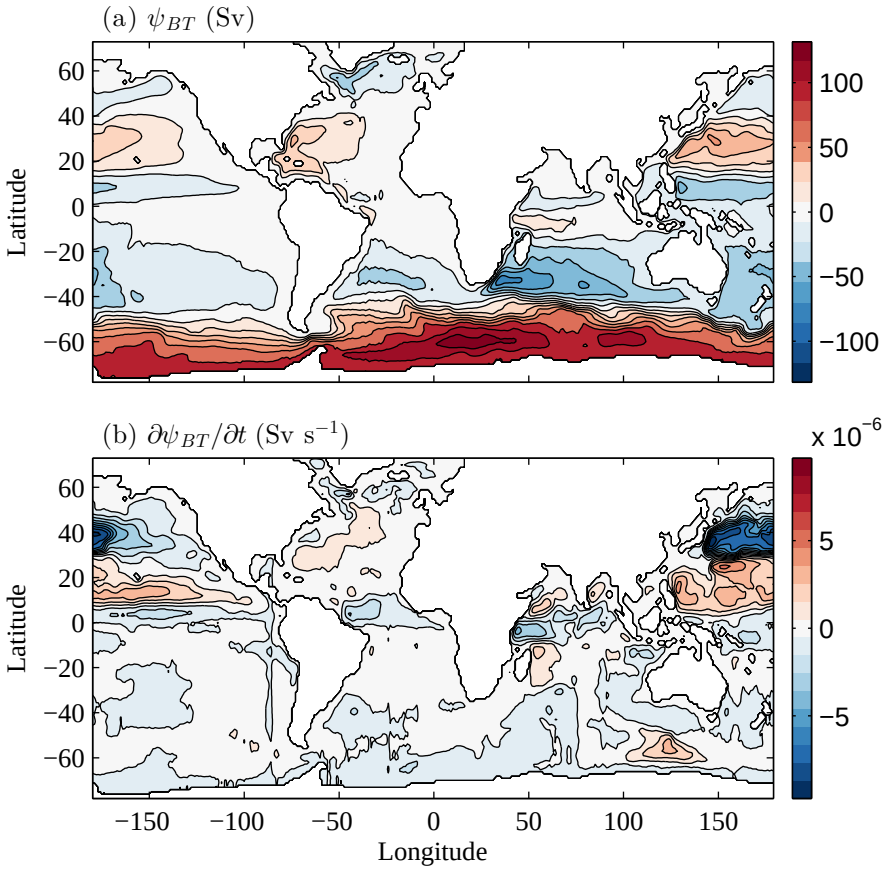

Figure 6.34: (a) Barotropic streamfunction, ψ_{BT}, and (b) acceleration of the barotropic streamfunction, $\partial\psi_{\mathrm{BT}}/\partial t$, in the final timestep of the global model integration. The contour interval is 15 Sv in (a) and 1×10^{-6} Sv s^{-1} in (b). The 0 contour has been omitted. Positive values indicate clockwise circulations looking down onto the $x-y$ plane.

the northern sinking cell visible near the southern limit of all panels in figure 6.38 is a signature of the anticyclonic gyre in subtropical southern hemisphere. The vigorous northern sinking cell visible in the subtropical south Atlantic in figure 6.37l is a signature of the gyre circulation reinforced by the modelled northwestward Benguela Drift.

In the absence of intense jets on the eastern boundary, the volume flux achieved in the meridional-depth plane remains at around 2 Sv (per degree of longitude), with

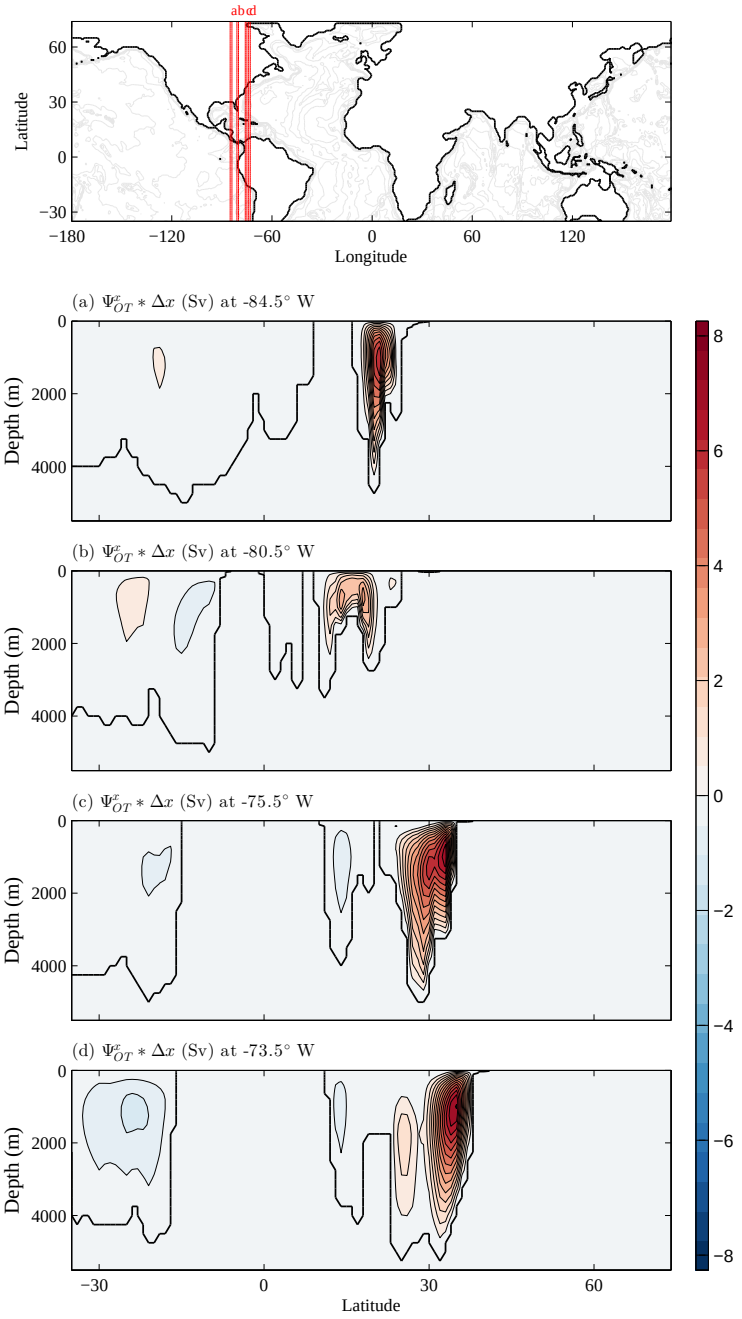

Figure 6.35: Zonal component of the overturning velocity potential, Ψ^x_{OT}, integrated across one grid cell width in the vicinity of the western boundary jet at (a) -70.5°W, (b) -67.5°W, (c) -60.5°W and (d) -56.5°W, as shown in the top panel. The contour interval is 0.5 Sv. The 0 Sv contour has been omitted. Positive values indicate sinking to the north. In the top panel the bathymetry is contoured in grey with an interval of 1000 m. In panels (a)-(d) the black contour delineates the ocean floor.

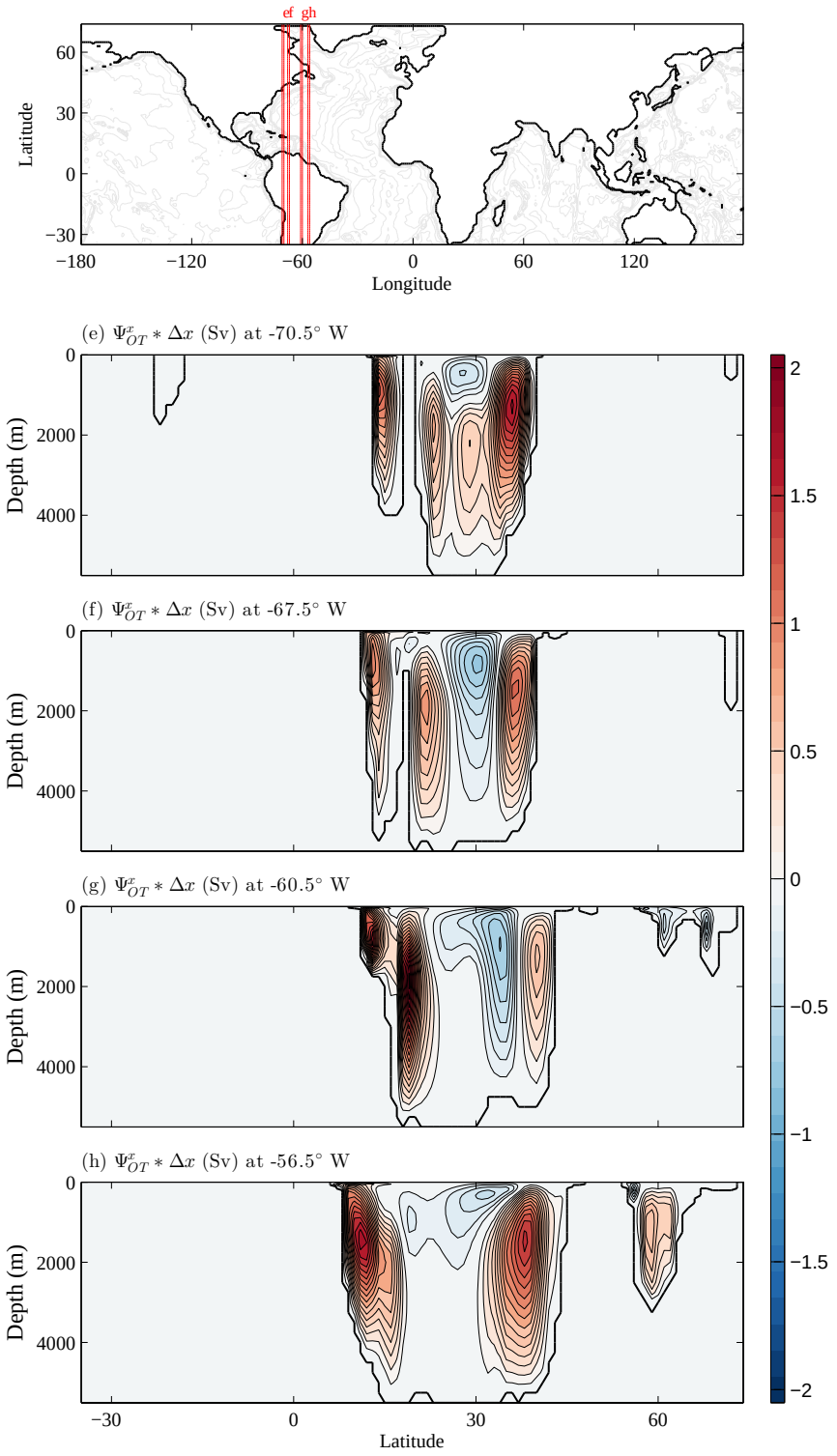

Figure 6.36: As for figure 6.35 but for longitudes (e) -70.5°W, (f) -67.5°W, (g) -60.5°W and (h) -56.5°W, as shown in the top panel. The contour interval is 0.1 Sv.

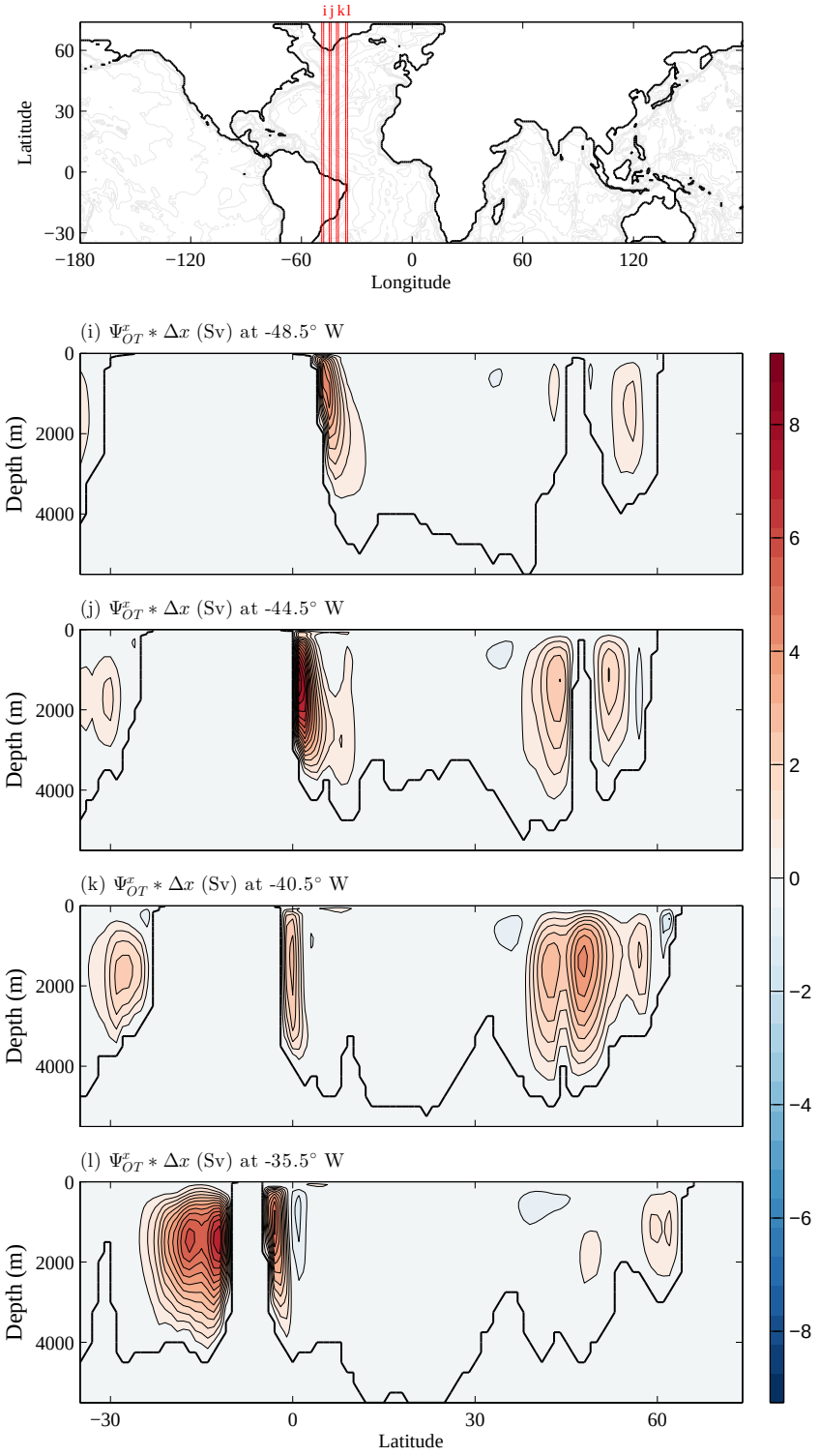

Figure 6.37: As for figure 6.35 but for longitudes (i) -48.5°W, (j) -44.5°W, (k) -40.5°W, and (l) -35.5°W. The contour interval is 0.5 Sv.

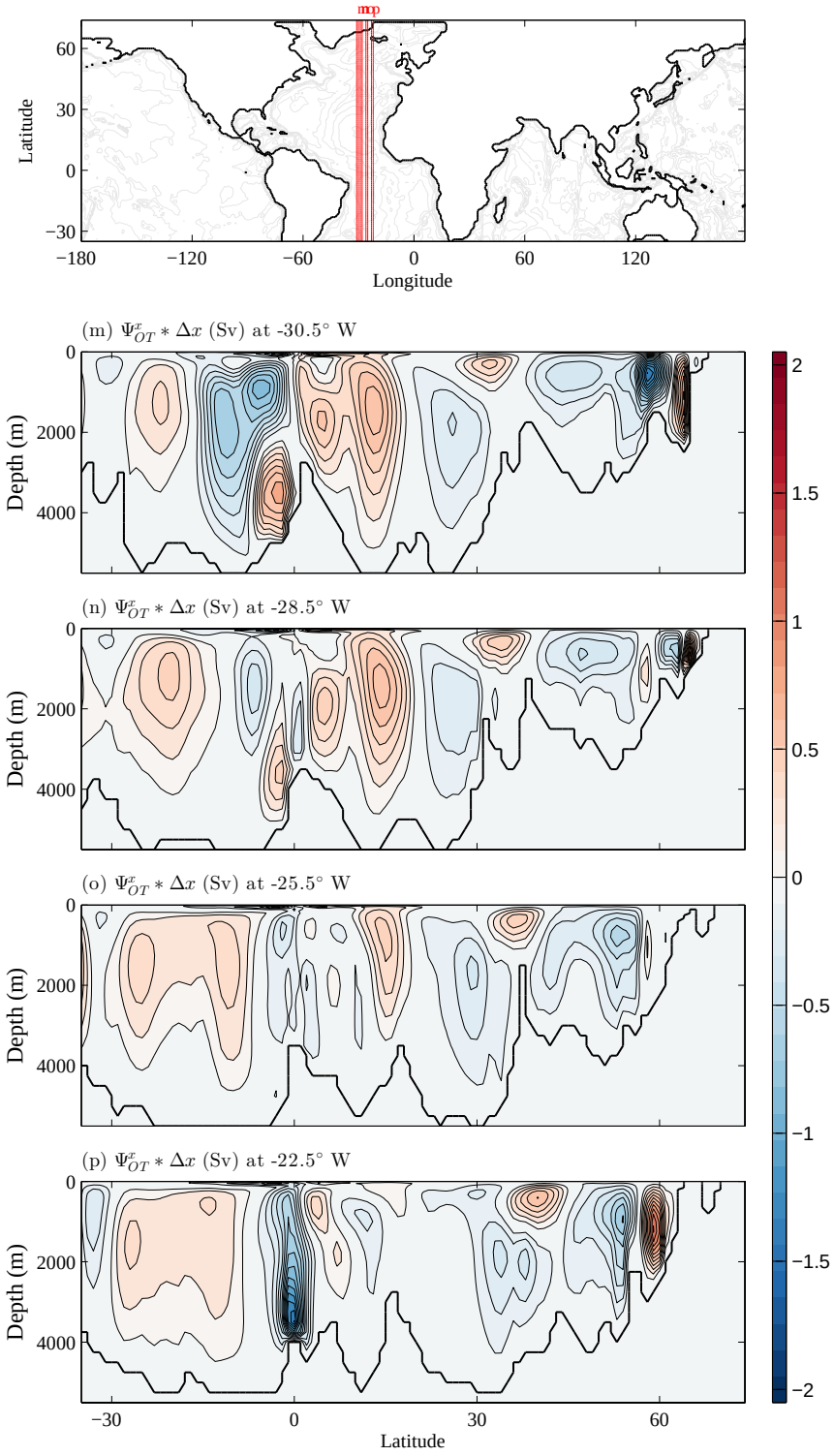

Figure 6.38: As for figure 6.35 but for longitudes (m) -30.5°W, (n) -28.5°W, (o) -25.5°W, and (p) -22.5°W. The contour interval is 0.1 Sv.

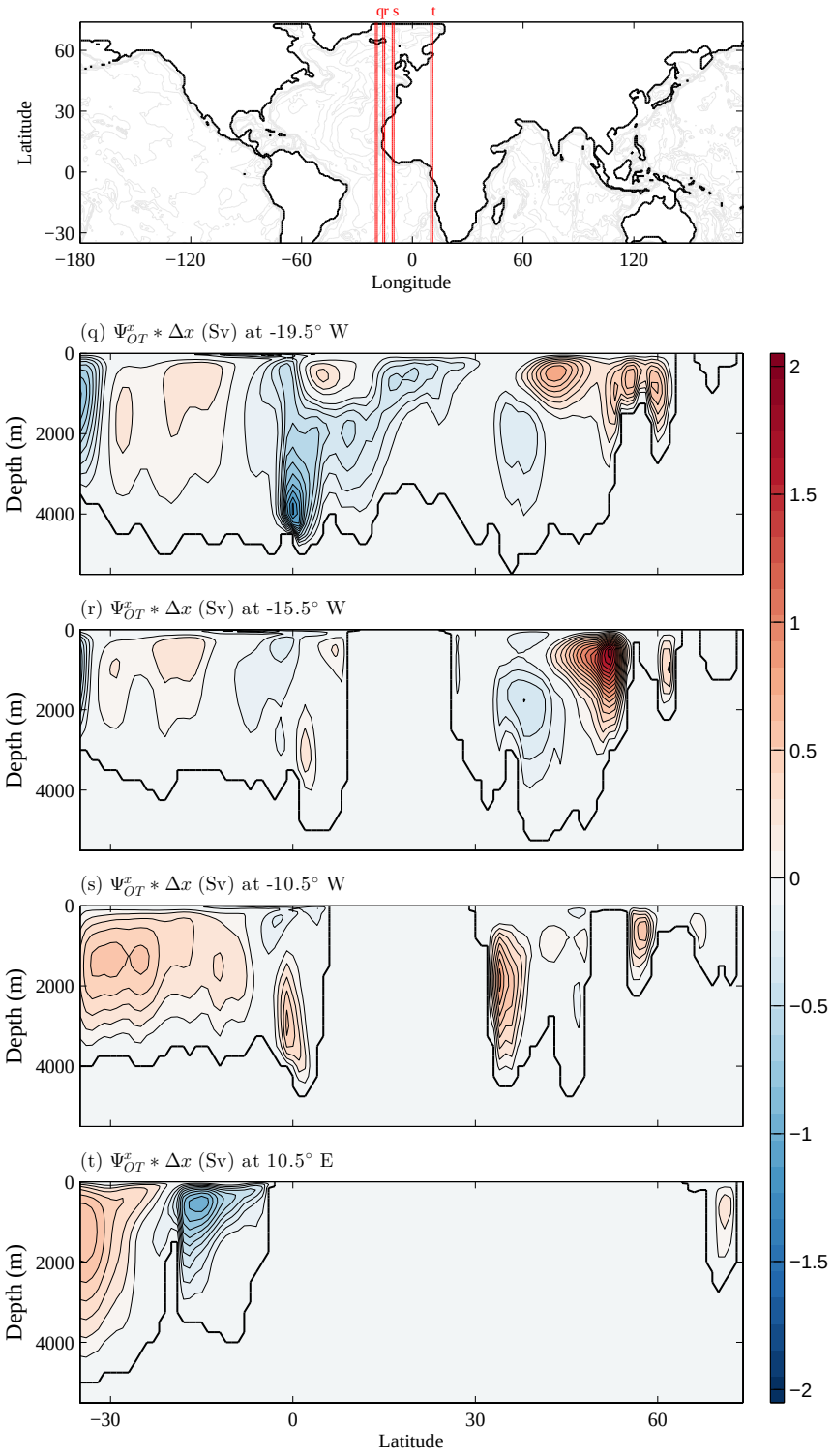

Figure 6.39: As for figure 6.35, but for longitudes (q) -19.5°W, (r) -15.5°W, (s) -10.5°W, and (t) 10.5°E. The contour interval is 0.1 Sv.

migration onto the eastern margin (figure 6.39). Strong signatures of the southern hemisphere subtropical gyre and Equatorial Currents are still visible in figure 6.39. The northern sinking cell near the northern margin at these longitudes is a signature of the North Atlantic Current entering the GIN seas.

To conclude our analysis of the MOC vertical shear mode, $\Psi^x_{\rm OT}$, we examine the basin integral to determine the total contribution to $\psi_{\rm AMOC}$. As for the idealised reentrant channel model presented above, we split the total zonal integral (figure 6.40a) into contributions from the basin interior, western boundary layer and eastern boundary layer (figure 6.40b,c,d respectively). Our definition of the Munk layer in figure 6.40c means that the northern sinking cells associated with the Antilles Current (between 15°N and 25°N) and the separated boundary jet (between 35°N and 65°N) are computed as a contribution from the basin interior.

The total zonal integral of $\Psi^x_{\rm OT}$, produces two distinct cells of northern sinking (figure 6.40a). These two cells closely resemble $\psi_{\rm AMOC}$ in the same latitudinal range (figure 6.32). In the latitude band spanning 24°N - 33°N, there is a notable difference where the vertical shears component, associated with the subtropical gyre circulation, drives a southern sinking cell of approximately 18 Sv, interrupting the interhemispheric overturning. In figure 6.41 we show the residual between $\psi_{\rm AMOC}$ and the basinwide integral of $\Psi^x_{\rm OT}$. This residual must be equal to the external mode of the AMOC.

As noted in the introduction to this chapter we do not, at present, rigorously solve the elliptic problem for the barotropic velocity potential, $\Psi_{\rm BT}$, in the realistic model geometry. However, we are able to access the external mode of overturning by using the barotropic streamfunction, $\psi_{\rm BT}$ shown in figure 6.34a, in place of $\Psi_{\rm BT}$ in the definition of the external mode. In the following section, we present a short analysis of the local MOC external mode. Our purpose is to assess the origins of the signal suggested in figure 6.41.

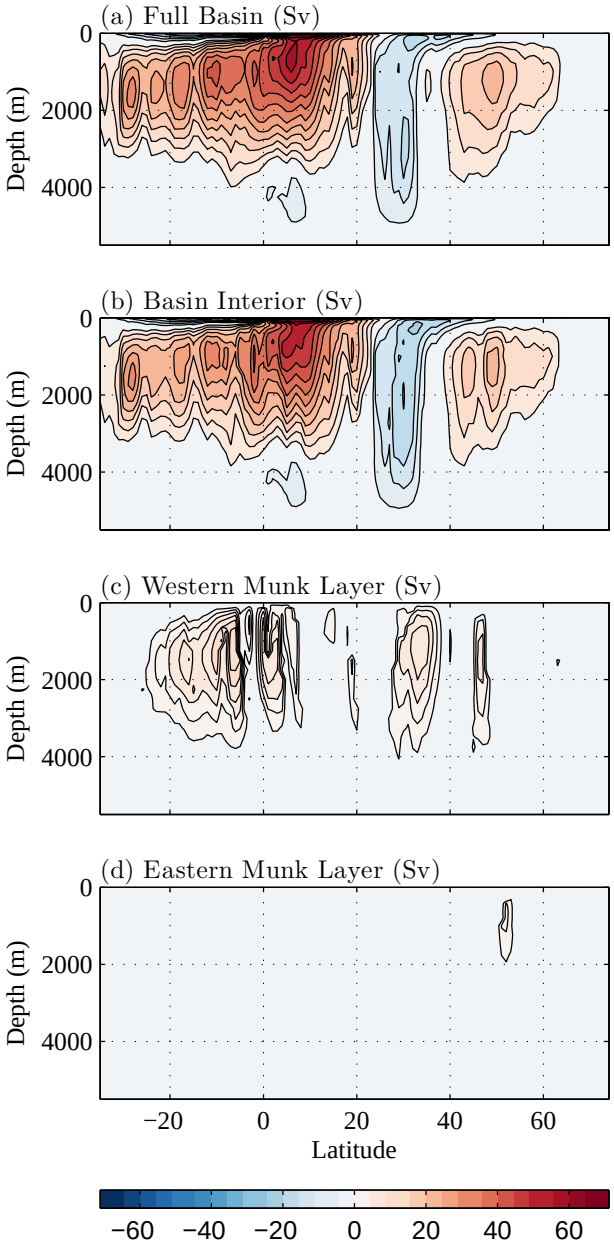

Figure 6.40: Zonal component of the overturning velocity potential, Ψ^x_{OT}, integrated across (a) the full Atlantic basin, (b) the basin interior, (c) the western boundary Munk layer and (d) the eastern boundary Munk layer. The contour interval is 5 Sv for (a)-(b) and 2 Sv for (c)-(d). The 0 Sv contour has been omitted.

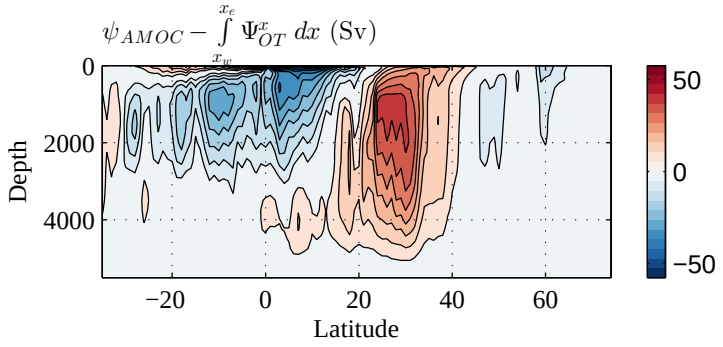

Figure 6.41: Residual between the modelled ψ_{AMOC} and the basinwide integral of the vertical shears component of the overturning velocity potential, Ψ^x_{OT}. We expect that this residual is accomplished as an external mode.

MOC External Mode

Where ψ_{BT} passes over bathymetric variations in the east-west direction, an external mode of the MOC is generated. In figure 6.42 we plot the MOC external mode component (computed using ψ_{BT}), integrated across the width of a grid cell, at a small selection of $y - z$ cross sections through the Atlantic basin. Only the main features will be discussed in detail. The strongest meridional overturning achieved by the external mode occurs adjacent to the western boundary (figure 6.42a), associated with the formation and separation of the boundary jet. The subtropical gyre maximum is located near the western boundary at approximately 30°N. Between 35°N and approximately 45°N transport is directed off the continental slope and onto the abyssal plain, following the separation of the boundary jet. This results in the northern sinking MOC north of 30°N in figure 6.42a, associated with a local transport of approximately 0.2 Sv (per degree of longitude). A stronger northern sinking MOC of approximately 0.5 Sv (per degree of longitude) is established on the Abaco shelf (Bahamas) as the boundary current system strengthens moving northwards.

As the subtropical gyre circulates over the MAR, external modes of the MOC

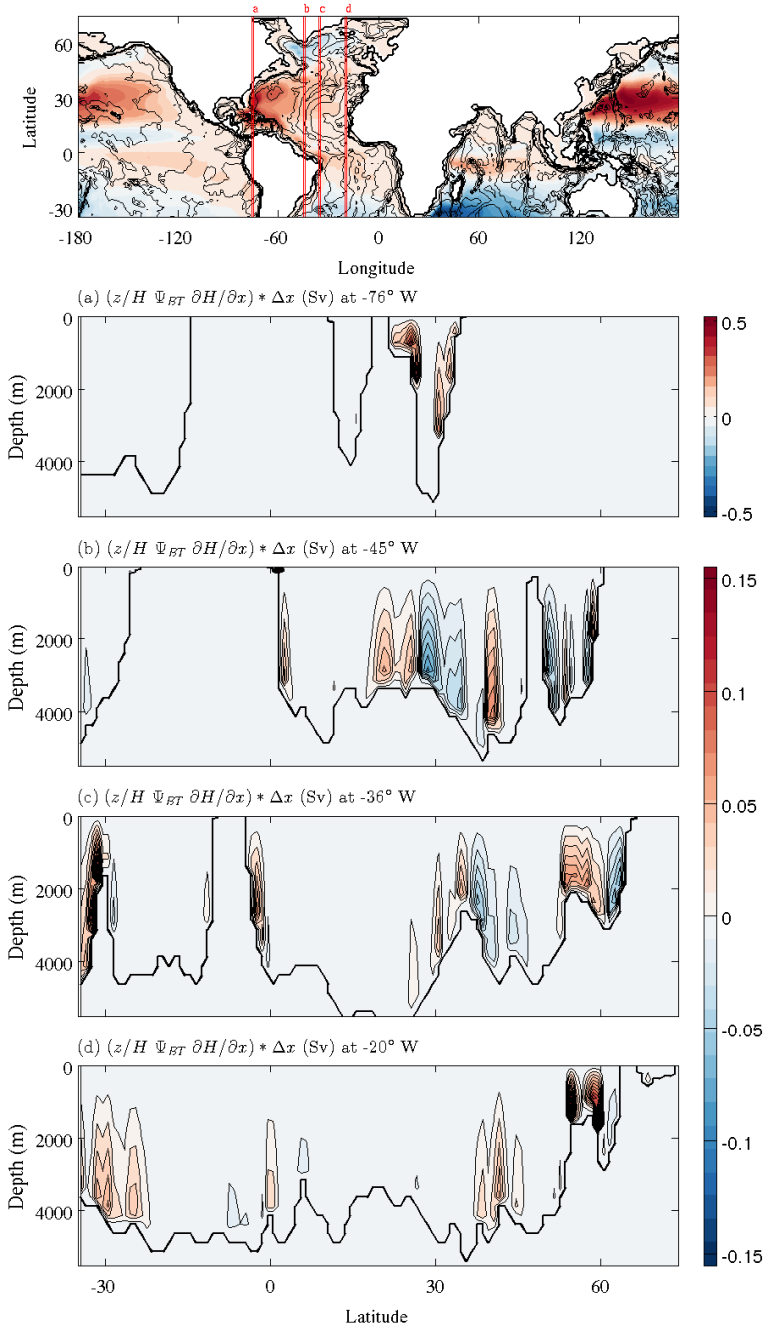

Figure 6.42: Zonal component of the overturning external mode, $z/H\ \psi_{\mathrm{BT}}\ \partial H/\partial x$, integrated across one grid cell width at (a) -76°W, (b) -45°W, (c) -36°W and (d) -20°W, as shown in the top panel. The contour interval is (a) 0.05 Sv, (b)-(d) 0.01 Sv The 0 Sv contour has been omitted. Positive values indicate sinking to the north. In the top panel coloured contours show the barotropic streamfunction, ψ_{BT} (see figure 6.34). The bathymetry is overlaid in black with an interval of 1000 m. In panels (a)-(d) the black contour delineates the ocean floor.

transport approximately 0.2 Sv in the local $y-z$ plane. On the western flank of the MAR at 45°W (figure 6.42b) a southern sinking MOC is established between 27°N-38°N as the circulation approaches the ridge to the north and departs from the ridge to the south. At 26°N the ridge axis is met and the external mode vanishes ($\partial H/\partial x = 0$). Between 18°N-25°N, the gyre transport is directed downslope towards the abyssal plain, reducing in strength towards the south. The result is downwelling throughout this latitude band, reducing in strength towards the south and generating a northern sinking MOC. Similar reasoning also explains the pattern of meridional overturning between 30°N-48°N on the eastern flank of the MAR at 36°W (figure 6.42c) and near 30°S on the western flank of the MAR at 20°W (figure 6.42d). Notable external modes of the MOC are also generated in the vicinity of the subpolar gyre and the high-latitude overflows (figures 6.42c-d near 60°N). At all longitudes, the external mode is bottom intensified due to the z/H weighting of ψ_{BT} in the calculation.

From this brief analysis, we suggest that local external modes generated (1) where the western boundary jet impinges along the continental slope, (2) where the subtropical and subpolar gyres pass over the MAR and (3) where fluid from the GIN Seas spills into the North Atlantic, may project onto the basinwide meridional overturning circulation. Despite our incomplete analysis, we are encouraged by the qualitative similarity between our expected external mode (figure 6.41) and that present by *Sime et al.* (2006) for the simulated AMOC in HadCM3. Consistent features include (1) cancellation between the local MOC at different longitudes preventing the external mode associated with the subpolar gyre circulation from projecting significantly onto the AMOC north of 40°N, and (2) the predominance of a northern sinking cell in the external mode AMOC between 10°N-35°N.

Proper diagnosis of the external mode in the rotational momentum framework is an essential topic for future work. Below we may proceed to examine the rotational momentum budget governing only the vertical shears component of the AMOC. In

the next section, we present a brief analysis of the zonal component of the vertical shears velocity potential, Ψ^x_{OT}, as this is helpful in understanding the rotational generation of the meridional overturning.

6.3.5 ZOC Overturning

ZOC Vertical Shear Mode

In figure 6.43 the ZOC vertical shear component, Ψ^y_{OT}, is shown integrated across the length of a grid cell, at a selection of $y-z$ cross sections through the Atlantic basin. In figures 6.43a-c, cross sections through the modelled subpolar gyre are shown. Through the basin interior and near the eastern margin, eastern sinking cells transporting approximately 2 Sv (per degree of latitude) are found, associated with the north-eastward North Atlantic Drift. At 60.5°N, an eastern sinking cell is also found on the western boundary, associated with the modelled Labrador Current flowing southeastwards along the continental slope. The western sinking cell adjacent to the western boundary in the vicinity of the Grand Banks (figure 6.43b-c) suggests the model simulates localised cyclonic circulation nested within the larger scale gyration, consistent with observations (e.g. *Rhein et al.*, 2011).

South of the Grand Banks, strong zonal overturning is found along the Eastern US Seaboard (figures 6.43d-f), where the northeastward Gulf Stream overlies the southwestward deep western boundary current, generating strong shear in the zonal velocity. The turning point of the resultant eastern sinking cells is located at approximately 1000 m depth. Further south, the modelled North Brazil and Antilles Currents follow a northwestwards trajectory along the continental slope and are associated with vigorous western sinking cells (figures 6.43g-i) transporting approximately 6-8 Sv (per degree of latitude). The final row in figure 6.43 shows cross sections through the modelled south Atlantic subtropical gyre. The interior limb of the gyre circulation between -20.5°S and -30.5°S flows northwestwards, transporting

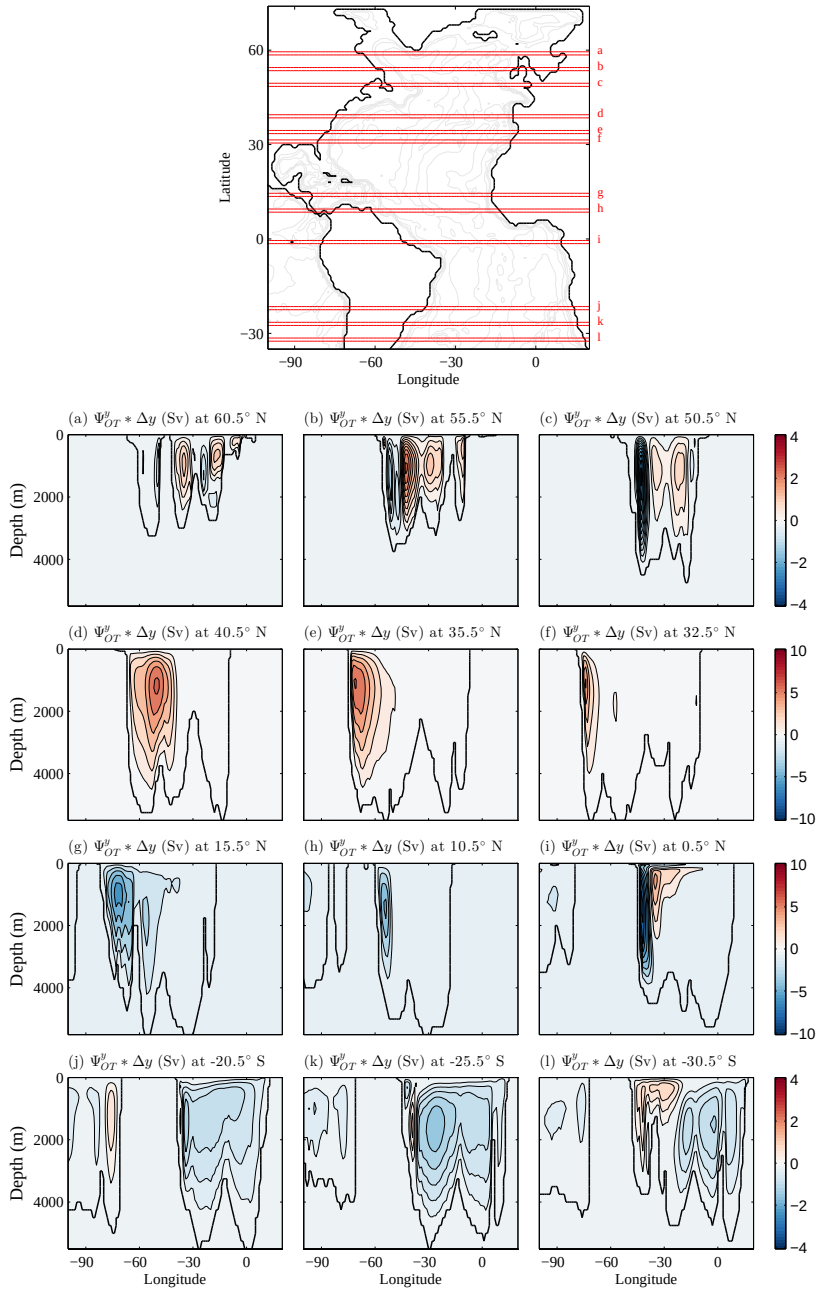

Figure 6.43: Meridional component of the overturning velocity potential, Ψ^y_{OT}, integrated across one grid cell length at (a) 60.5°N, (b) 55.5°N, (c) 50.5°N, (d) 40.5°N, (e) 35.5°N, (f) 32.5°N, (g) 15.5°N, (h) 10.5°N, (i) 0.5°S, (j) -20.5°S, (k) -25.5°S, and (l) -30.5°S ,as shown in the top panel. The contour interval is 0.25 Sv in panels (a)-(c),(j)-(l) and 1 Sv in panels (d)-(i). The 0 Sv contour has been omitted. Positive values indicate sinking to the east. In the top panel the bathymetry is contoured in grey with an interval of 1000 m. In panels (a)-(l) the black contour delineates the ocean floor.

approximately 1 Sv (per degree of latitude). The return flow also contributes to the western sinking ZOC as it follows the continental slope southwestwards, resulting in a zonal overturning cell that spans the basin width. The eastern sinking cell that emerges towards the southern limit of the Atlantic basin (figures 6.43j-l) may be a signature of the modelled Antarctic Circumpolar Current flowing northeastwards along the continental shelf of Argentina (i.e the modelled Malvinas Current).

6.3.6 Generation of the AMOC

Since our focus is on the dynamics governing ψ_{AMOC} we restrict out discussion below to consider only the relevant, zonal, component of vertical shears force function, $\mathrm{A}^{x}_{\mathrm{OT}}$.

Generation of MOC Vertical Shear Mode

In figure 6.44, the zonal component of the overturning force function, integrated across one grid cell, is shown for the buoyancy force at a selection of longitudes. These are chosen to capture the western boundary, interior, and eastern boundary circulation regimes. Along the Eastern US Seaboard we saw that the vertical shears component of ZOC, Ψ^{y}_{OT}, is described by an eastern sinking cell (figure 6.43d-f). This tilts positive planetary vorticity, f, into the local $y-z$ plane, generating a northern sinking cell adjacent to the western boundary, spanning approximately 10° of latitude (figures 6.44a-b). Near 35°N (figure 6.44a) the associated tendency of the volume flux is approximately 500 $\mathrm{m^3 s^{-2}}$. As the boundary jet separates this diminishes to approximately 300 $\mathrm{m^3 s^{-2}}$ (figure 6.44b).

As the North Brazil and Antilles Currents follow the continental slope northwestwards, we saw that Ψ^{y}_{OT} is described by a western sinking cell (figure 6.43g-i). This tilts positive planetary vorticity to generate a southern sinking cell adjacent to the western boundary. In the vicinity of the Antilles Current the associated tendency

of the volume flux is approximately 125 m^3s^{-2} (figure 6.44a). In the vicinity of the North Brazil Current, the associated tendency is approximately 100 m^3s^{-2} (figure 6.44b).

Towards the basin interior, the tendency of the volume flux diminishes and is notably small in the vicinity of the Equator (figures 6.44c-d). In the South Atlantic, we saw that $\Psi^y_{\rm OT}$ is described by a western sinking cell associated with the subtropical gyre circulation. This tilts negative planetary vorticity to generate a northern sinking cell spanning approximately 20° of latitude. As for the idealised overturning, we can detect an equatorwards shoaling of $\mathrm{A}^x_{\rm OT}\Big|_{\rm buoyancy}$, into the region where the largest velocity shear can work to tilt diminishing planetary vorticity.

At high northern latitudes $\mathrm{A}^x_{\rm OT}\Big|_{\rm buoyancy}$ can be understood by considering the ZOC associated with the Labrador and GIN Seas current system. For example, the western sinking ZOC associated with subgyre cyclonic circulations near the western boundary (figure 6.43b-c) tilts positive planetary vorticity to generate a southern sinking cell in the Labrador Sea (figure 6.44b). At these latitudes, the largest contribution to the acceleration of the vertical shears MOC is associated with the tilting of planetary vorticity by the North Atlantic Current. The associated volume flux tendency is approximately 175 Sv at 28.5°W (figure 6.44).

The Coriolis overturning force function, $\mathrm{A}^x_{\rm OT}\Big|_{\rm Coriolis}$, is approximately equal and opposite to $\mathrm{A}^x_{\rm OT}\Big|_{\rm buoyancy}$ everywhere (figure 6.45). The residual between the two is shown in figure 6.46 and is almost fully explained by the wind forcing (figure 6.47). In the subtropics the surface limb of the Hadley cell flows equatorwards driving westward (eastward) Ekman velocities in the northern (southern) hemisphere. The associated eastern (western) sinking ZOC tilts positive (negative) planetary vorticity to generate a southern (northern) sinking MOC (figure 6.47). In the North Atlantic, the midlatitude synoptic winds tend to follow a northwestward trajectory, driving eastward Ekman velocities, which result in a western sinking ZOC and a northern

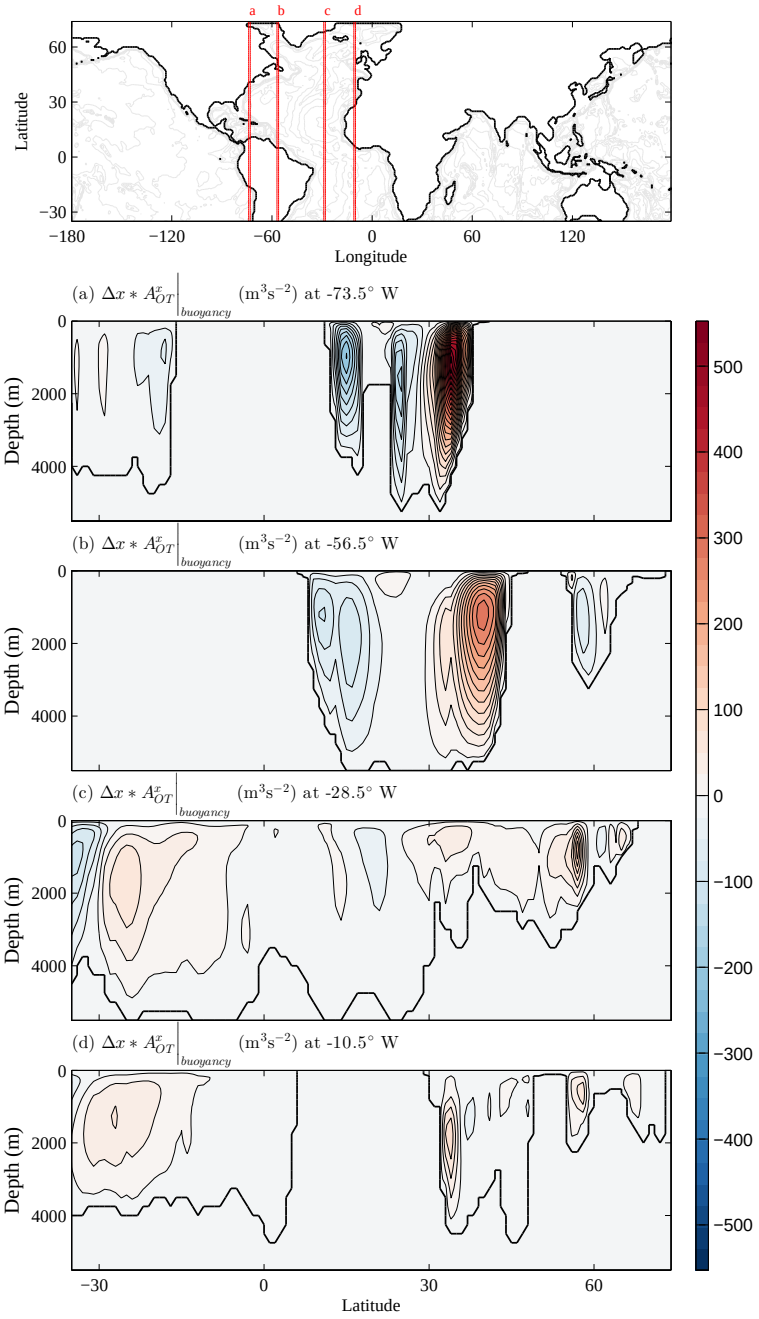

Figure 6.44: Zonal component of the buoyancy overturning force function, $\mathrm{A}^x_{\mathrm{OT}}\Big|_{\mathrm{buoyancy}}$, integrated across one grid cell width at (a) 73.5°W, (b) 56.5°W, (c) 28.5°W and (d) 19.5°W , for comparison to Ψ^x_{OT} in figures 6.35d, 6.36h, 6.38n and 6.39q. The contour interval is 25 $\mathrm{m^3s^{-2}}$. The 0 $\mathrm{m^3s^{-2}}$ contour has been omitted. Positive values indicate sinking to the north. In the top panel the bathymetry is contoured in grey with an interval of 1000 m. In panels (a)-(d) the black contour delineates the ocean floor.

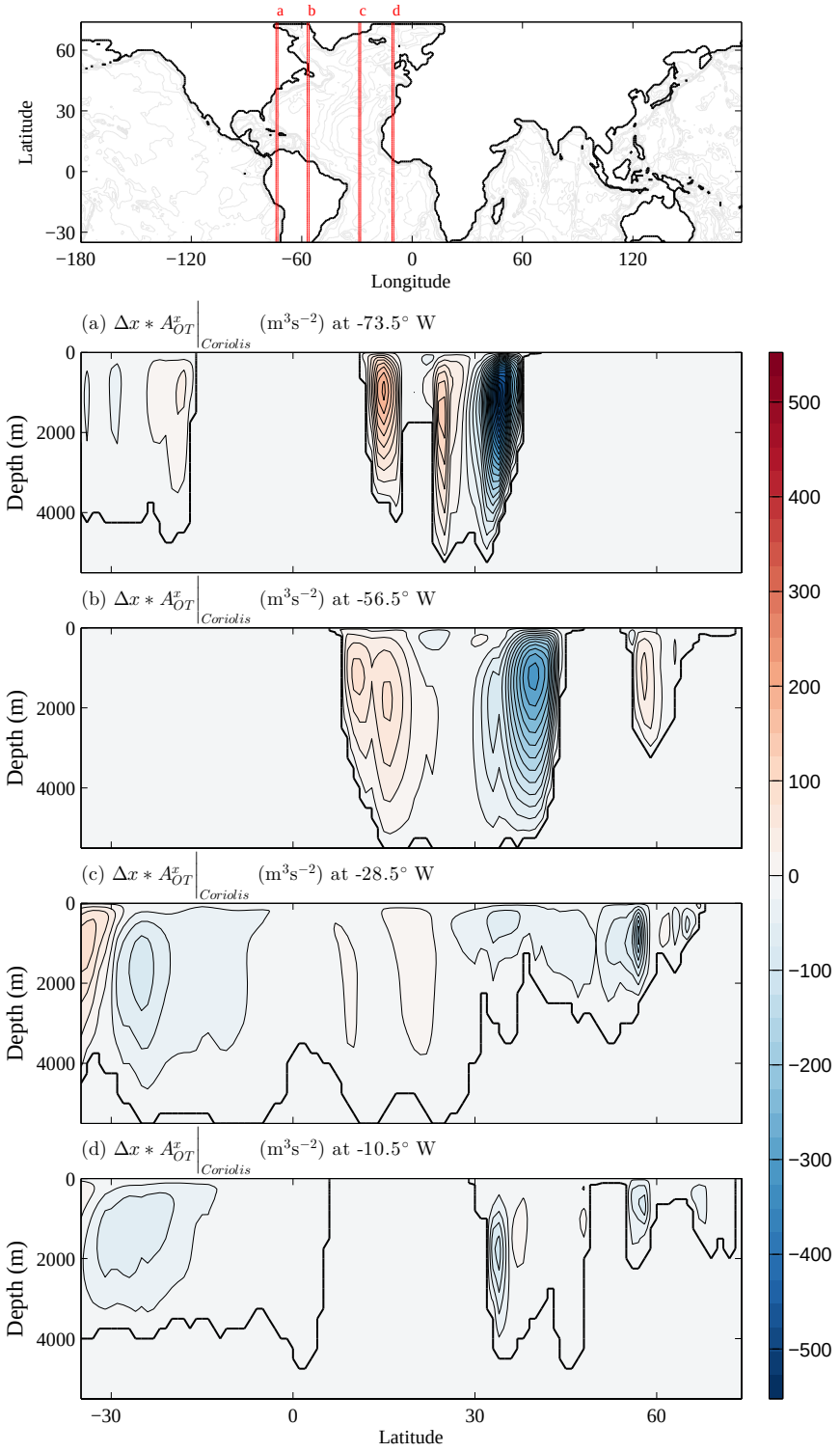

Figure 6.45: As for figure 6.44 but for the Coriolis overturning force function $\mathrm{A}^{x}_{\mathrm{OT}}\big|_{\mathrm{Coriolis}}$.

sinking MOC. At high northern latitudes, the polar synoptic winds flowing south-eastwards over the North Atlantic drive westward Ekman velocities, which result in an eastern sinking ZOC and a southern sinking MOC over the Labrador and western GIN Seas. The modelled Ekman velocity is confined to the surface layer of the model, but the vertical shear in the Ekman velocity, and consequently $\mathrm{A}^x_{\mathrm{OT}}\Big|_{\mathrm{wind}}$, extends through the full depth of the basin. Although it is not resolved in figure 6.47, close inspection of $\mathrm{A}^x_{\mathrm{OT}}\Big|_{\mathrm{wind}}$ confirms that the associated MOC does close in the surface layer (upper 10 m) of the model.

Where the rotational wind forcing (figure 6.47) cannot explain the deviation from geostrophic balance (figure 6.46), rotational dissipation and inertia must be considered. $\mathrm{A}^x_{\mathrm{OT}}\Big|_{\mathrm{dissipation}}$ is the same order of magnitude as $\mathrm{A}^x_{\mathrm{OT}}\Big|_{\mathrm{wind}}$, but is confined to the vicinity of the boundary jets and the surface layers (figure 6.48). $\mathrm{A}^x_{\mathrm{OT}}\Big|_{\mathrm{inertia}}$ is an order of magnitude smaller than $\mathrm{A}^x_{\mathrm{OT}}\Big|_{\mathrm{dissipation}}$ and is confined to the vicinity of the boundary jets (figure 6.49). At the Equator rotational inertia is nonzero, but it plays a negligible role in achieving cross-equatorial overturning, relative to the rotational wind forcing (figure 6.47).

In steady state, the residual overturning force function (computed by combining $\mathrm{A}^x_{\mathrm{OT}}$ for buoyancy, Coriolis, wind, inertia and dissipation) must be close to zero (a small offset is expected due to truncation error). However, here we examine the momentum budget in a single timestep and the tendency term may be non-negligible on such short (1 hour) timescales (*Ponte and Rosen*, 1994). The residual force function, $\mathrm{A}^x_{\mathrm{OT}}\Big|_{\mathrm{residual}}$, is plotted in figure 6.50. The maximum amplitude of the residual is 1 $\mathrm{m^3 s^{-2}}$. On integrating across the basin (figure 6.51), the net acceleration inferred is the same order of magnitude as the modelled tendency of ψ_{AMOC}.

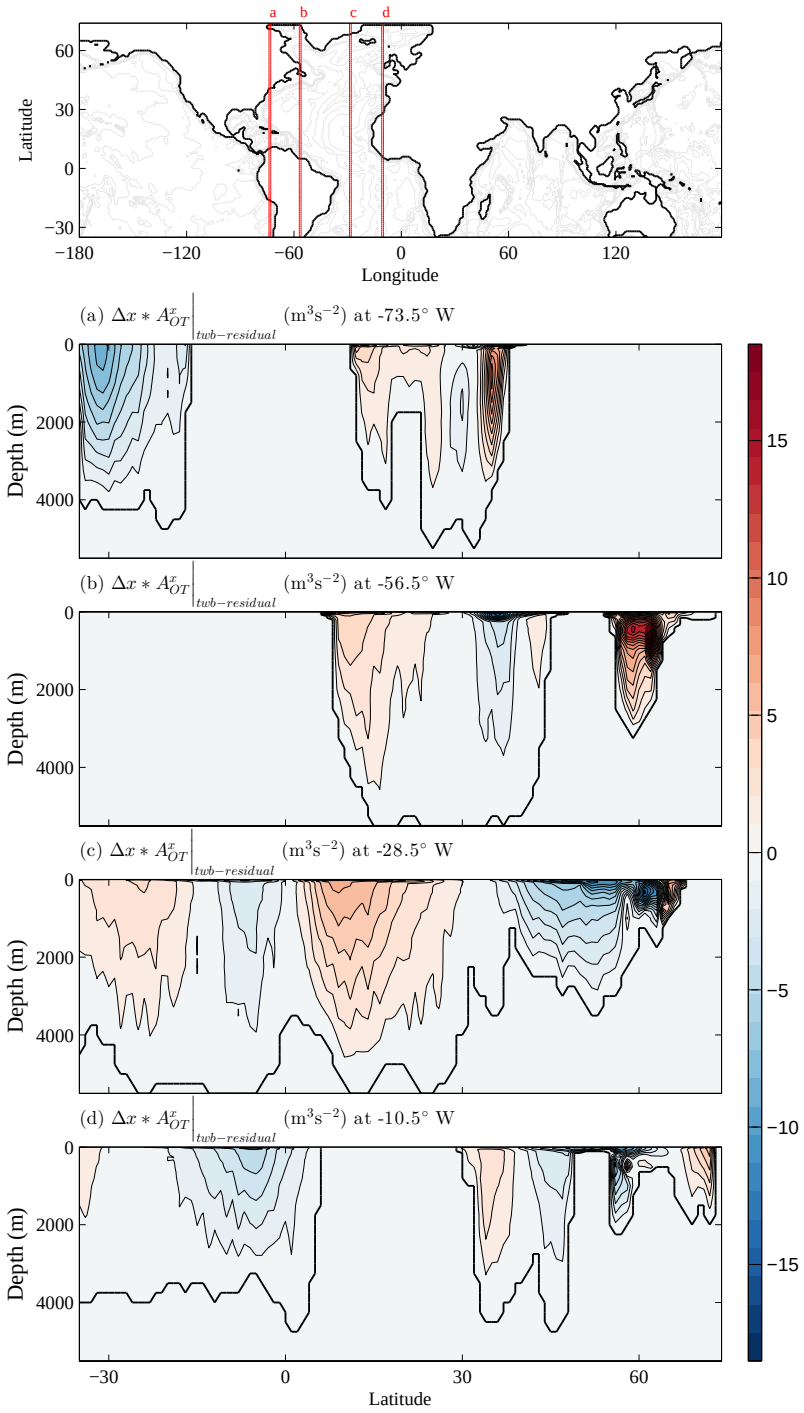

Figure 6.46: As for figure 6.45 but for the net overturning arising due to Coriolis and buoyancy forces combined, $\mathrm{A}^x_{\mathrm{OT}}\big|_{\mathrm{Coriolis}} + \mathrm{A}^x_{\mathrm{OT}}\big|_{\mathrm{buoyancy}}$. The contour interval is 0.5 $\mathrm{m}^3\mathrm{s}^{-2}$.

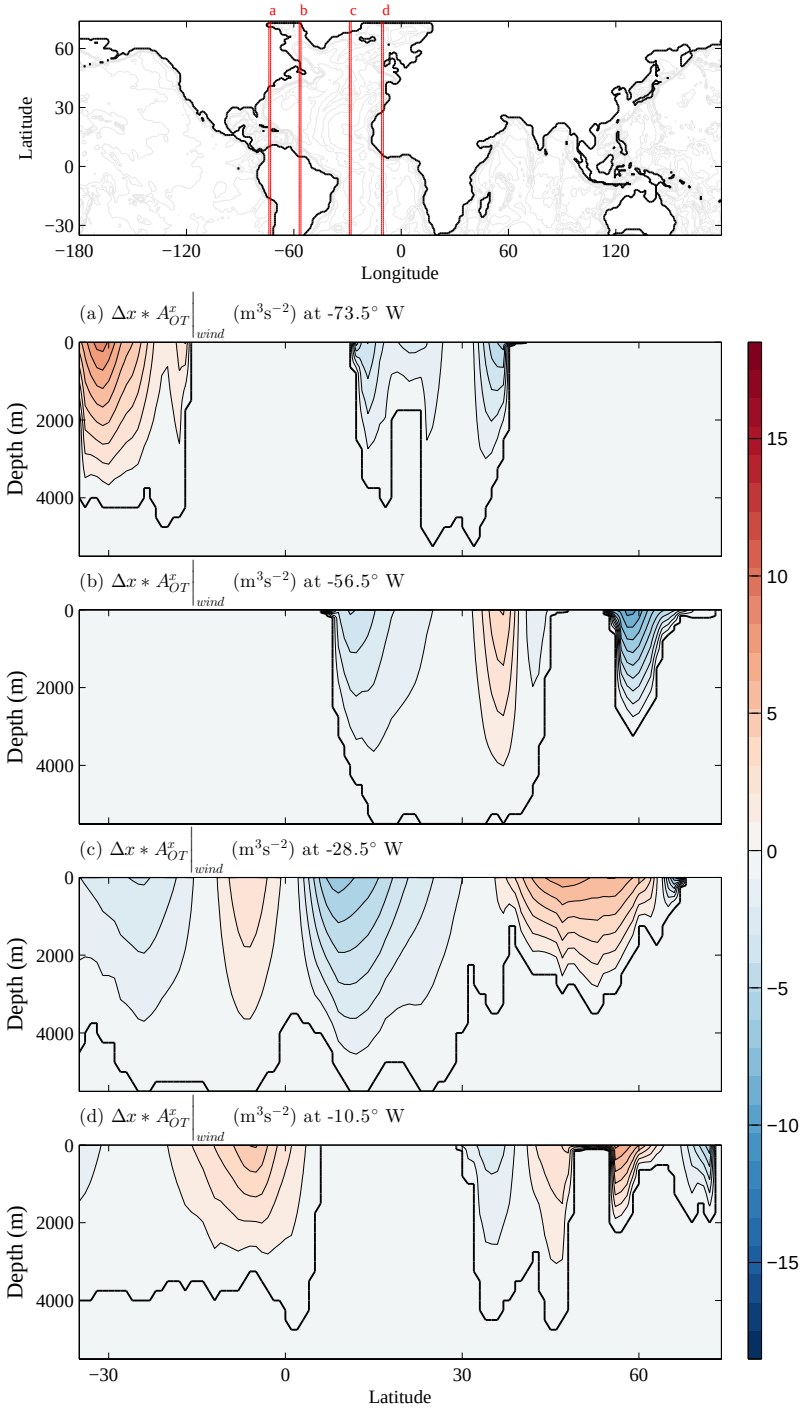

Figure 6.47: As for figure 6.45 but for the wind overturning force function $\mathrm{A}^x_{\mathrm{OT}}\big|_{\mathrm{wind}}$. The contour interval is 0.5 $\mathrm{m}^3\mathrm{s}^{-2}$.

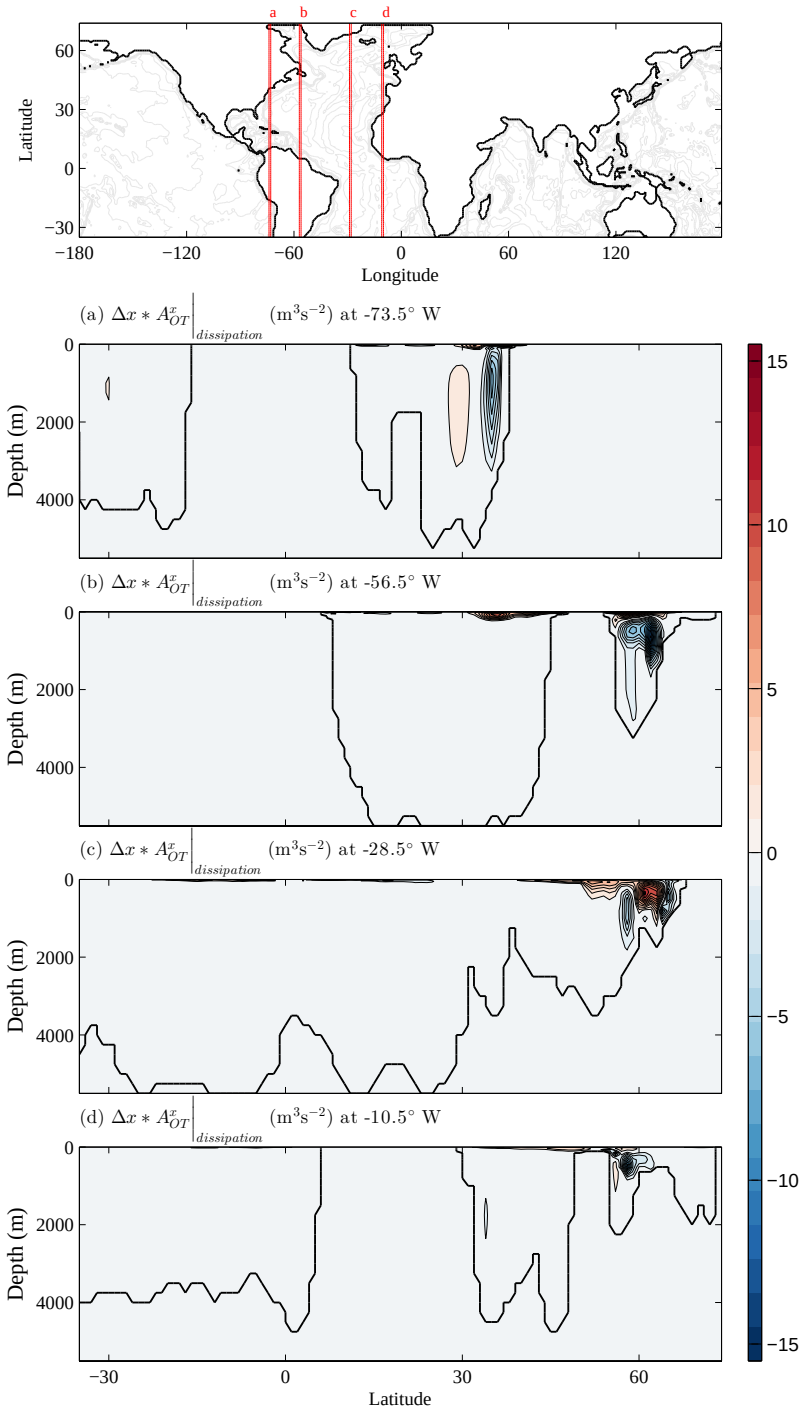

Figure 6.48: As for figure 6.45 but for the dissipation overturning force function $\mathrm{A}^x_{\mathrm{OT}}\big|_{\mathrm{dissipation}}$. The contour interval is 1 $\mathrm{m}^3\mathrm{s}^{-2}$.

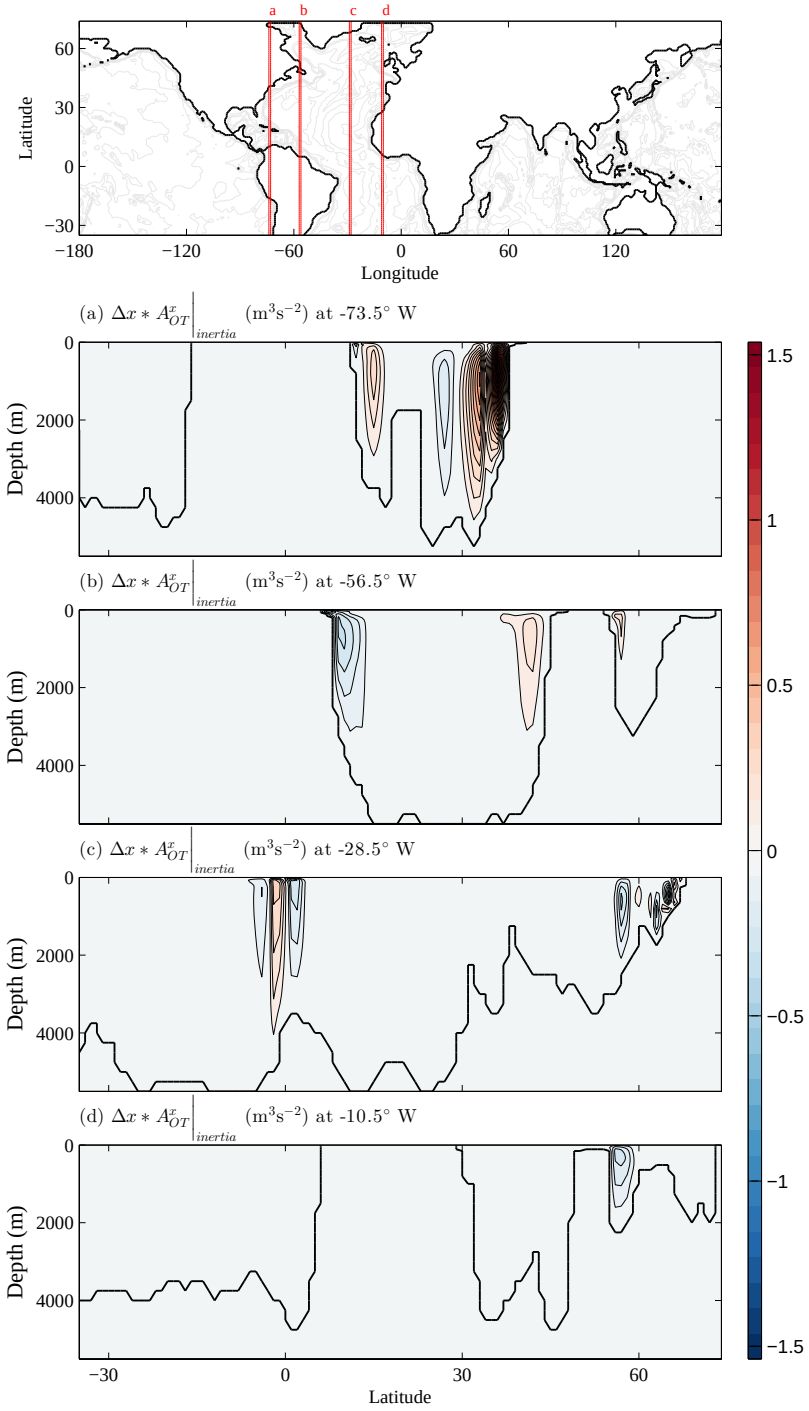

Figure 6.49: As for figure 6.45 but for the inertial overturning force function $\mathrm{A}^{x}_{\mathrm{OT}}\big|_{\mathrm{inertia}}$. The contour interval is 0.1 $\mathrm{m}^3\mathrm{s}^{-2}$.

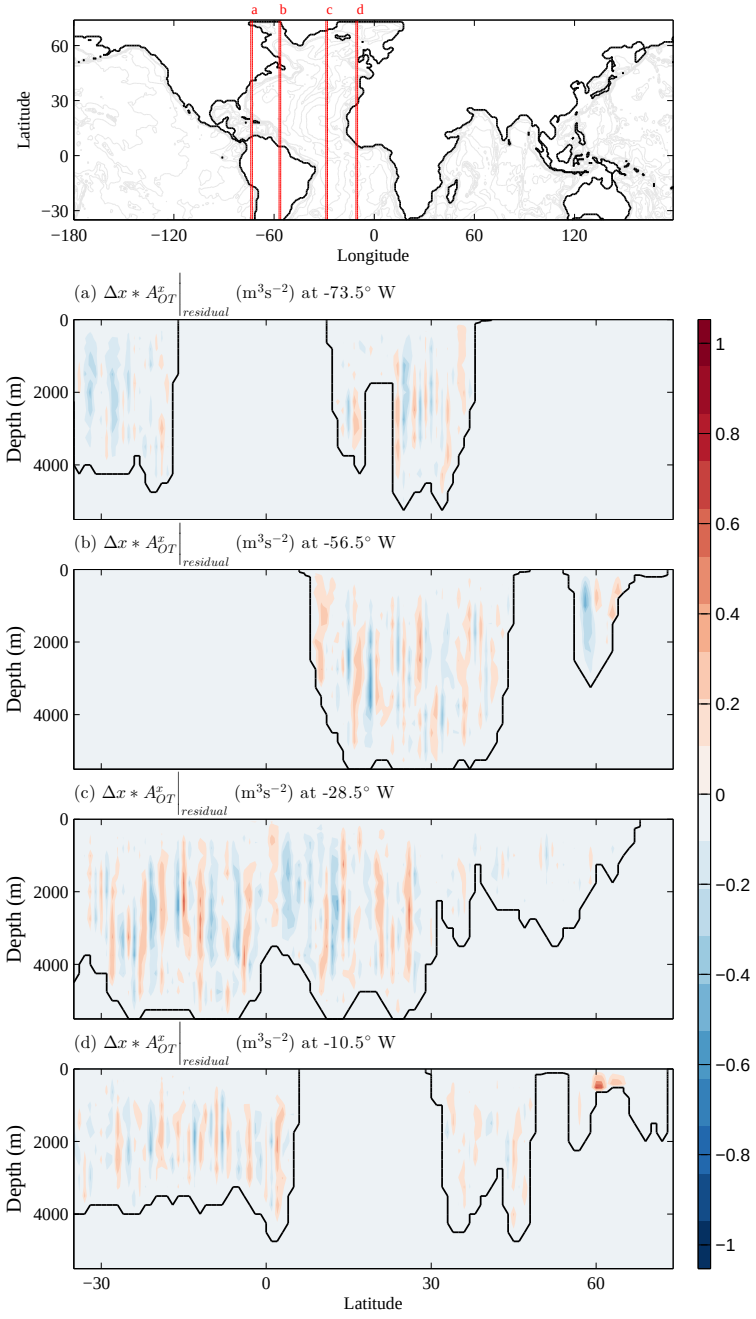

Figure 6.50: As for figure 6.45 but for the residual zonal component of the overturning force function (m^3s^{-2}), resulting from the sum of Coriolis, buoyancy, wind, dissipation and inertial force functions.

.

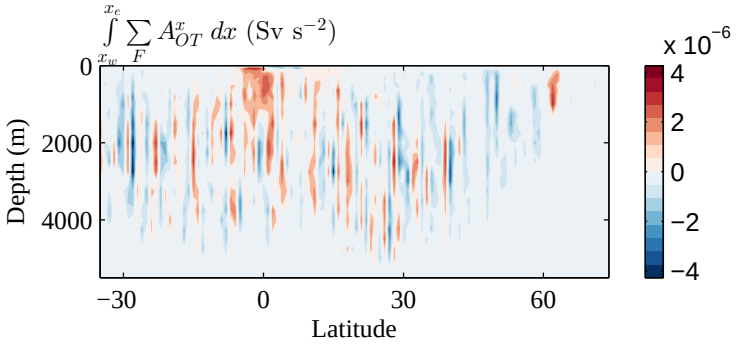

Figure 6.51: Basinwide integral of the residual zonal component of the overturning force function, $\mathrm{A}^x_{\mathrm{OT}}\Big|_{\mathrm{residual}}$, (Sv s^{-1}) resulting from the sum of Coriolis, wind, dissipation and inertial force functions.

6.4 Conclusions and Discussion

In this chapter, we have aimed to diagnose the rotational momentum budget governing the instantaneous 3-dimensional circulation in a GCM. Careful consideration was given to the proper discretisation of the rotational momentum terms to (i) achieve an accurate decomposition and (ii) facilitate comparison of the relevant terms with ψ_{AMOC}. Key details of the calculation were presented for the C-grid model.

To instill confidence in our approach, we started by exploring a highly idealized domain, wherein the Atlantic basin is represented as a flat-bottomed sector. In this case, we were able to show that the computation of the velocity potential, $\mathbf{\Psi}$, and force function, $\mathbf{A}$, is both straightforward and accurate. Even for this simple geometry, it is challenging to visualise the 3-dimensional circulation using velocity vectors. However, by examining components of $\mathbf{\Psi}$, the 3-dimensional circulation clearly emerges from profiles of the local MOC and ZOC. Although our focus is on the MOC, we have demonstrated that a clear view of the ZOC is of great help in understanding generation of the vertical shears MOC.

In a flat-bottom basin, the AMOC is fully accomplished as a vertical shears mode. By examining components of the associated vertical shears force function, $\mathrm{A}^x_{\mathrm{OT}}$, the maintenance of the modelled ψ_{AMOC} is elucidated. The circulation is in approximate thermal wind balance throughout the basin, which is manifested as equal and opposite $\mathbf{A}_{\mathrm{OT}}$ associated with the Coriolis and buoyancy forces. On the western boundary alone, the rotational buoyancy force accelerates an interhemispheric MOC, which displays notable qualitative similarity to the modelled ψ_{AMOC}. This is perhaps understood by noting that since the meridional velocity is almost exactly geostrophic everywhere and the basin is flat-bottomed, ψ_{AMOC} is proportional to the density difference between the east and west boundaries. We determine that the rotational buoyancy forcing is small on the eastern boundary - excluding the northernmost latitudes - and as a result, ψ_{AMOC} displays qualitative similarity to the buoyancy

A^x_{OT} on the western boundary at all latitudes further south. This observation has stimulated the derivation of a new scaling for ψ_{AMOC}, which will be presented in the next chapter of this thesis.

We have extended the analysis of the rotational momentum budget to a globally realistic domain, presenting solutions for the vertical shears component of the velocity potential, $\mathbf{\Psi}_{OT}$, and force function, $\mathbf{A}_{OT}$. The picture that emerges from this analysis is of a truly three-dimensional flow field, with far greater complexity than is alluded to by examining ψ_{AMOC} alone. In the South Atlantic, northern sinking meridional overturning is a signature of the interior, subtropical gyre circulation. Between the Equator and a latitude of approximately 35°N, the northern sinking meridional overturning is predominantly a signature of the attached western boundary jet system. Polewards of this latitude, the northern sinking meridional overturning is a signature of the North Atlantic Current. The zonally-integrated northern sinking cell comprises these three distinct dynamical regimes. With this view, it is perhaps not surprising that ψ_{AMOC} may not vary coherently across the full latitudinal extent of the zonally integrated cell, as suggested by recent observational (*Lozier et al.*, 2010) and modelling (*Bingham et al.*, 2007) studies. These studies present evidence for a disconnect in the meridional overturning at the southern boundary of the subpolar gyre, issuing a strong caution in extrapolating AMOC variations recorded at any one latitude to other parts of the basin. This also calls into question the suitability of ψ_{AMOC} as a sensible metric of oceanic variability and climate change.

6.4.1 Limitations

A serious limitation of the present study is the failure to compute the barotropic velocity potential, Ψ_{BT}, and associated force function, A_{BT}, in a realistic domain with multiply connected boundaries. The challenge is in determining the proper Dirichlet condition prior to inverting the associated elliptic problems. In sections 5.2.4 and

5.2.6 we presented solution methods for determining the Dirichlet conditions on Ψ_{BT} and A_{BT} respectively. It is likely that at present, our calculation is failing to correctly identify all distinct bounding segments and assign to each one a single Dirichlet condition.

The diagnosis of the rotational momentum budget governing the external mode of the MOC is an essential extension to the work presented in this chapter. The external mode is an elusive quantity in observations, presenting a challenge in monitoring the AMOC. Diagnosis of the external mode would be a significant contribution in allowing us to assess the representativeness of hydrographic estimates of the ψ_{AMOC}, where the measured geostrophic vertical shears transport must be superimposed on a reference level velocity to obtain the absolute transport. Uncertainties in bottom pressure (or velocity) measurements can plague the calculation of the reference level velocities. By monitoring latitudes where the external mode is negligible, these errors in transport estimate can be minimized (*Sime et al.*, 2006). This issue is particularly pertinent for the mooring array at 26°N (*Cunningham et al.*, 2007) where the external mode is not explicitly resolved. By assessing the residual between the full AMOC and the vertical shears component, we suggest that ψ_{AMOC} could be accomplished as an external mode at this latitude (in agreement with *Sime et al.*, 2006).

The decomposition has been applied to the instantaneous momentum balance, but can equally be applied to the time-mean momentum balance. An important extension would be to determine the relative variability achieved by external and overturning modes on different timescales, and subsequently, to elucidate the responsible forcing mechanisms. A suitable framework for the exploration of multidecadal variability would be a state estimation product. The numerical tools are in place to immediately follow this lead using the ECCO/GECCO products which work within the dynamical framework of the MITgcm, as used in the present study.

6.4.2 Implications

It is our hope that the work presented in this chapter has implications for future modelling and observational efforts. The potential implications for future observational efforts discussed above rely on the successful determination of the external mode in our future work. However, from the solutions already presented for the vertical shears MOC, we may immediately suggest that the force function and velocity potential components are powerful diagnostics for complex GCMs. We envisage that the rotational momentum framework will prove a useful tool in future ensemble experiments and inter-comparison projects, where - amid huge quantities of information - we seek to perform a mechanistic assessment of simulated differences as succinctly as possible.

The 2-dimensional AMOC streamfunction, ψ_{AMOC}, is a commonly favoured metric of oceanic variability and broader climate change. However, our analysis presented in this chapter suggests that the zonal integral may mask important features of the 3-dimensional flow field. At high latitudes, we showed that the subpolar gyre generates a complex array of counter-rotating meridional overturning cells. These are achieved both as vertical shears and external modes of the AMOC. Upon zonal integration, there is a large degree of cancellation, in both components; from our preliminary analysis, we suggest that the external mode entirely vanishes. In agreement with the recent study by *Thomas* (2012), we conclude that the net (zonally-integrated) volume transport is an over-simplification of the high-latitude circulation. We propose that the rotational momentum analysis makes a 3-dimensional view of the circulation more tractable and - in this example - has the potential to provide a more useful description of exchange between the subpolar oceans and the rest of the Atlantic basin.

Chapter 7

Key Role of Western Boundary Buoyancy Gradients

7.1 Introduction

Due to the complexity of the equations governing the ocean circulation, great effort has been invested in seeking a simple relation between ψ_{AMOC} and basic metrics of the ocean state. The AMOC has classically been viewed as a gravity current responding directly to the meridional density gradient (MDG). However, it is not clear how this picture fits with expectations from large scale thermal wind balance that the steady-state flow should circulate around density anomalies, not between them. Nevertheless, this simple argument, combined with the predicted decrease of high latitude sea surface density in most studies of future climate, has stimulated particular interest in the role of the MDG in the variability of ψ_{AMOC}.

7.1.1 Past Work

Classical analytical arguments (e.g. *Lineikin*, 1955; *Robinson and Stommel*, 1959) are based on the scaled equation for thermal wind balance, combined with the assump-

tion that zonal and meridional density gradients are proportional. This assumption, combined with the additional assumption that the scale depth, D, for the overturn is constant produces a linear relation between the AMOC and the MDG:

$$\psi_{\mathrm{AMOC}} \sim VLD \sim \frac{g\Delta_x \rho D^2}{\rho_0 f_0} \sim \frac{g\Delta_y \rho D^2}{\rho_0 f_0}, \tag{7.1}$$

where V and L are representative scales for the meridional velocity and basin width. g, ρ_o and f_0 are reference values for gravity, density and the Coriolis parameter respectively. The discrete meridional density difference (MDD), $\Delta_y \rho$, maintains a characteristic value from the surface to $z = -D$. Extensions to this theory have been presented to permit variations in D, leading to a range of power-law scalings. For example, *Munk* (1966) proposed that D is controlled by a vertical advective-diffusive balance so that

$$D \sim \frac{k_v}{W}, \tag{7.2}$$

where k_v is the vertical diffusivity and W is a representative scale for the vertical velocity. Substituting for D in (7.2)

$$\psi_{\mathrm{AMOC}} \sim VLD \sim \frac{g\Delta_y \rho \kappa_v^2}{W^2 \rho_0 f_0}. \tag{7.3}$$

W may be eliminated using the scaled continuity equation

$$WL \sim VD, \tag{7.4}$$

$$WL^2 \sim VDL, \tag{7.5}$$

$$W \sim \frac{\psi_{\mathrm{AMOC}}}{L^2}. \tag{7.6}$$

Substituting (7.6) into (7.3), the AMOC is seen to scale with the cube root of the MDD:

$$\psi_{\mathrm{AMOC}} \sim \left(\frac{gL^4k_v^2}{\rho_0 f_0}\right)^{1/3} \Delta_y \rho^{1/3}. \tag{7.7}$$

However, as discussed by *de Boer et al.* (2010), the assumed similarity between the strength of the meridional and zonal density differences $\Delta_y\rho \sim \Delta_x\rho$, is not necessarily valid. It is equivalent to assuming similarity between the characteristic zonal and meridional velocity scales, $U \sim V$. This may be true in the interior of the basin where pointwise thermal wind balance holds. This assumption is unrealistic if - as indicated in the previous chapter of this thesis - AMOC adjustment is contained within the boundary current system (see also *de Boer and Johnson*, 2007). In this case, V may exceed U by a few orders of magnitude.

A range of theoretical arguments have been proposed to relate zonal and meridional density differences on the basin scale, producing estimates of $\Delta_x\rho$ and $\Delta_y\rho$ that are of similar magnitude (*Wright and Stocker*, 1991; *Wright et al.*, 1995; *Marotzke*, 1997). Good agreement ($O(\Delta_x\rho) = O(\Delta_y\rho)$) has also been found in general circulation models (e.g *Park and Bryan*, 2000). As a result, substantial support for a linear AMOC-MDD relation has been provided by investigations using general circulation models configured in both highly idealised (*Hughes and Weaver*, 1994) and realistic (*Rahmstorf*, 1996; *Thorpe et al.*, 2001; *Griesel*, 2006; *Dijkstra*, 2008) domains.

Yet, a general consensus on the true AMOC-MDD relation is far from being reached. Many box model studies designed to probe the existence of multiple equilibrium states are often founded on the a priori assumption that the linear AMOC-MDD relation is valid (*Stommel*, 1961; *Rooth*, 1982; *Scott*, 2000). However, the *Stommel* (1961) model has also been adapted to prescribe the exchange between boxes as a nonlinear function of the MDD. *Cessi* (1994) proposes a dependence of the flow rate on the density difference squared, while *Park* (1999) assumes the *Bryan and Cox* (1967) scaling in equation (7.7), following published support for the dependence of

the AMOC on $k_v^{2/3}$ (e.g *Winton*, 1996; *Marotzke*, 1997; *Park and Bryan*, 2000). Further complication arises from GCM-based suggestions of an anti-correlation between the modelled AMOC and certain measures of the MDD (*Nilsson et al.*, 2003; *de Boer et al.*, 2010).

As discussed in detail by *de Boer et al.* (2010), the disagreement in the analysed AMOC-MDD relation is due in part to inconsistencies in the exact definition of the terms in the scaling. The vertical scale, D, is most commonly assumed to be the depth of the maximum overturning or the thermocline depth, and these two scales are often assumed to be equal. The MDD may be defined as the pole-to-equator density difference or the inter-hemispheric difference; measured at the sea surface or depth-averaged over D. Furthermore, with the exception of the study by *de Boer et al.* (2010), previous correlations between the AMOC and the MDD have only indicated mutual variability. It is more insightful to identify cause and effect. The experiment design in *de Boer et al.* (2010) will be discussed in detail in the following section. In summary, it allows the dynamic effects of density to be distinguished from the passive effects, so that the sensitivity of the AMOC to changes in the MDD can be unambiguously determined. The authors find a robust correlation between the AMOC and the MDD only when the MDD is depth-averaged between the surface and the turning point of the overturning. When alternative depth scales - including the traditional choice of the thermocline depth - are assumed, the modelled AMOC cannot be predicted from the MDD. For some choices of depth scale, a negative correlation is found between the AMOC and the depth-integrated MDD. This highlights the important role of the remote wind forcing, which the authors identify as a key mechanism modulating the turning depth of the overturn, thus implicitly contributing to the AMOC-MDD relation.

In chapter 5 of this thesis, we presented a new approach to map the rotational component of the forcing fields onto the local fluid acceleration. We introduced a

trio of scalar force functions allowing the projection of the forcing onto barotropic, zonal overturning and meridional overturning circulations to be viewed in isolation. In chapter 6 of this thesis, we demonstrated that in a flat-bottomed ocean, the structure of the rotational buoyancy forcing on the western boundary displays remarkable similarity to ψ_{AMOC}. This observation prompts the derivation of two new analytical AMOC-MDD scalings below, employing the rotational momentum approach to inform changes in both the strength and structure of the AMOC with the MDD.

7.1.2 Chapter Outline

We start by deriving a linear AMOC-MDG relation by examining the analytical expression for MOC generation by the rotational buoyancy forcing in section 7.2.1. Consistent with the empirical scaling presented by *de Boer et al.* (2010), it emerges that the relevant MDG is depth-integrated between the surface and the turning point of ψ_{AMOC}. Having presented this analytical scaling, we seek to provide empirical support. In section 7.2.2 we describe the design of the numerical experiment. We assess the performance of the scaling in section 7.2.3, illustrating how in the present framework, we may recover changes in both the strength and structure of the overturning by monitoring the MDG. Encouraged by the qualitative similarity of the buoyancy force function and ψ_{AMOC} on the western boundary, we conclude the results section by deriving a new scaling for the AMOC as a function of the MDG right on the western boundary.

7.2 A Linear AMOC-MDG Scaling

7.2.1 Derivation

In chapter 5 of this thesis, we showed that AMOC generation by a given force, $\mathbf{F}$, is described by the basinwide integral of the zonal component of the associated force

function, **A**:

$$\left.\frac{\partial \psi_{\mathrm{AMOC}}}{\partial t}\right|_{\mathbf{F}} = \int_{x_w}^{x_e} \left.\mathrm{A}^x\right|_{\mathbf{F}} dx, \tag{7.8}$$

where A^x can be decomposed into vertical shears, $\mathrm{A}^x_{\mathrm{OT}}$, and external mode, $z/H\ \mathrm{A}_{\mathrm{BT}}\ \partial H/\partial x$, contributions. The buoyancy force, acting only in the vertical, cannot generate an external mode. Consequently, AMOC generation by buoyancy forcing is fully described by the vertical shears mode:

$$\left.\frac{\partial \psi_{\mathrm{AMOC}}}{\partial t}\right|_{\mathrm{buoyancy}} = \int_{x_w}^{x_e} \left.\mathrm{A}^x_{\mathrm{OT}}\right|_{\mathrm{buoyancy}} dx. \tag{7.9}$$

In section 5.3.1, we showed analytically that $\left.\mathrm{A}^x_{\mathrm{OT}}\right|_{\mathrm{buoyancy}}$ describes AMOC generation by tilting of planetary vorticity, f, into the $y-z$ plane by vertical shear in the zonal geostrophic velocity, u_g:

$$\left.\mathrm{A}^x_{\mathrm{OT}}\right|_{\mathrm{buoyancy}} = f \int_{-H}^{z} u_g - \overline{u_g}^z \, dz = f \int_{-H}^{z} u_g \, dz - f\left[\overline{u_g}^z z\right]_{-H}^{z}. \tag{7.10}$$

Using the chain rule for integration we may write

$$\int_{-H}^{z} u_g \, dz = \left[u_g z\right]_{-H}^{z} - \int_{-H}^{z} \frac{\partial u_g}{\partial z} z \, dz. \tag{7.11}$$

Employing the geostrophic/thermal wind equation to replace the geostrophic velocity/velocity shear with pressure/density gradients it follows that

$$\left.\mathrm{A}^x_{\mathrm{OT}}\right|_{\mathrm{buoyancy}} = \frac{g}{\rho_0} \int_{z}^{0} \frac{\partial \rho}{\partial y} z \, dz + \frac{1}{\rho_0}\left[\left(\frac{\partial p}{\partial y} - \overline{\frac{\partial p}{\partial y}}^z\right) z\right]_{z}^{0}, \tag{7.12}$$

where the sense of integration has been reversed. Finally, the integral limit z is set equal to the depth at which the AMOC attains its maximum, $z = Z_{\max}(y,t)$. At

this stagnation point, the meridional pressure gradient vanishes leaving

$$\mathrm{A}^x_{\mathrm{OT}}\Big|_{\mathrm{buoyancy}} = \frac{g}{\rho_0}\int_{-Z_{\max}}^{0} \frac{\partial \rho}{\partial y} z \, dz. \tag{7.13}$$

Integrating across the basin yields an analytical expression relating the maximum AMOC (at $z = Z_{\max}$) to the depth-averaged MDG from (7.9)

$$\frac{\partial \psi_{\ \mathrm{AMOC}}}{\partial t}\Big|_{\mathrm{buoyancy}} = \int_{x_w}^{x_e} \frac{\partial \Psi^x_{\mathrm{OT}}}{\partial t}\Big|_{\mathrm{buoyancy}} dx = \frac{g}{\rho_0}\int_{x_w}^{x_e}\int_{-Z_{\max}}^{0} \frac{\partial \rho}{\partial y} z \, dz \, dx. \tag{7.14}$$

This is a complete description of AMOC generation by buoyancy forcing. Consistent with the empirical scaling presented by *de Boer et al.* (2010), it is suggested that ψ_{AMOC} scales linearly with the MDG, where the relevant MDG is depth-integrated between the surface and the turning point of ψ_{AMOC}. An unsatisfactory aspect of this scaling, however, is that to predict the response of ψ_{AMOC}, part of the solution must be known in advance; $Z_{\max}$ appears on the right hand side of (7.14). When the full depth force function (7.12) is retained, we avoid this issue, and can recover changes in both the strength and full-depth structure of ψ_{AMOC}. We now proceed to provide empirical support for the proposed linear AMOC-MDG relation.

7.2.2 Numerical Experiment Design

We perform an ensemble investigation based on the study by *de Boer et al.* (2010). The control integration (CONTROL) is the highly idealised reentrant channel model presented in chapters 2 and 6 of this thesis. The perturbed suite (WS) is designed to produce variations in $Z_{\max}$. Five perturbation experiments are run about CONTROL, in which the wind stress is multiplied by a factor $\alpha = 0.5$, 0.75, 1.5, 2.0 and 3.0. These integrations will be referred to as 050tau, 075tau, 150tau, 200tau and 300tau respectively. The eddy diffusivity, κ_{GM}, is held constant across the ensemble.

Arguments based on linear baroclinic instability (e.g *Killworth*, 1997) or mechanical energy balances (*Abernathey et al.*, 2011) suggest that κ_{GM} should increase with increasing wind stress. The present, unrealistic eddy representation is important in producing a broader range of AMOC turning points, $Z_{\max}(y,t)$, so that the scaling (7.14) may be properly tested.

All six model integrations are initialised from rest with a globally homogeneous salinity field and a horizontally homogeneous temperature field. Equilibration is assumed after 3000 model years, when there are no discernible trends in the basin mean kinetic energy or basin mean temperature. All results shown below are averaged over a final 10 year integration

7.2.3 Results: A Range of AMOC States

The steady-state ψ_{AMOC} differenced from CONTROL, is shown in figure 7.1 for all members of WS. The maximum AMOC is shown in figure 7.2. The AMOC weakens with diminished wind stress over the reentrant channel (050tau, 075tau) and is amplified for stronger winds (150tau, 200tau, 300tau), due to a linear dependence of the Ekman transport on α. As the westerly wind increases, enhanced northward export from the channel travels the length of the basin to the northern margin, becoming statically unstable and convecting. The enhanced return flow travels southwards to re-enter the channel at depth. Across the WS suite, the greatest anomalies of meridional overturning are found at high latitudes, where the parameterised eddies are activated in CONTROL. It is suggested that this pattern of amplification is due to an imbalance between the wind-induced and eddy-induced overturnings. The Ekman overturning is linearly dependent on the wind stress, whilst the eddy-driven overturning (limited by fixed κ_{GM}) remains relatively constant throughout the WS suite. The residual ψ_{AMOC} thus amplifies linearly with wind factor (figure 7.2) and the AMOC turning point, $Z_{\max}$, deepens to accommodate a greater northward

volume flux (figure 7.3).

7.2.4 Results: Empirical Support for the Linear Scaling

The modelled overturning is now compared to the prediction from the force function scaling (7.14), for all ensemble members. The MDG is computed as the zonally-and depth-integrated density, differenced between the northernmost grid point and the northern limit of the reentrant channel. The depth-integral is performed between the surface and the turning depth, $Z_{\max}$, at the northernmost grid point, for each ensemble member. Since the scaling (7.14) yields the tendency of ψ_{AMOC}, estimates are normalised by a frequency parameter to obtain a volume flux. Following *de Boer et al.* (2010) this parameter is chosen so that the average estimated ψ_{AMOC} is equal to the mean maximum ψ_{AMOC} in the modelled ensemble. Good agreement between the modelled and estimated maximum ψ_{AMOC} (figure 7.4) thus indicates that the scaling in (7.14) captures the sensitivity of ψ_{AMOC} to changes in $Z_{\max}$ and the MDG.

We have shown that AMOC generation by the buoyancy force scales linearly with the MDG. However, it still remains to be shown whether the absolute value of ψ_{AMOC} may be recovered from the MDG. A key result in chapter 6 of this thesis was the strong qualitative similarity between ψ_{AMOC} and the buoyancy force function right on the western boundary, $\mathrm{A}^x_{\mathrm{OT}}\Big|_{\mathrm{buoyancy}}(x_w, y, z)$, in the idealised experiment. This similarity is manifested throughout the WS suite (figure 7.5).

This observation encourages the development of a new scaling relating ψ_{AMOC} (in place of $\partial\psi_{\mathrm{AMOC}}/\partial t$) to the MDG on the western boundary.

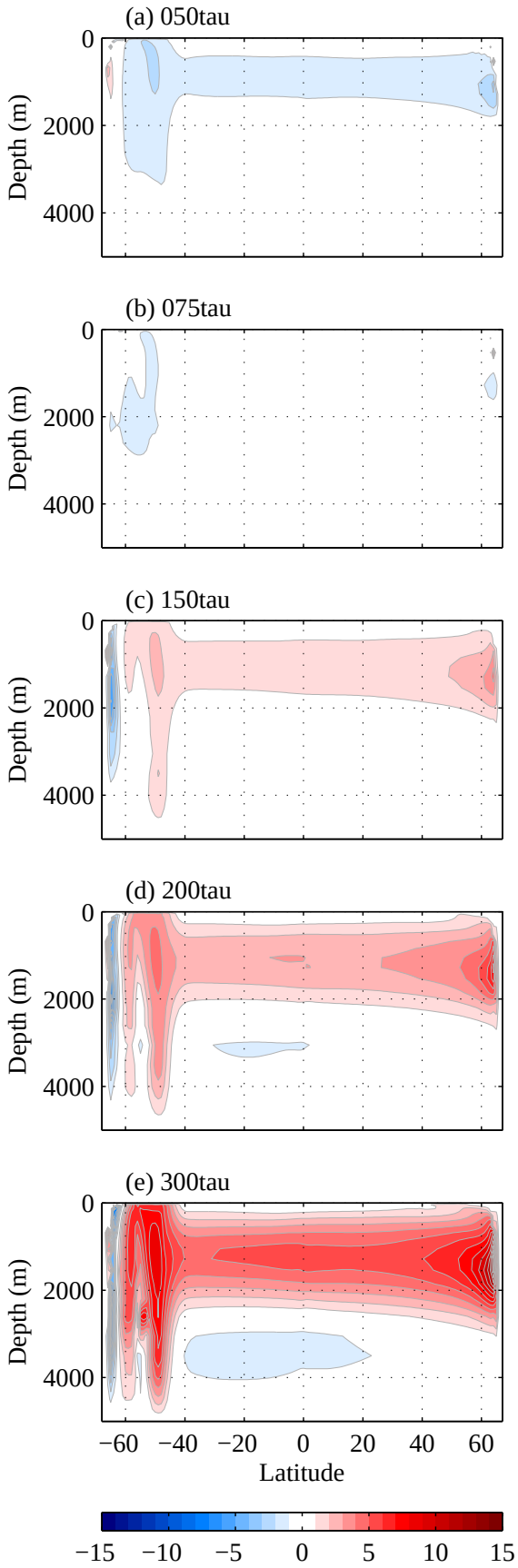

Figure 7.1: ψ_{AMOC} anomaly with respect to the CONTROL for WS ensemble members. The contour interval is 1 Sv (10^6 $\mathrm{m^3 s^{-1}}$). The 0 Sv contour has been omitted. ψ_{AMOC} in CONTROL is shown in figure 2.4 of chapter 2.

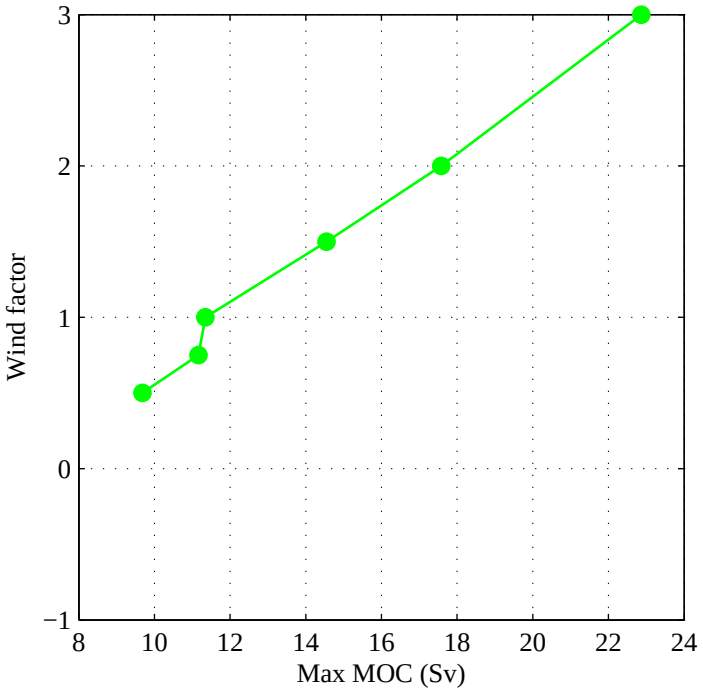

Figure 7.2: The maximum ψ_{AMOC} (Sv) for all members of the WS suite. The CONTROL maximum is plotted at a wind factor of 1.

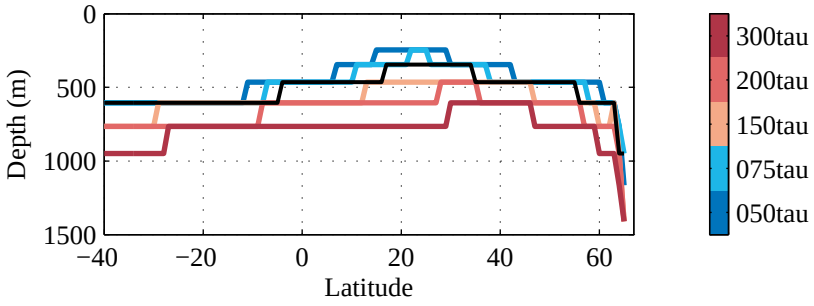

Figure 7.3: Depth of maximum ψ_{AMOC}, Z_{max}, as a function of latitude for the WS suite. The thin black line is Z_{max} for the control integration (corresponding to 100tau). The AMOC deepens for stronger winds (red) and shoals for weaker winds (blue).

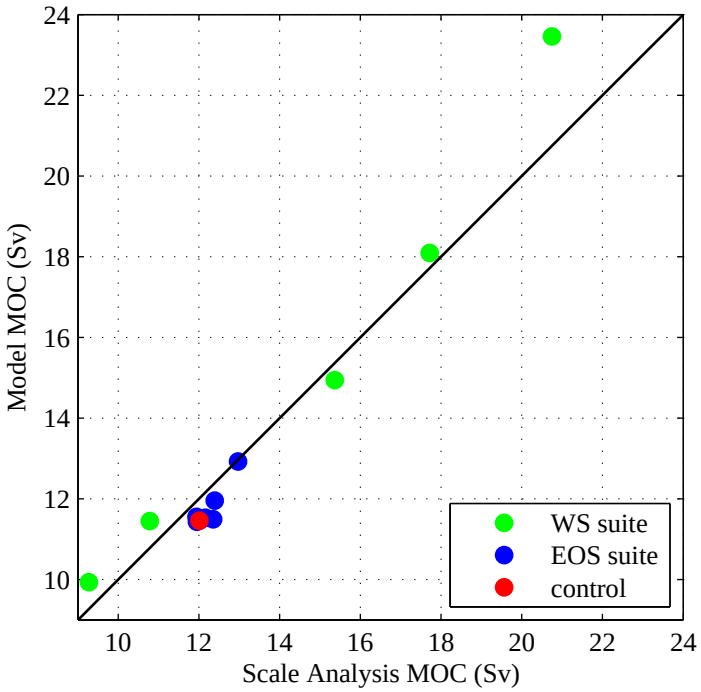

Figure 7.4: Maximum modelled ψ_{AMOC} versus the prediction from the scaling analysis in equation (7.14). Scaled values use a measure of the MDG computed as the difference in the zonally- and depth-integrated density between the northernmost grid point and the northern limit of the reentrant channel. Scaled values are normalised so that their average is equal to the mean modelled overturning.

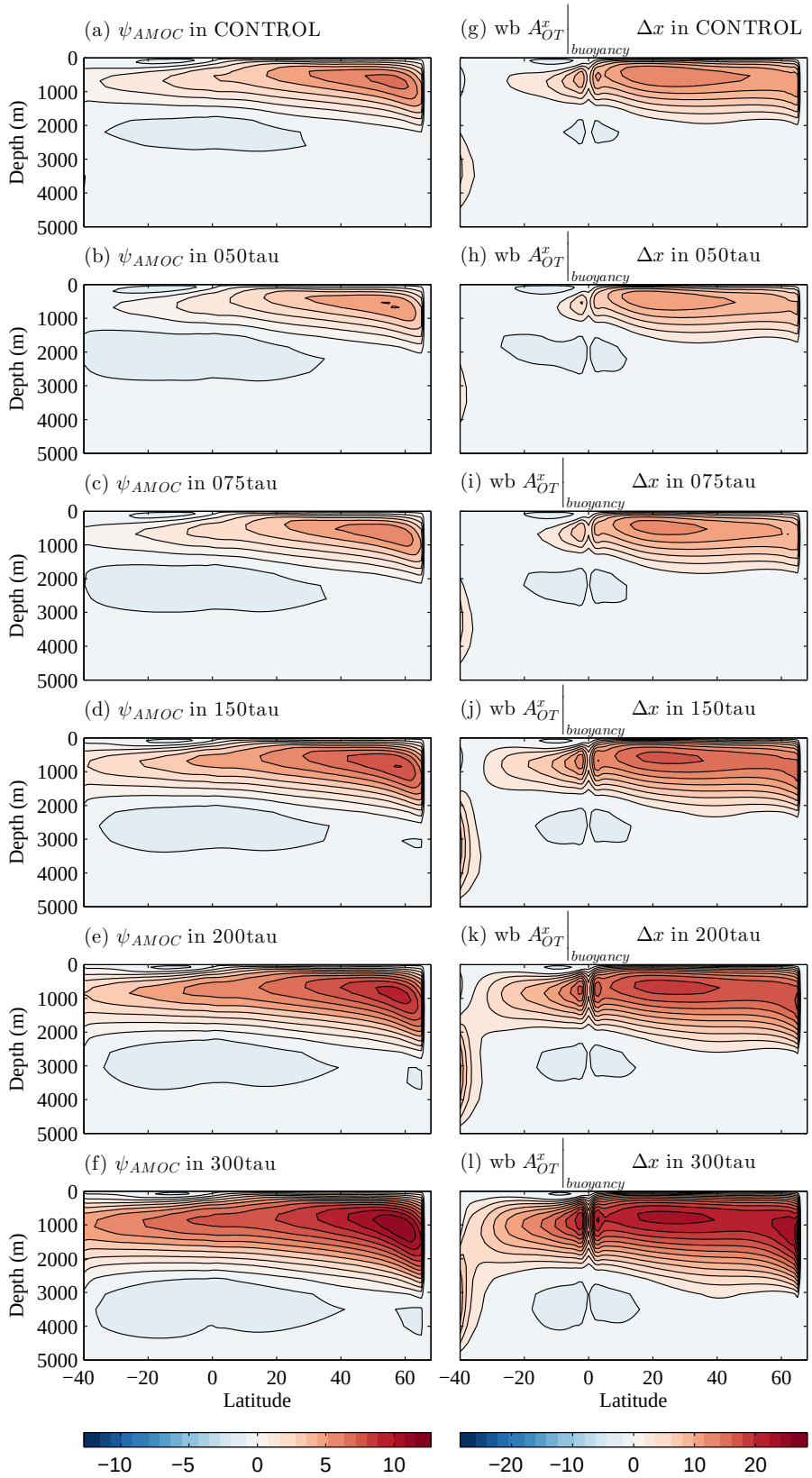

Figure 7.5: Modelled ψ_{AMOC} (left column) in (a) CONTROL and (b)-(f) the WS suite. Zonal component of the buoyancy vertical shears force function, $\mathrm{A}^x_{\mathrm{OT}}$, (right column) in (g) CONTROL and (h)-(l) the WS suite. The contour interval is 1 Sv in the left column and 2 $\mathrm{m}^3\mathrm{s}^{-2}$ in the right column. The zero contour has been omitted.

7.3 The "buoyancy-beta" Scaling

Here, we derive a new semi-empirical scaling for the AMOC. In pursuit of a general expression (i.e. that holds even in the presence of an external mode of the AMOC), we start with the definition of ψ_{AMOC} and work towards incorporating $\mathrm{A}^x_{\mathrm{OT}}\Big|_{\mathrm{buoyancy}}(x_w, y, z)$.

7.3.1 Derivation

Away from the coastlines, the large scale circulation is in geostrophic balance. Within the viscous boundary layers, ageostrophic dynamics are important for the flow perpendicular to the coast, however geostrophy governs the dynamics of the flow parallel to the coast. Consequently, we may approximate ψ_{AMOC} as the net volume flux due to the geostrophic component, v_g, of the full meridional velocity, v, without significant loss of accuracy:

$$\psi_{\mathrm{AMOC}} \approx \int_{x_w}^{x_e} \int_{-H}^{0} v_g \, dz \, dx. \tag{7.15}$$

Using the chain rule for integration, (7.15) may be rewritten as

$$\psi_{\mathrm{AMOC}} = \int_{x_w}^{x_e} \left(\Big[v_g z \Big]_{-H}^{0} - \int_{-H}^{0} z \frac{\partial v_g}{\partial z} \, dz \right) dx. \tag{7.16}$$

Assuming there is no net transport across a given latitude (i.e. assuming the Bering Strait is closed), the $[v_g z]$ term vanishes when integrated over the full width and depth of the basin. From thermal wind balance it follows that

$$\psi_{\mathrm{AMOC}} = \frac{g}{\rho_0 f} \int_{-H}^{0} z \, [\rho(x_e, y, z) - \rho(x_w, y, z)] \, dz, \tag{7.17}$$

where $\rho(x_w, y, z)$, $\rho(x_e, y, z)$ is the density at the western and eastern boundaries respectively. From thermocline adjustment theory (e.g. *Johnson and Marshall*, 2002a,b, 2004), $\rho(x_e, y, z)$ is expected to be latitudinally invariant. The authors show that the ocean responds to thermohaline anomalies through the propagation of coastally trapped waves along the western boundary to the Equator. This equatorward flow is in approximate geostrophic balance, leading to the attenuation of the associated pressure anomaly as the Equator is approached. The grossly diminished signal is then communicated to the eastern boundary through Equatorial Kelvin waves and transmitted northward and southward along the boundary by coastally trapped waves waves. On the eastern boundary the pressure anomaly cannot reamplify with poleward migration as westward propagating Rossby waves leak the signal into the interior. As a result, meridional density gradients cannot be sustained on the eastern boundary. It may be expected that the density, at any depth below the surface layer of direct atmospheric influence, will be uniform across the Equator and along the entire eastern boundary, $\rho(x, y_{eq}, z) \approx \rho(x_e, y, z)$ on timescales longer than the boundary wave transit time. At any latitude, y, the cross-basin density difference, $\rho(x_w, y, z) - \rho(x_e, y, z)$, can then be approximated as the density difference along the western boundary, between y and the Equator, $\rho(x_w, y, z) - \rho(x_w, y_{eq}, z)$.

To illustrate this, profiles of buoyancy, $b = g\rho/\rho_0$, as an anomaly from the layer mean, are shown along the western and eastern boundaries and across the Equator for the CONTROL experiment in figure 7.6. The argument presented above does not hold near the surface where density gradients are sustained by SSS and SST restoring. The argument also breaks down at high northern latitudes on the eastern boundary, where sustained convective adjustment perturbs the density field to significant depth. In figure 7.7, the buoyancy profiles are redrawn excluding the upper 1000 m of the water column. Consistent with expectations from theory, notable meridional density gradients are visible on the western boundary, but are absent

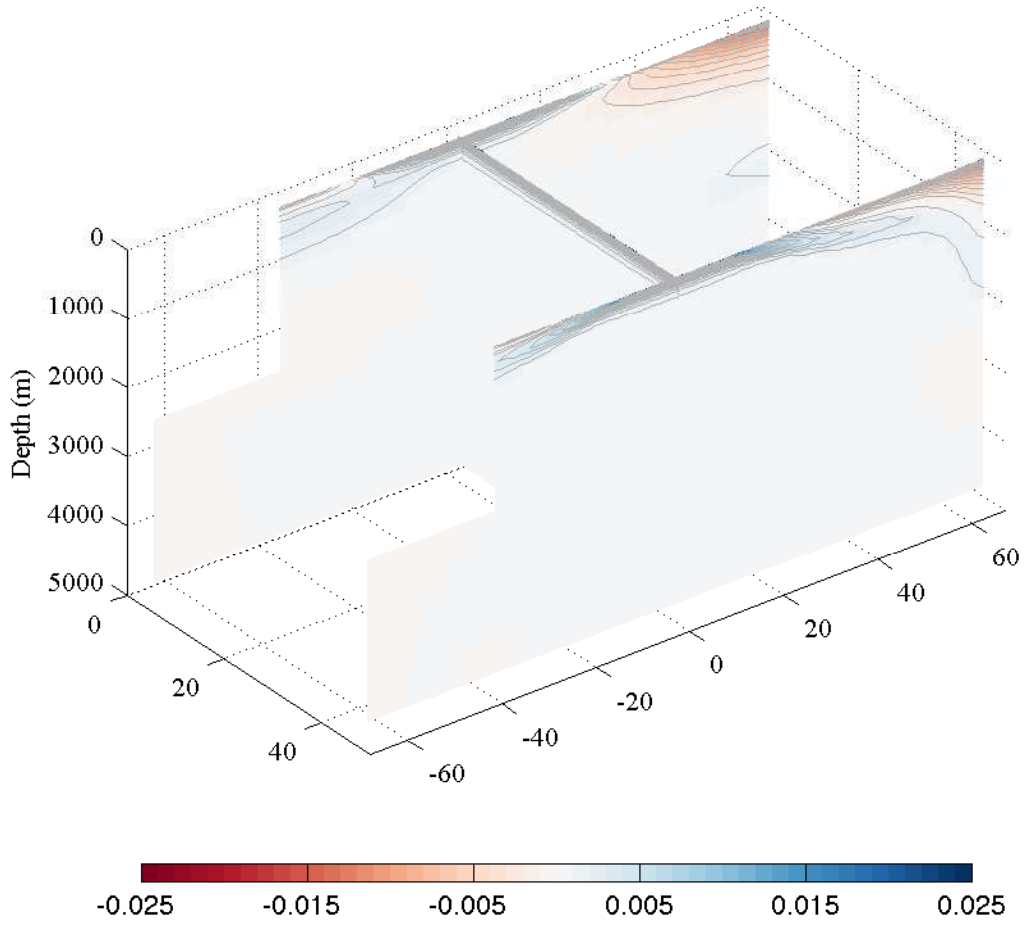

Figure 7.6: Profiles of buoyancy, $b = g\rho/\rho_0$, as an anomaly from the layer mean along the western boundary (at $x = 3$), eastern boundary (at $x = 48$) and across the Equator (at $y = 0$). The contour interval is 0.001 ms^{-2}. The 0 ms^{-2} contour has been omitted.

from the eastern boundary. At any given depth, the density is uniform across the Equator and along the eastern boundary, supporting the proposed approximation, $\rho(x_w, y, z) - \rho(x_e, y, z) \approx \rho(x_w, y, z) - \rho(x_w, y_{eq}, z)$. Final assurance is provided by plotting the cross-basin density difference versus the along-western-boundary density difference for all model layers (below 1000 m) in figure 7.8. The distinct measures of density difference are shown to be not only directly proportional, but almost

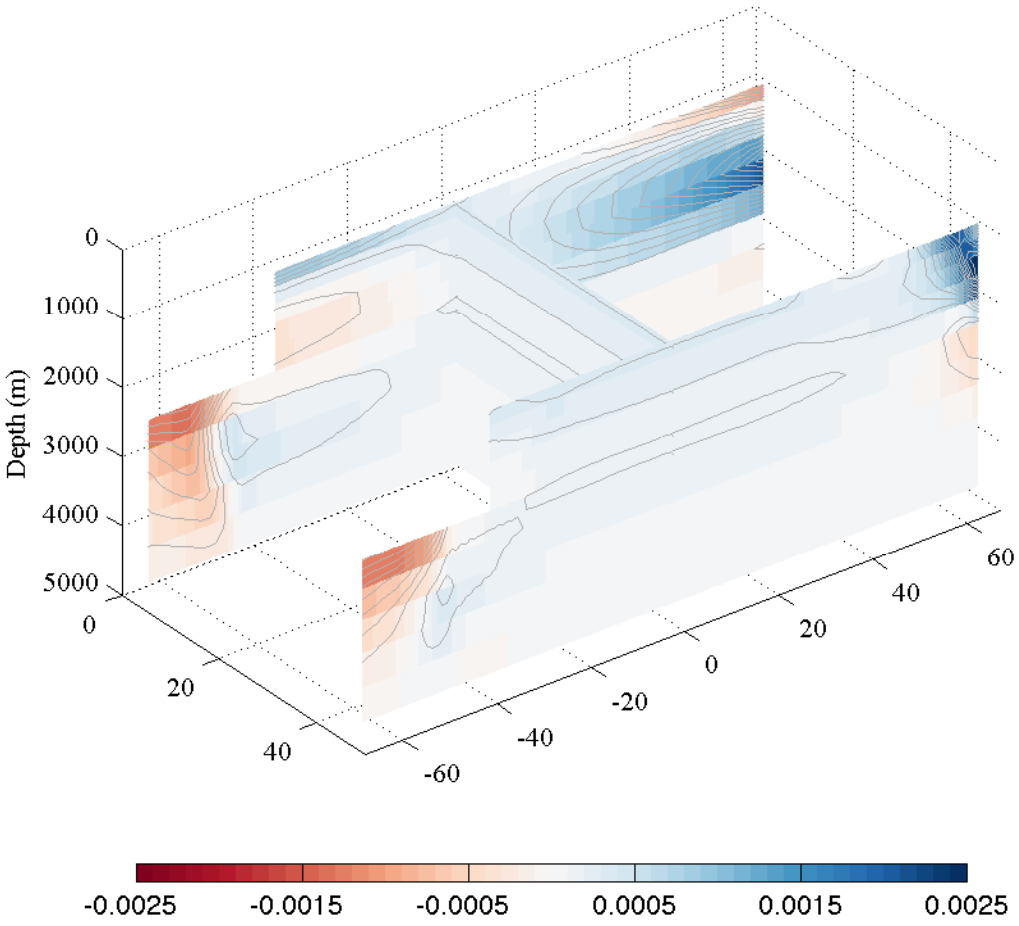

Figure 7.7: As for figure 7.6 but restricted to the column below 1000 m depth, where buoyancy anomalies are an order of magnitude smaller than in the upper ocean. The contour interval is 0.0001 ms^{-2}. The 0 ms^{-2} contour has been omitted. The key observation is that notable meridional buoyancy gradients exist along the western boundary. At any given depth the buoyancy is uniform across the Equator and along the eastern boundary (excluding high latitudes).

identical throughout the domain, excluding the latitudes spanned by the reentrant channel and high latitude convective adjustment. This analysis allows (7.17) to be

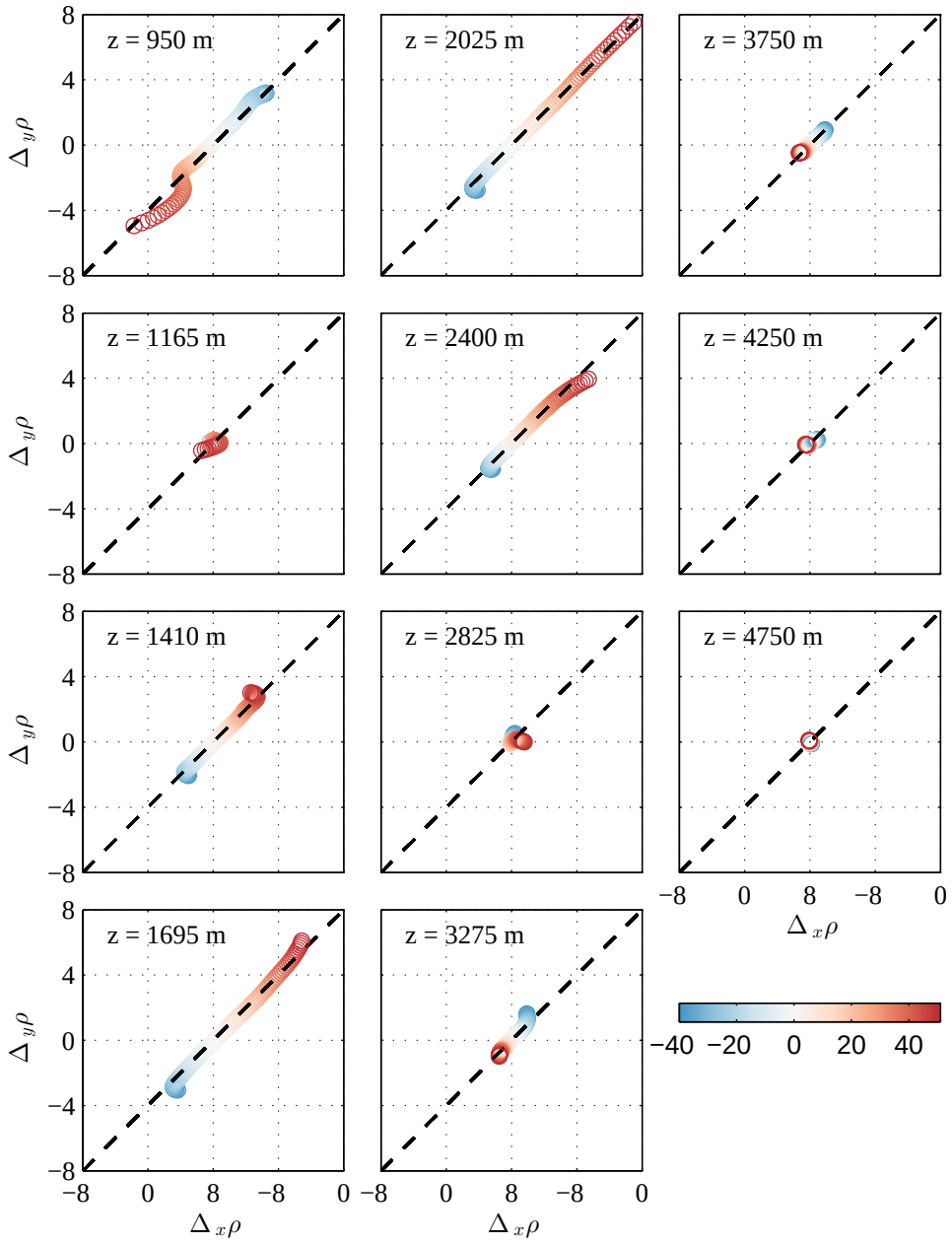

Figure 7.8: Cross-basin, $\Delta_x\rho$, versus along-western-boundary, $\Delta_y\rho$, density difference ($*10^4$ kgm^{-3}) for model layers 10 to 20. The depth at the middle of the layer is shown in the upper left corner of each panel. Colours indicate the latitude at which the density difference is measured. At any given latitude, y, the cross-basin density difference is $\rho(x_w, y, z) - \rho(x_e, y, z)$; the along-western boundary density difference is $\rho(x_w, y, z) - \rho(x_w, y_{eq}, z)$, and the two measures are shown to be almost identical.

approximated as follows:

$$\psi_{\mathrm{AMOC}} = -\frac{g}{\rho_0 f} \int_{-H}^{0} z \, [\rho(x_w, y, z) - \rho(x_w, y_{eq}, z)] \, dz. \tag{7.18}$$

Finally, by replacing the finite density difference with the continuous derivative

$$\psi_{\mathrm{AMOC}} = -\frac{g}{\rho_0 f} \int_{y_{eq}}^{y} \int_{-H}^{0} z \frac{\partial}{\partial y} \rho(x_w, y, z) \, dz \, dy, \tag{7.19}$$

we may substitute for the vertical shears component of the buoyancy force function, $\mathrm{A}^x_{\mathrm{OT}}\Big|_{\mathrm{buoyancy}}$, derived in equation (7.12):

$$f\psi_{\mathrm{AMOC}} = \int_{y_{eq}}^{y} \left(\mathrm{A}^x_{\mathrm{OT}}(x_w, y, z)\Big|_{\mathrm{buoyancy}} - c \right) \, dy, \tag{7.20}$$

where

$$c = \frac{1}{\rho_0} \left[\left(\frac{\partial}{\partial y} p(x_w, y, z) - \overline{\frac{\partial}{\partial y} p(x_w, y, z)}^{z} \right) z \right]_{-H}^{0} \tag{7.21}$$

describes a volume flux associated with the relaxation of meridional pressure gradients. We expect this term to vanish in the absence of bathymetric and free surface variations adjacent to the western boundary. Differentiating both sides of (7.20) by y and using the product rule for differentiation, it follows that

$$\beta\psi_{\mathrm{AMOC}} + f\frac{\partial \psi_{\mathrm{AMOC}}}{\partial y} \;=\; \mathrm{A}^x_{\mathrm{OT}}(x_w, y, z)\Big|_{\mathrm{buoyancy}} \;-\; c. \tag{7.22}$$

In the absence of strong diapycnal interior diffusion, we expect the large scale overturning to be quasi-adiabatic. As a result, we also expect that meridional variations in ψ_{AMOC} are small at any depth level, away from the high latitude sinking region.

By assuming $\partial\psi_{\mathrm{AMOC}}/\partial y \sim O(\beta\psi_{\mathrm{AMOC}}/f)$ we may write

$$\psi_{\mathrm{AMOC}} \approx \frac{1}{2\beta}\left(\mathrm{A}^{x}_{\mathrm{OT}}(x_w, y, z)\Big|_{\mathrm{buoyancy}} - c\right). \tag{7.23}$$

To distinguish between this approximation and the earlier AMOC scaling (7.14), equation (7.23) is termed the "buoyancy-beta" scaling.

7.3.2 Results: Empirical Support for the "buoyancy-beta" Scaling

In the left column of figure 7.9, estimates of ψ_{AMOC} from the buoyancy-beta scaling are plotted for CONTROL and all members of the WS ensemble. The error computed as the deviation of the scaled ψ_{AMOC} from the modelled ψ_{AMOC} is shown in the right column. The scaling exhibits notable qualitative skill across the entire range of AMOC states explored. Excluding the Equator and the high northern latitudes, quantitative agreement is reasonable between the northern edge of the reentrant channel and 50°N. At the Equator the error is larger (between 1-5 Sv) as the scaled estimate vanishes ($\mathrm{A}^{x}_{\mathrm{OT}}\Big|_{\mathrm{buoyancy}} = 0$). As shown in section 6.2.7 (see figure 6.15) of the previous chapter, dissipation and inertia are important here and a more complex dynamical framework is required to resolve the mechanism achieving cross-equatorial transport.

The buoyancy-beta scaling fails completely at the northern boundary, where it grossly overestimates the value of the streamfunction (by up to 20 Sv). As shown in figures (7.6 and 7.7) approximation of cross-basin buoyancy gradients by along-western-boundary buoyancy gradients is invalid here. As shown in figure 7.5, the assumption $\partial\psi_{\mathrm{AMOC}}/\partial y \approx 0$ also breaks down at the northern margin.

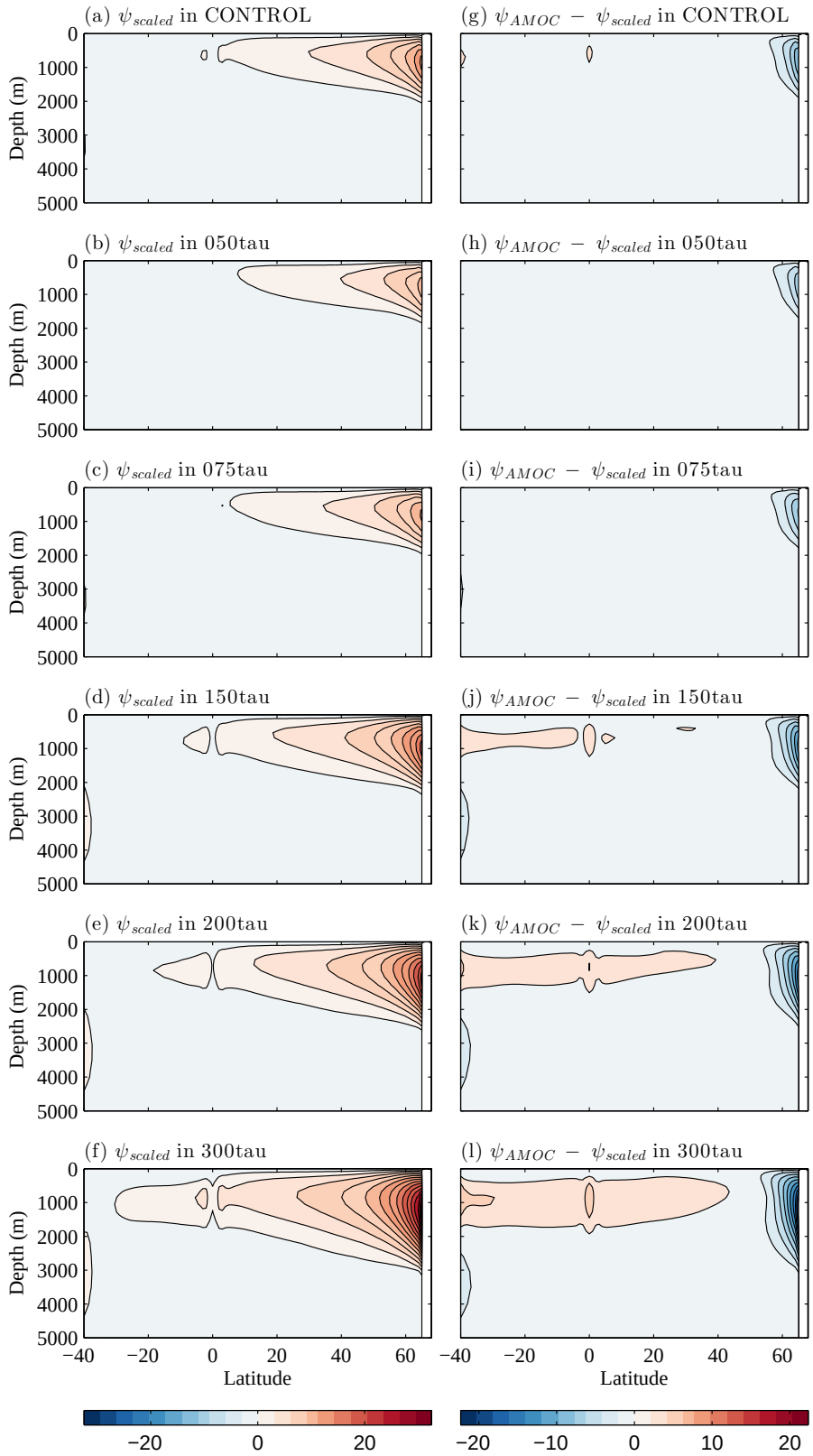

Figure 7.9: Estimated ψ_{AMOC} (left column) in (a) CONTROL and (b)-(f) the WS suite, using the buoyancy-beta scaling. Error in the buoyancy-beta scaling (right column) in (g) CONTROL and (h)-(l) the WS suite, computed as the residual between the modelled and scaled streamfunctions. The contour interval is 2 Sv. The 0 Sv interval has been omitted.

7.4 Conclusions and Discussion

Significant past efforts have been invested in deriving simple relations for the AMOC and basic metrics of the ocean state. By examining the projection of the rotational buoyancy forcing onto the local acceleration of ψ_{AMOC}, we have derived a linear AMOC-MDG relation (7.14). Consistent with the empirical study by *de Boer et al.* (2010), we have shown analytically that the positive linear relation is retrieved when the MDG is depth-integrated between the surface and the turning point of the overturning. We execute an ensemble of integrations, based closely on the study by *de Boer et al.* (2010), to produce a range of AMOC transport maxima in agreement with the linear scaling (figure 7.4). An important conclusion is that the relevant scale depth for the AMOC is the turning depth, Z_{max}, not the depth of the pycnocline, as is commonly assumed. This highlights the importance of remote dynamics in establishing the AMOC; although Z_{max} may be locally influenced by diapycnal mixing and surface buoyancy forcing, Southern Ocean processes may play a dominant role in modulating Z_{max} (e.g. *Gnanadesikan*, 1999).

Encouraged by the qualitative similarity between ψ_{AMOC} and the vertical shears component of the buoyancy force function, $\mathrm{A}^x_{\mathrm{OT}}\Big|_{\mathrm{buoyancy}}$ on the western boundary, we derived a new "buoyancy-beta" scaling (7.23), relating ψ_{AMOC} to $\mathrm{A}^x_{\mathrm{OT}}\Big|_{\mathrm{buoyancy}}(x_w, y, z)$ rescaled by 2β. This scaling requires that horizontal density gradients are negligible along the Equator and the eastern boundary, which is consistent with thermocline adjustment theory (e.g. *Johnson and Marshall*, 2002a,b, 2004) and the analysis presented in section 7.3.1. It further requires that meridional gradients in ψ_{AMOC} are small ($O(\beta\psi_{\mathrm{AMOC}}/f)$), which is expected away from high latitudes and in the absence of strong diapycnal diffusivity.

7.4.1 Limitations

The buoyancy force acts only in the vertical direction and as a result, cannot project onto an external mode of the AMOC. In a realistic basin, it is expected that an external mode may contribute significantly to ψ_{AMOC} where barotropic flows pass over topographic variations in the east-west direction (e.g where the boundary currents impinge on the continental slope, see section 6.3.4). The linear AMOC-MDG relation (7.14) is restricted to consider only how the buoyancy force projects onto the AMOC. As a result, we do not expect to recover ψ_{AMOC} variations due to the variability of the external mode, from the linear AMOC-MDG relation.

7.4.2 Implications

In contrast to the linear AMOC-MDG relation (7.14), the buoyancy-beta scaling is more generalized and is expected to be useful even in the presence of an external mode. However, further work is required to determine whether the entailed assumptions (discussed above) are restrictive in practice. For example, we may expect a notable density anomaly to be sustained near 35°N on the eastern boundary, associated with export of warm, salty waters from the Mediterranean. In this case, meridional density gradients may be non-negligible along the eastern boundary. Nonlinear forcing must also be considered to resolve the ageostrophic dynamics governing the equatorial crossing of the AMOC.

Chapter 8

Conclusions

In this thesis, we have explored the dynamics governing the Atlantic meridional overturning circulation (AMOC), via the application of two distinct and innovative tools. By employing (1) the numerical adjoint of an GCM, we have been able to explore the memory of the modelled subtropical AMOC to perturbations in the surface forcing fields, elucidating teleconnection mechanisms and quantifying expected anomalies in the AMOC on seasonal to decadal timescales. By deriving (2) the rotational momentum budget, we have provided firm foundations for the development of a powerful tool in visualising the force balance setting complex 3-dimensional circulations in hydrostatic GCMs. We have shown that it is particularly insightful to examine the rotational momentum balance in the western boundary region.

The reader is referred back to the summaries at the end of chapters 3, 4, 5, 6 and 7 for a detailed overview of their contents. Below, we briefly summarise our key results and suggest avenues for future work.

8.1 Adjoint Sensitivity Analysis

In chapter 3, we explored the linear sensitivity of the monthly mean subtropical AMOC, $\overline{\psi_{25\mathrm{N}}}^{month}$, to global surface fluxes of buoyancy and momentum. Our ap-

proach was to use a numerical adjoint. This is a powerful method in sensitivity analysis and allowed us to elucidate the pathways via which remotely forced anomalies may propagate to perturb the subtropical AMOC. We set out to present a full assessment of the teleconnections that may influence $\overline{\psi_{25\mathrm{N}}}^{month}$ on timescales of 1 month to 15 years. Many teleconnections visible in the adjoint framework are recognisable as "dual" analogues of mechanisms in the forward run (e.g Kelvin waves, Rossby waves and Gulf Stream advective pathways).

In chapter 4, we estimated the origins of AMOC variability on sub-seasonal to decadal timescales by projecting global surface fluxes of buoyancy and momentum from reanalysis onto corresponding sensitivity patterns derived in chapter 3.

8.1.1 Key Insights

Key insights provided by our investigation in chapters 3 and 4 include:

1. Significant memory of $\overline{\psi_{25\mathrm{N}}}^{month}$ to surface fluxes of momentum is confined to timescales of a few months. As a result, the subtropical AMOC responds most strongly to wind stress anomalies imposed in the immediate vicinity of 25°N and the local upstream coastal waveguides.

2. Significant memory of $\overline{\psi_{25\mathrm{N}}}^{month}$ to surface buoyancy fluxes spans multi-decadal timescales and is described by a large-scale oscillation in the sign of sensitivity between the eastern and western North Atlantic basin. This supports the findings by *Czeschel et al.* (2010), and leads to the counter-intuitive result that high latitude cooling could lead to an eventual decrease in the subtropical AMOC.

3. This oscillatory sensitivity appears to be sustained as a "thermal Rossby" mode (*Huck et al.*, 1999; *Te Raa and Dijkstra*, 2002), modified by the passage of baroclinic Rossby waves, radiated from the North-East Atlantic.

4. This oscillatory sensitivity appears to be extremely sensitive to the formulation of the surface boundary condition and the choice of model parameters. Conflicting with results presented by *Czeschel et al.* (2010), our oscillatory mode appears undamped over the full 15 year period of investigation. This is a surprising result in the presence of dissipation, mixing, and atmospheric damping of SSS and SST anomalies.

5. The dependence of $\overline{\psi_{25\mathrm{N}}}^{month}$ on the historical buoyancy forcing over the full (15 year) time window considered here (and presumably longer) is a negative result in terms of our ability to reconstruct seasonality in the subtropical AMOC using linear sensitivities. However, this is important in suggesting that the AMOC represents the integrated response to forcing over a long time period. The implication is that a mechanistic understanding of the observed variability at 26.5°N is a significant challenge.

6. Over the 15 year period of investigation, the largest amplitude sensitivities to surface fluxes of buoyancy and momentum are restricted to the Atlantic basin. In general, forcing anomalies in the South Atlantic and anywhere off the eastern boundary beween the Equator and 25°N are relatively impotent in stimulating variability in $\overline{\psi_{25\mathrm{N}}}^{month}$ on monthly to multi-decadal timescales. This supports the existence of an "equatorial buffer" (*Johnson and Marshall*, 2002a). Notable sensitivities that are found south of the Equator are either (1) restricted to the baroclinically unstable flanks of the subtropical gyre (2) located in the Agulhas retroflection region or (3) dependent upon interior pathways, as opposed to coastal waveguides (as shown by the subtropical gyre signal in the freshwater flux sensitivities).

7. Large $O(10$ Sv) transient anomalies in $\overline{\psi_{25\mathrm{N}}}^{month}$ are computed by projecting zonal wind stress anomalies onto patterns of linear sensitivity.

8.1.2 Broader Implications and Further Work

The results of this work have potentially important implications for our understanding of ocean dynamics and for future observational efforts. Principally, the existence of multi-decadal memory to high latitude buoyancy forcing cautions against inferring AMOC trends from short transport timeseries. Furthermore, it points towards high latitude monitoring as being of potentially greater value for climate prediction purposes. Determination of the extent to which these conclusions are dependent upon the model setup is an essential topic for future work. Key questions surround the exact physics setting the high latitude oscillation, the dependence of the oscillation on the full-depth restoring at the northern margin, and the sensitivity of the oscillation to the formulation of the surface thermohaline boundary conditions and selected model parameters. Obvious starting points could, for example, be (1) to determine a simple relation between the decay rate of the high latitude oscillation and the SSS and SST interaction coefficients and (2) to re-compute the sensitivity fields under mixed boundary conditions, the case thought to most closely approximate actual atmosphere-ocean interaction. Here, it is important to note that we have only examined a small fraction of the total data output by the adjoint model. There is a wealth of untapped information immediately available from our adjoint ensemble - regarding AMOC sensitivity to 3-dimensional hydrography and other model inputs - that we have not yet assessed. We envisage exploring linear sensitivity (1) throughout the global domain to mixing coefficients of heat and salt and (2) throughout the surface layer to SSS and SST interaction coefficients, in attempt to address the questions posed above.

Although the adjoint is an efficient method of obtaining rich, quantitative sensitivity information, we are restricted to select a particular model metric on which to focus our investigation. In this study, our metric of choice was the monthly mean northward volume flux across 25°N in the Atlantic basin. Modelling and observa-

tional evidence supports the suggestion that the AMOC may not vary coherently with latitude through the basin, with a break in coherence identified between the subtropical and subpolar gyres (*Bingham et al.*, 2007; *Lozier et al.*, 2010). An exciting avenue for future research would be to explore this break in coherence in the adjoint framework, by redefining a set of cost functions above 40°N. Furthermore, our focus on the monthly mean overturning was motivated by an early aim to explore the origins of seasonal variability in the subtropical AMOC (leading to the analysis in chapter 4). It would be insightful to compare linear sensitivities of AMOC transport averaged over different periods. This is motivated by spectral analysis of transport variability across the RAPID array, suggesting that Ekman variability dominates at timescales less than 100 days, whilst Gulf Stream and interior geostrophic transport variability dominates at seasonal and longer timescales (*Kanzow et al.*, 2010). We might expect the linear sensitivity of the time-averaged AMOC to represent that of its major component and thus differ notably between sub-seasonal and annual timescales. Furthermore, it would be insightful to determine the relative contribution of the western and eastern boundaries to the variability of the interior geostrophic transport, and to examine the sensitivity of the external mode separately. We envisage analysing sensitivity information specific to each of these contributions separately in our future work.

There is also great potential to extend our analysis in chapter 4, relating to the projection of forcing anomalies onto patterns of pure sensitivity. In particular, it would be interesting to pursue the potential causes of extreme, transient anomalies in the subtropical AMOC. This follows the detection of a dramatic reversal in the AMOC across the RAPID array during the winter of 2009/2010 which has yet to be explained (*Srokosz et al.*, 2012). Another important avenue for future work is a thorough investigation of the temporal origins of AMOC variability, with the aim of better understanding the low frequency variability driven by interannual heat flux

anomalies (see figure 4.7). Furthermore, we have yet to examine the spatial origins of AMOC variability on monthly to decadal timescales. A simple starting point would for example, be to examine the fractional contribution of each grid cell to the globally integrated transport for each month in the seasonal cycles shown in figure 4.2.

Finally, we note that the northward transport of volume may not be the most climatically significant metric to focus our attention upon. Although analysis of the available (3.5 year) timeseries of continuous measurements at 26.5°N indicates that fluctuations in volume and heat transports are well correlated (*Johns et al.*, 2011), linear sensitivity studies (*Heimbach et al.*, 2011) and analysis of potential predictability patterns (*Tiedje et al.*, 2012) suggest the relationship may be more complex. Adjoint models have already been applied to provide insights into the factors contributing to deep ocean heat storage (*Huang et al.*, 2003). Future work would target cost functions to elucidate the relationship between the AMOC and upper ocean heat content change.

8.2 Rotational Momentum Balance

In chapter 5 we presented a new tool that enables a clean diagnosis of the force balance controlling the circulation regime for a Boussinesq fluid in hydrostatic balance. Specifically, the tool is based on the development of the "rotational momentum" equations and the introduction of a set of scalar "velocity potentials" and corresponding "force functions". By design, we are able to examine the force balances controlling the overturning and depth-integrated circulation separately. Furthermore, the overturning was decomposed into "vertical shears" and "external mode" components for independent examination. We presented analytical solutions for the vertical shears component of the overturning.

In chapter 6 we applied the rotational momentum decomposition to the modelled

circulation in idealised Atlantic and globally realistic configurations of a hydrostatic GCM, with a focus on elucidating the dynamics of the simulated AMOC. We presented numerical solutions for the vertical shears velocity potential and corresponding force function in both cases. For the idealised basin, this fully described the modelled AMOC, and we were able to demonstrate that diagnosis of the rotational momentum budget can be both straightforward and highly accurate. For the realistic basin, an external mode also contributes to the AMOC, however this was not computed rigorously.

Finally, in chapter 7 we employed the rotational momentum equations to derive simple scalings relating the AMOC to specific measures of the meridional density gradient (MDG).

8.2.1 Key Insights

A key advantage of the approach is that, if two terms balance pointwise in the vorticity equation, the equivalant two terms balance pointwise in the rotational momentum equation. This allows for vorticity descriptions of the dynamics to be readily interpreted in terms of rotational force balances, the advantage being that (1) it is often simpler to think about force balances than vorticity sources and sinks and (2) rotational force balances are easy to visualise. Key insights provided by our investigation in chapters 5, 6 and 7 include:

1. In a flat-bottomed basin, the AMOC emerges as a residual overturning, accelerated by the tilting of planetary vorticity into the latitude-depth plane by vertical shear in the ageostrophic zonal velocity.

2. In a flat-bottomed basin, the AMOC displays strong qualitative similarity to the rotational buoyancy forcing right on the western boundary.

3. In a flat-bottomed basin, it may be shown analytically that the AMOC scales linearly with the depth-integrated MDG. The relevant depth scale is that at which the AMOC attains its maximum (consistent with the empirical scaling of *de Boer et al.*, 2010).

4. A new "buoyancy-beta" scaling has been derived relating the AMOC to the buoyancy forcing right on the western boundary. This is an exciting development as it has potential to work under more general forcing conditions in realistic basin geometries.

5. Even for the idealised model, scalar components of the velocity potential greatly simplify visualisation of the 3-dimensional flow field.

6. For the globally realistic model, the 2-dimensional AMOC streamfunction emerges as a serious over-simplification of the 3-dimensional flow field. This is especially true at high latitude in the North Atlantic, where the subpolar gyre generates a complex array of counter-rotating meridional overturning cells during its passage around the basin. These almost exactly cancel upon zonal integration.

8.2.2 Broader Implications and Further Work

The results of this work have potentially important implications for our understanding of ocean dynamics and for future modelling efforts.

A serious limitation of the present study is the failure to robustly diagnose the barotropic velocity potential, Ψ_{BT}, and associated force function, A_{BT}, in a realistic domain with multiply connected boundaries. In chapter 5, we derived the defining elliptic problems and associated Dirichlet boundary conditions for these scalar fields. It should certainly be possible therefore, to rigorously solve for both. It is likely that at present, our calculation is failing to correctly identify all distinct bounding

segments and assign to each one a single Dirichlet condition. Resolution of this issue is essential for instilling confidence that the rotational momentum analysis is both well defined and computationally tractable for complex geometries. This is undoubtedly, the most pressing topic for our future work.

Despite this issue, from the solutions presented for the vertical shears overturning, we may immediately suggest that the force functions and velocity potentials are powerful diagnostics for complex GCMs. As noted above, an interesting insight provided by our analysis is that the 2-dimensional AMOC streamfunction is a gross over-simplification of the 3-dimensional circulation, potentially obscuring important dynamics in the subpolar gyre region. We can envisage that the rotational momentum diagnostics will prove useful in enabling a more comprehensive assessment of the spatial distribution of overturning in GCM-based investigations. Similarly, for numerical ensembles we suggest that the rotational momentum diagnostics will provide useful means of comparison where - amid huge quantities of information - we seek to perform a mechanistic assessment of simulated differences as succinctly as possible. This was found to be true for the ensemble investigation in the idealised basin, presented in chapter 7. It is encouraging to note that the rotational momentum approach has already led to a significant new advance in unstructured-mesh ocean models (*Maddison et al.*, 2011) and been used to develop a new turbulence closure scheme (*San et al.*, 2011).

The decomposition has been applied to the instantaneous momentum balance, but can equally be applied to the time-mean momentum balance. An important extension would be to determine the relative variability achieved by external and overturning modes on different timescales, and subsequently, to elucidate the responsible forcing mechanisms. An excellent framework for the exploration of multidecadal variability would be a state estimation product. This synthesizes available observations (accompanied by uncertainty estimates) with a dynamical model to produce

a dynamically and kinematically self-consistent best-guess of the ocean state (*Wunsch and Heimbach*, 2007). The numerical tools are in place to immediately follow this lead using the ECCO/GECCO state estimates generated using the dynamical framework of the MITgcm, as used in chapters 6 and 7. Additional ideas for future work include re-visiting problems previously addressed with integral vorticity budgets. These include the classical problem of western boundary layer separation (*Munday and Marshall*, 2005) and processes controlling the Agulhas leakage (*Virdi*, 2010).

Finally, we note that the buoyancy-beta scaling is expected to be a useful scaling for the AMOC, even in the presence of an external mode. Further work is required to determine how restricitve the entailed assumptions (discussed in section 7.4) are in practice.

Bibliography

Abernathey, R., J. Marshall, and D. Ferreira (2011), The dependence of Southern Ocean meridional overturning on wind stress, *J. Phys. Oceanogr.*, *41*, 2261–2278, doi:10.1175/JPO-D-11-023.1. 7.2.2

Adcroft, A. J. (1995), Numerical algorithms for use in a dynamical model of the ocean, Ph.D. thesis, Imperial College, London. 2.4.5

Adcroft, A. J., C. N. Hill, and J. C. Marshall (1999), A new treatment of the Coriolis terms in C-grid models at both high and low resolutions, *Mon. Wea. Rev.*, *127*, 1928–1936, doi:10.1175/1520-0493(1999)127¡1928:ANTOTC>2.0.CO;2. 2.4.1

Allen, M. (1999), Do-it-yourself climate prediction, *Nature*, *401*, doi:10.1038/44266. 3.2.1

Allison, L., H. Johnson, and D. Marshall (2011), Spin-up and adjustment of the Antarctic Circumpolar Current and global pycnocline, *J. Mar. Res.*, *69*, 167–189, doi:10.1357/002224011798765330. 3.1

Antonov, J., R. Locarnini, T. Boyer, A. Mishonov, and H. Garcia (2006), *World Ocean Atlas 2005, Volume 2: Salinity*, 182 pp., NOAA Atlas NESDIS 62. 2.5.1, 2.2

Arakawa, A., and V. Lamb (1977), Computational design of the basic dynamical processes of the ucla general circulation model, *Methods in Computational Physics*, *17*, 174–267. 2.4.1

Balan Sarojini, B., J. Gregory, R. Tailleux, G. Bigg, A. Blaker, D. Cameron, N. Edwards, A. Megann, L. Shaffrey, and B. Sinha (2011), High frequency variability of the Atlantic meridional overturning circulation, *Ocean Sci.*, *7*, 471–486, doi:10.5194/os-7-471-2011. 4.3.1

Baringer, M., and J. Larsen (2001), sixteen years of Florida Current transport at 27°N, *Geophys. Res. Lett.*, *28*(16), doi:10.1029/2001GL013246. 1.2

Baringer, M., W. Johns, C. Meinen, D. Shoosmith, and H. Bryden (2008), On the structure of Florida Current variability. 1.2

Barkmeijer, J., R. Buizza, and T. Palmer (1999), 3D-Var Hessian singular vectors and their potential use in the ECMWF ensemble prediction system, *Q. J. R. Meteorol. Soc.*, *125*, 2333–2351, doi:10.1002/qj.49712555818. 3.2.1

Barnier, B. (1988), A numerical study on the influence of the Mid-Atlantic Ridge on nonlinear first-mode baroclinic Rossby waves generated by seasonal winds, *J. Phys. Oceanogr.*, *18*, 417–433, doi:10.1175/1520-0485(1988)018¡0417:ANSOTI>2.0.CO;2. 3.4.1

Biastoch, A., C. B"oning, and J. Lutjeharms (2008), Agulhas leakage dynamics affects decadal variability in Atlantic overturning circulation, *Nature*, *456*, 489–492, doi:10.1038/nature07426. 1.3, 3.4.1, 3.5

Bindoff, N., J. Willebrand, V. Artale, A. Cazenave, J. Gregory, S. Gulev, K. Hanawa, C. Le Quere, S. Levitus, Y. Nojiri, C. Shum, T. L.D., and A. Unnikrishnan (Eds.) (2007), *Observations: Oceanic Climate Change and Sea Level. In: Climate Change 2007: The Physical Science Basis. Contribution of Working Group I to the Fourth Assessment Report of the Intergovernmental Panel on Climate Change*, Cambridge University Press. 1.1

Bingham, R. J., C. W. Hughes, V. Roussenov, and R. G. Williams (2007), Meridional coherence of the North Atlantic meridional overturning circulation, *Geophys. Res. Lett.*, *34*, L23,606. 1.3, 6.4, 8.1.2

Bower, A., S. Lozier, S. Gary, and C. Böning (2009), Interior pathways of North Atlantic meridional overturning circulation, *Nature*, *459*, doi:10.1038/nature07979. 1.3

Bower, A., S. Lozier, and S. Gary (2011), Export of Labrador Sea water from the subpolar North Atlantic: A Lagrangian perspective, *Deep Sea Research Part II*, *58*, 1798–1818, doi:10.1016/j.dsr2.2010.10.060. 1.3

Brayshaw, D., B. Hoskins, and M. Blackburn (2008), The storm track response to idealized SST perturbations in an aquaplanet GCM, *J. Atmos. Sci.*, *65*, 2842–2860, doi:10.1175/2008JAS2657.1. 1.1

Broecker, W. (1991), The great ocean conveyor, *Oceanography*, *1*, 79–89, doi:10.1063/1.41925. 1.3

Bryan, F., and M. Cox (1967), A numerical investigation of the oceanic general circulation, *Tellus*, *19*, 54–80, doi:10.1111/j.2153-3490.1967.tb01459.x. 7.1.1

Bryan, K. (1984), Accelerating the convergence to equilibrium of ocean-climate models, *J. Phys. Oceanogr.*, *14*, 666–673, doi:10.1175/1520-0485(1984)014¡0666:ATCTEO>2.0.CO;2. 2.4.5

Bryden, H., H. Longworth, and S. Cunningham (2005), Slowing of the atlantic overturning circulation at 25°n, *Nature*, *438*, 655–657, doi:10.1038/nature04385. 1.1, 1.2

Bugnion, V., and C. Hill (2006), Equilibration mechanisms in an adjoint ocean general circulation model, *Ocean Dynamics*, *56*, 51–61, doi:10.1007/s10236-005-0052-z. 3.1.1, 3.4

Bugnion, V., C. Hill, and P. Stone (2006a), An adjoint analysis of the meridional overturning circulation in a hybrid coupled model, *J. Clim.*, *19*, 3732–3750. 3.1.1, 3.4.2

Bugnion, V., C. Hill, and P. Stone (2006b), An adjoint analysis of the meridional overturning circulation in an ocean model, *J. Clim.*, *19*, 3732–3750. 3.1.1, 3.4.2, 3.4.4

Cacuci, D. (1981), Sensitivity theory for nonlinear systems. i. nonlinear functional analysis approach, *J. Math. Phys.*, *22*, 2794–2802, doi:10.1063/1.525186. 3.1

Cai, W., R. Greatbatch, and S. Zhang (1998), Interdecadal variability in an ocean model driven by a small, zonal redistribution of the surface buoyancy flux, *J. Phys. Oceanogr.*, *25*, 1998–2010. 2.5.2

Campin, J.-M. (2010), Mitgcm support forum. 6.2.2, 6.3.2

Campin, J.-M., A. Adcroft, C. Hill, and J. Marshall (2004), Conservation of properties in a free-surface model, *Ocean Modelling*, *6*, 221–244, doi:10.1016/S1463-5003(03)00009-X. 3.4.1

Cessi, P. (1994), A simple box model study of stochastically forced thermohaline flow, *J. Phys. Oceanogr.*, *24*, 1911–1920, doi:10.1175/1520-0485(1994)024¡1911:ASBMOS>2.0.CO;2. 7.1.1

Cessi, P., and S. Louazel (2001), Decadal oceanic response to stochastic wind forcing, *J. Phys. Oceanogr.*, *31*, 3020–3029. 3.5

Cessi, P., and P. Otheguy (2003), Oceanic teleconnections: remote response to decadal wind forcing, *J. Phys. Oceanogr.*, *33*, 1604–1617, doi:10.1175/2400.1. 3.1

Cessi, P., and W. Young (1996), Some unexpected consequences of the interaction between convective adjustment and horizontal diffusion, *Physica D: Nonlinear Phenomena*, *98*, 287–300, doi:10.1016/0167-2789(96)00118-2. 2.4.4

Chelton, D., and M. Schlax (1996), Global observations of oceanic Rossby waves, *Science*, *272*(5259), 234–238. 3.4.1

Chelton, D., R. DeSzoeke, M. Schlax, K. El Naggar, and N. Siwertz (1998), Geographical variability of the first baroclinic Rossby Radius of Deformation, *J. Phys. Oceanogr.*, *28*, 433–460, doi:10.1175/1520-0485(1998)028¡0433:GVOTFB>2.0.CO;2. 2.4.4

Chelton, D., M. Schlax, M. Freilich, and R. Milliff (2004), Satellite measurements reveal persistent small-scale features in ocean winds, *Science*, *13*, 978–983, doi:10.1126/science.1091901. 4.3.1

Chen, F., and M. Ghil (1995), Interdecadal variability of the thermohaline circulation and high-latitude surface fluxes, *J. Phys. Oceanogr.*, *22*, 161–167. 2.5.2

Chidichimo, M., T. Kanzow, S. Cunningham, W. Johns, and J. Marotzke (2010), The contribution of eastern-boundary density variations to the Atlantic meridional overturning circulation at 26.5°N, *Ocean Sci.*, *6*, 475–490, doi:10.5194/os-6-475-2010. 1.2, 4.3.2

Colin de Verdiere, A., and T. Huck (1999), Baroclinic instability: An oceanic wavemaker for interdecadal variability, *J. Phys. Oceanogr.*, *29*, 893–910. 2.5.2, 3.4.2

Cox, M. (1984), A primitive equation, three-dimensional model of the ocean, *GFDL Ocean Group Tech. Rep. 1*, GFDL/Princeton University, Princeton, N.J., 141 pp. 2.4.4

Cunningham, S., T. Kanzow, D. Rayner, M. Baringer, W. Johns, J. Marotzke, H. Longworth, E. Grant, J. J.-M. Hirschi, L. Beal, C. Meinen, and H. Bryden (2007), Temporal variability of the Atlantic meridional overturning circulation at 26.5°N, *Science*, *317*(5840), 935–938, doi:10.1126/science.1141304. 1.2, 6.4.1

Curry, R., B. Dickson, and I. Yashayaev (2003), A change in the freshwater balance of the Atlantic Ocean over the past four decades, *nature*, *426*, 826–829. 1.1

Cushman-Roisin, B., and J.-M. Beckers (2011), *Introduction to Geophysical Fluid Dynamics. Physical and Numerical Aspects*, Academic Press. 2.4.2

Czeschel, L., D. Marshall, and H. Johnson (2010), Oscillatory sensitivity of the Atlantic overturning to high-latitude forcing, *Geophys. Res. Lett.*, *37*, L10,601, doi:10.1029/2010GL043177. 3.1.1, 3.4.1, 3.4.2, 3.4.4, 3.5, 2, 4

Czeschel, L., C. Eden, and R. Greatbatch (2012), On the driving mechanism of the annual cycle of the Florida Current transport, *J. Phys. Oceanogr.*, *42*, 824–839, doi:10.1175/JPO-D-11-0109.1. 3.1.1, 3.4.4, 3.5.1

Danabasoglu, G., and J. McWilliams (1995), Sensitivity of the global ocean circulation to parameterizations of mesoscale tracer tansports, *J. Clim.*, *8*, 2967–2987, doi:10.1175/1520-0442(1995)008¡2967:SOTGOC>2.0.CO;2. 2.4.4

Danabasoglu, G., J. McWilliams, and P. Gent (1994), The role of mesoscale tracer transport in the global ocean circulation, *Science*, *264*(5162), 1123–1126, doi:10.1126/science.264.5162.1123. 2.4.4, 2.5.1

Davis, R. (1976), Predictability of sea surface temperature and sea level pressure anomalies over the North Pacific Ocean, *J. Phys. Oceanogr.*, *6*, 249–266, doi:10.1175/1520-0485(1976)006¡0249:POSSTA>2.0.CO;2. 2.4.2

de Boer, A., and H. Johnson (2007), Inferring the zonal distribution of measured changes in the meridional overturning circulation, *Ocean Sci.*, *3*, 55–57, doi:10.5194/os-3-55-2007. 7.1.1

de Boer, A., A. Gnanadesikan, N. R. Edwards, and A. Watson (2010), Meridional density gradients do not control the Atlantic overturning circulation, *J. Phys. Oceanogr.*, *40*, 368–380, doi:10.1175/2009JPO4200.1. 7.1.1, 7.1.2, 7.2.1, 7.2.2, 7.2.4, 7.4, 3

Delworth, T., and M. Mann (2000), Observed and simulated multidecadal variability in the Northern Hemisphere, *16*, 661–676. 1.1

Delworth, T., S. Manabe, and R. Stouffer (1993), Interdecadal variations of the thermohaline circulation in a coupled ocean-atmosphere model, *J. Clim.*, *6*, 1900–1989. 1.1

Dengler, M., F. Schott, C. Eden, P. Brandt, J. Fischer, and R. Zantopp (2004), Break-up of the Atlantic deep western boundary current into eddies at 8°s, *Nature*. 1.3

Dickson, B., I. Yashayaev, J. Meincke, B. Turrell, S. Dye, and J. Holfort (2002), Rapid freshening of the deep North Atlantic Ocean over the past four decades, *Nature*, *416*, 832–837. 1.1

Dijkstra, H. (2008), Scaling of the Atlantic meridional overturning circulation in a global ocean model, *Tellus*, *60*, 749–760, doi:10.1111/j.1600-0870.2008.00326.x. 7.1.1

Dijkstra, H., L. te Raa, M. Sch, eits, and J. Gerrits (2006), On the physics of the Atlantic Multidecadal Oscillation, *Ocean Dynamics*, *56*, 36–50, doi:10.1007/s10236-005-0043-0. 3.4.2

Dong, B., and R. Sutton (2002), Variability in North Atlantic heat content and heat transport in a coupled ocean-atmosphere GCM, *Clim. Dyn.*, *19*, 485–497, doi:10.1007/s00382-002-0239-7. 1.1

Doos, K., and D. Webb (1994), The Deacon Cell and the other meridional cells of the southern ocean, *J. Phys. Oceanogr.*, *24*, 429–442. 2.5.1

Döscher, R., C. Böning, and P. Herrmann (1994), Response of circulation and heat transport in the North Atlantic to changes in the thermohaline forcing in northern latitudes, *J. Phys. Oceanogr.*, *24*, 2306–2320. 3.5.1

Duplessy, J., E. Bard, M. Arnold, N. Shackleton, J. Duprat, and L. Labeyrie (1991), How fast did the ocean-atmosphere system run during the last deglaciation., *103*, 27–40. 3.1

Durney, C., and C. Johnson (1969), *Introduction to modern electromagnetics*, 471 pp., McGraw-Hill. 5.2.1

Durran, D. (1999), *Numerical Methods for Wave Equations in Geophysical Fluid Dynamics*, 465 pp., Springer-Verlag. 2.4.4, 2.5.2

Errico, R. (1997), What is an adjoint model?, *Bull. Amer. Meteor. Soc.*, *78*, 2577–2591, doi:10.1175/1520-0477(1997)078¡2577:WIAAM>2.0.CO;2. 3.1.1, 3.2, 3.2.2

Farrell, B., and P. Ioannou (1996), Generalized stability theory. part i: Autonomous operators, *J. Atmos. Sci.*, *53*, 2025–2040. 3.1.1

Farrell, P., D. Ham, S. Funke, and M. Rognes (2012), Automated derivation of the adjoint of high-level transient finite element programs, *CoRR*, *abs/1204.5577*. 3.2.4

Frame, D., T. Aina, C. Christensen, N. Faull, S. Knight, C. Piani, S. Rosier, K. Yamazaki, Y. Yamazaki, and M. Allen (2009), The climate*prediction*.net BBC climate change experiment: design of the coupled model ensemble, *Phil. Trans. R. Soc. A*, *367*(1890), 855–870, doi:10.1098/rsta.2008.0240. 3.2.1

Frankcombe, L. M., H. Dijkstra, and A. von der Heydt (2008), Sub-surface signatures of the Atlantic multidecadal oscillation, *Geophys. Res. Lett.*, *35*, L19,602, doi:10.1029/2008GL034989. 2.5.2

Fu, L.-L. (2004), The interannual variability of the North Atlantic Ocean revealed by combined data from TOPEX/Poseidon and Jason altimetric measurements, *Geophys. Res. Lett.*, *31*, L23,303, doi:10.1029/2004GL021200. 3.4.1

Galanti, E., and E. Tziperman (2003), A midlatitude-ENSO teleconnection mechanism via baroclinically unstable long Rossby waves, *J. Phys. Oceanogr.*, *33*, 1877–1888, doi:10.1175/1520-0485(2003)033¡1877:AMTMVB>2.0.CO;2. 3.4.1

Ganachaud, A., and C. Wunsch (2000), Improved estimates of global ocean circulation, heat transport and mixing from hydrographic data, *Nature*, *408*, 453–457, doi:10.1038/35044048. 1.1

Gent, P., and J. C. McWilliams (1990), Isopycnal mixing in ocean circulation models, *J. Phys. Oceanogr.*, *20*, 150–155, doi:10.1175/1520-0485(1990)020¡0150:IMIOCM>2.0.CO;2. 2.4.4

Gent, P., J. Willebrand, T. McDougall, and J. C. McWilliams (1995), Paremeterizing eddy-induced tracer transports in ocean circulation models., *J. Phys. Oceanogr.*, *25*, 463–474, doi:10.1175/1520-0485(1995)025¡0463:PEITTI>2.0.CO;2. 2.4.4

Gerdes, R., C. Kberle, and J. Willebrand (1991), The influence of numerical advection schemes on the results of ocean general circulation models, *Clim. Dyn.*, *5*(4), 211–226, doi:10.1007/BF00210006. 2.4.4

Giering, R. (2010), *Transformation of algorithms in Fortran, Users Manual, Version 1.15 (TAF Version 1.9.70)*, *Fast*Opt. 3.2.3, 3.2.4

Giering, R., and T. Kaminski (1998), Recipes for adjoint code construction, *Assoc. Comput. Mach. Transactions on Mathematical Software*, *24*, 437–474, doi:10.1145/293686.293695. 3.2.2, 3.2.3

Giles, M., and N. Pierce (1997), Adjoint equations in CFD: duality, boundary conditions and solution behaviour, *AIAA Paper*, pp. 97–1850. 3.2.3

Giles, M., and N. Pierce (2000), An introduction to the adjoint approach to design, *Flow, Turbulence and Combustion*, *65*, 393–415. 3.2.3

Gnanadesikan, A. (1999), A simple predictive model for the structure of the oceanic pycnocline, *Science*, *283*, doi:10.1126/science.283.5410.2077. 3.1.1, 7.4

Greatbatch, R. J. (1994), A note on the representation of steric sea level in models that conserve volume rather than mass, *J. Geophys. Res.*, *99*, 12,767–12,771. 2

Greatbatch, R. J. (1998), Exploring the relationship between eddy-induced transport velocity, vertical momentum transfer, and the isopycnal flux of potential vorticity, *J. Phys. Oceanogr.*, *28*, 422–432, doi:10.1175/1520-0485(1998)028¡0422:ETRBEI>2.0.CO;2. 2.4.4

Greatbatch, R. J., and K. Peterson (1996), Interdecadal variability and oceanic thermohaline adjustment, *J. Geophys. Res.*, *101*, 20,467–20,483, doi:10.1029/96JC01531. 3.1, 3.5.1

Greatbatch, R. J., and S. Zhang (1995), An interdecadal oscillation in an idealized ocean basin forced by constant heat flux, *J. Clim.*, *8*, 82–91. 2.5.2

Gregory, J., K. Dixon, R. Stouffer, A. Weaver, E. Driesschaert, M. Eby, T. Fichefet, H. Hasumi, A. Hu, J. Jungclaus, I. Kamenkovich, A. Levermann, M. Montoya, S. Murakami, S. Nawrath, A. Oka, A. Sokolov, and R. Thorpe (2005), A model intercomparison of changes in the Atlantic thermohaline circulation in response to increasing atmospheric CO_2 concentration, *Geophys. Res. Lett.*, *32*, L12,703, doi:10.1029/2005GL023209. 4.3

Griesel, A. (2006), The relation of meridional pressure gradients to North Atlantic deep water volume transport in an ocean general circulation model, *Clim. Dyn.*, *26*, 781–799, doi:10.1007/s00382-006-0122-z. 7.1.1

Griewank, A. (1992), Achieving logarithmic growth of temporal and spatial complexity in reverse automatic differentiation, *Optimization Methods and Software*, *1*, 35–54, doi:10.1080/10556789208805505. 3.2.4

Griewank, A. (2000), *Evaluating Derivatives: Principles and Techniques of Algorithmic Differentiation*, Philidelphia. 3.2.3

Griffies, S. (1998), The Gent-McWilliams skew flux, *J. Phys. Oceanogr.*, *28*, 831–841, doi:10.1175/1520-0485(1998)028¡0831:TGMSF>2.0.CO;2. 2.4.4

Griffies, S. (2004), *Fundamentals of Ocean Climate Models*, 518 pp., Princeton University Press. 2.1, 2.4.4

Haine, T., and T. Hall (2002), A generalized transport theory: water-mass composition and age, *J. Phys. Oceanogr.*, *32*, 1932–1946, doi:10.1175/1520-0485(2002)032<1932:AGTTWM>2.0.CO;2. 3.1

Haine, T., H. Zhang, D. Waugh, and M. Holzer (2008), On transit-time distributions in unsteady circulation models, *Ocean Modelling*, *21*, 35–45, doi:10.1016/j.ocemod.2007.11.004. 3.1

Hallberg, R. (1997), Localized coupling between surface and bottom-intensified flow over topography, *J. Phys. Oceanogr.*, *27*, 997–998. 3.4.1

Ham, D. (2006), On techniques for modelling coastal and ocean flow with unstructured meshes, Ph.D. thesis, TU Delft. 2.4.1

Haney, R. (1971), Surface thermal boundary condition for ocean circulation models, *J. Phys. Oceanogr.*, *1*, 241–248, doi:10.1175/1520-0485(1971)001<0241:STBCFO>2.0.CO;2. 2.4.2

Heimbach, P., C. Hill, and R. Giering (2002), Automatic generation of efficient adjoint code for a parallel Navier-Stokes solver, doi:10.1007/3-540-46080-$2_1$07. 3.2.4, 3.2

Heimbach, P., D. Menemenlis, M. Losch, J. Campin, and C. Hill (2010), On the formulation of sea-ice models. part2: Lessons from multi-year adjoint sea icea export sensitivities through the Canadian Arctic Archipelago, *Ocean Modelling*, *33*(1-2), 145–158, doi:10.1016/j.ocemod.2010.02.002. 3.1.1

Heimbach, P., C. Wunsch, R. Ponte, G. Forget, C. Hill, and J. Utke (2011), Timescales and regions of the sensitivity of Atlantic meridional volume and heat transport: Toward observing system design, *Deep Sea Res.*, *58*, 1858–1879, doi:10.1016/j.dsr2.2010.10.065. 3.1, 3.1.1, 3.1.2, 3.2.2, 3.4, 3.4.1, 3.4.1, 8.1.2

Hirschi, J., J. Baehr, J. Marotzke, J. Stark, S. Cunningham, and J.-O. Beismann (2003), A monitoring design for the Atlantic meridional overturning circulation, *Geophys. Res. Lett.*, *30*(1413), doi:10.1029/2002GL016776. 1.2

Hirst, A., and T. McDougall (1996), Deep-water properties and surface buoyancy flux as simulated by a z-coordinate model including eddy-induced advection, *J. Phys. Oceanogr.*, *26*, 1320–1343, doi:10.1175/1520-0485(1996)026<1320:DWPASB>2.0.CO;2. 2.4.4

Holland, W., and L. Lin (1975), On the origin of mesoscale eddies and their contribution to the general circulation of the ocean. i. a preliminary numerical experiment, *J. Phys. Oceanogr.*, *5*, 642–657. 1.3

Holton, J. R. (2004), *An Introduction to Dynamic Meteorology*, 535 pp., Elsevier. 5.3.2

Hoteit, I., B. Cornuelle, A. Köhl, and D. Stammer (2005), Treating strong adjoint sensitivities in tropical eddy-permitting variational data assimilation, *Q. J. R. Meteorol. Soc.*, *131*, 3659–3682, doi:10.1256/qj.05.97. 3.3.4

Huang, B., P. Stone, and C. Hill (2003), Sensitivities of deep-ocean heat uptake and heat content to surface fluxes and subgrid-scale parameters in an ocean general circulation model with idealized geometry, *J. Geophys. Res.*, *108*(3015), doi:10.1029/2001JC001218. 8.1.2

Huang, R. (1993), Real freshwater flux as a natural boundary condition for the salinity balance and thermohaline circulation forced by evaporation and precipitation, *J. Phys. Oceanogr.*, *23*, 2428–2446. 3.4.1

Huang, R. (2010), *Ocean Circulation: Wind-Driven and Thermohaline Processes*, 791 pp., Cambridge University Press. 2

Huck, T., A. Colin de Verdiere, and A. Weaver (1999), Interdecadal variability of the thermohaline circulation in box-ocean models forced by fixed surface fluxes., *J. Phys. Oceanogr.*, *29*, 865–892. 2.5.2, 2.6, 3.4.1, 3.4.2, 3.5, 3

Huck, T., G. Vallis, and A. Colin de Verdiere (2001), On the robustness of interdecadal modes of the thermohaline circulation, *J. Clim.*, *14*, 940–963. 2.5.2, 3.4.2

Hughes, T., and A. Weaver (1994), Multiple equilibria of an asymmetric two-basin ocean model, *J. Phys. Oceanogr.*, *24*, 619–637, doi:10.1175/1520-0485(1994)024<0619:MEOAAT>2.0.CO;2. 7.1.1

Iselin, C. (1939), The influence of vertical and lateral turbulence on the characteristics of the waters at mid-depths, *Trans. Amer. Geophys. Un.*, *20*, 414–417. 2.4.4

Jackett, D., and T. McDougall (1995), Minimal adjustment of hydrographic profiles to achieve static stability, *J. Atmos. Ocean. Technol.*, *12*, 381–389, doi:10.1175/1520-0426(1995)012<0381:MAOHPT>2.0.CO;2. 2.4.3

Jayne, S., and J. Marotzke (2001), The dynamics of ocean heat transport variability, *Rev. Geophys.*, *39*, 385–411. 1.1, 2.5.2

Johns, W., M. Baringer, L. Beal, S. Cunningham, T. Kanzow, H. Bryden, J. Hirschi, J. Marotzke, C. Meinen, B. Shaw, and R. Curry (2011), Continuous array-based estimates of Atlantic ocean heat transport at 26.6°N, *J. Clim.*, *24*, 2429–2449, doi:10.1175/2010JCLI3997.1. 1.1, 8.1.2

Johnson, H., and D. Marshall (2002a), A theory for surface Atlantic response to thermohaline variability, *J. Phys. Oceanogr.*, *32*, 1121–1132, doi:10.1175/1520-0485(2002)032<1121:ATFTSA>2.0.CO;2. 3.1, 3.4.1, 3.4.1, 3.5, 7.3.1, 7.4, 6

Johnson, H., and D. Marshall (2002b), Localization of abrupt change in the north atlantic thermohaline circulation, *Geophys. Res. Lett.*, *29*, doi:10.1029/2001GL014140. 3.5, 7.3.1, 7.4

Johnson, H., and D. Marshall (2004), Global teleconnections of meridional overturning circulation anomalies, *J. Phys. Oceanogr.*, *34*, 1702–1722, doi:10.1175/1520-0485(2004)034<1702:GTOMOC>2.0.CO;2. 3.1, 7.3.1, 7.4

Jones, H., and J. Marshall (1993), Convection with rotation in a neutral ocean: A study of open-ocean deep convection, *J. Phys. Oceanogr.*, *23*, 1009–1039, doi:10.1175/1520-0485(1993)023<1009:CWRIAN>2.0.CO;2. 2.4.2

Kalnay, E., M. Kanamitsu, R. Kistler, W. Collins, D. Deaven, L. Gandin, M. Iredell, S. Saha, G. White, J. Woollen, Y. Zhu, M. Chelliah, W. Ebisuzaki, W. Higgins, J. Janowiak, K. Mo, C. Ropelewski, J. Wang, A. Leetmaa, R. Reynolds, R. Jenne, and D. Joseph (1996), The NCEP/NCAR 40-year reanalysis project, *Bull. Amer. Meteor. Soc.*, *77*, 437–471, doi:10.1175/1520-0477(1996)077<0437:TNYRP>2.0.CO;2. 2.2

Kanamitsu, M., W. Ebisuzaki, J. Woolen, S.-K. Yang, J. Hnilo, M. Fiorino, and G. Potter (2002), NCEP-DOE AMIP-II Reanalysis (R-2), *Bull. Amer. Met. Soc.*, *83*, 16311643, doi:10.1175/BAMS-83-11-1631. 2.5.2

Kanzow, T., S. Cunningham, D. Rayner, J.-M. Hirschi, W. Johns, M. Baringer, H. Bryden, L. Beal, C. Meinen, and J. Marotzke (2007), Observed flow compensation associated with the MOC at 26.5°n in the Atlantic, *Science*, *317*(5840), 938941, doi:10.1126/science.1141293. 1.2

Kanzow, T., S. Cunningham, W. Johns, J. J.-M. Hirschi, J. Marotzke, M. Baringer, C. Meinen, M. Chidichimo, C. Atkinson, L. Beal, H. Bryden, and J. Collins (2010), Seasonal variability of the Atlantic meridional overturning circulation at 26.5°N, *J. Clim.*, *23*, 56785698, doi:10.1175/2010JCLI3389.1. 1.1, 1.2, 1.2, 4.3.2, 8.1.2

Kawase, M. (1987), Establishment of deep ocean circulation driven by deep-water production, *J. Phys. Oceanogr.*, *17*, 2294–2317, doi:10.1175/1520-0485(1987)017<2294:EODOCD>2.0.CO;2. 3.1, 3.1.1

Kerr, R. (2000), A North Atlantic climate pacemaker for the centuries, *Science*, *288*, 1984–1985. 1.1

Key, R., A. Kozyr, C. Sabine, K. Lee, R. Wanninkhof, J. Bullister, R. Feely, F. Millero, C. Mordy, and T. Peng (2004), A global ocean carbon climatology: results from Global Data Analysis Project, *Global Biogeochemical Cycles*, *18*, doi:10.1029/2004GB002247. 3.1

Killworth, P. (1997), On the parameterization of eddy transfer: Part 1: Theory, *J. Mar. Res.*, *55*, 1171–1197, doi:10.1357/0022240973224102. 7.2.2

Killworth, P. (2003a), Long extratropical planetary wave propagation in the presence of slowly vary- ing mean flow and bottom topography. part i: The local problem., *J. Phys. Oceanogr.*, *33*, 784–801. 3.4.1

Killworth, P. (2003b), Long extratropical planetary wave propagation in the presence of slowly varying mean flow and bottom topography. part ii: Ray propagation and comparison with observations, *J. Phys. Oceanogr.*, *33*, 802–821. 3.4.1

Killworth, P., and J. Blundell (1999), The effect of bottom topography on the speed of long extratropical planetary waves, *J. Phys. Oceanogr.*, *29*, 2689–2708. 3.4.1

Knight, J., R. Allan, C. Folland, M. Vellinga, and M. Mann (2005), A signature of persistent natural thermohaline circulation cycles in observed climate, *Geophys. Res. Lett.*, *32*, L20,708, doi:10.1029/2005GL024233,. 1.1

Kohl, A. (2005), Anomalies of meridional overturning: mechanisms in the North Atlantic, *J. Phys. Oceanogr.*, *35*, 1455–1472, doi:10.1175/JPO2767.1. 3.4.1

Large, W. G., J. C. McWilliams, and S. C. Doney (1994), Oceanic vertical mixing: a review and a model with a nonlocal boundary layer parameterization, *Rev. Geophys.*, *32*(4), 363–403, doi:10.1029/94RG01872. 2.4.4

Lea, D., M. Allen, and T. Haine (2000), Sensitivity analysis of the climate of a chaotic system, *Tellus A*, *52*, 523–532, doi:10.1034/j.1600-0870.2000.01137.x. 3.3.4, 3.5.1

Lee, T., and J. Marotzke (1998), Seasonal cycles of meridional overturning and heat transport of the Indian Ocean, *J. Phys. Oceanogr.*, *28*, 923–943, doi:10.1175/1520-0485(1998)028<0923:SCOMOA>2.0.CO;2. 3.4.1, 5.2.3

Lineikin, P. (1955), On the determination of the thickness of the baroclinic layer in the sea, *Dokl. Akad. Nauk USSR*, *101*, 461–464. 7.1.1

Locarnini, R., A. Mishonov, J. Antonov, T. Boyer, and H. Garcia (2006), *World Ocean Atlas 2005, Volume 1: Temperatur. S. Levitus, Ed.*, 182 pp., NOAA Atlas NESDIS 61. 2.5.1, 2.2

Lorbacher, K., S. Marsland, J. Church, S. Griffies, and D. Stammer (2012), Rapid barotropic sea level rise from ice sheet melting, *J. Geophys. Res.*, *117*, C06,003, doi:10.1029/2011JC007733. 3.4.1, 3.4.1

Lorenz, E. (1963), Deterministic nonperiodic flow, *J. Atmos. Sci.*, *20*, 130–141, doi:10.1175/1520-0469(1963)020<0130:DNF>2.0.CO;2. 3.4.4

Lozier, S. (1997), Evidence for large-scale eddy-driven gyres in the North Atlantic, *Science*, *277*, 361–364. 1.3

Lozier, S., V. Roussenov, M. Reed, and R. Williams (2010), Opposing decadal changes for the North Atlantic meridional overturning circulation, *Nature Geoscience*, *3*, 728–734, doi:10.1038/ngeo947. 1.3, 6.4, 8.1.2

Maddison, J. R., D. P. Marshall, C. C. Pain, and M. D. Piggott (2011), Accurate representation of geostrophic and hydrostatic balance in unstructured mesh finite element modelling, *Ocean Modelling*, *39*, 248–261, doi:10.1016/j.ocemod.2011.04.009. 8.2.2

Mahajan, S., R. Zhang, and T. Delworth (2011), Impact of the Atlantic meridional overturning circulation (AMOC) on Arctic surface air temperature and sea ice variability, *J. Clim.*, *24*, 6573–6581. 1.1

Manabe, S., and R. Stouffer (1988), Two stable equilibria of a coupled ocean-atmosphere model, *J. Clim.*, *1*, 841–866. 1.1

Marotzke, J. (1997), Boundary mixing and the dynamics of three-dimensional thermohaline circulations, *J. Phys. Oceanogr.*, *27*, 1713–1728, doi:10.1175/1520-0485(1997)027<1713:BMATDO>2.0.CO;2. 7.1.1

Marotzke, J., R. Giering, K. Zhang, D. Stammer, C. Hill, and T. Lee (1999), Construction of the adjoint MIT ocean general circulation model and application to Atlantic heat transport sensitivity, *J. Geophys. Res.*, *104*(C12), 29,529–29,547, doi:10.1029/1999JC900236. 3.1.1

Marshall, D., and H. Johnson (2013), in preparation. 3.5.1

Marshall, D. P. (2011), Rossby wormholes, *J. Mar. Res.*, *69*, 309–330, doi:10.1357/002224011798765213. 3.4.1

Marshall, D. P., and H. R. Pillar (2011), Momentum balance of the wind-driven and meridional overturning circulation, *J. Phys. Oceanogr.*, *41*, 960–978, doi:10.1175/2010JPO4528.1. 5.1.2

Marshall, D. P., and C. E. Tansley (2001), An implicit formula for boundary current separation, *J. Phys. Oceanogr.*, *31*, 1633–1638, doi:10.1175/1520-0485(2001)031<1633:AIFFBC>2.0.CO;2. 5.1.2

Marshall, J., and F. Schott (1999), Open-ocean convection: Observations, theory, and models, *Rev. Geophys.*, *37*(1), 1–64, doi:10.1029/98RG02739. 2.4.4

Marshall, J. C., A. Adcroft, C. Hill, L. Perelman, and C. Heisey (1997a), A finite-volume, incompressible navier stokes model for studies of the ocean on parallel computers, *J. Geophys. Res.*, *102*, 5753–5766, doi:10.1029/96JC02775. 2.3

Marshall, J. C., C. Hill, L. Perelman, and A. Adcroft (1997b), Hydrostatic, quasihydrostatic, and nonhydrostatic ocean modeling, *J. Geophys. Res.*, *102*, 5733–5752, doi:10.1029/96JC02776. 2.3, 5.2.6

Meehl, G., T. Stocker, W. Collins, P. Friedlingstein, A. Gaye, J. Gregory, A. Kitoh, R. Knutti, J. Murphy, A. Noda, S. Raper, I. Watterson, A. Weaver, and Z.-C. Zhao (2007), Global climate projections, in *Climate Change 2007: The Physical Science Basis. Contribution of Working Group I to the Fourth Assessment Report of the Intergovernmental Panel on Climate Change*, edited by S. Solomon, D. Qin, M. Manning, Z. Chen, M. Marquis, K. Averyt, M. Tignor, and H. Miller, Cambridge University Press, Cambridge, United Kingdom and New York, NY, USA. 3.1

Mikolajewicz, U., and R. Voss (2000), The role of the individual air-sea flux components in CO_2 induced changes of the ocean's circulation and climate, *Clim. Dyn.*, *16*, 627–642. 4.3

Montgomery, R. (1938), Circulation in upper layers of southern North Atlantic deduced with the use of isentropic analysis, p. 55, MIT. 2.4.4

Munday, D. R., and D. P. Marshall (2005), On the separation of a barotropic western boundary current from a cape, *J. Phys. Oceanogr.*, *35*, 1726–1743, doi:10.1175/JPO2783.1. 5.1.2, 8.2.2

Munk, W. (1950), On the wind-driven ocean circulation, *J. Meteorol.*, *7*, 79–93. 6.2.6

Munk, W. (1966), Abyssal recipes, *Deep-Sea Res.*, *13*(4), 707–730, doi:10.1016/0011-7471(66)90602-4. 7.1.1

Nilsson, J., G. Bröstrom, and G. Walin (2003), The thermohaline circulation and vertical mixing: does weaker density stratification give stronger overturning?, *J. Phys. Oceanogr.*, *33*, 2781–2795, doi:10.1175/1520-0485(2003)033<2781:TTCAVM>2.0.CO;2. 7.1.1

Pardaens, A., J. Gregory, and J. Lowe (2011), A model study of factors influencing projected changes in regional sea level over the twenty-first century, *Clim. Dyn.*, *36*, 2015–2033, doi:10.1007/s00382-009-0738-x. 1.1

Park, Y. (1999), The stability of thermohaline circulation in a two-box model, *J. Phys. Oceanogr.*, *29*, 3101–3110, doi:10.1175/1520-0485(1999)029<3101:TSOTCI>2.0.CO;2. 7.1.1

Park, Y., and K. Bryan (2000), Comparison of thermally driven circulations from a depth-coordinate model and an isopycnal layer model. part 1: Scaling-law sensitivity to vertical diffusivity, *J. Phys. Oceanogr.*, *30*, 590–605, doi:10.1175/1520-0485(2000)030<0590:COTDCF>2.0.CO;2. 7.1.1

Pedlosky, J. (1987), *Geophysical Fluid Dynamics*, 710 pp., Springer-Verlag. 5.1.1, 6.2.7

Pedlosky, J. (1996), *Ocean Circulation Theory*, 453 pp., Springer-Verlag. 2.4.4

Pillar, H. (2007), Momentum balance of a barotropic, wind-driven gyre, Undergraduate honors thesis, University of Reading. 5.1.2

Plumb, R., and J. Mahlman (1987), Three-dimensional propagation of transient quasi-geostrophic eddies and its relationship with eddy forcing of the time-mean flow, *J. Phys. Oceanogr.*, *43*, 1825–1836. 2.4.4

Pohlmann, H., M. Botzet, M. Latif, A. Roesch, M. Wild, and P. Tschuk (2004), Estimating the decadal predictability of a coupled AOGCM, *J. Clim.*, *17*, 4463–4472, doi:10.1175/3209.1. 1.3

Ponte, R., and R. Rosen (1994), Oceanic angular momentum and torques in a general circulation model, *J. Phys. Oceanogr.*, *24*, 1966–1977, doi:10.1175/1520-0485(1994)024<1966:OAMATI>2.0.CO;2. 6.3.6

Rahmstorf, S. (1996), On the freshwater forcing and transport of the Atlantic thermohaline circulation, *J. Clim.*, *12*(12), 799–811, doi:10.1007/s003820050144. 7.1.1

Redi, M. (1982), Oceanic isopycnal mixing by coordinate rotation, *J. Phys. Oceanogr.*, *12*, 1154–1158, doi:10.1175/1520-0485(1982)012<1154:OIMBCR>2.0.CO;2. 2.4.4

Rhein, M., D. Kieke, S. Hüttl-Kabus, A. Roessler, C. Mertens, R. Meissner, B. Klein, C. Böning, and I. Yashayaev (2011), Deep water formation, the subpolar gyre, and the meridional overturning circulation in the subpolar north atlantic, *Deep-Sea Res.*, *58*, 1819–1832, doi:10.1016/j.dsr2.2010.10.061. 6.3.5

Rhines, P., and W. Young (1982), Homogenization og potential vorticity in planetary gyres, *J. Fluid Mech.*, *122*, 347–367. 1.3

Richardson, P. (2008), On the history of meridional overturning circulation schematic diagrams, *Prog. Oceanogr.*, *76*, 466–486, doi:10.1016/j.pocean.2008.01.005. 1.3

Robinson, A. R., and H. Stommel (1959), The oceanic thermocline and the associated thermohaline circulation, *Tellus*, *11*, 295–308, doi:10.1111/j.2153-3490.1959.tb00035.x. 7.1.1

Rooth, C. (1982), Hydrology and ocean circulation, *Prog. Oceanogr.*, *11*, 131–149. 7.1.1

Röske, F. (2006), A global heat and freshwater forcing dataset for ocean models, *Ocean Modelling*, *11*, 235–297, doi:10.1016/j.ocemod.2004.12.005. 2.5.2

Sabine, C., R. Feely, N. Gruber, R. Key, K. Lee, J. Bullister, R. Wanninkhof, C. Wong, D. Wallace, B. Tilbrook, F. Millero, T.-H. Peng, A. Kozyr, T. Ono, and A. Rios (2004), The oceanic sink for anthropogenic CO_2, *Science*, *305*(5682), 367–371, doi:10.1126/science.1097403. 1.1, 1.2

San, O., A. Staples, Z. Wang, and T. Iliescu (2011), Approximate deconvolution large eddy simulation of a barotropic ocean circulation model, *Ocean Modelling*, *40*, 120–132. 8.2.2

Scott, J. (2000), The roles of mixing, geothermal heating and surface buoyancy forcing in ocean meridional overturning dynamics, Ph.d. thesis, Massachusetts Institute of Technology, Massachusetts Institute of Technology. 7.1.1

Sime, L. C., D. P. Stevens, K. J. Heywood, and K. I. Oliver (2006), A decomposition of the Atlantic Meridional Overturning, *J. Phys. Oceanogr.*, *36*, 2253–2270, doi:10.1175/JPO2974.1. 6.3.4, 6.4.1

Sirkes, Z., and E. Tziperman (1997), Finite difference of adjoint or adjoint of finite difference?, *Mon. Wea. Rev.*, *125*, 3373–3378, doi:10.1175/1520-0493(1997)125<3373:FDOAOA>2.0.CO;2. 3.2.3

Sloyan, B., and S. Rintoul (2000), The southern ocean limb of the global deep overturning circulation, *J. Phys. Oceanogr.*, *31*, 143–173. 1.1

Solomon, S., D. Qin, M. Manning, M. Marquis, K. Averyt, M. Tignor, H. Miller Jr, and Z. Chen (Eds.) (2007), *Climate Change 2007: The Physical Science Basis*, Cambridge University Press. 1.1

Srokosz, M., M. Baringer, H. Bryden, S. Cunningham, T. Delworth, S. Lozier, J. Marotzke, and R. Sutton (2012), Past, present, and future changes in the Atlantic meridional overturning circulation, *BAMS*, pp. 1663–1676. 1.2, 1.3, 1.4, 8.1.2

Stammer, D. (2008), Response of the global ocean to Greenland and Antarctic ice melting, *J. Geophys. Res.*, *113*(C06022), doi:10.1029/2006JC004079. 3.1

Stepanov, V., and C. Hughes (2006), Propagation of signals in basin-scale ocean bottom pressure from a barotropic momdel, *J. Geophys. Res.*, *111*, C12,002, doi:10.1029/2005JC003450. 3.4.1

Stommel, H. (1948), The westward intensification of wind-driven ocean currents, *Trans. Amer. Geophys. Union*, *29*, 202–206. 5.1.1

Stommel, H. (1958), The abyssal circulation, *Deep-Sea Res.*, *4*, 149–184. 1.3

Stommel, H. (1961), Thermohaline convection with two stable regimes of flow, *Tellus*, *13*(2), 224–230, doi:10.1111/j.2153-3490.1961.tb00079.x. 7.1.1

Stommel, H., and A. B. Arons (1960), On the abyssal circulation of the world ocean – II. An idealized model of the circulation pattern and amplitude in oceanic basins, *Deep-Sea Res.*, *6*, 217–233, doi:10.1016/0146-6313(59)90075-9. 5.1.1

Straub, D. (1994), Dispersion of Rossby waves in the presence of zonally varying topography, *Geophys. Astrophys. Fluid Dyn.*, *75*, 107–130. 3.4.1

Sverdrup, H. U. (1947), Wind-driven currents in a baroclinic ocean; with application to the equatorial currents of the eastern pacific, *Proc. Nat. Acad. Sci. U.S.*, *33*, 318–326, doi:10.1073/pnas.33.11.318. 5.1.1

Tailleux, R. (2004), A WKB analysis of the surface signature of long extratropical baroclinic Rossby waves over topography., *Ocean Modelling*, *6*, 191–219. 3.4.1

Tailleux, R. (2006), The quasi-nondispersive regimes of long extratropical baroclinic Rossby waves over (slowly varying) topography, *J. Phys. Oceanogr.*, *36*, 104–121. 3.4.1

Tailleux, R., and J. McWilliams (2000), Acceleration, creation, and depletion of wind-driven, baroclinic Rossby waves over an ocean ridge, *J. Phys. Oceanogr.*, *30*, 2186–2213. 3.4.1

Tailleux, R., and J. McWilliams (2002), Energy propagation of long extratropical Rossby waves over slowly varying zonal topography, *J. Fluid Mech.*, *473*, 295–319. 3.4.1

Takahashi, T., and Coauthors (2009), Climatological mean and decadal changes in surface ocean pCO_2, and net sea-air CO_2 flux over the global oceans, *Deep-Sea Res.*, *56*, 554–577, doi:10.1016/j.dsr2.2008.12.009. 1.1, 1.2

Te Raa, L., and H. Dijkstra (2002), Instability of the thermohaline ocean circulation on interdecadal timescales, *J. Phys. Oceanogr.*, *32*, 138–160. 2.5.2, 2.6, 3.4.1, 3.4.2, 3.5, 3

Thomas, M. (2012), Sverdrup balance and three dimensional variability of the meridional overturning circulation, Ph.D. thesis, University of East Anglia. 6.4.2

Thorpe, R., J. Gregory, T. Johns, R. Wood, and J. Mitchell (2001), Mechanisms determining the Atlantic thermohaline circulation response to greenhouse gas forcing in a non-flux-adjusted coupled climate model, *J. Clim.*, *14*, 3102–3116, doi:10.1175/1520-0442(2001)014<3102:MDTATC>2.0.CO;2. 4.3, 7.1.1

Tiedje, B., A. Köhl, and J. Baehr (2012), Potential predictability of the North Atlantic heat transport based on an oceanic state estimate, *J. Clim.*, *25*, 8475–8486, doi:10.1175/JCLI-D-11-00606.1. 1.3, 8.1.2

Timmermann, A., Y. Okumura, S.-I. An, A. Clement, B. Dong, E. Guilyardi, A. Hu, J. Jungclaus, M. Renold, T. Stocker, R. Stouffer, R. Sutton, S.-P. Xie, and J. Yin (2007), The influence of a weakening of the Atlantic meridional overturning circulation on ENSO, *J. Clim.*, *20*, 4899–4919, doi:10.1175/JCLI4283.1. 1.1

Toggweiler, J., and B. Samuels (1995), Effect of Drake Passage on the global thermohaline circulation, *Deep-Sea Res.*, *42*, 477–500. 3.1.1

Trenberth, K., and J. Caron (2001), Estimates of meridional atmosphere and ocean heat transport, *J. Clim.*, *14*, 3433–3443, doi:10.1175/1520-0442(2001)014<3433:EOMAAO>2.0.CO;2. 1.1, 1.1

Tziperman, E., and W. Thacker (1989), An optimal-control/adjoint-equations approach to studying the oceanic general circulation, *J. Phys. Oceanogr.*, *19*, 1471–1485, doi:10.1175/1520-0485(1989)019<1471:AOCEAT>2.0.CO;2. 3.2.3

Vallis, G. K. (2006), *Atmospheric and Oceanic Fluid Dynamics*, 745 pp., Cambridge University Press, Cambridge, U.K. 1.2, 5.1.1, 5.3.1

Vellinga, M., and R. Wood (2002), Global climatic impacts of a collapse of the Atlantic thermohaline circulation, *Climatic change*, *54*(3), 251–267, doi:10.1023/A:1016168827653. 1.1

Venaille, A., G. Vallis, K. Smith, and K. Shafer (2011), Baroclinic turbulence in the ocean: Analysis with primitive equation and quasigeostrophic simulations, *J. Phys. Oceanogr.*, *41*(9), 1605–1623, doi:10.1175/JPO-D-10-05021.1. 2.4.4

Veronis, G. (1975), The role of models in tracer studies, pp. 133–146, Natl. Acad. Sci. 2.4.4

Virdi, A. (2010), The influence of the Agulhas leakage on the overturning circulation from momentum balances, Master's thesis, University of Reading. 8.2.2

Warren, B. (1999), Approximating the energy transport across oceanic sections, *J. Geophys. Res.*, *104*, 7915–7920. 1

Waterman, S., and S. Jayne (2011), Eddy-mean flow interactions in the along-stream developments of a western boundary current jet: An idealized model study, *J. Phys. Oceanogr.*, *41*, 682–707, doi:10.1175/2010JPO4477.1. 2.4.4

Weaver, A., J. Vialard, and D. Anderson (2003), Three- and four-dimensional variational assimilation with a general circulation model of the Tropical Pacific Ocean. part i: Formulation, internal diagnostics, and consistency checks, *Mon. Wea. Rev.*, *131*, 1360–1378, doi:10.1175/1520-0493(2003)131<1360:TAFVAW>2.0.CO;2. 3.2.3

Winton, M. (1996), The role of horizontal boundaries in parameter sensitivity and decadal-scale variability of coarse-resolution ocean general circulation models., *J. Phys. Oceanogr.*, *26*, 289 – 304, doi:10.1175/1520-0485(1996)026<0289:TROHBI>2.0.CO;2. 2.5.2, 7.1.1

Winton, M. (2003), On the climatic impact of ocean circulation, *J. Clim.*, *16*, 2875–2889. 1.1

Woollings, T., J. Gregory, J. Pinto, M. Reyers, and D. Brayshaw (2012), Response of the North Atlantic storm track to climate change shaped by ocean-atmosphere coupling, *Nature Geoscience*, *5*, 313–317, doi:10.1038/ngeo1438. 1.1

Wright, D., and T. Stocker (1991), A zonally averaged ocean model for the thermohaline circulation. Part 1: Model development and flow dynamics, *J. Phys. Oceanogr.*, *21*, 1713–1724. 7.1.1

Wright, D., C. Vreugdenhil, and T. Hughes (1995), Vorticity dynamics and zonally averaged ocean circulation models, *J. Phys. Oceanogr.*, *25*, 2141–2154, doi:10.1175/1520-0485(1995)025<2141:VDAZAO>2.0.CO;2. 7.1.1

Wunsch, C. (1996), *The Ocean Circulation Inverse Problem*, 458 pp., Cambridge University Press, Cambridge, U.K. 1.1, 1.1

Wunsch, C. (2005), The total meridional heat flux and its oceanic and atmospheric partition, *J. Clim.*, *18*, 4374–4380. 1.1

Wunsch, C. (2012), Predicting the ocean circulation, Talk given at the Earth Sciences Department, Oxford University, on 10/02/2012. 4.3.2

Wunsch, C., and P. Heimbach (2007), Practical global oceanic state estimation, *Physica D*, *230*, 197–208, doi:10.1016/j.physd.2006.09.040. 8.2.2

Wunsch, C., and P. Heimbach (2008), How long to oceanic tracer and proxy equilibrium?, *Q. Sci. Rev.*, *27*, 637–651, doi:10.1016/j.quascirev.2008.01.006. 3.1

Zanna, L., and E. Tziperman (2005), Nonnormal amplification of the thermohaline circulation, *J. Phys. Oceanogr.*, *35*(9), 1593–1605. 3.1.1

Zanna, L., and E. Tziperman (2008), Optimal surface excitation of the thermohaline circulation, *J. Phys. Oceanogr.*, *38*(8), 1820–1830. 3.1.1

Zanna, L., P. Heimbach, A. Moore, and E. Tziperman (2011), Optimal excitation of interannual Atlantic meridional overturning circulation variability, *J. Clim.*, *24*, 413–427. 3.1.1

Zanna, L., P. Heimbach, A. Moore, and E. Tziperman (2012), Upper ocean singular vectors of the North Atlantic climate with implications for linear predictability and variability, *Q. J. R. Meteorol. Soc.*, *138*(663), 500–513. 3.1.1

Zhai, X., H. Johnson, and D. Marshall (2011), A model of Atlantic heat content and sea level change in response to thermohaline forcing, *J. Clim.*, *24*, 5619–5632, doi:10.1175/JCLI-D-10-05007.1. 3.5.1

Zhang, R., and T. Delworth (2005), Simulated tropical response to a substantial weakening of the atlantic thermohaline circulation, *J. Clim.*, *18*, 1853–1860. 1.1

Zhang, R., and T. Delworth (2006), Impact of Atlantic multidecadal oscillations on India/Sahel rainfall and Atlantic hurricanes, *Geophys. Res. Lett.*, *33*, L17,712. 1.1

Zika, J., M. England, and W. Sijp (2012), The ocean circulation in thermohaline coordinates, *J. Phys. Oceanogr.*, *42*, 708–724. 2.5